Dissertation
submitted to the
Combined Faculties for the Natural Sciences and for Mathematics
of the Ruperto-Carola University of Heidelberg, Germany
for the degree of
Doctor of Natural Sciences

presented by
Diplom-Physikerin Claudia Fensterer
born in Landau i. d. Pfalz

Oral examination: 01.02.2011

Holocene Caribbean Climate Variability reconstructed from Speleothems from Western Cuba

Referees: Prof. Dr. Augusto Mangini
Prof. Dr. Werner Aeschbach-Hertig

Abstract

Proxy records offer a high potential tool to investigate past climate variability. Stalagmites as a natural archive have the advantage that they are absolutely datable and past changes in precipitation or temperature can be highly resolved by the use of stable isotopes such as $\delta^{18}O$ and $\delta^{13}C$.
This study uses three stalagmites from north-western Cuba to investigate past precipitation variability in the Northern Caribbean. The records cover the whole Holocene and reveal variability on several time scales. Frequency analysis initially suggest solar forcing as a main driver, but it is shown that a high correlation to Northern Atlantic sea surface temperature, namely the Atlantic multidecadal oscillation, exist. This connection is visible on multidecadal as well as millennial time scales, i. e. the Bond cycles. During North Atlantic cold events, such as the Little Ice Age, the Bond events, the 8.2 ka event and the Younger Dryas, the Cuban records show drier conditions. A possible driver is the strength of the thermohaline circulation. If the thermohaline circulation is in a weaker phase, lower North Atlantic sea surface temperatures are possibly leading to a southward Inter-tropical convergence zone and drier conditions in Cuba. The records also reveal close connection to the Pacific El Niño-Southern Oscillation, which might be driven by the Atlantic itself. This study offers the first continuous Holocene stalagmite records from the Caribbean region and further contribute to the understanding of Atlantic and Pacific teleconnections on Northern Caribbean climate variability during the Holocene.

Zusammenfassung

Klimaarchive bieten ein großes Potential um die natürliche Klimavariabilität der Vergangenheit zu untersuchen. Stalagmiten haben den Vorteil der absoluten Datierbarkeit und vergangene Schwankungen in Niederschlag oder Temperatur können hochaufgelöst durch stabile Isotope wie $\delta^{18}O$ und $\delta^{13}C$ rekonstruiert werden.
Die vorliegende Studie verwendet drei Stalagmiten aus Nord-West Kuba um die Niederschlagsvariabilität der Vergangenheit in der nördlichen Karibik zu untersuchen. Die Archive decken das gesamte Holozän ab und zeigen eine Variabilität auf verschiedenen Zeitskalen. Frequenzanalysen deuten auf eine solare Modulation des Niederschlags hin, aber es wird gezeigt, dass eine wichtige Verbindung zu Nord Atlantischen Meeresoberflächentemperaturen, der Atlantisch Multidekadischen Oszillation, existiert. Diese Verbindung ist sichtbar auf multidekadischen Zeitskalen, aber auch auf Jahrtausenden, den Bond-Zyklen. Während Kältepisoden im Nordatlantik, wie z. B. in der kleinen Eiszeit, den Bond-Events, dem 8.2 ka-Event und der Jüngeren Dryas, zeigen die kubanischen Stalagmiten trockenere Bedingungen. Ein möglicher Antriebsmechanismus ist die Stärke der thermohalinen Zirkulation. Ist die thermohaline Zirkulation in einer schwächeren Phase, so sinken Nordatlantische Meeresoberflächentemperaturen, was zu einer südlichen Verschiebung der Innertropische Konvergenzzone und trockeneren Bedingungen in Kuba führt. Die Archive deuten auch auf eine Verbindung zur Pazifischen El Niño-Südlichen Oszillation hin, die möglicherweise von dem Atlantik selbst gesteuert wird. Die vorliegende Studie stellt die ersten Stalagmiten Archive des Karibischen Raumes vor, die das komplette Holozän abdecken und trägt zum Verständnis der Einflüsse von Atlantischen und Pazifischen Telekonnektionen auf die Niederschlagsvariabilität im Holozän in der nördlichen Karibik bei.

Contents

1 Introduction

The recent discussion of anthropogenic influence on climate denotes the importance of climate science. The report of the Intergovernmental Panel of Climate Change (IPCC) [2007] summarizes present knowledge about climate change with important implications for politics. To give projections for future trends in temperature or precipitation changes, climate models are used to simulate the effect of anthropogenic emissions of CO_2 on the Earth's climate. However, direct climate observations are often too short or unavailable to validate such climate models. Palaeo science offers a possibility to study past variations in climate and to extend the observational records back in time. Informations are stored in natural archives such as ice cores, sediment, tree rings, coral or speleothems. Stalagmites offer the advantage of being absolutely datable and highly resolved archives. Hence, speleothems are used to study past climate variability to characterize naturally occurring changes in precipitation or temperature and to investigate possible forcing mechanisms.

The analysis of palaeo proxy data shows, that climate during the Holocene experienced several abrupt climate changes [*Mayewski et al.* 2004]. However, the state of the art does not yet allow satisfying answers about the question if the observed changes are coincidental processes or if quasi-periodic forcing mechanisms underly. Therefore, studying the Holocene climate variability is of major scientific interest. Forcing mechanisms are thought to be of external nature, such as orbital parameters or solar influence. Also, internal drivers such as the thermohaline circulation, greenhouse gases and atmospheric circulation are possible candidates. Atmospheric circulation patters can be transmitted at large distance due to teleconnection patterns.

The Caribbean area offers a highly interesting study site. Located in the subtropics close to the Isthmus of Panama, the Caribbean is influenced by both Pacific and Atlantic, oceanic as well as atmospheric processes, e. g. the Inter-tropical Convergence Zone, the Atlantic Multidecadal Oscillation and teleconnections patterns such as El Niño-Southern Oscillation and the North Atlantic Oscillation. The competing influence of these modes of climate variability on tropical Atlantic climate is called the Tropical Atlantic Variability. The Caribbean therefore represents an important area to obtain information about past natural climate variability in the tropical region and its relationship to climate forcing mechanisms.

The important role of climate in human history has been suggested in the Caribbean area. E. g., several droughts are thought to have caused the collapse of the Maya

civilization on the Yucatan peninsula [*Hodell et al.* 1995, *Haug et al.* 2003]. In addition, Caribbean islands are especially vulnerable to natural phenomena such as hurricanes, tsunamis and earthquakes. Knowledge of precipitation patterns is therefore essential in policy [*Jury et al.* 2007].

This study was conducted within the DFG SPP INTERDYNAMIK ('Integrierte Analyse zwischeneiszeitklicher Klimadynamik'). The project CaribClim combines coral records of Bonaire (University of Bremen, Cyril Giry), stalagmite records from northwestern Cuba and climate models (University of Bremerhaven, Wei Wei) to gather insights about the control of seasonality and interannual to centennial climate changes in the Caribbean during the Holocene. Scientific questions within CaribClim are:

- What is the natural range of seasonality and interannual to centennial climate variability?
- Did the amplitudes and periodicities of interannual to centennial climate variability change during the Holocene?
- Did the strength of the seasonal cycle of hydrologic balance (and temperature) change?
- Which forcing mechanisms control the reconstructed climate variations?

Figure 1.1: *Schematic overview of location and proxies used in project CaribClim.*

Three well dated stalagmites covering the whole Holocene are presented in this study. Stable isotopes measured along the growth axis of each stalagmite are used as a proxy for past precipitation changes. Time resolution of the stalagmites allows the study of frequency and wavelet analysis for multidecadal to millennial timescales. Based on observed past climate variability, the study investigates possible forcing mechanisms. Stalagmite datings were conducted by C. Fensterer at the Heidelberg Academy of Science. This study was supervised by Prof. Dr. A. Mangini. Further measurements were

accomplished by C. Fensterer in cooperation with the University of Bristol (Prof. Dr. Denis Scholz, Dr. Dirk Hoffmann). The studied stalagmites were provided by Dr. Jesus Pajón of the Cuban Institute of Anthropology. Dr. Pajón also conducted the monitoring program in two caves in Cuba to study the cave environment. Measurements of stable isotopes were done at University of Innsbruck by Prof. Dr. C. Spötl. Dr. Manfred Mudelsee (Alfred Wegener Institute for Polar and Marine Research, Bremerhaven) assisted in the frequency analysis of the presented records.

This study first will give an overview of the studied cave location, processes for stalagmite growth, dating methods and influences on isotopes in stalagmites (Section 1). The second section will present forcing mechanisms of precipitation patterns in the Caribbean area, both in observed climate as well as in proxy archives. The role of Pacific and Atlantic influences on Caribbean climate variability is discussed. Section 3 shows results for stalagmite datings, isotopic records and spectral analysis. Section 4 discusses the observed results and sets the records in the context of regional and Atlantic/ Pacific climate variability, followed by a conclusion and outlook in Section 5.

2 Basics and Methods

2.1 Location, geological setting

Three stalagmites were studied from north-western Cuba. The location of the area of the cave systems is indicated in Fig. 2.1. Two stalagmites, Cuba Grande (CG) and Cuba Pequeño were collected in the Dos Anas cave system. The third stalagmite, Cuba Medio (CM) was collected in Santo Tomas cave system. Both cave systems are located in the Sierra de los Organos (Fig. 2.1) in the Province of Pinar del Rio. The Dos Anas cave system is part of the Majaguas cave system (total length of over 30 km) which is located in the Sierra de San Carlos (Fig. 2.1). The Santo Tomas cave system is located farer north in the Sierra de Quemados, approximately in a distance of 25 km to Dos Anas cave system. The karstified area is of Jurassic origin.

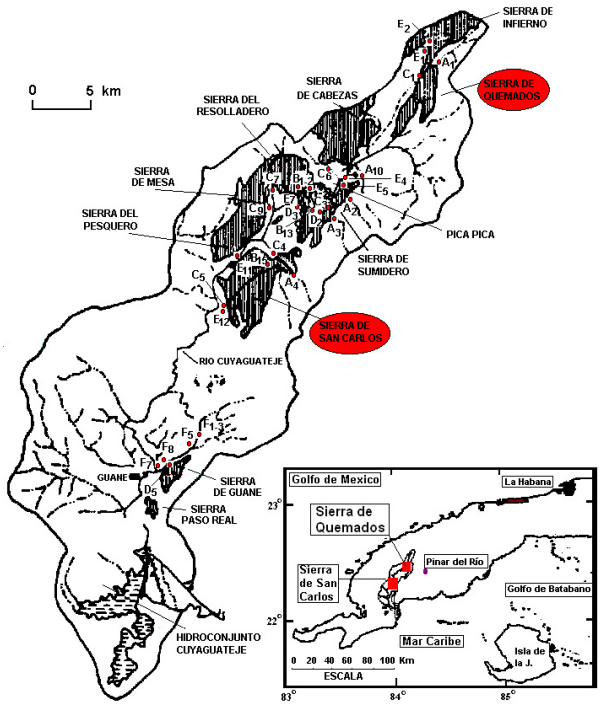

Figure 2.1: *Location of the cave systems in north-western Cuba in the Sierra de los Organos. Maps provided by J. Pajón.*

This karst area is part of Cuban's geologically oldest part and consist of carbonates, which developed around 170 million of years ago [*Pajón et al.* 2001]. Carbonate dissolution processes lead to the present visible mountains (Fig. 2.2). Subsurface water streams eroded the karstified material which lead to enormous cave systems. Collapse of some caves lead to the present characteristic cone karst formations, the 'Mogotes'. The formations can reach a height up to 400 m.

Figure 2.2: *Cone karst formations in western Cuba. Picture provided by J. Pajón.*

2.1.1 Dos Anas cave System

A map of the Dos Anas cave system (22° 23' N, 83° 58' W) is shown in Fig. 2.3. The cave system has a total length of ca. 14 km [*Pajón et al.* 2001]. Stalagmite Cuba Grande (CG) grew in Dos Anas cave at an elevation of ∼100 m above sea level and ∼150 m under the surface. The sampling location, which lies in the Salon de la Cimitarra (Fig. 2.3), is located in a distance of ca. 1.5 km from the cave entrance. The 720 mm long stalagmite sample is extremely white (Fig. 2.4, left). Cuba Pequeño (CP) grew in Hospitality gallery (Fig. 2.3) ∼90 m above sea level in a distance of 200 m to CG. The stalagmite is 420 mm long (Fig. 2.4, right).

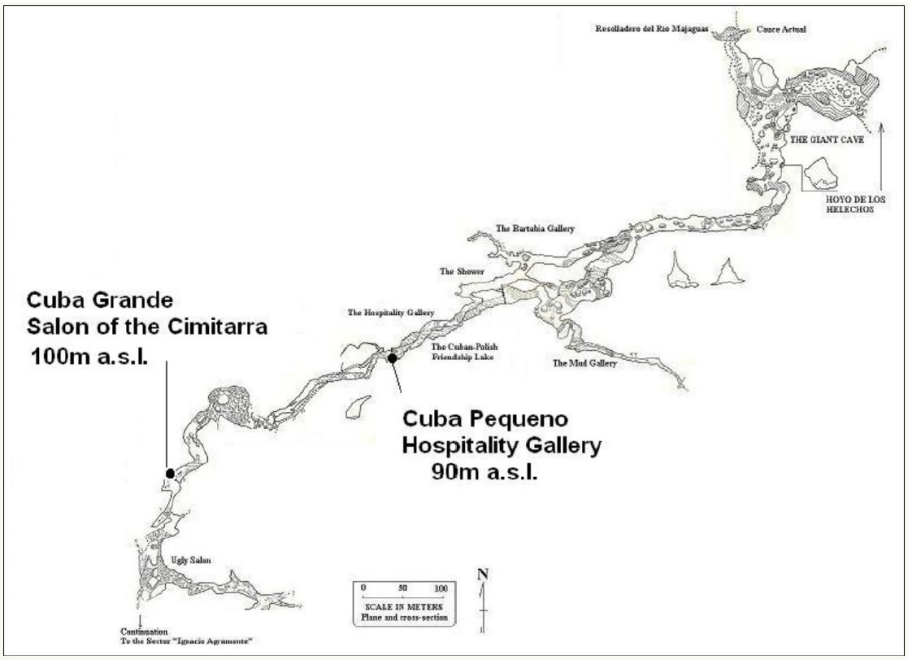

Figure 2.3: *Map of Dos Anas cave system. Map provided by J. Pajón.*

Figure 2.4: *Studied stalagmites in their natural environment before removing the sample from the cave. Left: CG, Salon de la Cimitarra. Right: CP, Hospitality gallery. Pictures provided by J. Pajón and P. Terzan.*

2.1.2 Santo Tomas cave System

The Santo Tomas cave system (22° 31' N, 83° 51 W) has a total length of ca. 46 km. Stalagmite Cuba Medio grew in Torch cave. The cave system shows several stages of cave development (Fig 2.5), stalagmite CM was removed from level 4, approximately in a height of 170 m above sea level with ≈60 m ground above. A map of the cave system can be found in Fig. 2.6. The stalagmite is shown in Fig. 2.7 and has a length of 520 mm.

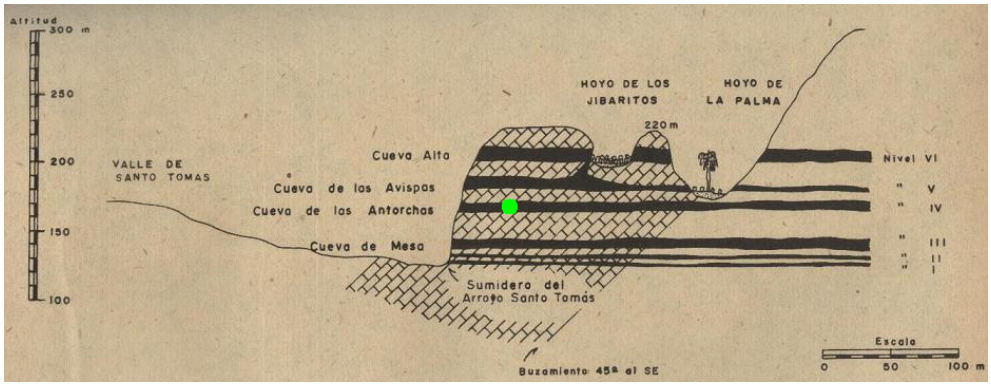

Figure 2.5: *Vertical profile of Santo Tomas cave system. The location of stalagmite CM is indicated on level 4. Figure adapted from Núñez Jiménez et al. [1988].*

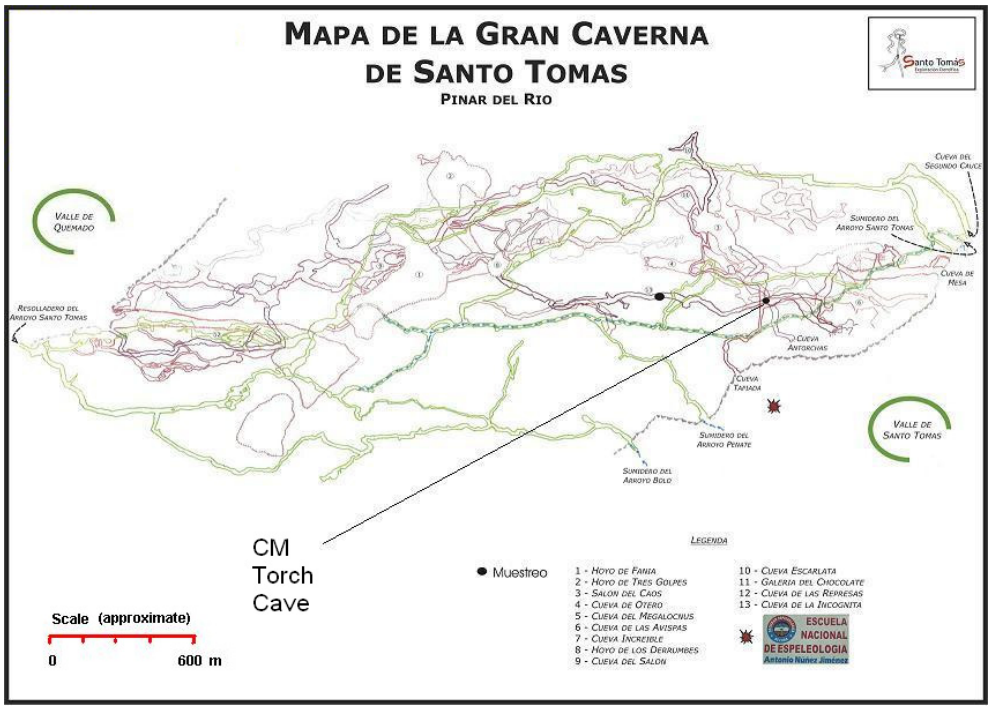

Figure 2.6: *Map of the Santo Tomas cave system. Figure adapted from Parise et al. [2005].*

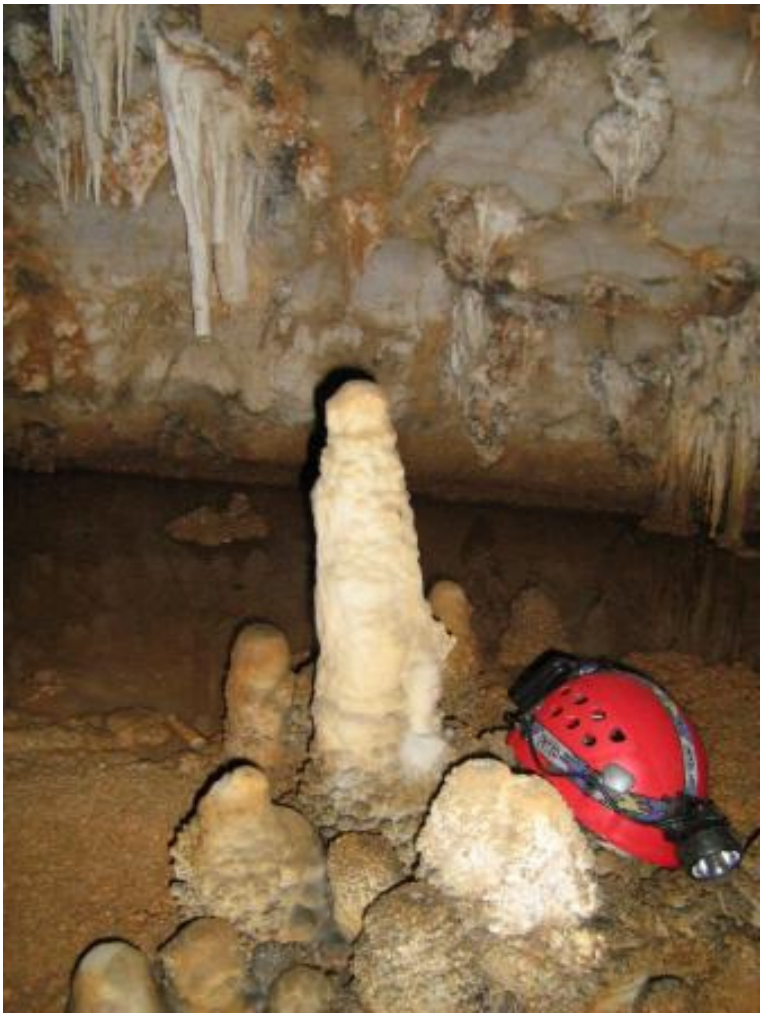

Figure 2.7: *Stalagmite CM in its natural environment before removing the sample from the cave. Picture provided by J. Pajón.*

2.2 Formation of Speleothems

Speleothems, such as stalagmites, stalactites or flowstones, are secondary cave deposits. The basic requirement for their formation is the presence of carbonate $CaCO_3$ in the host rock. Another prerequisite is sufficient water and CO_2 supply. The most common source of elevated pCO_2 is the vegetation above the cave. Roots of plants add CO_2 to the soil zone by respiration or decay of organic material. In the free atmosphere, the mixing ratios are ≈350 ppm and can reach values up to 100000 ppm in the soil zone [*McDermott* 2004]. Processes are summarized in the different soil zones in Fig. 2.8. If water seeps through the soil, it gets enriched in CO_2. Carbonic acid is produced [*Fairchild et al.* 2006]:

$$H_2O + CO_{2(aq)} \rightleftharpoons H_2CO_3 \tag{2.1}$$

Carbonic acid dissolves according to:

$$H_2O + H_2CO_3 \rightleftharpoons HCO_3^- + H_3O^+ H_2O + HCO_3 - \rightleftharpoons CO_3^{2-} + H_3O^+ \tag{2.2}$$

The resulting acid solution dissolves the carbonate hostrock in the 'dissolution region' [*Fairchild et al.* 2006]:

$$CO_2 + H_2O + CaCO_3 \rightleftharpoons Ca^{2+} + 2HCO_3^- \tag{2.3}$$

The equilibrium reaction between carbonate dissolution and precipitation can then be written as:

$$Ca^{2+} + 2HCO_3^- \rightleftharpoons CaCO_3 \downarrow + H_2O + CO_2 \uparrow \tag{2.4}$$

Equilibrium of Ca^{2+} and HCO_3^- in the drip water above a stalagmite depends on several parameters. E. g., temperature, pCO_2 and whether dissolution occurs in an open or closed system play a crucial role [*Kaufmann* 2003, *McDermott* 2004]. The pCO_2 of cave air is higher than outside the cave (depending on the cave ventilation), but much lower than in the soil zone. Therefore, the CO_2, which is dissolved in the water entering the cave, degases and drip waters become supersaturated with respect to calcite so that $CaCO_3$ can precipitate forming speleothems [*Scholz and Hoffmann* 2008]. According to [*Fairchild et al.* 2006], this zone is called the 'precipitation region'. Stalagmite growth was first quantitatively described by *Dreybrodt* [1988] and *Dreybrodt* [1999]. Other models describing growth rate and shape of a stalagmite depending on cave temperature, drip rate, pCO_2 of the soil zone and the cave can be found in [*Kaufmann* 2003], [*Mühlinghaus et al.* 2007] and [*Romanov et al.* 2008].

The predominant mineral which precipitates in cave systems is calcite. However, also aragonite and gypsum are found in stalagmites. The dissolution of carbonates can also result in accumulation of trace elements in the drip water, e. g. Mg and Sr. Mg-rich solutions or biogenic effects can lead to the formation of aragonite. Those elements

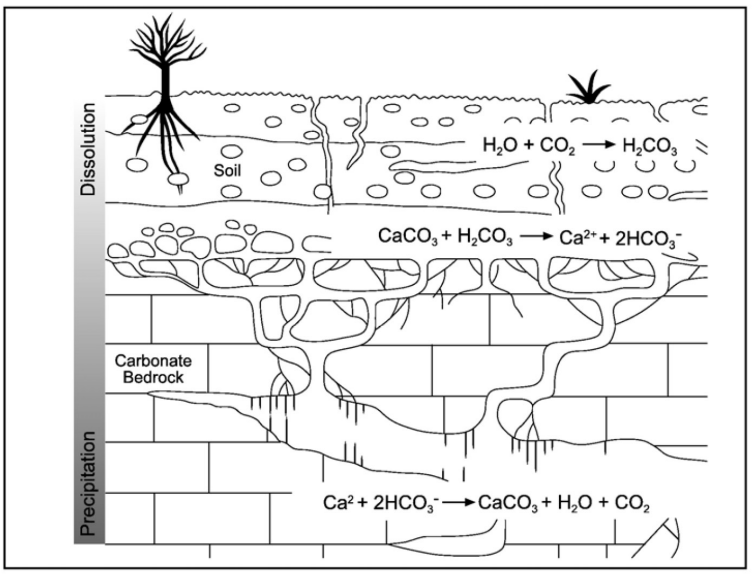

Figure 2.8: *Dissolution and precipitation regions in the kart system. Figure adapted from Fairchild et al. [2006].*

form divalent cations in the solution which substitute Ca in the carbonate crystal lattice [*Fairchild and Treble* 2009]. For such species, the distribution or partition coefficient can be used to relate solution and mineral composition [*Morse and MacKenzie* 1990]:

$$\frac{c(Tr)}{c(Ca)}_{CaCO_3} = K_{Tr}\frac{c(Tr)}{c(Ca)}_{solution} \tag{2.5}$$

where Tr is the trace ion and K_{Tr} is the distribution coefficient, which may also vary to greater or lesser extent with temperature, precipitation rate, crystal morphology or other aspects of solution composition [*Fairchild and Treble* 2009]. E. g., for calcite, the partition coefficient for Mg was found to be 0.031 at 25 °C by *Huang and Fairchild* [2001]. The authors note, that for Sr, the K_{Sr} is mainly in the range of 0.057 to 0.078. K_{Tr} differs significantly for aragonite and hence it is important to distinguish between those two phases [*Fairchild and Treble* 2009]. E. g., the partition coefficient for aragonite was found to be 0.002 for Mg [*Brand and Veizer* 1983]. Due to the different partitioning behavior, aragonite itself is both strongly enriched in Sr and depleted in Mg [*McMillan et al.* 2005]. The Ca site in the calcite structure (6 coordination) can easily be taken by smaller bivalent cations than Ca^{2+}, e. g. Mg^{2+}, whereas the Ca site in aragonite (9 coordination) is substituted by larger bivalent cations, such as Sr^{2+} [*Terakado and Masuda* 1988]. High Mg solutions therefore inhibit calcite nucleation and growth since Mg is not readily accepted in the aragonite lattice and therefore its level drops substantially as aragonite precipitation initiates [*McMillan et al.* 2005]. However, in caves it might also indicate evaporative processes [*Richards and Dorale* 2003]. Mg/Ca ratios as indicator for aragonite was studied in *McMillan et al.* [2005] and *Holzkämper et al.* [2009].

2.3 U-series dating methods

U-series dating is a precise method for dating speleothems younger than 500 ka [*Richards and Dorale* 2003]. The method is based on disequilibrium which establishes between parent U isotopes and their long-lived daughters. Three naturally occurring decay chains exist, starting with a long living actinide nuclide of ^{238}U, ^{235}U or ^{232}Th. Half lives of those nuclides are 4.58 Ga for ^{238}U, 0.7 Ga for ^{235}U and 14 Ga for ^{232}Th (Fig. 2.9 for ^{238}U). All actinides occur with their daughter nuclides, which have shorter half lives. In the decay chain of ^{238}U, ^{234}U has a half-live of 245 ka and ^{230}Th of 75 ka. Therefore, undisturbed naturally occurring materials with an age of several million years are in secular equilibrium. Geochemical processes can fractionate nuclides and produce disequilibrium. The quantification of time is possible due to the return to equilibrium [*Bourdon et al.* 2003, *Ivanovich and Harmon* 1993].

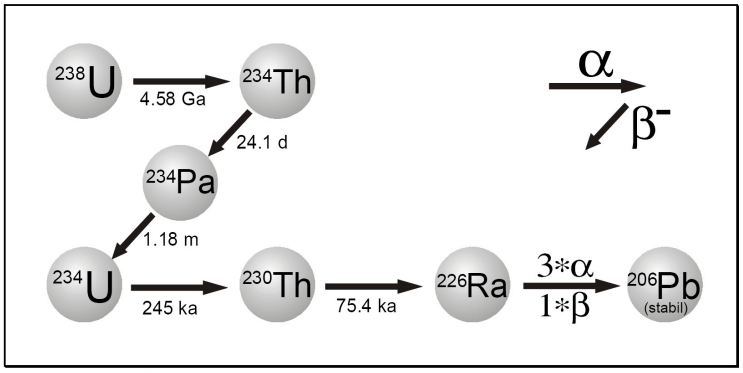

Figure 2.9: *Decay chain of ^{238} subdivided into alpha- and beta-decay with respective half-lives. Figure adapted from Neff [2001].*

2.3.1 U and Th geochemistry

In the continental crust, typical U concentrations range from 0.1 μg/g (basalt) to 6 μg/g (granite). Typically, limestone incorporates around 2 μg/g, but also values up to 100 μg/g are found in speleothems. Limestone has Th concentrations from 0 to 2.4 μg/g and up to 10 μg/g in speleothems [*Ivanovich and Harmon* 1993].

The utility of U-series dating methods is that several natural processes can disrupt the state of equilibrium between parent and daughter isotopes. The first fractionation can occur from the radioactive α decay of ^{238}U to ^{234}U and is due to the α-recoil effect [*Ivanovich and Harmon* 1993]. During the decay, the crystal structure is damaged by the α particle [*Bourdon et al.* 2003]. Also, the atom is displaced from its original position. This results in the daughter nuclide ^{234}U to be more easily remobilized than its parent during weathering processes. The second fractionation occurs due to the different geochemical behaviour of Th and U. U is much more soluble and mobile

in aqueous solutions than Th. U naturally exists in two oxidation states (U^{4+} and U^{6+}). At the surface, it mainly occurs as the U^{6+} form as uranyl-ion $(UO_2)^{2+}$. In a reducing environment the ion can also exist as U^{4+}, being insoluble and less mobile than U^{6+}. Th (mainly Th^{4+}) on the other hand is insoluble in natural waters and mainly transported adsorbed to particles or in minerals. Th is therefore not incorporated during precipitation of secondary carbonates such as corals, speleothems or travertines [*Ivanovich and Harmon* 1993, *Richards and Dorale* 2003].

2.3.2 Calculation of Th/U ages

The activity A of a number of atoms of a nuclide is the number of decay events per unit of time. In this work all activities and activity ratios are indicated by parenthesis (e.g. (^{238}U)) and are given in decays per minute [dpm]. The equation of decay for given a number of atoms, N, of a nuclide is as follows:

$$A = \frac{dN}{dt} = -\lambda N \tag{2.6}$$

Integration of 2.6 leads to:

$$N(t) = N_0 \cdot e^{-\lambda t} \tag{2.7}$$

N(t): Number of atoms at the time t
N_0: Number of atoms at the time t = 0
λ: decay constant $[a^{-1}]$

λ is inversely related to the half live $T_{1/2}$:

$$\lambda = \frac{\ln 2}{T_{1/2}} \tag{2.8}$$

The equation of decay for the daughter atoms can be written as:

$$\frac{dN_2}{dt} = -\lambda_2 N_2 + \lambda_1 N_1 \tag{2.9}$$

The first term describes the decay of the daughter nuclide and the second term describes the production of the daughter nuclide by decay of the mother.

For Th/U-dating the following assumptions are made:

1. $(^{230}Th)_{initial}$ is zero, the isotope is not incorporated during the precipitation of secondary carbonate due to its insolubility

2. The system remains closed after deposition, i.e. U and Th are not remobilized.

Based on these assumptions, the age t of a sample can be calculated iteratively by the following equation using $(^{234}U/^{238}U)$ and $(^{230}Th/^{234}U)$ (see *Ivanovich and Harmon*

[1993] for derivation):

$$\left(\frac{^{230}Th}{^{234}U}\right)(t) = \frac{1 - e^{-\lambda_{230}t}}{\left(\frac{^{234}U}{^{238}U}\right)} + \left(1 - \frac{1}{\left(\frac{^{234}U}{^{238}U}\right)}\right) \frac{\lambda_{230}}{\lambda_{230} - \lambda_{234}} \left(1 - e^{-(\lambda_{230} - \lambda_{234})t}\right) \quad (2.10)$$

The equation can be illustrated graphically as shown in Fig. 2.10 and 2.11.

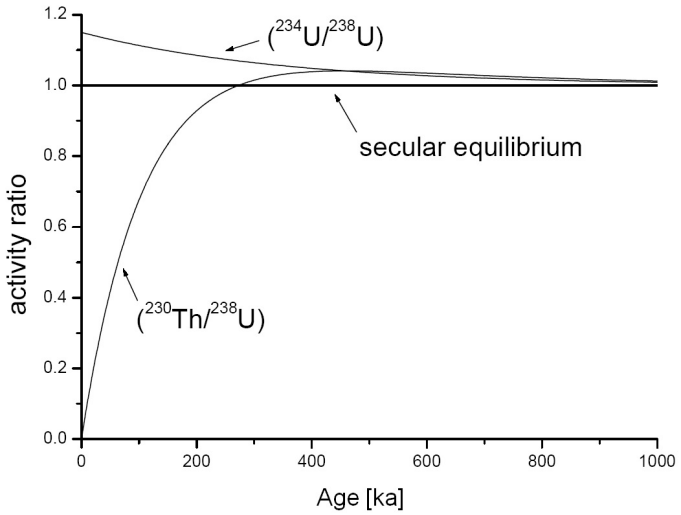

Figure 2.10: *Evolution of the relevant activity ratios. Figure adapted from Neff [2001].*

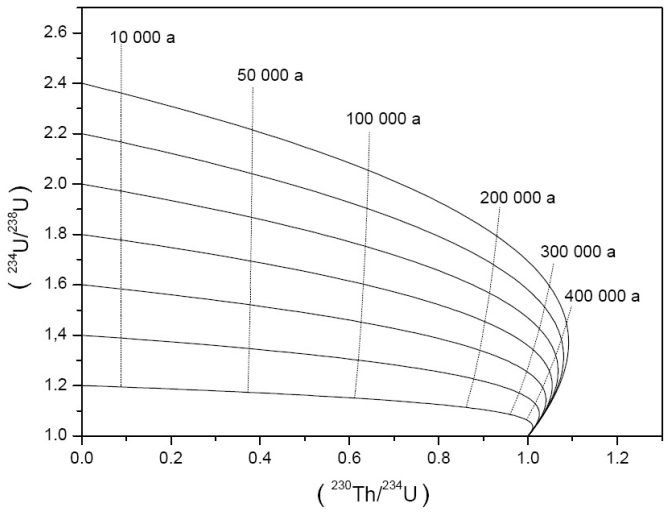

Figure 2.11: *Variation of the ($^{234}U/^{238}U$) and ($^{230}Th/^{234}U$) ratios with time in a closed system with no initial ^{230}Th. The vertical lines are so-called isochrons, the near horizontal lines show the development of the activity ratios with time for different initial $^{234}U/^{238}U$ ratios. Figure adapted from Neff [2001].*

The $\left(^{234}U/^{238}U\right)$ ratio can also be written in the δ-notation in ‰:

$$\delta^{234}U = \frac{\left(\frac{^{234}U}{^{238}U}\right)_{meas} - \left(\frac{^{234}U}{^{238}U}\right)_{eq}}{\left(\frac{^{234}U}{^{238}U}\right)_{eq}} \cdot 1000 = \left(\left(\frac{^{234}U}{^{238}U}\right)_{meas} - 1\right) \cdot 1000 \tag{2.11}$$

where $\left(\frac{^{234}U}{^{238}U}\right)_{eq}$ denotes equilibrium.

2.3.3 Correction for initial detrital contamination

As indicated above, a basic assumption of U-series dating is that all ^{230}Th present in a sample is formed in situ by radioactive decay of co-precipitated U and that the crystal remains a closed system after deposition [*Ivanovich and Harmon* 1993]. However, small quantities of initial ^{230}Th are often incorporated during precipitation of speleothem $CaCO_3$ by detrital contamination of clay minerals or biogenous material. Usually, the ^{232}Th concentration is used as a proxy for initial ^{230}Th [*Ludwig and Titterington* 1994], and the ^{230}Th/^{232}Th activity ratio indicates whether a correction needs to be applied. As a threshold for mass spectrometric analysis an activity ratio between 100 and 300 has been suggested [*Li et al.* 1989, *Richards and Dorale* 2003].

There are different methods to estimate the extent of contamination with initial ^{230}Th:

1. direct measurement of the isotopic composition of the contaminating phase using isochron techniques on multiple sub samples [*Ludwig and Titterington* 1994].

2. assuming an a-priori estimate for the isotopic composition of the contaminating phase [*Ivanovich and Harmon* 1993, *Dorale et al.* 1998, *Hellstrom* 2006], e.g., the bulk earth ^{232}Th/^{238}U concentration ratio of the upper crust of 3.8 [*Wedepohl* 1995] and secular equilibrium for ^{230}Th, ^{234}U and ^{238}U.

The second approach is based on the assumption that the detrital material is several millions of years old so that activity ratios of all isotopes of the ^{238}U decay chain series are in secular equilibrium. Numerous measurements of ^{232}Th and ^{238}U of the Earth's upper crust yielded a mean mass ratio of ^{232}Th/^{238}U $\approx 3.8 \pm 1.0$ [*Wedepohl* 1995]. Thus, the concentrations of non-authigenic ^{238}U, ^{234}U and ^{230}Th can be calculated and corrected for, using the following equations:

$$c\left(^{238}U_{detr}\right) = \frac{c\left(^{232}Th_{meas}\right)}{c\left(^{232}Th_{detr}/^{238}U_{detr}\right)} = \frac{c\left(^{232}Th_{meas}\right)}{3.8} \tag{2.12}$$

The activity (^{238}U) of the detrital ^{238}U concentration c($^{238}U_{detr}$) can then be calculated by:

$$\left(^{238}U\right)_{detr} = -N\lambda = -\frac{N_A \cdot c(^{238}U_{detr})}{238} \cdot \lambda_{238} \tag{2.13}$$

$$\Rightarrow (^{238}U)_{detr} = c(^{238}U_{detr}) \cdot 0.7478 \tag{2.14}$$

where 0.7478 is the factor for calculating the specific activity of (^{238}U) in dpm/g from a concentration in μg/g, and N_A is the Avogadro constant. Since the isotopes of the ^{238}U decay chain in the detritus are in secular equilibrium, their activities are equal $\left(^{238}U\right)_{detr} = \left(^{234}U\right)_{detr} = \left(^{230}Th\right)_{detr}$. The detrital contribution can be subtracted from the measured activities of the isotopes ^{238}U, ^{234}U and ^{230}Th, so that the age determination is done with activities of pure carbonate:

$$\left(^{238}U\right)_{carb} = \left(^{238}U\right)_{meas} - \left(^{238}U\right)_{detr} \quad (2.15)$$

$$\left(^{234}U\right)_{carb} = \left(^{234}U\right)_{meas} - \left(^{234}U\right)_{detr} \quad (2.16)$$

$$\left(^{230}Th\right)_{carb} = \left(^{230}Th\right)_{meas} - \left(^{230}Th\right)_{detr} \quad (2.17)$$

Depending on the (^{230}Th/^{232}Th) of the sample, the correction may have a significant effect on the ^{230}Th-^{234}U-^{238}U activity ratios, and it is obvious that the accuracy of the corrected ratios depends on the accuracy of the correction factor. Using the a-priori estimate, the effect of propagating the assumed uncertainty of the isotopic composition of the contaminating phase through the age calculation may also be quite severe [*Hellstrom* 2006]. Thus, in case that a correction for detrital contamination is applied, precise direct measurement of the isotopic composition of the contaminating phase is required. The composition of detrital phases can be very different from the a-priori assumed bulk earth value, e.g., due to partial leaching effects, Th adsorbtion, alpha recoil or non silicate origin of the detrital phase prior to deposition [*Hellstrom* 2006]. An alternative approach for accounting for detrital contamination is studied in Section 4.1 since the isochron technique was not applicable for the studied stalagmite.

2.3.4 MC-ICPMS and TIMS

The two most precise analytical techniques for the determination of U and Th isotope ratios are multi-collector inductively coupled plasma mass spectrometry (MC-ICPMS) and thermal ionization mass spectrometry (TIMS) [*Scholz and Hoffmann* 2008]. MC-ICPMS is a plasma source mass spectrometer (Fig. 2.12). The ion source is a torch, in which Ar plasma is generated by a radio frequency (RF) coil. Purified dissolved U and Th samples are nebulized and mixed with Ar sample gas. The mixture is injected into the plasma (T ≈8000 °C) and almost completely ionized [*Scholz and Hoffmann* 2008]. At the transfer from the plasma at atmospheric pressure into the mass spectrometer at high vacuum, more than 90 % of the ions are lost. Inside the mass spectrometer, ions are accelerated by an extraction voltage via electrical lenses into the mass-analyzer section, which usually consists of an electrostatic analyzer (ESA) module and an magnetic analyzer. The ESA is essentially an energy filter. The total U amount which is needed per analysis is of about 5-10 ng [*Hoffmann et al.* 2007].

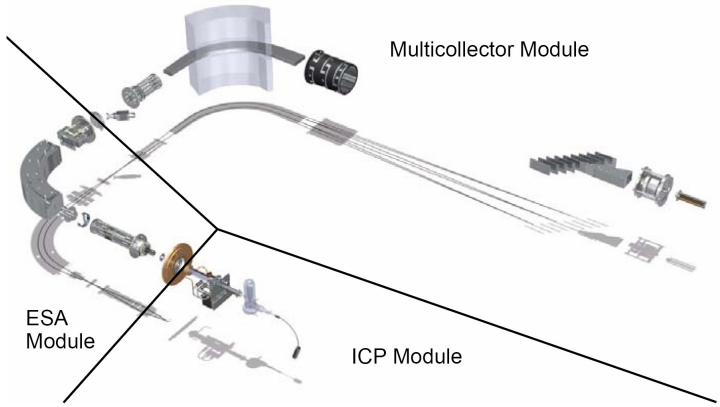

Figure 2.12: *Components of MC-ICPMS. Figure adapted from Finnigan [2004].*

The TIMS is a solid source mass spectrometer. Purified U and Th solutions are placed on a Rhenium filament, which is placed in the ion source of the mass spectrometer [*Scholz and Hoffmann* 2008]. The sample chamber then is evacuated to vacuum and the filament heated by an electric current. Atoms are thermally released and ions accelerated by a high potential ion source, the ion beam is focused into a mass analyzer section (Fig. 2.13). The mass analyzer is a magnetic field. The total U amount needed for one analysis is in the range of a few tens to hundreds of nanograms, precision of a few permill can be achieved [*Scholz and Hoffmann* 2008].

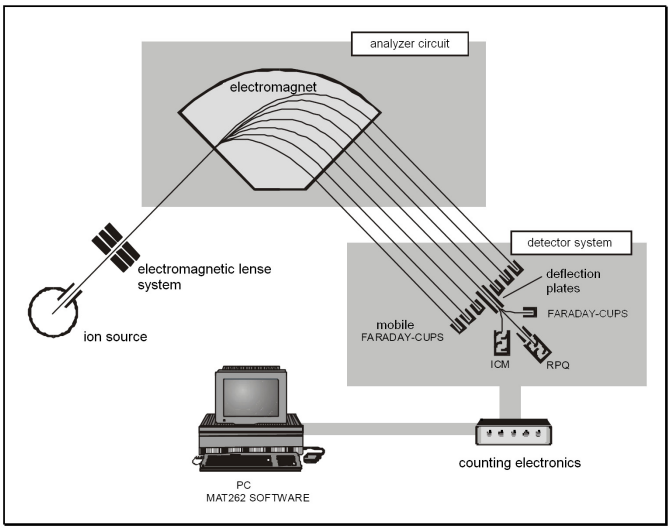

Figure 2.13: *Components of TIMS. Figure adapted from Neff [2001].*

The key difference between both methods is the transfer efficiency of isotopes, which is $\ll$1% with TIMS, but $\sim$1% with MC-ICP-MS [*Scholz and Hoffmann* 2008]. For young samples with low uranium content, the MC-ICPMS technique thus enables both

a higher precision of ^{230}Th/U-dating and to use smaller sample sizes. Further, this method offers faster sample throughput and sample-standard switching while keeping instrumental tuning constant, which enables the use of an external standard bracketing procedure for corrections of instrumental bias [*Hoffmann et al.* 2007]. Using MC-ICPMS can also have some disadvantages compared to TIMS, such as higher background intensities, potential interferences, greater instrumental mass fractionation and decreased abundance sensitivity [*Hoffmann et al.* 2007].

Chemical preparation of the samples follows the methods described in *Hoffmann et al.* [2007] and *Hoffmann* [2008] for MC-ICPMS and in *Scholz et al.* [2004] for TIMS. Different U and Th spikes were used in both laboratories. The calibration of both spikes and an inter-laboratory comparison is described in *Hoffmann et al.* [2007]. The comparison did not show any significant differences for the two spike solutions. The quoted age uncertainties in this work include uncertainties from the detrital correction. Details about uncertainties of MC-ICPMS can be found in *Hoffmann et al.* [2007]. All uncertainties are quoted at 95 % confidence level.

2.4 Speleothems as paleoclimatic archive

During the last decades, speleothems were increasingly being recognized as palaeoclimatic archive. A wide variety of parameters can be investigated from speleothems. In addition, stalagmites offer a high temporal resolution compared to sea sediments for example. With U-series dating methods, stalagmites can be dated precisely, also beyond the limit (≈45 ka) of radiometrically dated archives such as marine sediments or ice cores. However, a disadvantage of speleothems is that a single deposit may or may not represent global/hemispheric climate conditions such as ice cores do. To overcome this, it is necessary to look at a large number of locations of terrestrial archives [*Holzkämper* 2004]. This work uses stable isotopes profiles (^{18}O/^{16}O and ^{13}C/^{12}C ratios) to reconstruct past climate variability. Stable isotopes in carbonate deposits are influenced by several parameters and provide a great potential for climatic interpretations.

^{18}O/^{16}O and ^{13}C/^{12}C ratios are usually expressed in the δ notation which gives the deviation of the isotopic ratio of the sample relative to that of a standard [*Lachniet* 2009a]:

$$\delta^{18}O = \frac{^{18}O/^{16}O_{sample} - ^{18}O/^{16}O_{standard}}{^{18}O/^{16}O_{standard}} \cdot 1000 \tag{2.18}$$

Here, the standard for carbonates is the Vienna Pee Dee Belemnite (PDB) and that for waters (also used for meteoric waters) the Vienna Standard Mean Ocean Water (VSMOW). The conversion of δ^{18}O values given against one of the standards into the other one is given by [*Lachniet* 2009a]:

$$\delta^{18}O_{VSMOW} = 1.03091 \cdot \delta^{18}O_{VPDB} + 30.86 \tag{2.19}$$

$$\delta^{18}O_{VPDB} = 0.97006 \cdot \delta^{18}O_{VSMOW} - 29.94 \tag{2.20}$$

The main factors which influence the observed $\delta^{18}O$ values are

1. the isotopic composition of the water which charges the deposit, i. e. precipitation and groundwater and
2. the conditions under which calcite is precipitated from the solution.

The first important factor is the composition of precipitation and groundwater. Meteoric waters (snow and rain) show a close relationship to climatic parameters such as air temperature or amount of precipitation [*Vuille et al.* 2003, *Lachniet* 2009a]. In the tropics, the seasonal cycles of temperature and $\delta^{18}O$ composition of precipitation are often opposed to each other, high (low) temperatures coincide with more depleted (enriched, higher) $\delta^{18}O$ values. This phenomenon is usually interpreted in the sense that the $\delta^{18}O$ composition of precipitation reflects precipitation amount rather than temperature, because at low latitudes high temperatures and rainy season tend to coincide [*Vuille et al.* 2003]. This 'amount effect' is caused by small scale vertical convection. As condensation proceeds, the isotopically enriched molecules are preferentially removed, leaving the isotopic composition of the remaining vapor increasingly lighter. As oceanic air moves inland and loses water, the remaining atmospheric water vapor becomes progressively depleted in heavy isotopes ('continental effect'). Once the water vapour reaches an orographic obstacle, the adiabatic cooling and precipitation associated with rising air masses will further contribute to the depletion of this air masses ('altitude effect') [*Grabczak et al.* 1983, *Gonfiantini et al.* 2001]. The isotopic composition of precipitation can also shift due to a change of the dominant source regions ('source effect') for precipitation at a given site [*Charles et al.* 1994, *Cole et al.* 1999] or because of a change in the seasonality of precipitation ('seasonality effect'). On longer timescales, the $\delta^{18}O$ values of the ocean play also a crucial role. on glacial/interglacial transitions, the evaporation of ocean water preferentially removes the light stable isotopes into the vapour, the $\delta^{18}O$ values of the ocean will increase as the volume of freshwater stored on the continents as ice increases [*Lachniet* 2009a]. An overview of effects is given in table 2.1.

The second important driver of the $\delta^{18}O$ in carbonate precipitates is the isotopic fractionation. Fractionation is the process by which one isotope is favored over the other during a phase change (e. g., liquid evaporating to vapor, or precipitation of $CaCO_3$ from dissolved bicarbonate in drip waters) [*Lachniet* 2009a]. It can be defined as:

$$\alpha_{A-B} = \frac{R_A}{R_B} \tag{2.21}$$

where α is the equilibrium fractionation and R is the isotopic ratio (e. g. $^{18}O/^{16}O$) between substances A and B [*Sharp* 2007]. Fractionations are typically expressed in the form of $1000\ln\alpha$.

Two cases can be distinguished, namely oxygen-isotope equilibrium fractionation and kinetic (disequilibrium) fractionation between water and precipitated $CaCO_3$ [*Lachniet*

Temperature effect	+0.17 to +0.9‰/°C	*Dansgaard* [1964], *Rozanski et al.* [1993], *Lachniet* [2009a]
Altitude effect	-2 to -3 ‰/km	*Gonfiantini et al.* [2001], *Poage and Chamberlain* [2001] *Fleitmann et al.* [2004], *Lachniet and Patterson* [2006]
Amount effect	-1.24 ‰/100mm for Belize and Guatemala	*Lachniet and Patterson* [2009c]
	-1.6 to -2.85 ‰/100mm for Panama	*Lachniet and Patterson* [2006], *Lachniet et al.* [2004b]
	-2.2 to -2.75 ‰/100mm for Barbados	*Jones et al.* [2000]
	-2 ‰/100mm for Oman	*Fleitmann et al.* [2004]
Ice volume effect	+1 to +1.2 ‰ during max. Quaternary ice volume	*Schrag et al.* [1996], [2002], *Lea et al.* [2002], *Sharp* [2007]
Continental effect	δ^{18}O ↓ if distance to ocean ↑	*Dansgaard* [1964], *Rozanski et al.* [1993], *Clark and Fritz* [1997]

Table 2.1: *Summary of important influences on the $\delta^{18}O$ of precipitation. The seasonality and source effect are described in the text.*

2009a]. For the equilibrium case, the temperature at the time of growth is an important factor. The fractionation results in the preferential incorporation of δ^{18}O in the $CaCO_3$, which has stiffer bonds [*Sharp* 2007]. For synthetic calcite, an equilibrium fractionation factor relationship was determined by *Kim and O'Neil* [1997]:

$$1000 \ln \alpha_{calcite-aragonite} = 18.03(10^3 T^{-1}) - 32.42 \tag{2.22}$$

where $1000\ln\alpha_{calcite-water}$ is the fractionation between the calcite and water, and T the temperature in K. The slope of δ^{18}O varying with temperature ranges from -0.18 to -0.23 ‰/°C for temperatures of 35 °C and 5 °C, respectively [*Lachniet* 2009a]. Together with an estimate of the temperature dependence of precipitation δ^{18}O, palaeo temperatures can be reconstructed. E. g., a combined method can be found in [*Mangini et al.* 2005] for stalagmites from the Austrian Alps. If kinetic fractionation occurs, a quantitative estimate of palaeo temperatures is impossible. The kinetic fractionation is due to irreversible physical or chemical processes and can occur if evaporation of water takes place in cave environments [*Lachniet* 2009a].

The equilibrium or kinetic fractionation can be studied by the δ^{18}O and δ^{13}C values along single growth layers of a stalagmite [*Hendy* 1971]. If δ^{13}C rise with increasing dis-

tance from the growth axis of a stalagmite, whereas δ^{18}O values remain constant, this might be indicative of equilibrium conditions [*McDermott* 2004]. If both isotopes increase, this indicates kinetic fractionation, because evaporation of water or CO_2 affects both isotopes.

The equilibrium fractionation is also dependent upon the carbonate mineralogy, e. g. calcite and aragonite [*Lachniet* 2009a]. Under equilibrium conditions, the fractionation equation for synthetic aragonite can be written as [*Kim et al.* 2007]:

$$1000 \ln \alpha_{aragonite-water} = 17.88(10^3 T^{-1}) - 31.14 \tag{2.23}$$

Fig. 2.14 shows the temperature dependency of the fractionation of aragonite in comparison to calcite in equilibrium [*Lachniet* 2009a] (fractionation factors used of *Kim and O'Neil* [1997], *Kim et al.* [2007] and *Patterson et al.* [1993]). Aragonite will be precipitated with δ^{18}O values 0.7 to 0.8 ‰ higher than calcite [*Kim et al.* 2007]. These values are consistent with experimental work [*Tarutani et al.* 1969] and δ^{18}O measurements indicating 0.6 to 1.4 ‰ higher δ^{18}O values in aragonite than in co-occuring calcite in Carlsbad Caves, New Mexico, USA [*Gonzalez and Lohmannn* 1988] and in Grotte De Clamouse, France [*Frisia et al.* 2002, *McMillan et al.* 2005].

For this study mainly δ^{18}O is used as a palaeoclimate proxy. However, δ^{13}C is also used to study kinetic fractionation along several growth layers.

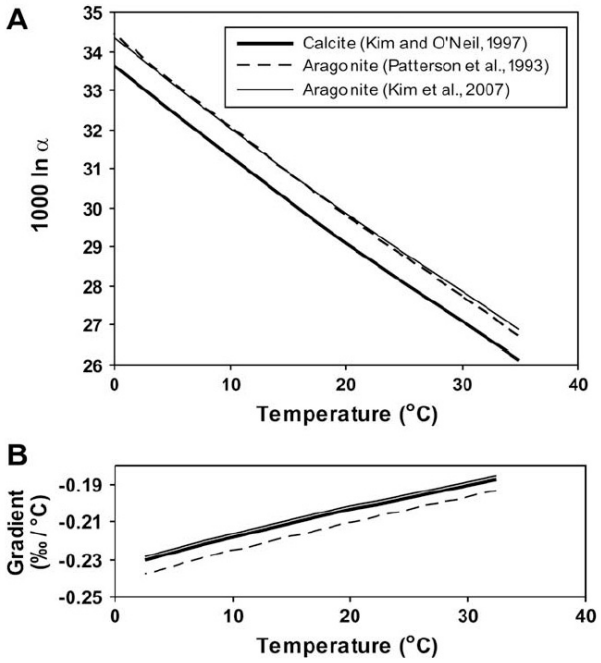

Figure 2.14: *A: Equilibrium $\delta^{18}O$ fractionation between water and $CaCO_3$ as a function of temperature; B: Gradient of $\delta^{18}O$ equilibrium fractionation as a function of temperature. Figure adapted from Lachniet [2009a].*

3 Caribbean Climate Variability

The Caribbean area is located in a region, which is both directly and indirectly influenced by many atmospheric processes, mainly competing effects between Atlantic and Pacific teleconnection patterns. In this chapter, the main climatic features in the investigated area will be discussed, followed by a section dealing with climate variability on various timescales. The last section will give an overview of already available reconstructions of past climate from the Caribbean and also North Atlantic and Pacific regions, which also indicate controlling factors of past climate variability on various timescales.

3.1 Climatic Parameters in the Caribbean

3.1.1 Annual precipitation pattern

The basic controlling factor of both the Atlantic and the eastern Pacific Oceans regarding trade winds, the Hadley cell circulation, and interactions occurring between land surfaces and atmosphere at specific time scales is the Inter-tropical convergence zone (ITCZ) [*Poveda et al.* 2006], Fig. 3.1. The ITCZ is a region close to the equator, where trade winds converge, air ascends, low atmospheric pressure occurs together with deep convective clouds and high precipitation [*Henderson-Sellers and Robinson* 1986]. The meridional oscillation of the ITCZ responds to the seasonal insolation cycle, lagging the zenithal position by approximately one month [*Poveda et al.* 2006]. This oscillation exerts a strong regional control on the annual hydroclimatological cycle. As shown in Fig. 3.1, sea surface temperatures (SSTs) in the Caribbean vary over the year with a maximum in northern hemisphere summer ($\sim$29 °C) and a minimum in winter ($\sim$26 °C).

Observational air temperatures in north western Cuba (Isabel Rubio, averaged over 1952-1960 and 1981) are shown in Fig. 3.2 (red). They indicate a connection to SSTs in the Caribbean on a seasonal timescale. The data are available at the Global Historical Climate Network (GHCN) [*Vose et al.* 1992].

Fig. 3.2 (blue) shows the evolution of precipitation over the year (Guane, 1950-1960, *Vose et al.* [1992]) which is closely connected to SST in the Tropical North Atlantic (TNA) and the Caribbean Sea. A diagnostic for convective development are regions which are denoted by SSTs greater than 26.5 °C [*Gray* 1968, *Taylor et al.* 2002]. Prior to the onset of the Caribbean rainfall season (March), SSTs of the tropical North

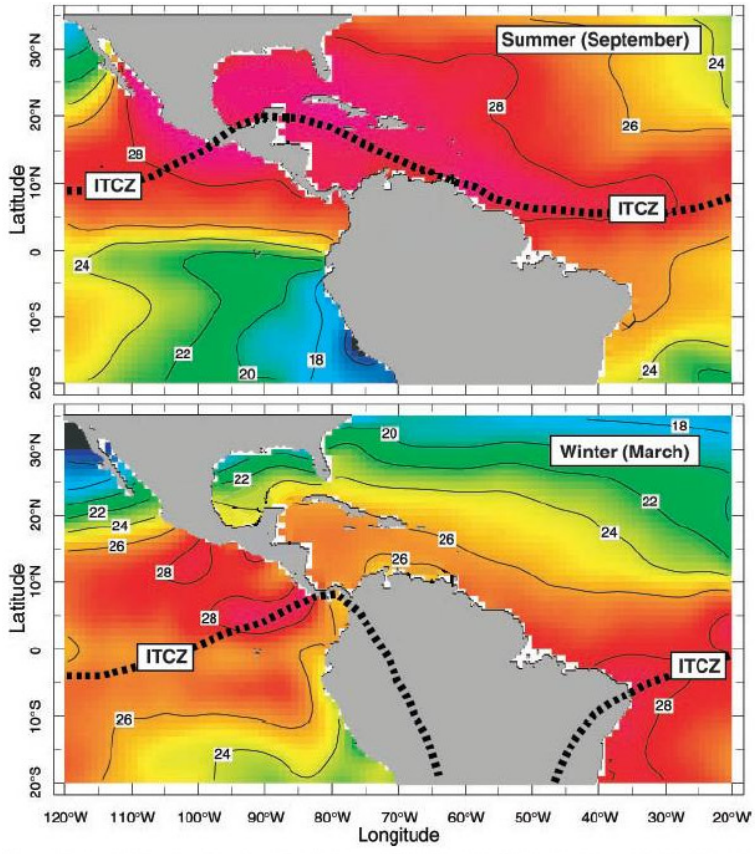

Figure 3.1: *Seasonal variations of the position of the ITCZ over Mesoamerica and northern South America, indicated for summer (September, top) and winter (March, bottom) conditions. The variations control the pattern and timing of regional rainfall. Number and colours reflect sea surface temperatures in degrees Celsius. Illustration adapted from Haug et al. [2003].*

Atlantic are well below this threshold, only the far western Caribbean is capable of supporting convective activity [*Taylor et al.* 2002], Fig. 3.3. At the onset of the Caribbean rainfall season (May), the warm SSTs gradually spread eastward in the ensuing months. By August, which is the start of the late rainfall season, the region of favourable SST encompasses the entire Caribbean and extends through the mid TNA and main development region (MDR). The MDR is defined as a latitudinal band from 10-20 °N, which *Goldenberg and Shapiro* [1996] denote the main development region for easterly waves which are convection centers that frequently mature into tropical storms and hurricanes [*Taylor et al.* 2002].

The climate of the Caribbean basin can generally be classified as dry-winter tropical climate [*Rudloff* 1981], with significant subregional variations in annual totals, length of the rainy season and timing of rainfall maxima [*Giannini et al.* 2000]. The rainy season occurs as easterly trade winds produced by the North Atlantic Subtropical High

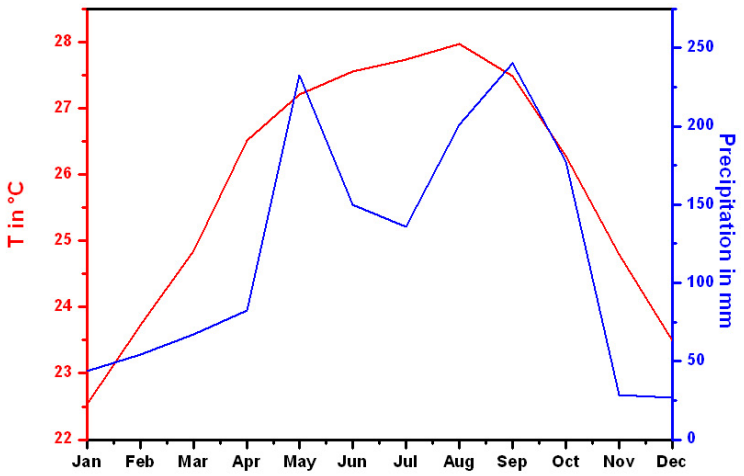

Figure 3.2: *Seasonal variations of air temperature (red) and amount of precipitation (blue) from observational data.*

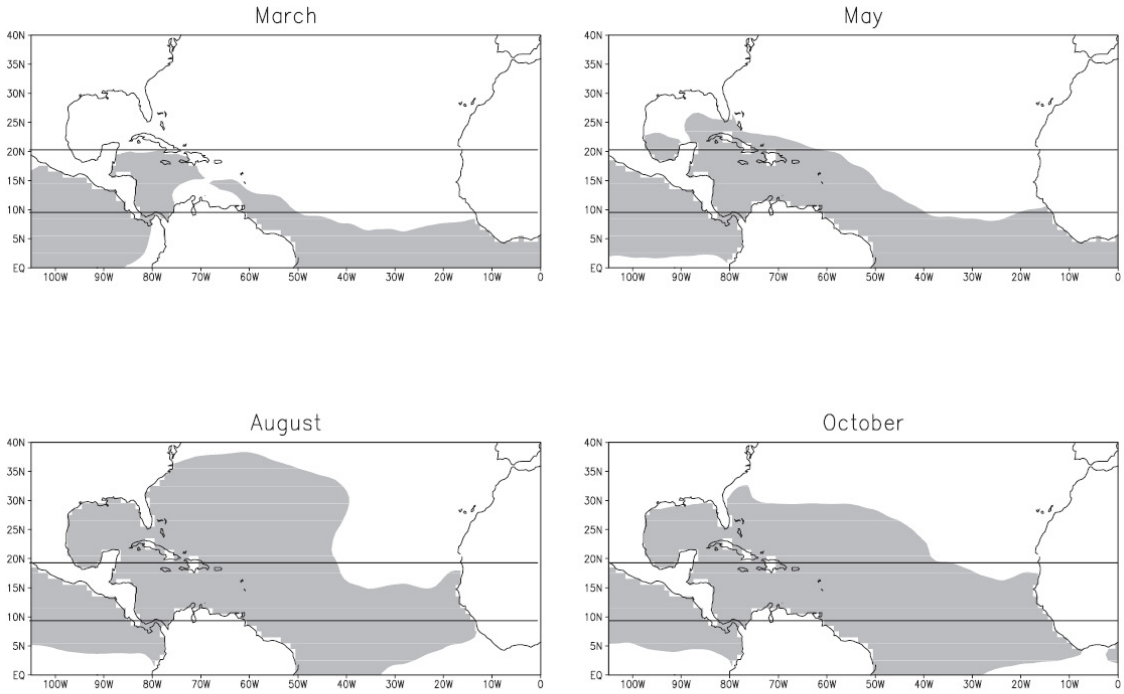

Figure 3.3: *Climatological evolution of the tropical North Atlantic warm pool during the Caribbean rainy season. Shading indicates regions with waters warmer than 26.5 °C, parallel lines indicate the MDR. Figure adapted from Taylor et al. [2002].*

(NASH) transport moisture from the Atlantic into the Caribbean Sea, where the flow intensifies forming the Caribbean Low Level Jet (CLLJ) [*Amador* 1998, *Amador and Magaña* 1999, *Mestas-Nuñez et al.* 2005, *Mestas-Nuñez et al.* 2007, *Hodell et al.* 2008]. During boreal summer in the western Caribbean, the CLLJ splits into two branches,

as shown in Fig 3.4 [*Mestas-Nuñez et al.* 2007]. One branch turns northward bringing moisture to the western Gulf of Mexico, and the southerly branch of the CLLJ continues westward carrying moisture across the Central American isthmus to the Pacific. During boreal winter, the NASH dominates the Intra-American Sea, and moisture transport is shifted south of the Yucatan Peninsula [*Hodell et al.* 2008]. Low moisture transport marks the subsidence related to the descending limb of the Hadley Cell (centered at ~20 °N) [*Waliser et al.* 1999].

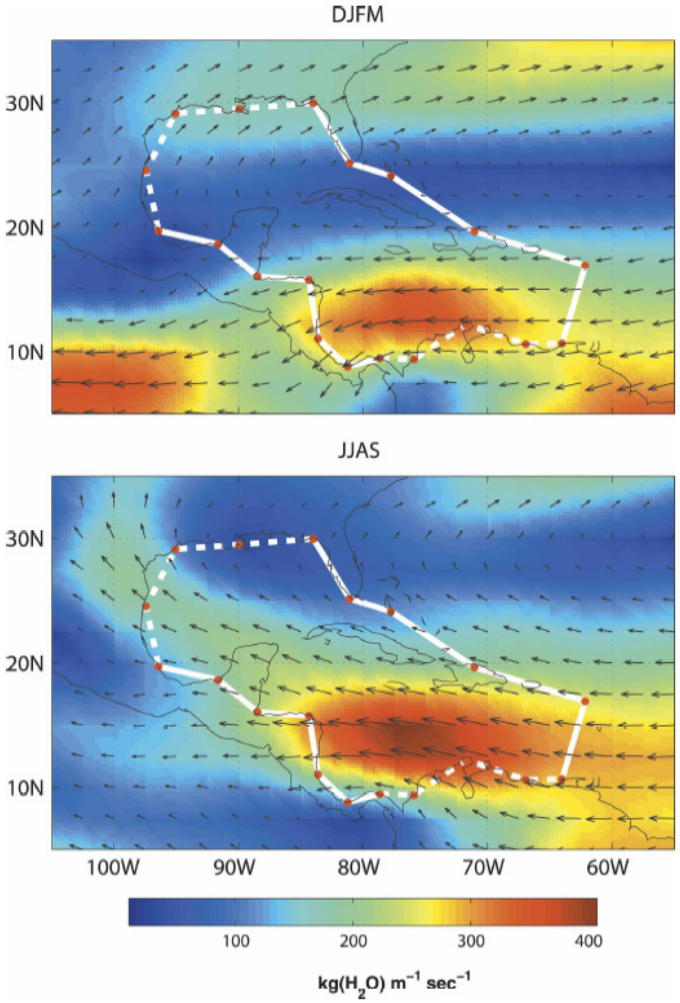

Figure 3.4: *December to March (top) and June to September (bottom) averages of the monthly vertically integrated water vapour flux vectors calculated from 1960 to 2003 by Mestas-Nuñez et al. [2007]. The magnitudes of the vectors are colour contoured. The thick lines indicate intra American sea (IAS) boundary segments as used in Mestas-Nuñez et al. [2007].*

In most parts of the Caribbean, the rainfall season runs from May through November and is bimodal in nature [*Taylor et al.* 2002], Fig. 3.2, with an initial maximum in May, a relative minimum in June, July and August followed by a second peak in September

and October [*Rudloff* 1981, *Giannini et al.* 2000, *Chen and Taylor* 2002, *Jury et al.* 2007]. The general precipitation pattern differs in the southernmost Caribbean off the Venezuelan coast, which receives less rainfall and has a primary rain season during the winter (November, December, January) [*Martis et al.* 2002].

Four geographic precipitation regions can be distinguished across the Caribbean Islands related to annual cycles and interannual fluctuations of rainfall. Precipitation patterns are more unimodal and largest in the northwest Caribbean and become more bimodal towards lower latitudes, 3.5) [*Jury et al.* 2007]. The studied cave systems lie in Cluster 1, which is characterized by a significant rainfall maximum in early summer around May. This maximum slowly declines in a southeasterly direction through Clusters 2 and 3 and is replaced by a late-summer maximum around October for cluster 4. Cluster 1 also exhibits a relatively large contribution of May-July rainfall to annual precipitation and relatively low contributions of November-December rainfall. Being further north and on the edge of the tropical rainfall belt, this cluster exhibits a larger annual cycle. Clusters further to the southeast are situated at lower latitude, where the rainy season tends to spread across the year.

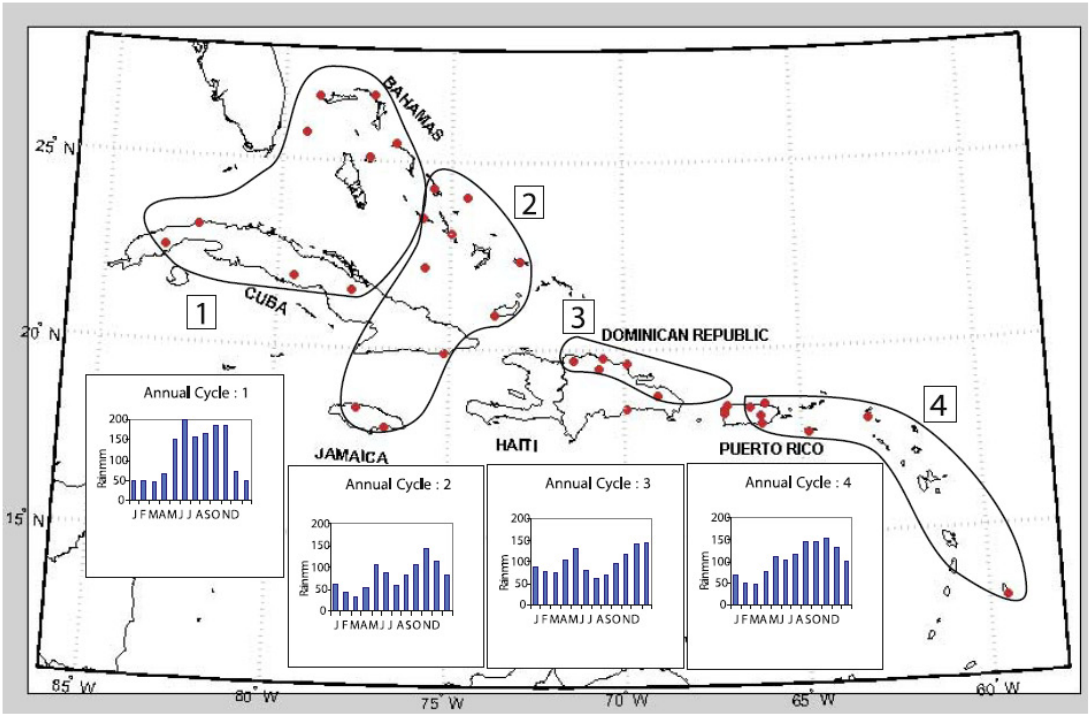

Figure 3.5: *Locations and geographic extent of the four precipitation clusters identified by Jury et al. [2007]. Annual cycles are also indicated (blue).*

The warm season (May-October) is dominated by conditions favorable to convection, i. e. warm SSTs and, therefore, a deep, unstable boundary layer, easterly propagation of disturbances, convergence of winds towards the basin from both the Atlantic and

Pacific. The midsummer drought (MSD) is associated with the temporary intensification of the North Atlantic High [*Hastenrath* 1976, *Hastenrath* 1978, *Hastenrath* 1984, *Granger* 1985, *Jury et al.* 1997, *Giannini et al.* 2000, *Gamble et al.* 2008]. The expansion of the NAHP translates into stronger trade winds, cooler sea surface temperatures, increased subsidence and diminished Caribbean rainfall, but is not consistent over the region [*Giannini et al.* 2000]. During the cold season (November to April) subsidence dominates the region, stifling convection, which results in a dry winter season. The bimodal rainfall pattern is most pronounced in the western Caribbean. The authors also found that the bimodal pattern of annual rainfall centered around a MSD accounts for 66 % of the total variance of the annual cycle of Caribbean rainfall and is most pronounced in the western Caribbean. The study of *Gamble et al.* [2008] suggests that the NAHP impacts the eastern Caribbean first and then progresses westwards as the summer develops.

3.1.2 δ^{18}O in the tropical Americas

The seasonal variation of the δ^{18}O signal of rainfall in Havana, Cuba, is shown in Fig. 3.6a (data from the IAEA Global Isotopes in Precipitation Network (GNIP) *IAEA/WMO* [2006]) averaged over the years 2002-2004 (green). The signal is inversely related to the amount of precipitation (blue, data from *Vose et al.* [1992]). The δ^{18}O signal over the tropical Americas has been studied with atmospheric general circulation models (AGCMs) and compared to observational data in the study of *Vuille et al.* [2003]. The δ^{18}O signal shows an annual mean value of around -3 ‰ in the Caribbean area (Fig. 3.6b). The difference between DJF and JJA values is shown in Fig. 3.7a for GNIP data and Fig.3.7b for the GCM ECHAM-4 T106 [*Vuille et al.* 2003], red meaning more depleted values in JJA. In the midlatitudes, this effect can be explained by the temperature control of δ^{18}O values of precipitation. Towards lower latitudes, on the seasonal timescale the δ^{18}O values are clearly controlled by precipitation amount, and more depleted values occur during the rainy season (JJA in the north). This shift of controlling factors of δ^{18}O in rainfall marks the boundary region to conditions close to the equatorial regions, which might offer the potential to reconstruct paleomonsoon intensity and the past extent of the ITCZ with the help of anually resolved δ^{18}O paleorecords [*Vuille et al.* 2003].

The δ^{18}O signal in Panama rainfall has been studied by *Lachniet* [2009b]. The authors note a clear connection to the amount effect on rainfall. Considering the source effect, the authors investigate northerly and southerly wind directions. An important finding is that observed northerly and southerly δ^{18}O rain values are not statistically different, although the south-westerly wind direction has the lowest δ^{18}O value due to its association with the wettest months in September to November [*Lachniet* 2009b].

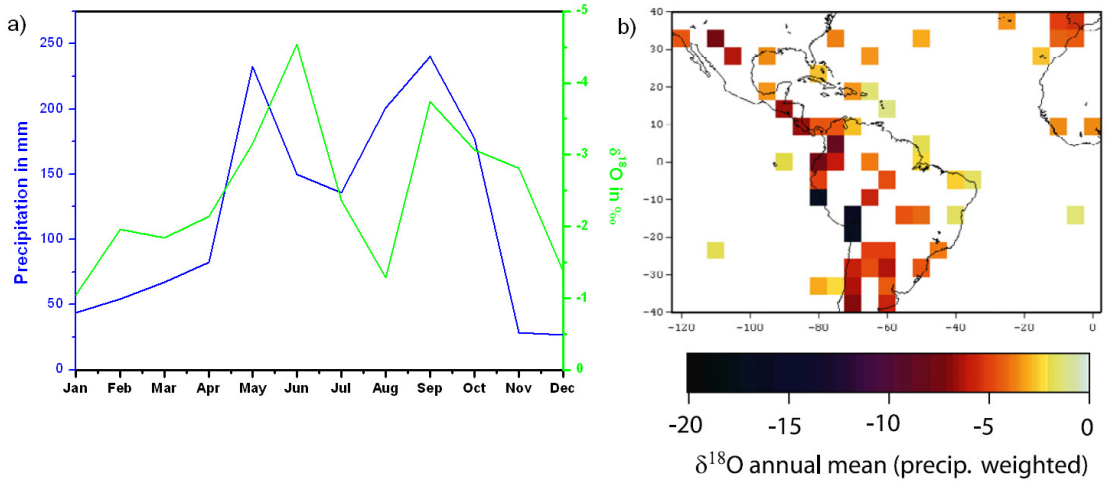

Figure 3.6: *a) GNIP $\delta^{18}O$ station data of Havana, 2002-2004, this study. b) Annual mean of GNIP $\delta^{18}O$ station data over the tropical Americas, various record lengths [Vuille et al. 2003].*

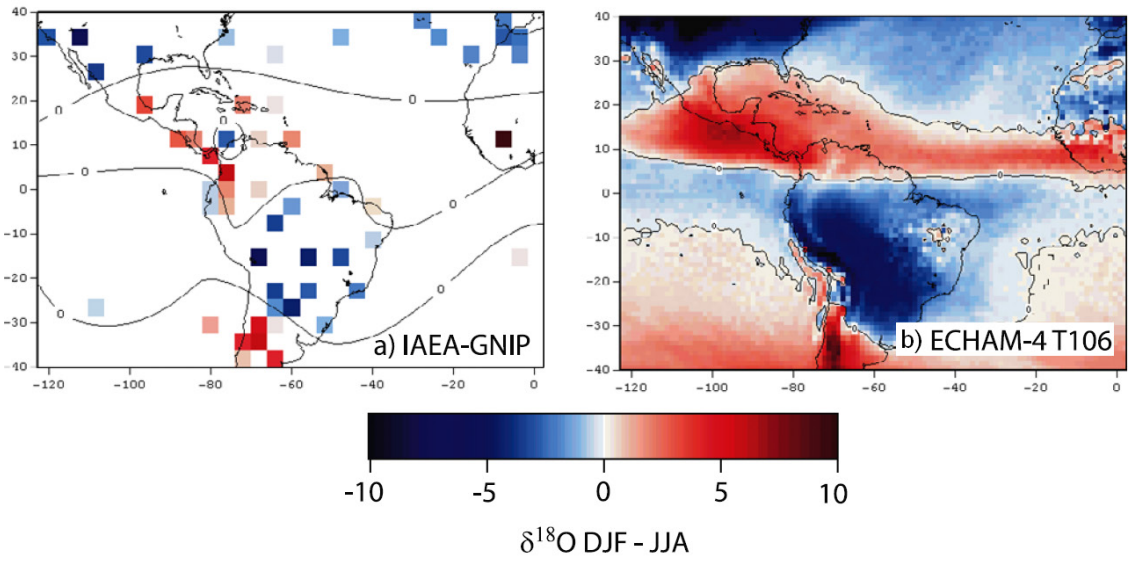

Figure 3.7: *The $\delta^{18}O$ signal of DJF minus JJA for a) GNIP station data and b) the ECHAM-4 T106 model of Vuille et al. [2003].*

3.2 Atmospheric Teleconnection Patterns in the Caribbean

Climate variability is usually characterized in terms of 'anomalies', where an anomaly is the difference between the instantaneous state of the climate system and the climatology (the mean state computed over many years representative of the era under consideration) [*Hurrell et al.* 2003]. Caribbean climate anomalies are strongly connected to Tropical Atlantic Variability (TAV) [*Hurrell et al.* 2006]. This includes the movement

of the ITCZ, as well as the influence of the North Atlantic Oscillation (NAO), the El Niño-Southern Oscillation phenomenon (ENSO) and the Atlantic Multidecadal Oscillation (AMO) [*Hurrell et al.* 2006], which all operate on different timescales ranging from subdecadal to multidecadal. In the next section, an overview of these teleconnection patterns will be given including their variability on different timescales.

3.2.1 El Niño Southern Oscillation

The tropical Pacific climate displays a zonal assymetry, being warmer in the west than in the east [*Chiang* 2009] (Fig. 3.8, middle panel). The tropical western Pacific possesses a warm pool of water exceeding 28.5 °C, and moist convection is located here as well as over the maritime continent. In the eastern Pacific, the cold tongue SST is typically below 25 °C, too cold to maintain convection of moisture. The equatorial thermocline (i. e., the sharp vertical gradient in ocean temperature separating the warm surface layer from the colder interior ocean) is deeper in the eastern Pacific than in the west. Equatorial upwelling driven by easterly trades, thus, upwells colder water in the eastern equatorial Pacific than in the west [*Chiang* 2009]. With the introduction of a slight zonal SST gradient with warmer SST to the west and colder SST to the east, the convection favors the west and surface low pressure will be generated there. The resulting zonal pressure gradient drives stronger surface easterlies, which in turn drive surface ocean currents, which move equatorial surface waters to the west, deepening the thermocline to the west. This results in colder upwelled waters in the east, enhancing the initial zonal SST gradient (Fig. 3.8, lower panel, La Niña conditions). This feedback mechanism, called Bjerknes feedback [*Bjerknes* 1969], also works in the opposite direction, leading to El Niño conditions (Fig. 3.8, upper panel), in which the thermocline tilt reduces, the cold tongue disappears and moisture convection shifts to the central equatorial Pacific. A delayed oscillator mechanism [*Battisti and Hirst* 1989] acts to terminate the developed El Niño conditions. Wind perturbations in the central equatorial Pacific produce eastward propagating equatorial ocean planetary waves initiating El Niño, but also produce westward propagating waves after reflecting off the western boundary with a delay, shoaling the thermocline in the eastern Pacific and ending El Niño. All together, the Bjerknes feedback and the delayed oscillator produce a powerful interannual variation in tropical climate known as the El Niño-Southern Oscillation (ENSO). ENSO is one of the largest source of interannual variability in present-day global climate [*Chiang* 2009].

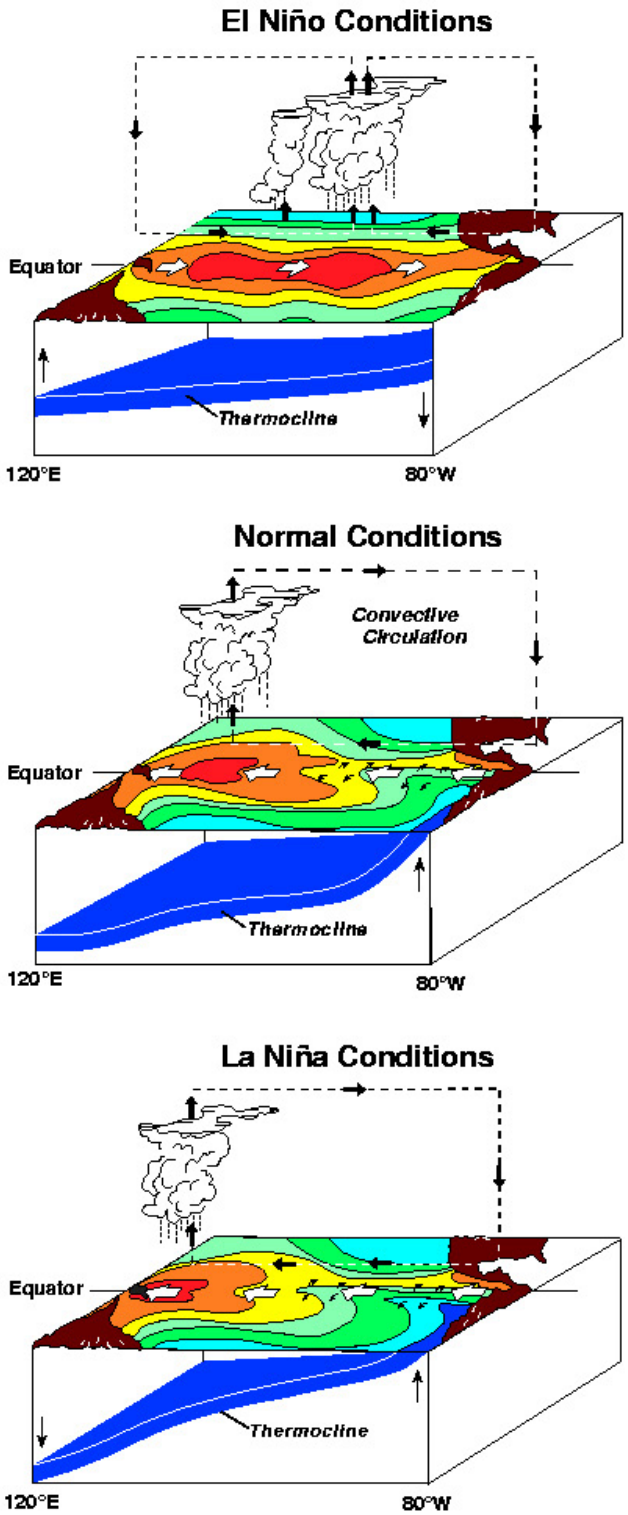

Figure 3.8: *The different phases of the El Niño-Southern Oscillation. Upper panel: El Niño conditions, middle panel: normal conditions, lower panel: La Niña conditions. Picture accessed at http://www.pmel.noaa.gov/tao/ on 7.6.2010.*

The changes of atmospheric circulation patterns during a mature phase of El Niño are indicated in greater detail in Fig. 3.9 from *Wang* [2002a]. During an El Niño event, both the Walker circulation cell and the midlatitude zonal cell (MZC) are weakened. The anomalous Hadley cell in the eastern Pacific during the mature phase shows the air rising in the tropical region, flowing northward in the upper troposphere, descending in the midlatitude and returning to the Tropics in the lower troposphere. The anomalous Hadley cell in the western Pacific has an opposite rotation as that of the anomalous Hadley cell in the eastern Pacific. The remote influence of ENSO on the tropical North Atlantic has been suggested by *Wang* [2002b] and is shown in Fig. 3.10. Following a mature phase of El Niño, the authors note a stronger Walker circulation over the Atlantic. This leads to a weakening of the Hadley cell, ascending motion in the Tropical North Atlantic and low SLP in the TNA region. Following this, a decrease in North east trade winds is observable, leading to an increase of TNA SSTs.

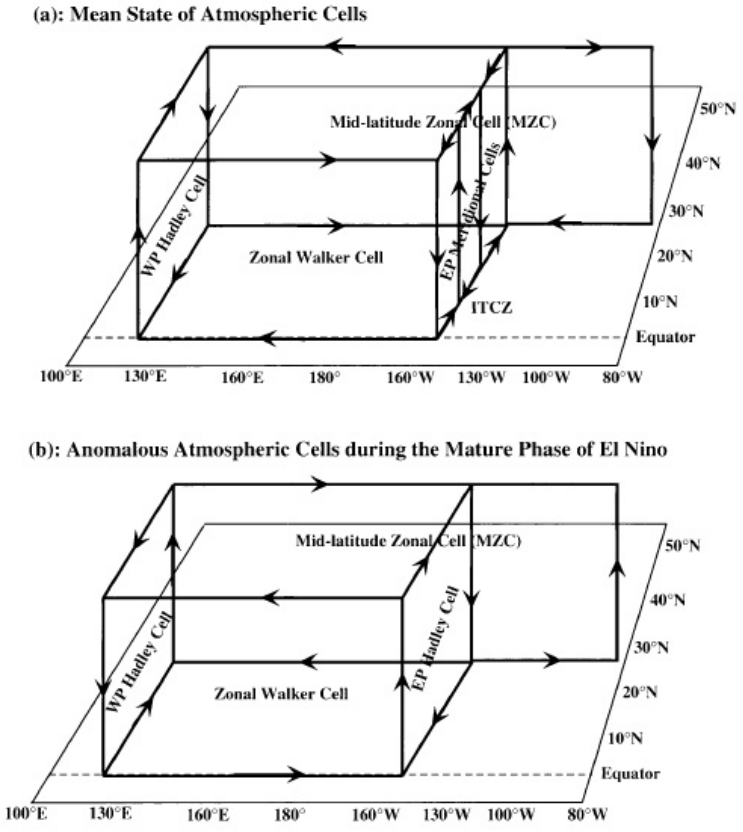

Figure 3.9: *Diagrams of (a) mean state of atmospheric circulation cells and (b) anomalous atmospheric circulation cells during the mature phase of El Niño (adapted from Wang [2002a]).*

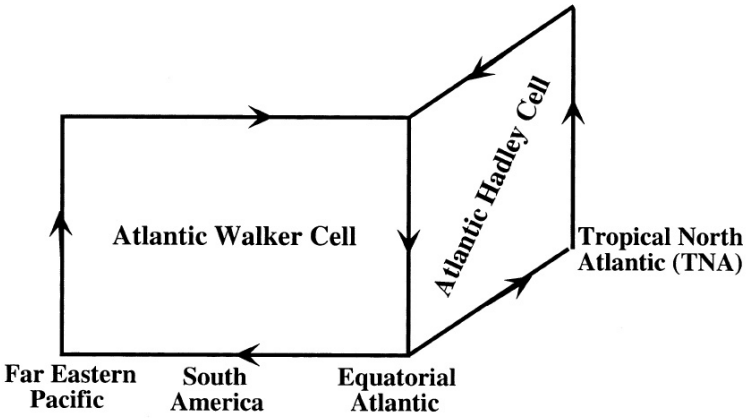

Figure 3.10: *Diagram showing how Pacific El Niño affects the TNA. Figure adapted from Wang [2002b].*

According to *Trenberth* [1997], El Niño can be said to occur if 5-month running means of SST anomalies in the Niño 3.4 region (Fig. 3.11) exceed 0.4 °C for 6 months or more. With this definition, El Niño occurs 31 % of the time and La Niña 23 % of the time. Most El Niños begin in northern spring or summer and peak from November to January in SSTs [*Trenberth* 1997]. A timeseries of the SST of the Niño 3 region is shown in Fig. 3.12. In addition, the sea level pressure of Darwin (Australia) is shown, beeing an index of the atmospheric southern oscillation. The most important feature is that the irregular oscillations occur about every 4 years. Usually, a periodicity of 2-7 years is taken as defining the ENSO band. There is no satisfactory theory explaining, why this is the case or what sets the average period of the ENSO cycle [*Cane* 2005]. A wavelet analysis of the Niño 3 SST has been done by *Jevrejeva et al.* [2003] and is shown in Fig. 3.13.

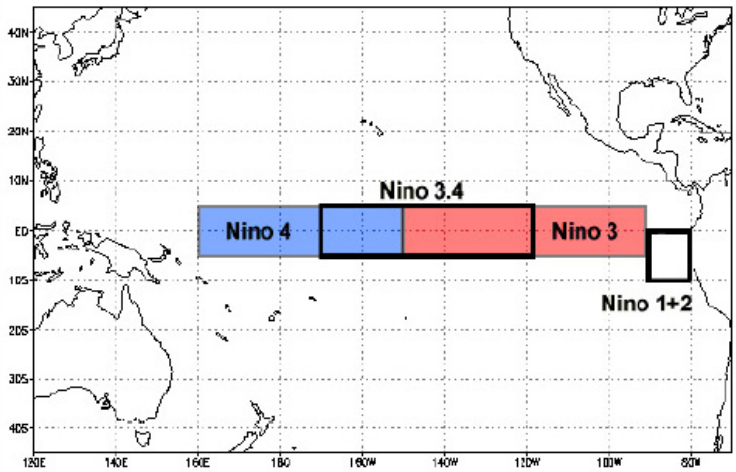

Figure 3.11: *Location of different Niño regions. Accessed via http://www.srh.noaa.gov/images/mlb/enso/nino-regions.gif on 19.7.2010.*

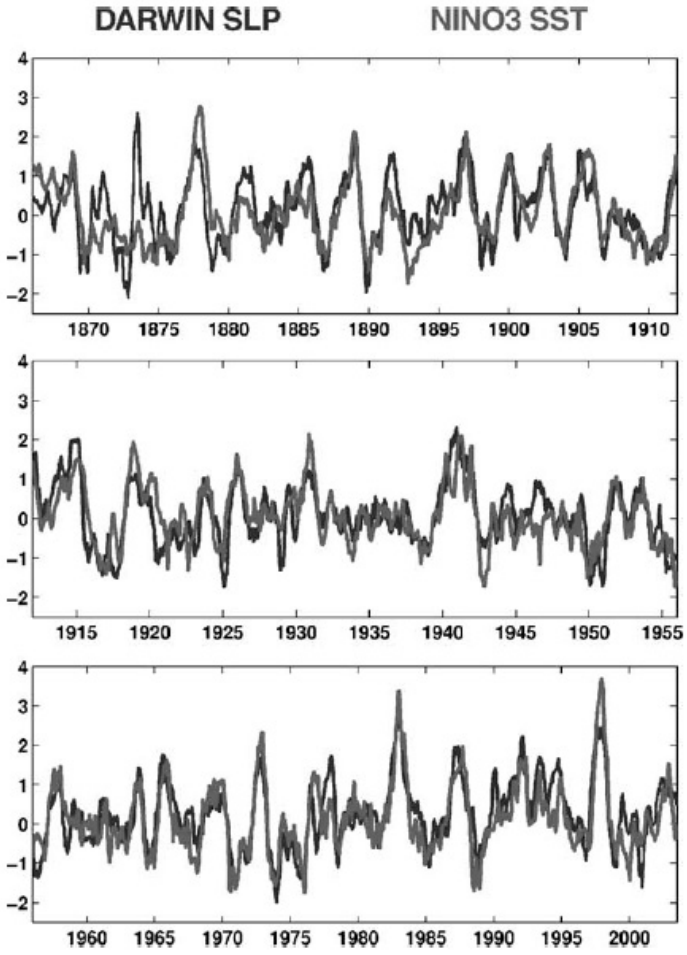

Figure 3.12: *Measures of the ENSO, 1866-2003. Grey: SST of the Niño 3 region, black: sea level pressure in Darwin, Australia, as a measure of the atmospheric Southern Oscillation [Cane 2005].*

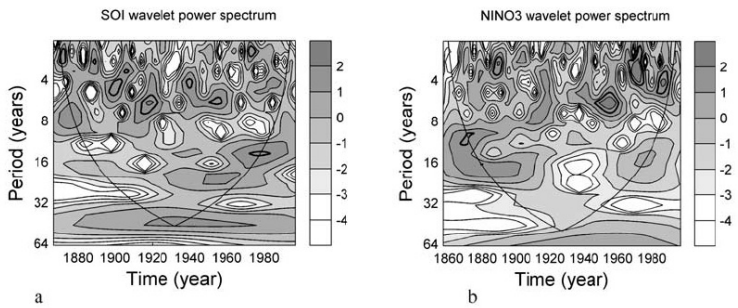

Figure 3.13: *The wavelet power spectrum of (a) Southern Oscillation Index (SOI) and (b) Nino3 index, studied by Jevrejeva et al. [2003].*

3.2.2 North Atlantic Oscillation

The NAO refers to a redistribution of atmospheric mass between the Arctic and the subtropical Atlantic and swings from one phase to another producing large changes in the mean wind speed and direction over the Atlantic, the heat and moisture transport between the Atlantic and the neighboring continents, and the intensity and number of storms, their paths, and their weather [*Hurrell et al.* 2003]. A detailed review on the NAO is given by *Wanner et al.* [2001]. In general, the NAO teleconnection pattern shows a meridional displacement of atmospheric mass over the Northern Atlantic area. The state can be described by the standardized air pressure difference between the Azores High and the Iceland Low. The resulting index, the NAO index, is a measure of the strength of the westerly flow, positive phases being connected with strong westerlies and vice versa (Fig. 3.14). Together with the ENSO phenomenon, the NAO is a major source of seasonal to interdecadal variability in the global atmosphere. On interannual to shorter timescales the dynamics of the NAO can be explained as an internal mode of variability of atmospheric circulation. However, on interdecadal timescales

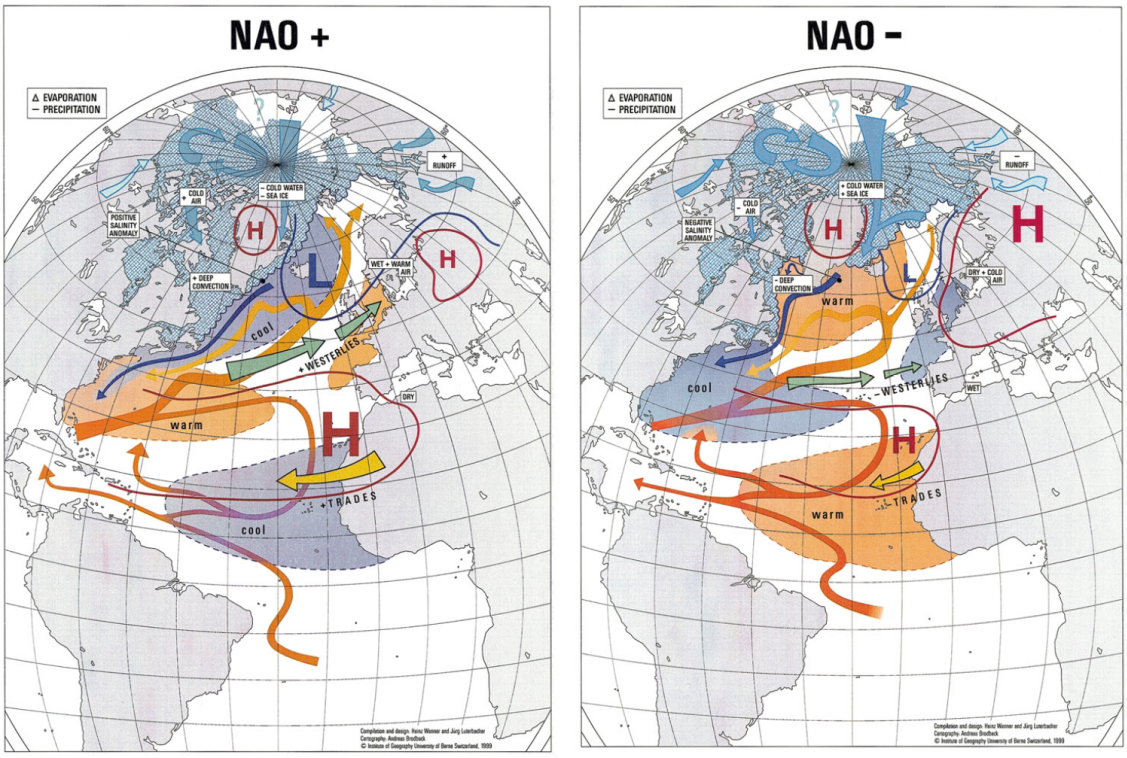

Figure 3.14: *The North Atlantic Oscillation in its positive (left) and negative (right) phase. Surfaces mark SSTs and sea-ice extension, arrows show the flow systems in ocean, atmosphere and rivers, blue and red lines indicate near surface sea level pressures and white rectangles describe characteristic climate conditions or important processes. Figures from Wanner et al. [2001].*

the variability might also be influenced by ocean and sea-ice processes [*Wanner et al.* 2001].

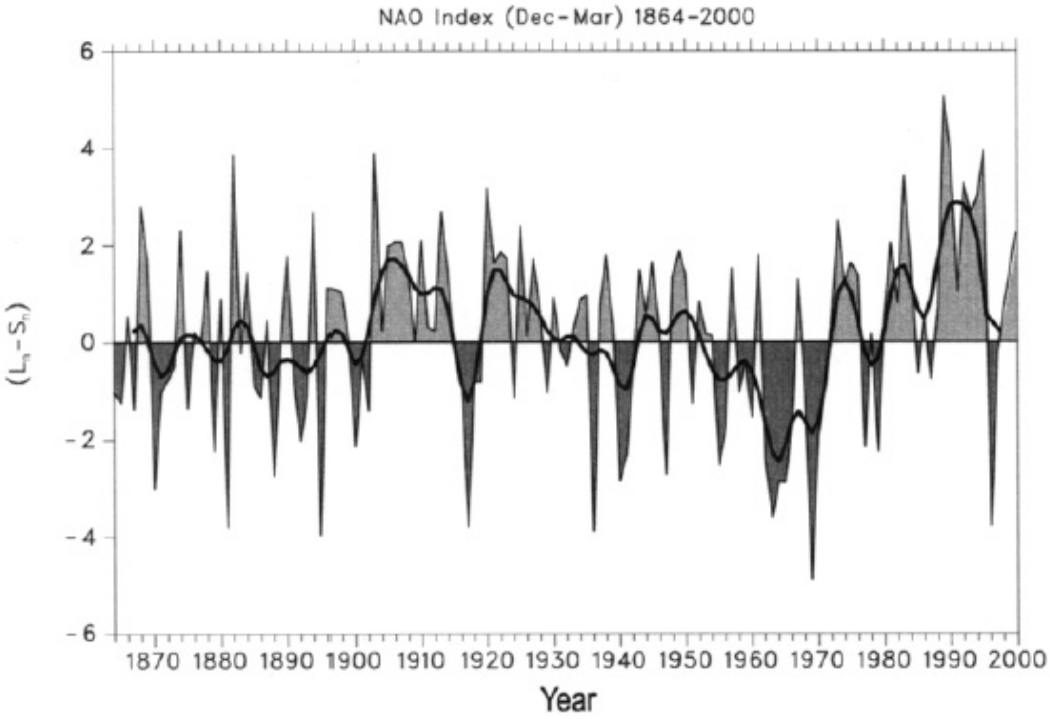

Figure 3.15: *The NAO index over time, defined as the difference of normalized pressure between Lisbon and Stykkisholmur for the winter months. Thick lines are 7-point low pass filtered time series. Figure from Wanner et al. [2001].*

The NAO index over time is shown in Fig. 3.15. Several authors computed spectral analysis of the NAO index with different methods and different time series. The NAO displays fluctuations on multiple timescales ranging from interannual to interdecadal, and the relative contributions of these components are not constant in time [*Wanner et al.* 2001]. E.g., *Pozo-Vàzquez et al.* [2000] note a variability with periods of 2.5, 5-6 and 8 a. *Stephenson et al.* [2000] identify periods of 2.5 and 8 a. A wavelet analysis of the annual NAO index done by *Wanner et al.* [2001] shows high frequency power at bands of 2-10 a and 64 a. A wavelet analysis of the winter NAO index was also done by *Jevrejeva et al.* [2003] and shows that, in general, NAO consist of the leading signals with quasiperiodicity, namely, 2.2-2.4, 7.8, and 12.8 a. However, *Wanner et al.* [2001] note that it is not a specific dynamical process being the cause of the quasi-periodicity. Different authors point to possible mechanisms representing specific timescales and occurring in the atmosphere, ocean or in the coupled atmosphere-ocean-ice system. The 2.5 a periodicity is speculated to be connected to the Quasi-Biennial Oscillation (QBO) [*Reed et al.* 1961]. For the period of 6-10 a, oscillations in the Arctic ocean-sea-ice-atmosphere system could play a role [*Mysak and Venegas* 1998]. *Schlesinger and*

Ramankutty [1994] attribute a variability of 60-70 a to a possible internal oscillation of the atmosphere-ocean system.

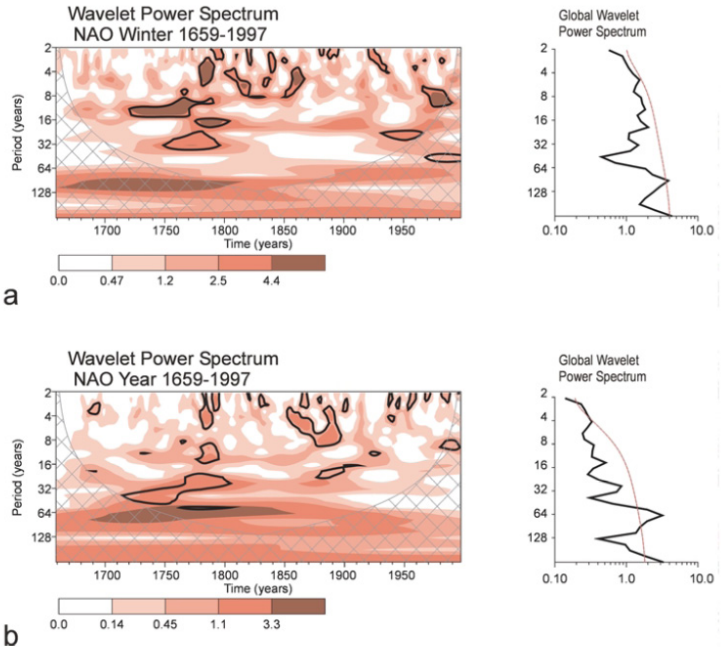

Figure 3.16: *The wavelet power spectrum of the NAO index from 1659 to 1997. (a) for winter DJFM and (b) for annual mean (January to December). Adapted from Wanner et al. [2001].*

3.2.3 Atlantic Multidecadal Oscillation

The Atlantic Multidecadal Oscillation (AMO) is a near-global scale mode of observed multidecadal climate variability with alternating warm and cool phases over large parts of the Northern Hemisphere [*Knight et al.* [2006], *Kerr* [2000]].

Multidecadal variations in regional climate have shown significant impacts during the twentieth century. Some of these phenomena have been linked to multidecadal variations in Atlantic Sea Surface Temperatures [*Knight et al.* 2006], e. g., North East Brazilian [*Folland et al.* 2001] and African Sahel rainfall [*Folland et al.* 1986, *Rowell et al.* 1995, *Rowell* 2003], Atlantic hurricanes [*Goldenberg et al.* 2001] and North American and European summer climate [*Enfield et al.* 2001, *McCabe et al.* 2004, *Sutton and Hodson* 2005]. These SST variations have been called the 'Atlantic Multidecadal Oscillation' (AMO) and are part of a coherent temperature variation across much of the Northern Hemisphere [*Knight et al.* 2005].

Fig. 3.17a shows the spatial distribution of correlations between local monthly SST anomalies and the modal reconstruction over the indexed region (northern rectangle), the general area where the mode amplitude is the strongest (Goldenberg 2001). The main development region for hurricane formation is indicated by the dashed lines. The

authors define an index of the AMO as the decadally filtered area-averaged North Atlantic (95 °W- 30 °E, 0 °-70 °N, excluding the Mediterranean and the Hudson Bay) SST anomaly after linear detrending. Although the signal is stronger in the North Atlantic, it is global in scope. For the multidecadal variations shown here, the coherence between the MDR and northern North Atlantic is a robust feature. The SST fluctuations in the far North Atlantic could be used as a proxy for changes in the MDR [*Goldenberg et al.* 2001]. Fig. 3.17b shows the AMO phases over time. Cool AMO phases (blue) occurred in the 1900s-1920s and 1960s-1980s, while a warm phase (red) occurred in the 1930s-1950s [*Goldenberg et al.* 2001]. Over the instrumental period, the AMO exhibited a 65-80 year cycle with a range of 0.4 °C [*Gray et al.* 2004, *Kerr* 2005]. The AMO appears to have returned to a warm phase beginning in the mid 1990s.

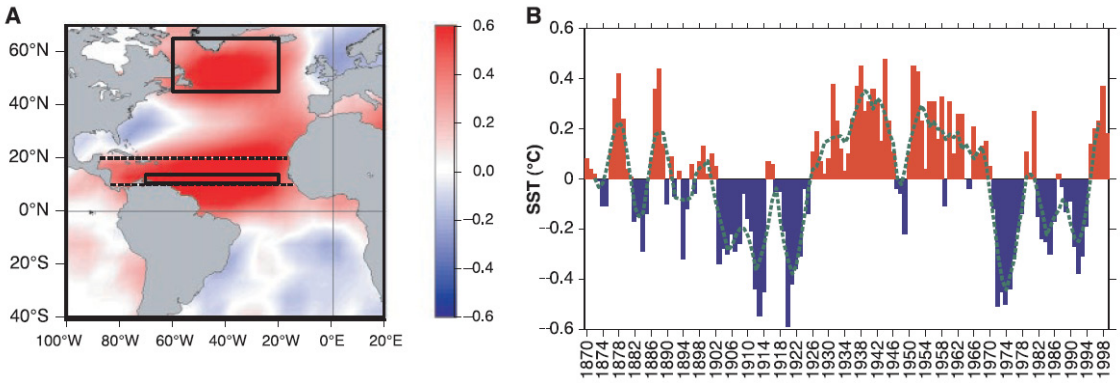

Figure 3.17: *Atlantic sector of non-ENSO global SST variability for 1870-2000 referred to as the Atlantic multidecadal mode. (A) Spatial distribution of correlations between local monthly SST anomalies and the modal reconstruction over the indexed region (northern rectangle). Dashed lines give north and south boundaries of the main development region (MDR). (B) Temporal reconstruction (annual means, dashed line is 5-year running mean) of the mode-related variability averaged over the rectangular area in (A). Figure adapted from Goldenberg et al. [2001].*

Fig. 3.18 shows a reconstruction of the SST signal and sea level pressure (SLP). Phase 0 ° shows the start of the cycle where SST anomalies over most of the central North Atlantic are positive and increasing [*Delworth and Mann* 2000]. Positive SLP anomalies are seen in the subtropical North Atlantic with negative SLP anomalies at higher latitudes of the North Atlantic. This phase resembles a positive phase of the NAO. Inferred from the anomalous SLP gradients this leads to enhanced westerlies. The fact that positive SST anomalies underlie the enhanced westerlies implies that the positive SST anomalies are not being maintained by surface heat flux anomalies induced by changes in wind speed. Anomalous winds should enhance the climatological westerlies and the air sea heat flux leading to a cooling of the oceanic surface layer [*Delworth and Mann* 2000]. Maximum positive SST anomalies are reached in phase

90 °, approximately 13 years later. There is a shift of SLP anomalies such that negative anomalies overlie the positive SST anomalies in the eastern and central North Atlantic, with positive SLP anomalies over the northwest Atlantic. The other half of the cycle would correspond to the same panels, but with signs reversed and adding 180 ° to the indicted phases.

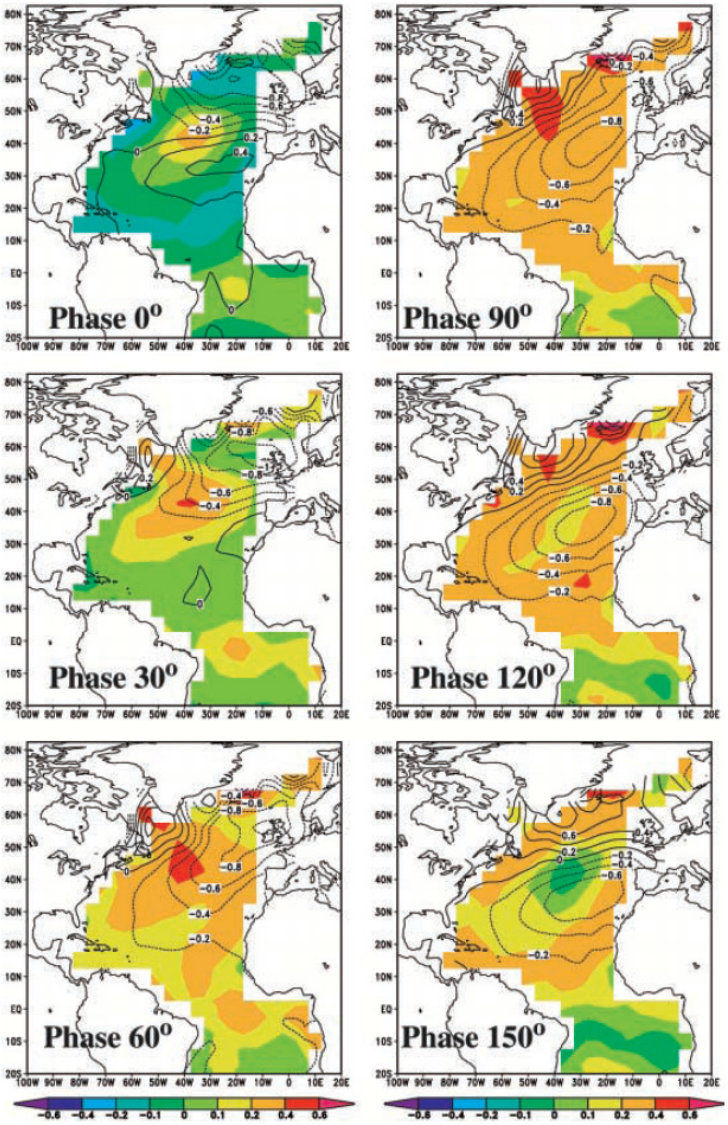

Figure 3.18: *Reconstruction of the ∼52 year signal in SST and SLP from Kushnir et al. [1997]. Colours denote SST in °C whereas contours depict SLP in hPa. Each panel is separated in time by approximately 4.3 years.*

A number of mechanisms have been discussed to account for such multidecadal variability. Internal variability of the coupled ocean-atmosphere-ice system such as the variations of the thermohaline circulation (THC, AMOC) in the North Atlantic has been proposed as a mechanism for this variability [*Bjerknes* 1964, *Stocker and Mysak*

1992, *Delworth et al.* 1993, *Delworth et al.* 1997, *Timmermann et al.* 1998]. It has also been theorized that multidecadal fluctuations of solar irradiance may lead to this variability [*Cubasch et al.* 1997, *Lean and Rind* 1998, *Waple et al.* 2000] either as a direct response to changes in solar forcing or through some interaction with internal modes of the coupled system. The study of *Delworth and Mann* [2000] describe results from a coupled ocean-atmosphere climate model in order to discuss the role of the THC. During phase 0 °, there is a good agreement of SST and SLP. In an additional analysis they showed that the simulated East Greenland Current is anomalously weak during this period, thereby reducing the export of relatively cold, fresh water and sea ice from the Arctic into parts of the North Atlantic. This reduction contributes to the enhancement of the THC by reducing the freshwater transport into the convective regions of the modelled North Atlantic, effectively increasing near surface salinity, density, convection and the THC [*Delworth et al.* 1997]. Proceeding forward in time, to 60 °, results show increasing positive temperature anomalies in the North Atlantic associated with an increasing THC. After reaching maximum SST and maximum THC, the THC begins to weaken, which is related to the presence of an anomalous anticyclonic gyre in the upper 1000 m of the central North Atlantic. This gyre is induced by positive thermal anomalies associated with enhanced THC. This gyre reduces the transport of salt into the convective regions, reducing near-surface density, convection and the THC, which reduces SST.

The influence of the AMO on North American as well as European climate has been studied with the HadCM3 climate model by *Knight et al.* [2006]. This study also seeks to explain multidecadal variability in North Eastern Brazil (NEB) as well as Sahel rainfall and hurricane frequency over the Atlantic. The warm phase between the 1930s-1950s coincides with decreased NEB rainfall and United States (US) river flows, as well as enhanced Sahel rainfall and hurricane formation. Conversely, the 1960s-1980s were a period of high NEB rainfall and US river flows whereas Sahel rainfall and Atlantic hurricane formation were reduced [*Knight et al.* 2006]. In the near-centennial AMO band [*Knight et al.* 2005], the warm AMO phase (Fig. 3.19a) is associated with a northward displacement of precipitation over the tropical Atlantic Ocean, along with a northward cross-equatorial wind anomaly (Fig. 3.19e) [*Knight et al.* 2006]. These changes imply a shift in the mean inter-tropical convergence zone (ITCZ) to the north of its climatological MAM position, and hence a reduction in NEB rainfall. As the cycle of AMO phases proceeds, the temperature pattern eventually reverses (Fig. 3.19d), forcing an anomalous southerly ITCZ located closer to NEB and so wetter decades (Fig. 3.19h). Similarly, the authors note for Sahel rainfall that with a warm AMO phase (Fig. 3.19a) tropical precipitation in the Atlantic sector shifts northward (Fig. 3.19i). Along with consistent changes in the trade winds, this implies northward displacement of the mean ITCZ. Northward movement of the JJA climatological ITCZ brings increased precipitation to the Sahel. This coincides with anomalous westerly

winds carrying moist Atlantic air into the region, as shown in previous studies [*Rowell et al.* 1992]. In agreement with *Sutton and Hodson* [2005], *Knight et al.* [2006] also found a connection between the AMO and European Climate. The authors note, that in observations of central England temperature as well as climate models, there is a significantly positive correlation in most seasons.

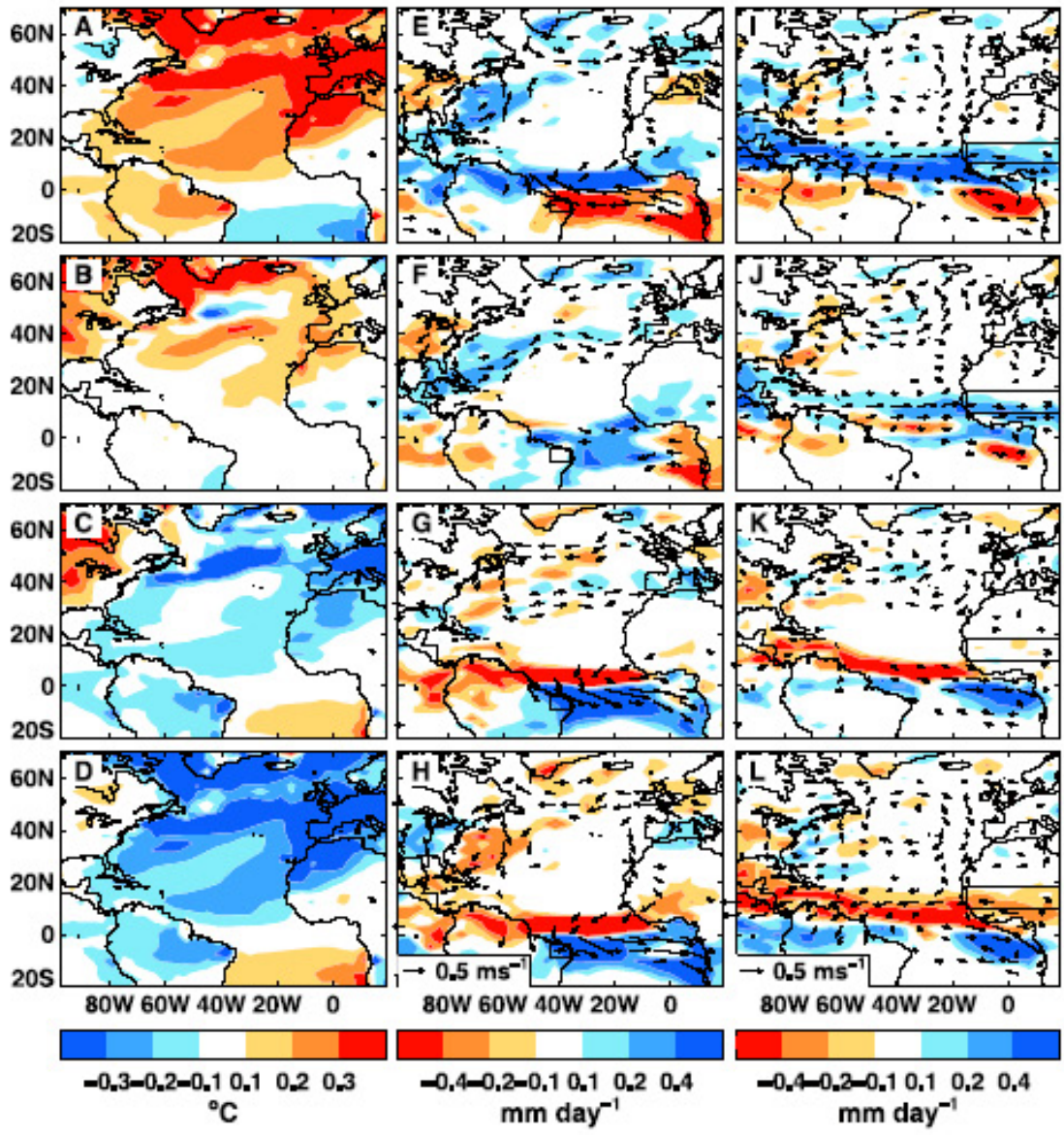

Figure 3.19: *Analysis of simulated decadal mean near-surface air temperature and decadal mean precipitation for the phases 0° (maximum in mean northern hemisphere temperature) of the signal detected in the frequency band from 70 years^{-1} to 180 years^{-1}, 60°, 120°, 180°. (a)-(d): mean annual temperature, (e-h): March to May precipitation, (i)-(h): JJA precipitation. 850hPa wind anomalies are indicated by arrows. Figure adapted from Knight et al. [2006].*

A mechanism for the observed variability of 70-80 years in the AMO signal was proposed by *Vellinga and Wu* [2004]. The authors note, that internal THC variability is concentrated on centennial time scales. The THC can impact surface climate via an interhemispheric SST contrast of about 0.1 °C in the Tropics. Anomalous northward ocean heat transport associated with a strong phase of the Atlantic THC generates a cross-equatorial SST gradient. This causes the ITCZ to move to a more northerly position with increased strength. The extra rainfall resulting from the anomalous ITCZ imposes a freshwater flux and produces a salinity anomaly in the tropical North Atlantic. Such sustained salinity anomalies slowly propagate towards the subpolar North Atlantic with a lag of 5-6 decades. The accumulated low-salinity water lowers upper-ocean density, which causes the THC to slow down, the oscillation then enters the opposite phase. A schematic view is given in Fig. 3.20.

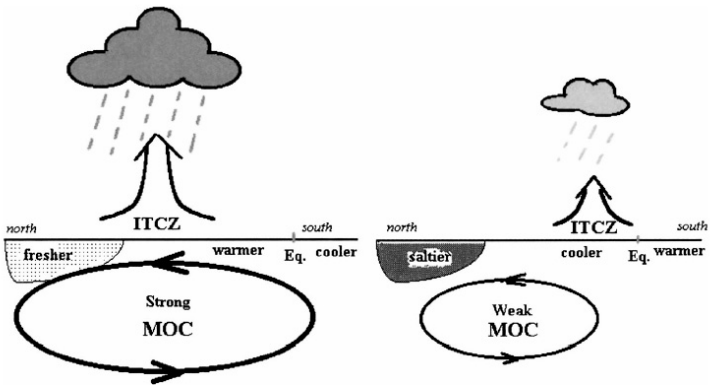

Figure 3.20: *Schematic mechanism responsible for centennial THC fluctuations. When the THC is strong (left), the ITCZ shifts northward, in response to enhanced SST gradient across the equator. Fresh anomalies in the upper ocean propagate northward and weaken the overturning, which results in the weak phase (right). Figure adapted from Vellinga and Wu [2004].*

Multidecadal variations in observed major hurricane activity in the period 1944 to 2000 have been associated with the AMO by *Goldenberg et al.* [2001], Fig. 3.21. They attribute this influence to changes in tropical atmospheric circulation, which alter the tropospheric vertical shear in the main hurricane development region, with high shear reducing storm formation [*Knight et al.* 2006]. Local SST greater than 26.5 °C is usually considered to be a necessary condition for tropical cyclone development [*Gray* 1968], and higher SST can increase overall activity [*Shapiro* 1982, *Shapiro and Goldenberg* 1998, *Saunders and Harris* 1997]. The relationship of simulated mean MDR shear with global SSTs shows negative correlations in the North Atlantic confirming the AMO link [*Knight et al.* 2006].

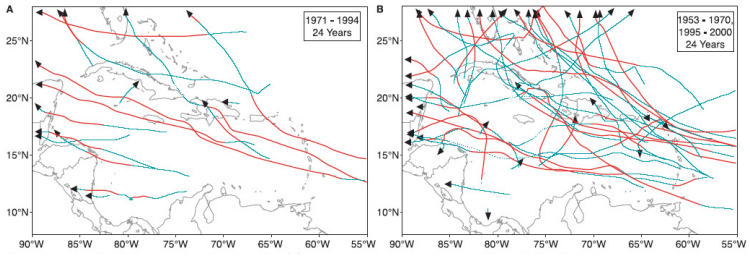

Figure 3.21: *Contrast of Caribbean hurricanes between colder (A) and warmer (B) values of the AMO. Green lines indicate non-major hurricanes, red lines major hurricane intensities. Figure adapted from Goldenberg et al. [2001].*

AMO and NAO

An analysis of the connection between the AMO and the NAO has been done by *Walter and Graf* [2002]. The authors note, that since the late 1960s/early 1970s and during the first three decades of the twentieth century, the North Atlantic SST is strongly correlated to the regional atmospheric circulation in the North Atlantic sector, i.e., the North Atlantic Oscillation. This coincides with an AMO negative phase. During these periods the NAO index is characterized by pronounced decadal variability and mainly positive values. In contrast, the NAO index is only weakly correlated to North Atlantic SST from the 1930s to the early 1960s, when the NAO index is characterized by weak decadal variability. These time periods coincide with a positive AMO phase. Remote influences, in particular from the tropical Pacific region, become important, especially for SST in the western tropical North Atlantic [*Walter and Graf* 2002].

ENSO and NAO

According to [*Giannini et al.* 2001a], ENSO and the NAO appear to be independent manifestations of climate variability, eventhough their influence overlaps in the North Atlantic region. The authors note that a correlation between indices of the two phenomena is not significant. The study, which spans the entire 20th century, does not reveal any consistent relationship. For example, a warm ENSO event is more frequently associated with a positive NAO during the earlier and later parts of the last century and with a negative NAO during the intervening period. The positive NAO phase occurs with ENSO events of either sign during recent decades [*Giannini et al.* 2001a].

THC and ENSO

Progress has also been made in understanding how changes in the THC transmit their influence to the Tropics [*Chiang* 2009]. It appears that the atmosphere plays a major role in determining the global climate changes to THC slowdown [*Chiang et al.* 2008, *Timmermann et al.* 2005]. A strong northern cooling source is needed which in case

of an THC slowdown comes from sea-ice feedback [*Cheng et al.* 2007]. *Chiang et al.* [2008] argue that the atmosphere transmits this cooling signal to the northern Tropics, creating the THC signature of an interhemispheric thermal gradient dominated by NH cooling and shifting the ITCZ southward. Tropical convection reorganizes during an THC slowdown, which could in turn affect the global climate through teleconnections. Thus, the Tropics could play the role of globalising the climate changes indicated by the North Atlantic [*Chiang* 2009]. The question, whether ENSO can be affected by changes in the THC have been studied by *Dong and Sutton* [2002]. In model experiments, an THC slowdown can be initiated with an infusion of freshwater in the high North Atlantic. The authors found, that El Niño was systematically initiated six to seven years after the THC was abruptly slowed, which was also found by *Timmermann et al.* [2007]. Those studies suggest that THC and ENSO are in fact connected. *Schmittner et al.* [2000] showed how ENSO could influence THC in turn. A permanent El Niño like condition could lead to reduced atmospheric freshwater export from the Atlantic, leading to a fresher Atlantic and reduced THC. Second, changes in the tropical Atlantic could result in changes in surface winds in such a way as to reduce THC through the interaction between surface and density driven ocean circulations.

Dong et al. [2006] used a coupled ocean-atmosphere model in order to seek explanations for the observed multidecadal modulation of the ENSO variance by Atlantic ocean SSTs. Fig. 3.22 shows the observed AMO index (solid) and changes in the amplitude of ENSO, ENSO variability (dashed). The figure suggests that weak (strong) ENSO variability coincides with the positive (negative) phase of the AMO with a correlation coefficient of -0.68. The monthly Niño 3 SST standard deviation was found to be 22 % lower during the AMO warm phase (1930-1960) relative to the cold phase (1965-1995). *Dong et al.* [2006] note, that whether this apparent association between Atlantic SST and ENSO variance is coincidence or due to a causal link between the Atlantic and tropical Pacific Oceans, is unclear. However, the study seeks to investigate the influence of Atlantic SSTs on Pacific ENSO variability. Their major conclusion is that positive latent heating anomalies over the tropical North Atlantic are generated in response to a warm phase of the AMO. The remote response to this mechanism involves suppressed convection and anomalous easterly winds over the central and western equatorial Pacific, which deepens the thermocline in the west Pacific. The deepening propagates eastward into the central and eastern Pacific, which weakens the coupled instability through which ENSO events grow (e.g., *Zebiak and Cane* [1987]) and reduces ENSO variance.

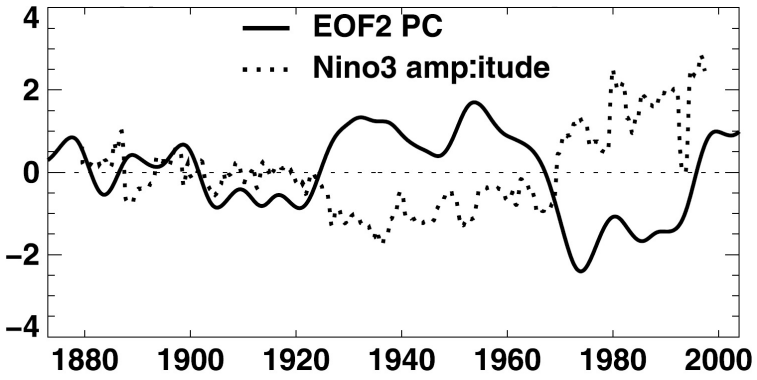

Figure 3.22: *AMO index (solid) and normalized anomalous ENSO magnitude (monthly Nino 3 index standard deviation in a 13 year window, dashed) based on observations. Figure adapted from Dong et al. [2006].*

The study of *Zhang and Delworth* [2005] investigates the tropical response to a substantial weakening of the Atlantic Thermohaline Circulation on millenial timescales consistent with paleoproxy studies from Indian and Asian summer monsoon regions. The authors show that a large reduction of Atlantic THC, which is simulated by input of freshwater to a GCMs model's North Atlantic, can result in a southward shift of the ITCZ over the Atlantic and Pacific leading to an El Niño-like pattern in a southeastern tropical Pacific and weakened Indian and Asian summer monsoon. Fig. 3.23 shows the results of SST in response to input of freshwater into the North Atlantic (upper panel) as well as SLP (lower panel). Fig. 3.24 shows a schematic diagram of the involved processes. The most important process for the Caribbean area is the movement of the ITCZ, which also moves northward during an positive phase of the THC as indicated in the figure. The blue circle over the Central American coast emphasizes the important region of atmospheric linkage between the Atlantic and Pacific. The anomalous surface zonal wind over the northern tropical Pacific strengthens the trade winds, whereas over the southern tropical Pacific, it weakens trade winds [*Zhang and Delworth* 2005].

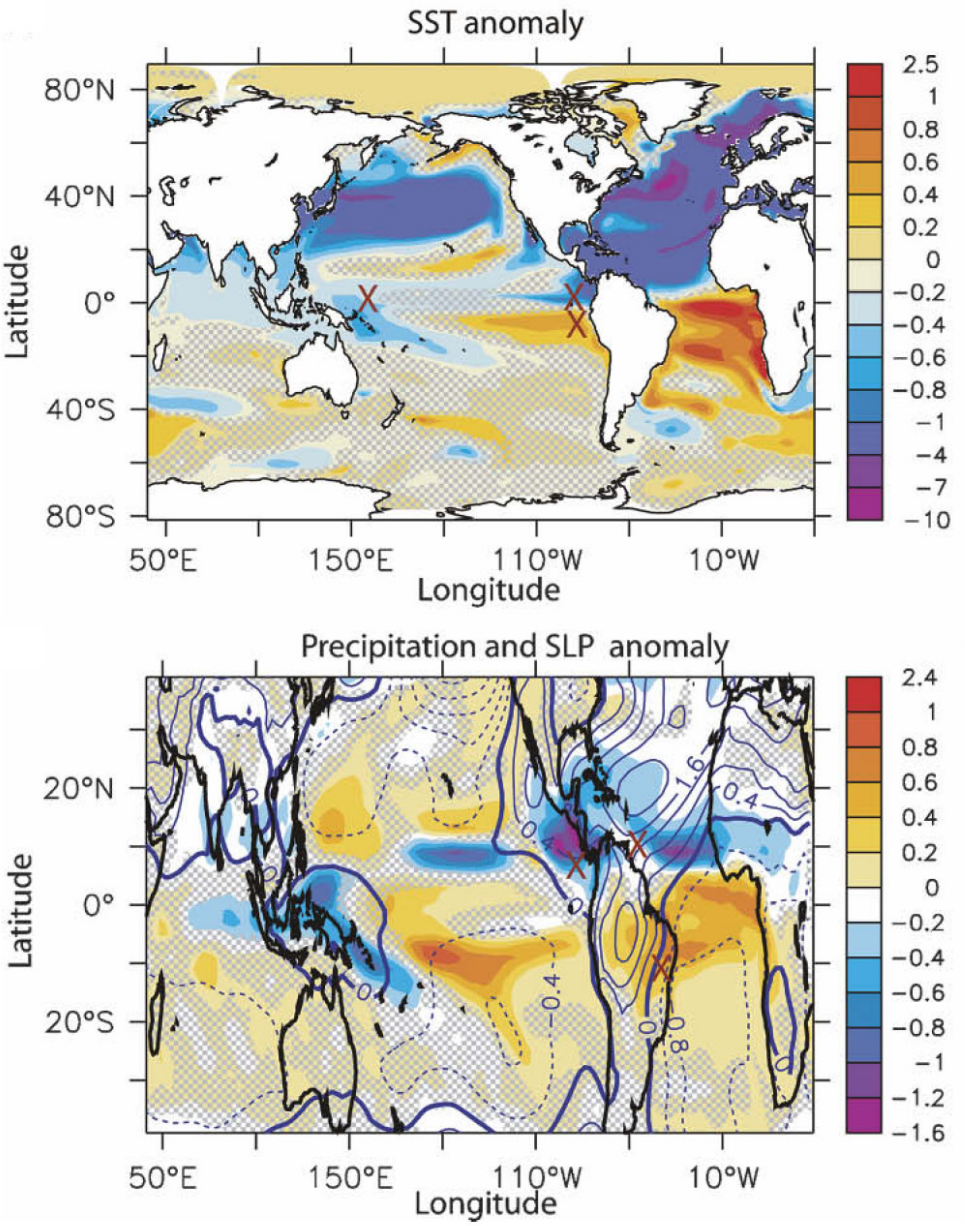

Figure 3.23: *Annual mean SST anomaly after reduced AMOC (upper panel) and SLP (lower panel). Figure adapted from Zhang and Delworth [2005].*

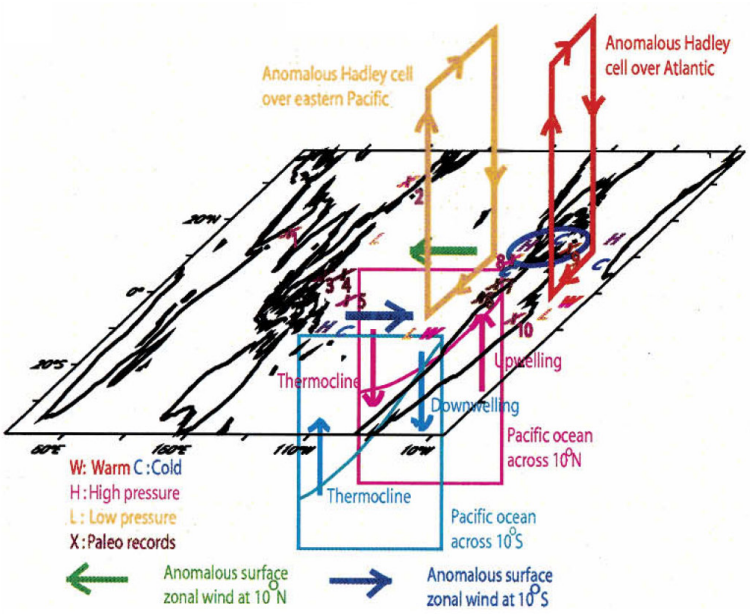

Figure 3.24: *Schematic diagram of global tropical responses to the North Atlantic freshwater forcing and the proposed mechanism. Figure adapted from Zhang and Delworth [2005].*

3.2.4 Summary of Caribbean Teleconnection patterns

It has been shown that a variety of teleconnection patterns operate in the Caribbean area. Important drivers of Caribbean climate variability is thought to be connected to the Pacific as well as the Atlantic teleconnection patterns. Highlighted teleconnections are ENSO, which is thought to operate on subdecadal timescales in the Pacific area. The ENSO system is marked by two opposite states, El Niño (warmer eastern Pacific) and La Niña (colder eastern Pacific) with both anomalous Hadley cell circulation and Walker circulation. The anomalous circulation patterns of the El Niño phase also influence the tropical North Atlantic, weakening trade winds and enhancing SSTs.

The North Atlantic Oscillation is another main driver of Caribbean climate anomalies. The NAO operates on subdecadal, decadal and multidecadal timescales. The oscillation moves between the NAO^+ and NAO^- phase. NAO^+ phases are marked by anomalous low SLP over Iceland and anomalous high SLP over the Azores, leading to low SSTs in the tropical North Atlantic area. The multidecadal pattern is thought to be connected to an internal oscillation of the atmosphere-ocean system.

The Atlantic Multidecadal Oscillation is alternating between warm and cool phases of the whole Northern Atlantic. The AMO is thought to be connected to changes in the thermohaline circulation, stronger THC leading to warmer SSTs in the North Atlantic area. Averaged SSTs over the Northern Atlantic region are observed to be more negatively related, however, the mechanism is not yet fully understood. The

AMO seems to be an important factor influencing the position of the ITCZ and the hurricane development. The ITCZ shows a more northern position during positive AMO phases and hurricane formation is increased.

Several studies investigated the link between changes in the THC and ENSO. Observations show that during a positive AMO phase (strong THC), ENSO variance can be reduced. Further model studies show that a reduction in THC can move the ITCZ in the Atlantic as well as Pacific southward. This mechanism is connected with El Niño-like conditions on millennial timescales.

3.3 Caribbean Climate variability

3.3.1 Seasonal to interannual timescales

A number of studies have analyzed Caribbean precipitation patterns and recognized the atmospheric and oceanic influence from the North Atlantic and eastern Pacific on seasonal to interannual timescales [*Jury et al.* 2007]. The influence of ENSO and NAO, respectively, has been discussed in several papers. E. g., the dependance of ENSO has been discussed in *Hastenrath* [1976], *Ropelewski and Halpert* [1986], *Rogers* [1988], *Enfield* [1996], *Malmgren et al.* [1998], *Enfield and Alfaro* [1999], *Giannini et al.* [2000], *Giannini et al.* [2001a], *Giannini et al.* [2001b], *Chen and Taylor* [2002], *Taylor et al.* [2002], *Martis et al.* [2002], *Jury et al.* [2007] and *Spence et al.* [2004]. NAO teleconnections via the North Atlantic anticyclone and its trade winds are thought to be responsible for NAO-influenced precipitation anomalies and were studied in *Malmgren et al.* [1998], *George and Saunders* [2001], *Giannini et al.* [2001a], *Giannini et al.* [2001b] and *Jury et al.* [2007]. Caribbean precipitation anomalies are influenced by the competition between the North-Atlantic subtropical high sea level pressure system and the eastern Pacific ITCZ, which influence the convergence patterns on seasonal and interannual timescales [*Giannini et al.* 2000]. The modulation by the tropical Atlantic and the tropical Pacific have an influence on both the early and the late rainfall season in the Caribbean [*Taylor et al.* 2002].

In order to understand the influence of changes in SST in the Pacific on Caribbean rainfall anomalies, several studies have shown a negative correlation (e.g., *Hastenrath* [1976], *Ropelewski and Halpert* [1986], [1987], [1989] and [1996] and *Rogers* [1988]. All authors note a dry Caribbean-warm Pacific relationship. A common feature of these studies is a focus on the latter portion of the rainfall seasons (e.g., July-November), given its abundance of rainfall and its coincidence with peak hurricane activity [*Chen and Taylor* 2002].

The seasonal variability in rainfall over Cuba in the range between 84.4-80.6°W and 23.8-20°N was extracted from the NCEP NCAR Reanalysis project [*Kalnay et al.* 1996]. To show the difference between El Niño years and La Niña years, the precipitation rate in height of the sea surface is plotted in Fig. 3.25 in the year of a starting ENSO

event and the following year. El Niño and La Niña years have been extracted following the definition mentioned in chapter 3.2.1 over the period from 1948 to 2009. The data clearly show a reduction of rainfall during the start of an El Niño event (late rain season of upper panel), a reversal of the precipitation anomaly at the end of the year and an increase during the following early rainy season.

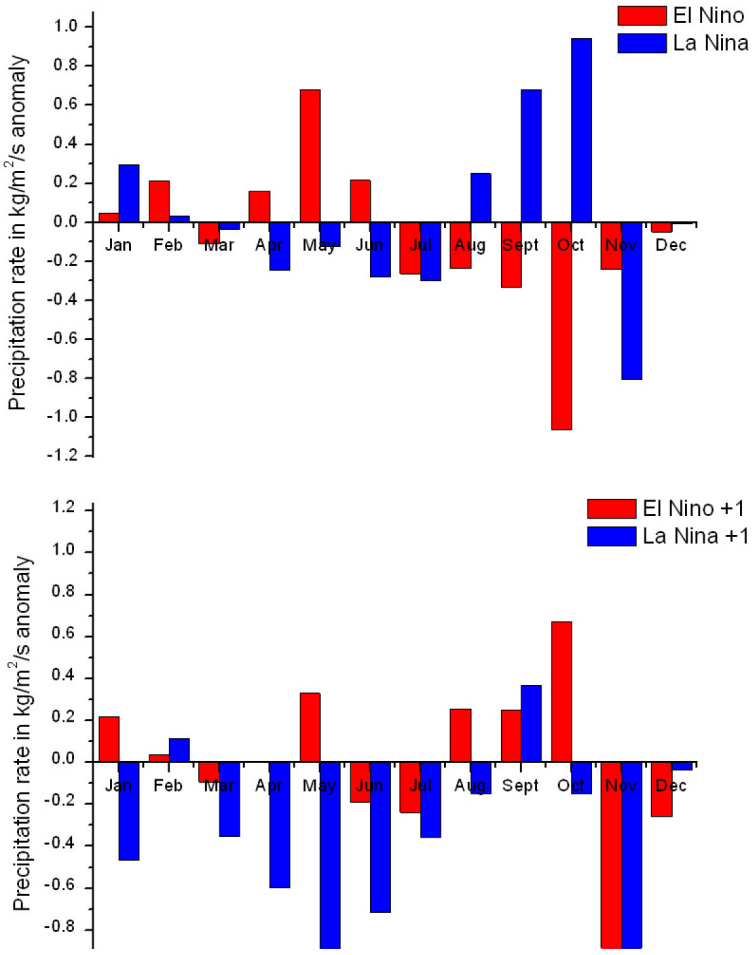

Figure 3.25: *Rainfall anomalies during El Niño years, La Niña years and mean climatology at the start of an ENSO event (upper panel) and during the following year (lower panel).*

Interannual variability in the early season is strongly influenced by anomalies in sea surface temperatures of the Tropical North Atlantic (TNA) with positive anomalies over a narrow latitudinal band (0°-20°) being associated with enhanced Caribbean rainfall following an El Niño event. The spatial pattern of significant correlation between Pacific SST (Niño 3) and Caribbean rainfall suggests a strong influence of the El Niño/La Niña phenomenon on the late season. A warm Pacific is associated with a depressed late season and vice versa [*Taylor et al.* 2002].

George and Saunders [2001] discussed the influence of the NAO on Caribbean precipitation anomalies. The authors suggest that wintertime NAO is correlated with

spring and early summer sea surface temperature anomalies in the TNA and Atlantic midlatitudes. Thus, a positive NAO leads to stronger trade winds, enhanced wind-induced latent heat flux, TNA cooling and lower TNA atmospheric moisture content. The switch from an initial increase as can be seen in Fig. 3.26 to an annually dominant spring decrease can be explained by a shift in wind direction impacting the northern Caribbean. Initially the mean flow comes from the northeast originating over the NAO related warm mid-latitude anomaly. Thus, the northern Caribbean receives increased moisture rainfall. From spring onwards, the wind direction becomes more easterly originating over the TNA. With reduced evaporation over the cool TNA SST anomaly, the Caribbean experiences reduced rainfall [*George and Saunders* 2001].

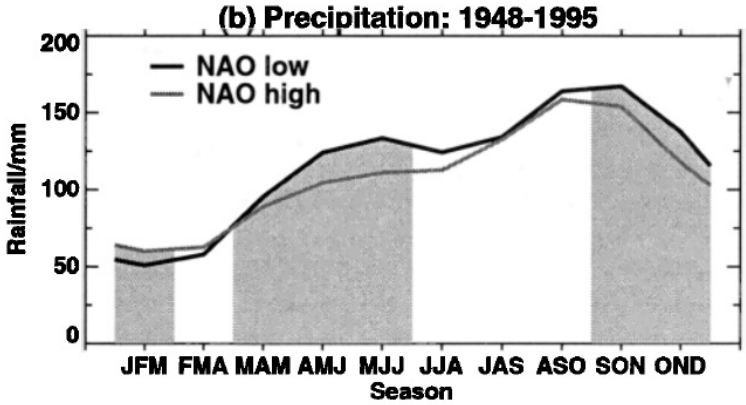

Figure 3.26: *Seasonality of rainfall patterns over the Caribbean during NAO phases. Figure adapted from George and Saunders [2001].*

Jury et al. [2007] studied precipitation anomalies in the time period from 1951-1981 in the above mentioned clusters in detail. Cluster 1, which includes Cuba, exhibits cycles around 5 years early in the record and around 3 years between 1961 and 1975 that are largely in phase with ENSO. In addition, if the different rainfall seasons are individually considered with respect to the preceding winter season (DJF) values of the climatic indices, the ENSO signal shows a significant positive association in the NW Caribbean in MAMJJ with a 3-month lead time. The values for other clusters are also positive. For summer/fall seasonal rainfall in ASON with a 9-month lead, the associations are still positive in the NW and become weakly negative towards the SE Caribbean. The NAO, on the other hand, is negatively related in both early and late rainy seasons for all clusters. However, the authors note that the ENSO connection seems to be more pronounced in the western Caribbean than in the eastern Caribbean.

A study by *Seager et al.* [2009] divides the precipitation analysis into two seasons, the rainy season ranging from May through October, and the dry season from November to April. The analysis shown in Fig. 3.27 indicates precipitation anomalies in the circum-Caribbean with SST in the Tropical Pacific (TP) and the TNA. Results for the

winter half year (Nov-April) are shown in a) and b). The authors note that during El Niño, higher SST in the TP lead to wetter winters in the Northern Caribbean. The influence of TNA SST seems to be insignificant. Through the summer season, during an El Niño event central America and northern South America appear to receive less precipitation. Also, if the TNA has higher SST, the precipitation in the Caribbean is higher.

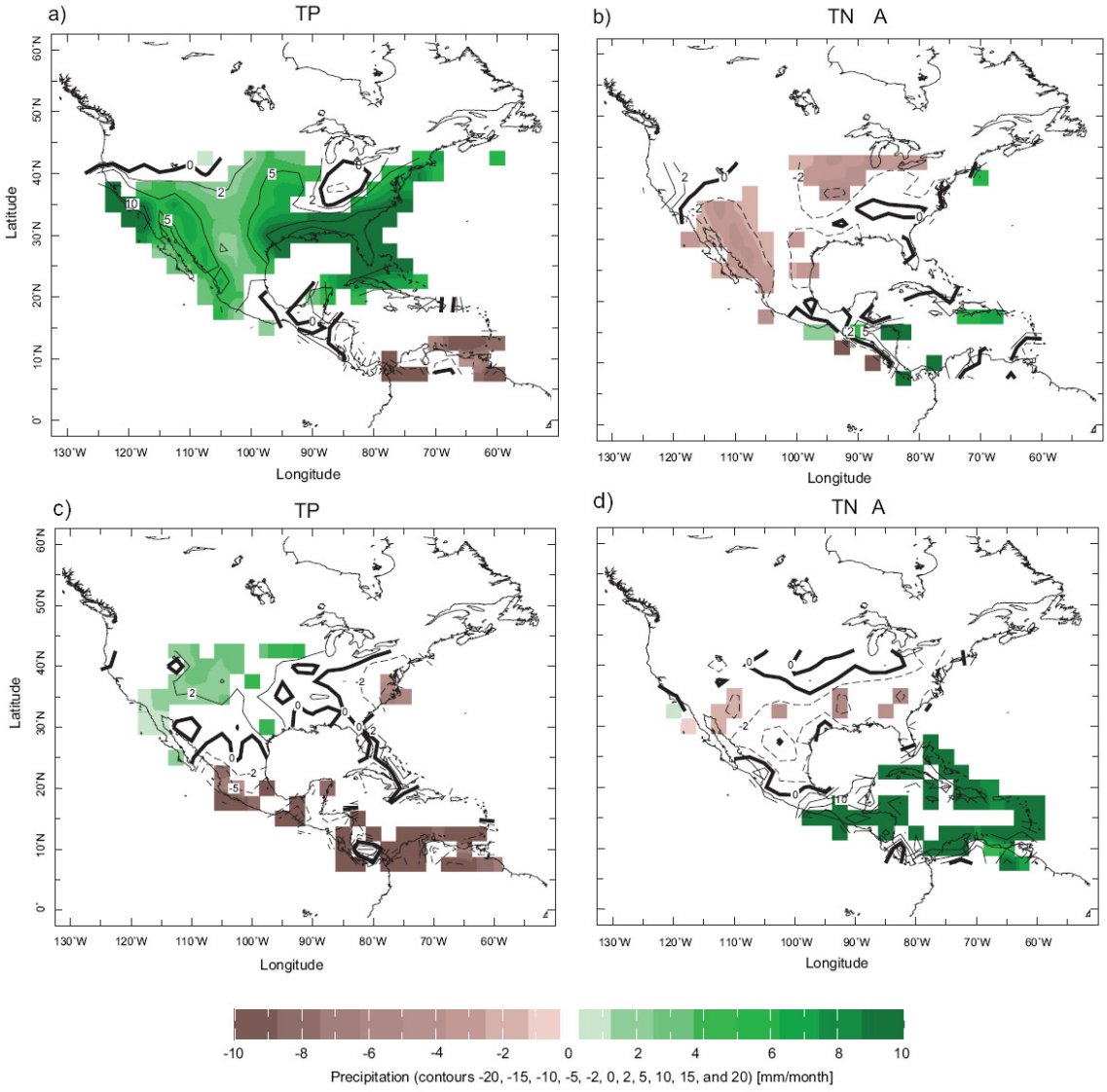

Figure 3.27: *Precipitation anomalies regarding the winter (Nov-Apr) due to changes in tropical Pacific SSTs (a) and TNA (b), and summer anomalies (May-October) for TP (c) and TNA (d). Adapted from Seager et al. [2009].*

However, in addition to the observational data from 1951-1981 of *Jury et al.* [2007], the study of *Giannini et al.* [2001a] also used a merged analysis of satellite retrieved and rain gauge data, covering 1979 to 2001. The authors studied interdecadal changes

in the ENSO teleconnection to the Caribbean region and the NAO. The typical signature of ENSO events in the Caribbean/Central American region is a reversal in the sign of the correlation of the Niño3 index with rainfall between the year of ENSO onset (0) and the following year (+1). The reversal starts during winter (peak of ENSO) in the northwestern corner of the basin (Yucatan and Cuba), which is the region which is directly affected by extratropical fronts (Schultz et al 1998), and spreads to the Antilles in spring of year (+1). E.g., rainfall anomalies during winter are mostly negative during a warm ENSO event, reversing into positive rainfall anomalies during the following spring. The authors note that during dry conditions during the summer of a starting El Niño event, rainfall is associated with locally divergent surface circulation engendered by the eastward shift of deep convection in the pacific Ocean. Wet conditions following a warm El Niño event are associated with the lagged warming of the tropical North Atlantic Ocean. The authors also give a merged analysis between the ENSO and NAO behavior on seasonal to interdecadal timescales. The variability in the strength of the North Atlantic High is governed mainly by the North Atlantic oscillation with a positive phase of the NAO implying a stronger than normal high and vice versa. The NAO is strictly negatively correlated with Caribbean rainfall indirectly via anomalous SSTs associated with anomalies in the surface wind speed at tropical latitudes and directly via anomalous subsidence. The combined effect of the two phenomena is found to be strongest when the two signals interfere constructively: (1) During summer following winters characterized by positive NAO conditions, the dryness associated with a developing warm ENSO event adds to the dryness associated with a positive SLP anomaly in the subtropical North Atlantic. (2) During the spring following winters characterized by a negative NAO phase, the wetness that follows a warm ENSO event is augmented by the wetness associated with the warmer-than-average tropical North Atlantic SSTs [*Giannini et al.* 2001a].

Rainfall patterns over Panama have been studied by *Lachniet* [2009b]. During warm events in the Caribbean Sea, increased temperatures lead to enhanced evaporation, greater specific humidity, deeper convection and a more northerly position of the ITCZ which brings enhanced rainfall to Panama [*Poveda et al.* 2006]. This effect dominates during the early wet season [*Lachniet* 2009b]. In contrast, the ITCZ moves southward during Pacific warm events, resulting in relatively dry conditions in southern Central America, which is most pronounced in the late wet season.

3.3.2 ENSO and δ^{18}O

ENSO is the strongest climatic signal on interannual timescales and has a significant imprint on climate in many parts of the tropical Americas [*Vuille et al.* 2003]. To study climate anomalies and the climatic control on δ^{18}O on interannual and longer timescales, the following analysis were done by *Vuille et al.* [2003]. As mentioned in chapter 3.2.1, the authors use climate models for their analysis. After removing the seasonal cycle by

subtracting the long-term monthly mean from individual monthly values, the simulation reproduces the El Niño related precipitation increase over the eastern equatorial Pacific and the decrease over northern tropical south America extending into the tropical North Atlantic. According to their model results (ECHAM T106), Cuba receives more precipitation in DJF during an El Niño phase than during La Niña. The summer (JJA) tends to be drier than during La Niña. The overall pattern in the Caribbean is drier conditions both in winter (DJF) and summer (JJA) than during La Nina. The authors note that warm (cold) anomalies over tropical South America tend to coincide with dry (wet) episodes.

The correlation between Niño 3.4 SST anomalies and monthly anomalies of δ^{18}O in precipitation is shown in Fig. 3.28. In general, based on IAEA observational network (Fig. 3.28a), the δ^{18}O signal in precipitation is significantly more enriched during a warm phase of ENSO over tropical South America. Over the north Atlantic, the eastern equatorial Pacific and southern South America the signal is reversed. Also the ECHAM T106 model seems to be able to capture those features (Fig. 3.28). Obviously, the change in the δ^{18}O values in the tropics associated with ENSO is primarily a response to changes in precipitation rather than temperature. The ENSO related temperature signal is of the same sign over the tropical continent and eastern Pacific whereas both precipitation and δ^{18}O show a distinct dipole pattern with increased precipitation over the eastern equatorial Pacific and decreased precipitation over tropical South America during a warm ENSO phase. The shift in the Walker circulation during ENSO is the most likely cause to explain this dipole pattern seen in both the observed and modeled precipitation and δ^{18}O fields [*Vuille et al.* 2003]. According to these model results, the δ^{18}O value of precipitation in the Caribbean area is enriched during a warm ENSO phase.

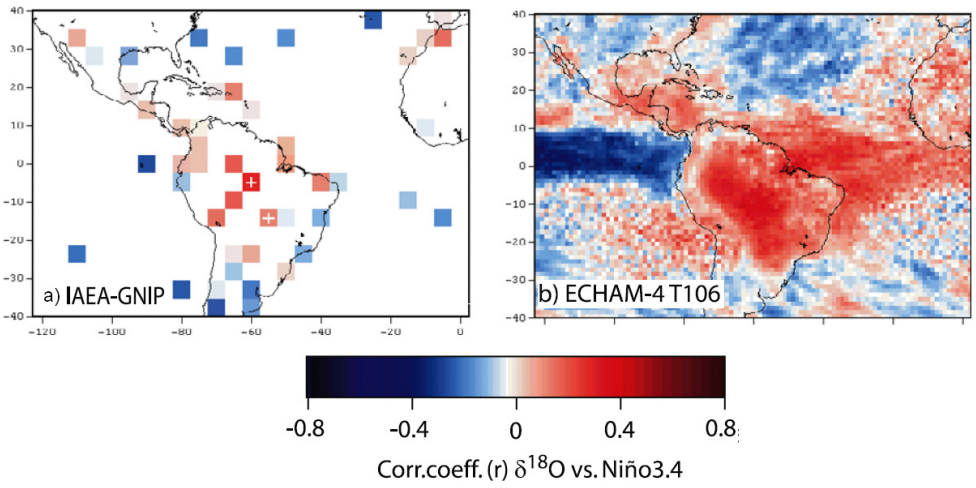

Figure 3.28: *Correlation coefficient between δ^{18}O values and Nino3.4 from (a) GNIP data base and (b) ECHAM T106 model. Figure adapted from Vuille et al. [2003].*

The δ^{18}O signal in rainfall over Panama in connection to the ENSO phenomenon was studied by *Lachniet* [2009b] . During warm events in the Caribbean Sea, increased temperatures lead to enhanced evaporation, greater specific humidity, deeper convection and a more northerly position of the ITCZ, which brings enhanced rainfall and lower δ^{18}O values to Panama [*Poveda et al.* 2006]. This effect dominates during the early wet season in Panama [*Lachniet* 2009b]. In contrast, the ITCZ moves southward during Pacific warm events, resulting in relatively dry conditions and high δ^{18}O values in southern Central America, which is most pronounced in the late wet season [*Lachniet* 2009b].

3.3.3 Interdecadal to multidecadal timescales

The Northern Caribbean, including Cuba, reveals a strong decadal signal according to the study of *Chen and Taylor* [2002]. During the early 1920s, 1960s and early 1970, the climate over the Northern Caribbean was wetter. On the other hand, the authors note a tendency for dry conditions in the late 1930s, 1940s and late 1970s onward. The Northern Caribbean and the Caribbean basin seem to operate in anti-phase on these timescales.

However, the interdecadal to multidecadal climate anomalies in the Caribbean have not yet been connected to general circulation patterns [*Jury* 2009]. A possible suggestion was made by *Sutton and Hodson* [2005]. The authors studied multidecadal climate variations over the Atlantic region. In their study they compared the analysis of observational data with model results. Fig. 3.29 (left) indicates the influence of the warm AMO (1931-1960) vs. the cold AMO phase (1961-1990) on precipitation anomalies, which was calculated from observational data. The result of a SST forced model run with the HadAM3 model is shown on the right and indicates changes in precipitation over the sea surface. The authors note a clear connection of Caribbean precipitation to the AMO.

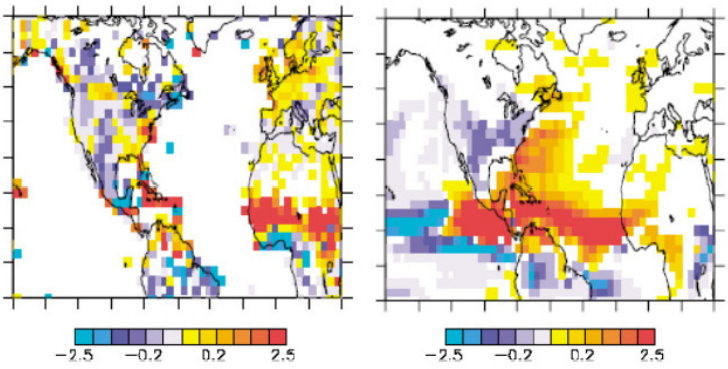

Figure 3.29: *Influence of a positive AMO phase vs. a negative AMO phase as derived from observational data (left) and climate model results (right). Note increased precipitation over the Caribbean. Figure adapted from Sutton and Hodson [2005].*

An analysis of NCEP NCAR data for sea surface precipitation rate over Cuba (prescribed in chapter 3.3.1) is also shown in Fig. 3.30. The data clearly indicate the connection to the AMO. In the positive phase of the AMO, Cuba receives more rainfall than in the negative phase of the AMO.

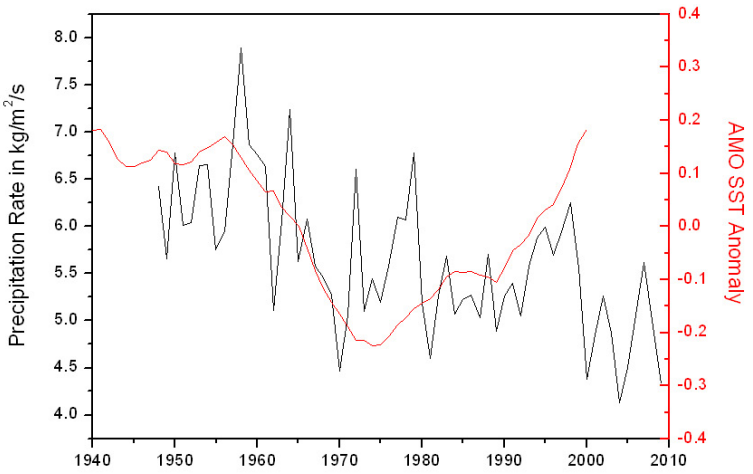

Figure 3.30: *Rainfall amount over Cuba in comparison with the AMO.*

Together with the study of [*Knight et al.* 2006], the connection of the AMO to Caribbean SST and precipitation can be described with the movement of the ITCZ on multidecadal timescales. A warmer phase of the AMO leads to higher SST in the Caribbean as well as more precipitation. Higher SST in the Caribbean are connected to a more northward position of the ITCZ as well as higher evaporation rates and, therefore, higher precipitation [*Lachniet* [2009b], *Poveda et al.* [2006]].

3.4 Past Climate Reconstructions

3.4.1 Holocene climate reconstructions

Solar variability

Reconstructions of solar variability in the past millennia are based on cosmogenic isotopes (^{10}Be, ^{14}C). Their production is modulated by solar magnetic activity, and concentrations can be measured in ice cores (e.g., ^{10}Be) or tree rings (^{14}C) (e.g., *Bard et al.* [2000], *Solanski et al.* [2004], *Muscheler et al.* [2005], *Jones et al.* [2009]). An overview of Holocene proxy data including ice cores is given by *Wanner et al.* [2008]. The band pass filtered reconstructions of solar variability are shown in Fig. 3.31. E.g., the distinct peaks of the 208 year in the frequency spectra is attributed to the solar Suess (or de Vries) cycle, the 87 year cycle accordingly to the Gleissberg cycle [*Wanner et al.* 2008].

Changes of insolation are not solely due to the energy output of the sun, but also the

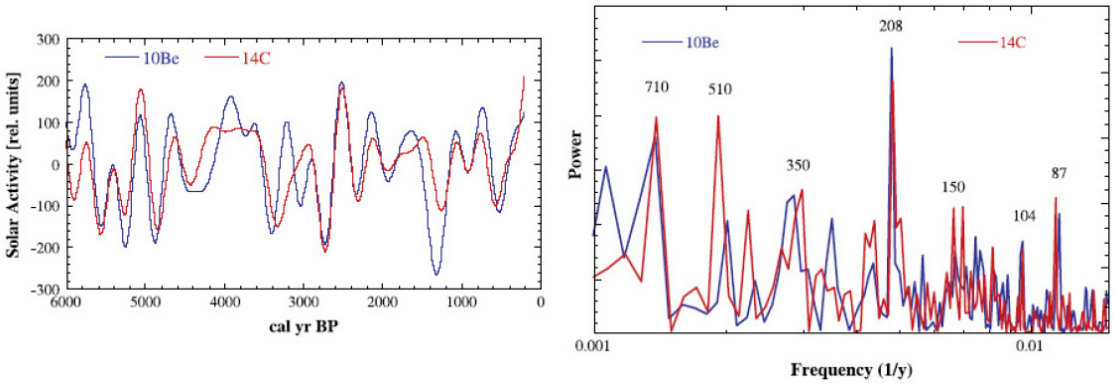

Figure 3.31: *left: Reconstructions of solar activity based on ^{10}Be and ^{14}C production rates. Both curves were bandpass filtered with a window of 300-3000 years. Right: Power spectra of the two solar activity records spanning the last 10000 years. Figures adapted from Wanner et al. [2008].*

position and the orientation of the Earth relative to the Sun. The orbital parameters of the Earth change with main periodicities of 400000 and 100000 years due to orbital eccentricity. Changes in the Earth's axial tilt lead to periodicities of 40000 years, the precession of the Earth's axis to changes on 20000 years. The orbital cycles according to the Milancovitch theory can be calculated precisely [*Berger* 1978]. Fig. 3.32 shows the calculated changes in insolation for the last 6000 years [*Wanner et al.* 2008]. The changes were calculated for each latitudinal band of 10 degrees relative to its mean insolation during the last 6000 years. Fig. 3.32c shows the changes in seasonality of insolation, the difference between June and December. 6000 years ago, the seasonality was dominant in the northern hemisphere and decreased steadily. Around 3000 years ago the situation reversed and the seasonality became larger in the southern hemisphere [*Wanner et al.* 2008].

Knudsen et al. [2009] studied solar variations during the Holocene combining ^{14}C data from the IntCal04 record and ^{10}Be data from the GRIP ice core. Joint spectral analysis of the two nuclide records suggests that the periodic behavior of the Sun was particularly pronounced between 6000-4500 and 3000-2000 a BP, with dominating periodicities of 88, 150, 220, and 400 years, while this rhythmic behavior faded during other time intervals. The authors note that subtle but systematic differences between the amplitude spectra may point to an interplay between the climate system and the 220- and 400-year solar cycles during intervals when these were particularly prominent.

North Atlantic variability

A Holocene sediment record of North Atlantic drift ice was presented by *Bond et al.* [2001]. The authors note, that surface winds and surface ocean hydrography in the sub-

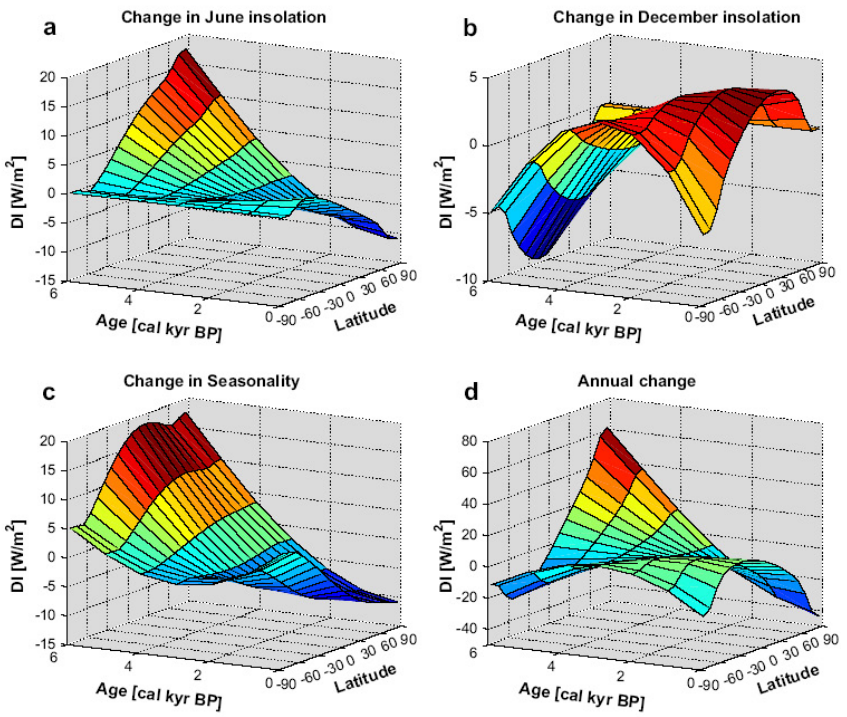

Figure 3.32: *Calculated deviations of insolation from the long term mean values as a function of latitude for the past 6000 years. (a) June (boreal summer), (b) December (austral summer), (c) seasonality (differences between June and December), (d) annual mean. Figure adapted from [Wanner et al. 2008].*

polar North Atlantic appear to have been influenced by variations in solar output on a 1500 year cycle. Surface hydrographic changes may have impacted production of North Atlantic deep Water, potentially providing an additional mechanism for amplifying the solar signals and transmitting them globally.

Another record from the tropical North Atlantic has been published by *deMenocal et al.* [2000]. Their record of sea-surface temperature (SST) variations off West Africa documents a series of abrupt, millennial-scale cooling events, which punctuated the Holocene warm period. These events evidently resulted from increased southward advection of cooler temperate or subpolar waters to this subtropical location or from enhanced regional upwelling. The authors note, that the most recent of these events was the Little Ice Age, which occurred between 1300 to 1850 A.D., when subtropical SSTs were reduced by 3 to 4 °C. These events were synchronous with the Holocene changes in subpolar North Atlantic SSTs shown by *Bond et al.* [1997], documenting a strong, in-phase link between millennial-scale variations in high- and low-latitude climate during the Holocene.

Holocene records from the North- and South Atlantic region as well as the Pacific region have been studied by *Debret et al.* [2009]. A strong mid-Holocene transition

has been identified by wavelet analysis in several sea ice records from the circum-Antarctic area, ice core records (Taylor dome, Byrd) and tropical marine records. The Holocene pattern confirms the importance of external forcing during the Early Holocene (solar activity: 1000 years and 2500 years during the entire Holocene). The authors note, that the second part of the Holocene is then marked by the gradual appearance of internal forcing (thermohaline circulation around 1500 years), associated with a stabilization of the signal. Coupling between ocean and atmosphere seems to play a fundamental role in the observed frequencies, which vary accordingly in the Atlantic, circum- Antarctic and Pacific areas. The North Atlantic area seems to be the instigator of thermohaline circulation as shown by its sensitivity to meltwater discharges during the Early Holocene, even though each sector is independent with regards to its frequency content (around 1600 years for Atlantic Area; around 1250 years for Antarctica) [*Debret et al.* 2009].

ENSO variability

ENSO variability during the Holocene also has been documented in several climate records. E. g., *Moy et al.* [2002] present a lake sediment record from southern Equador for the last 12000 years. Frequency analysis of measured red intensity shows that changes on timescales of 2-8 years become more frequent during the Holocene until around 1200 years ago and then decline towards present. Those changes on subdecadal timescales have been attributed to warm ENSO events. The authors also find that periods of high and low ENSO activity alternate on a timescale of about 2000 years, which are superimposed on this long term trend. The long term trend has been attributed to orbitally induced changes in insolation. The authors suggest that internal ENSO dynamics are a possible cause for the millennial scale variability.

Another marine sediment record is presented by *Rein et al.* [2005], spanning the last 20000 years. The authors note that the onset of stronger El Niño activity in Peru started around 17000 years ago, contemporaneous with Heinrich event 1. Maximum El Niño activity occurred during the early and late Holocene. As a recurrence period of very strong El Niño events, the authors note 60-80 years. The events were weak before and during the beginning of the Younger Dryas, during the middle of the Holocene and during medieval times.

3.4.2 Holocene Climate variability in the Caribbean

Climate variability in the Caribbean area has been reconstructed from several different natural archives including lake sediments, marine sediments, coral records as well as stalagmite records. In general, many forcing mechanisms have been proposed to control Holocene climate variability in the Caribbean area. *Haug et al.* [2001] and [2003] provided a Holocene sediment record reconstructing Titanium concentrations of

the Cariaco Basin in the southern Caribbean. As a forcing mechanism the authors offer the movement of the ITCZ. The record shows in general southward position of the ITCZ during the Younger Dryas, rapidly followed by a period of increased precipitation attributed to a more northward position of the ITCZ. Since the Holocene thermal maximum, the record reveals a southward migration of the ITCZ, following solar insolation changes on orbital timescales. During a time interval between 2800 and 3800 years ago and during the Little Ice Age, the record reveals high-amplitude fluctuations and precipitation minima. Another Holocene record from the Cariaco basin has been interpreted as being a signal for the strength of trade winds [*Hughen et al.* 1996, 1998]. The Cariaco records also recover a dry period with stronger tradewinds during the Younger Dryas. During the medieval climate anomaly (MCA), the ITCZ was interpreted in a northward position opposite to the Little Ice Age (LIA), which is connected to a southward migration of the ITCZ. In *Haug et al.* [2003], dry periods occurring in the record were connected to the collapse of the Maya civilization during the Terminal Classic Period, with extended dry periods punctuated by intense multi-year droughts centered around 810, 860 and 910 A.D. A similar finding has also been suggested by *Hodell et al.* [1991], who reconstructed past precipitation changes during the Holocene from lake sediments from Haiti, as well as *Hodell et al.* [1995], *Curtis et al.* [1996], *Hodell et al.* [2005a], *Hodell et al.* [2005b] and *Hodell et al.* [2001]. *Hodell et al.* [2001] also found a 208 a variability in a sediment record on the Yucatan peninsula. Together with the record from Haiti, *Mangini et al.* [2007] suggest a connection via the NAO to a stalagmite record of Barbados, indicating increased seasonality during NAO^+ conditions. A connection to the ENSO phenomenon has been documented in stalagmite records from the western Caribbean by [*Lachniet et al.* 2004b]. This study suggests drier conditions on the Isthmus of Panama during El Niño events. A hurricane record from Puerto Rico was developed by *Donnelly and Woodruff* [2007], who report less hurricane activity during stronger El Niño events during the last 6 ka. In a 85 ka record from Guatemala [*Hodell et al.* 2008] lake sediment records have been connected to Northern latitude climate variability such as changes in the thermohaline circulation. During the 8.2 ka event, a connection to northern climate changes have also been found in a stalagmite record from Costa Rica [*Lachniet et al.* 2004a]. Detailed studies on past changes in sea surface temperatures were conducted by *Black et al.* [2004], [2007] indicating multidecadal to centennial variability connected to solar variability.

In order to study past climatic changes in the Caribbean area, this study presents three well dated highly resolved paleorecords covering the whole Holocene. The great advantage of speleothem research is, e.g., in comparison to deep sea sediments, the ability to absolute dating and high resolution proxy records on nearly subdecadal timescales. This study will lead to further insights on natural climate variability on multidecadal to millennial timescales in the Northern Caribbean during the Holocene. Such an understanding is crucial for successfully predicting Caribbean climate change

in simulations of future greenhouse warming.

4 Compilation of isotopic records, spectral investigation and cave monitoring

This study uses three stalagmite samples from north-western Cuba in order to investigate past climate variability in the Caribbean. Two stalagmites were dated with a combination of two Th/U-series dating methods, the TIMS (thermal ionization mass spectrometry) and MC-ICPMS (multi-collector inductively coupled plasma mass spectrometry) method. The study shows that an initially used correction of ages can not be used and establishes a new correction method, which can also be attributed to the second stalagmite CP (Cuba Pequeño) from the same cave system. This has significant implications for the age models and, therefore, frequency and wavelet analysis of the isotope records. In this chapter, the age models and the stable isotope data are presented and investigated, as well as further measurements of aragonite/calcite content are shown. Results from the cave monitoring, which was performed in 2008 to get further insights about processes inside the cave, will be discussed.

4.1 Chronology of Cuban stalagmites

4.1.1 Chronology of Cuba Grande

Stalagmite Cuba Grande (CG) has extremely low ^{230}Th concentrations. Thus, the effect of potential contamination with initial ^{230}Th is very large. Since no distinct growth layers are visible, isochrons (s. section 2.3) are not applicable and an alternative method is used to constrain the (^{238}U/^{232}Th) of the contaminating phase. First, a robust age model using uncorrected (^{230}Th/^{238}U) and (^{234}U/^{238}U) ratios is derived from sub samples with low ^{232}Th concentration measured with high precision MC-ICPMS. Then the dating results of samples with elevated ^{232}Th concentration are compared with this age model in order to estimate the (^{238}U/^{232}Th) of the contaminating phase. This enables derivation of a sample specific (^{230}Th/^{232}Th) for the correction [*Fensterer et al.* 2010].

22 MC-ICPMS and TIMS U-series ages were determined along the growth axis of CG. Ten MC-ICPMS measurements were performed using a ThermoFinnigan Neptune MC-ICPMS at the Bristol Isotope Group, and twelve analyses were performed on a Finnigan MAT 262 RPQ TIMS at the Heidelberg Academy of Sciences. All uncorrected ^{230}Th/U dating results of CG are shown in Fig. 4.1, and a table with all data can be

found in the supplementary information. Ages are given in ka before the year 2000 (ka b2k). The 720 mm long stalagmite sample consists of pure white calcite, as confirmed by X-ray diffraction analysis. No distinct growth layers are visible (Fig. 4.1). The U content of the samples ranges from 90 to 200 ng/g. ^{230}Th concentrations vary between 0.01 and 0.06 pg/g per sample. For both methods sample masses between 0.5 and 1 g were used for one analysis. The average span of time included in one sample should, thus, be the same for MC-ICPMS and TIMS. Due to the smaller sample size required for analysis, however, the precision of the MC-ICPMS ages is much higher. Analysis of small concentrations of ^{230}Th is more precise using the MC-ICPMS technique, hence the focus of further examinations is on the MC-ICPMS data. Seven ages determined by MC-ICPMS suggest nearly constant stalagmite growth rate during the last ~1370 years. The calculated age model using a linear fit has a slope of $0.00190(\pm 2 \cdot 10^{-5})$ ka/mm, which corresponds to a growth rate of $526(\pm 11)$ μm/a. The fit was forced through the origin since the dripsite was active when the stalagmite was removed from the cave. Three ages at 13, 27 and 540 mm distance from top (DFT) are not in stratigraphic order and have, thus, not been considered for this fit. The ages determined by the TIMS method generally exhibit older ages than the MC-ICPMS data and larger scatter (Fig. 4.1).

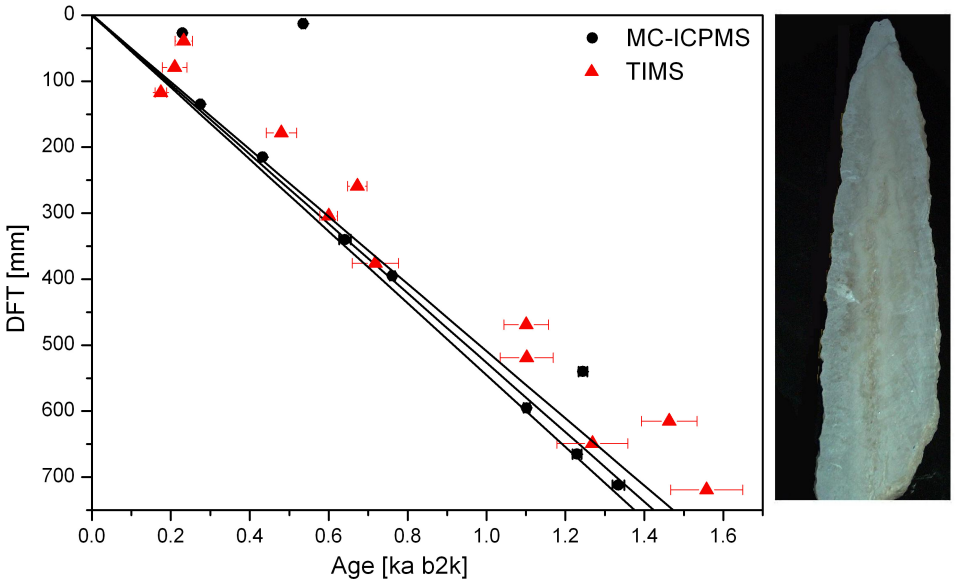

Figure 4.1: *(left) Ages of CG determined by the MC-ICPMS (black circles) and the TIMS method (red triangles), without any detrital correction. Ages are given in ka b2k as a function of distance from top (DFT) in mm. The age model (black line) and the corresponding 95 % confidence limits are also shown. (right) Picture of stalagmite CG.*

Fig. 4.2 shows the uncorrected ages determined by MC-ICPMS in comparison to the (^{230}Th/^{232}Th) of the samples. The three samples at 13, 27 and 540 mm DFT show a substantially lower (^{230}Th/^{232}Th) than the other samples suggesting a higher degree of detrital contamination. Since these three ages do not plot on the straight line determined by the less contaminated ages, this suggests that the applied correction using a (^{238}U/^{232}Th) of 0.8 is inadequate to account for the effect of detrital contamination. The samples at 13, 27 and 540 mm DFT show a (^{230}Th/^{232}Th) ratio below 80, which this study uses as a threshold to identify results that require a detritus correction.

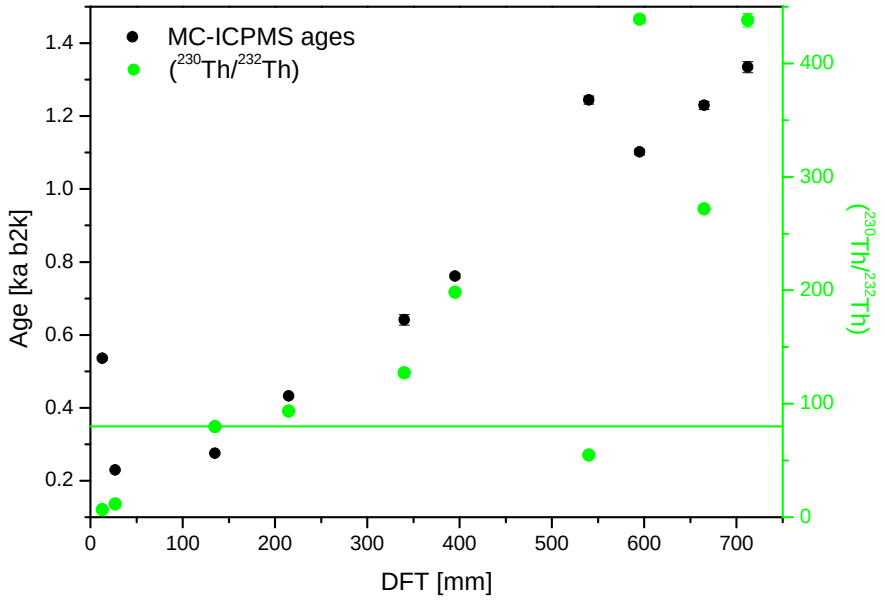

Figure 4.2: *MC-ICPMS dating results (black circles) and (^{230}Th/^{232}Th) (green circles). The three ages at 13, 27 and 540 mm DFT are not in stratigraphic order, and the corresponding samples have a significantly lower (^{230}Th/^{232}Th) than 80 (green line).*

A strict constraint for the age of sub-samples taken along the growth axis of a stalagmite is, that ages must become progressively older from top to bottom [*Scholz and Hoffmann* 2008, *Hellstrom* 2006, *Beck et al.* 2001, *Musgrove et al.* 2001]. The ages at 13, 27 and 540 mm DFT are not in stratigraphic order and therefore do not fulfill this criterion (Figs. 4.1 and 4.2). Assuming that the true age-depth relationship for stalagmite CG is described by the linear age model determined using the samples with low ^{232}Th content (Fig. 4.1), the (^{238}U/^{232}Th) for the correction of the samples with elevated ^{232}Th can be estimated. The activity ratios of the samples at 13, 27 and 540 mm DFT need to be corrected with (^{238}U/^{232}Th) ratios of 6.1, 8.7 and 9.6, respectively, in

order to obtain corrected ages in agreement with the linear age-depth model. The mean of the three ($^{238}U/^{232}Th$) ratios is 8($\pm$4) (2σ standard deviation of the average value), almost an order of magnitude larger than the bulk earth factor, which is normally used to account for detrital contamination. This ($^{238}U/^{232}Th$) is now used to recalculate all ages determined by MC-ICPMS and TIMS. The results are shown in Fig. 4.3.

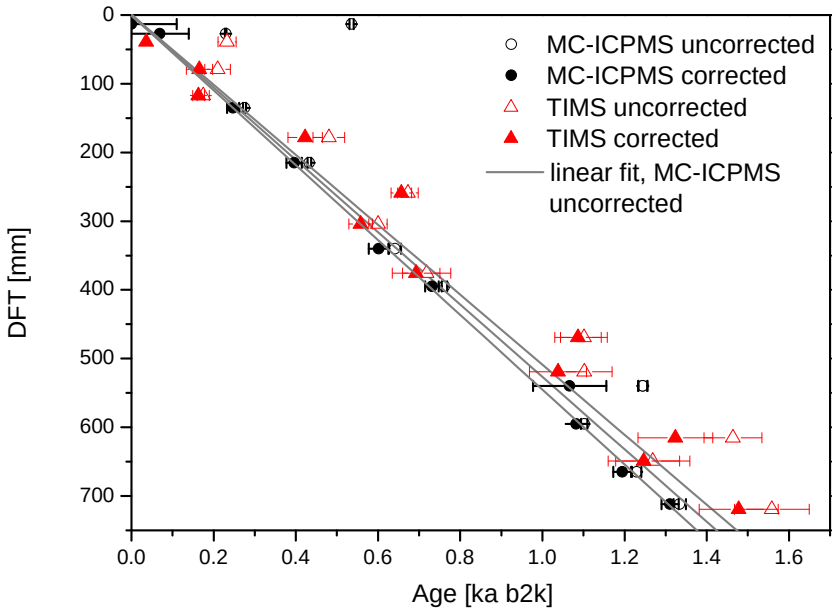

Figure 4.3: *MC-ICPMS dating results, corrected with a ($^{238}U/^{232}Th$) of 8 (filled black circles) and without correction (open black circles). TIMS ages are shown as filled red triangles for the corrected results, red open triangles for uncorrected. The age model determined by the uncorrected MC-ICPMS data is shown as a gray line.*

The corrected age of the uppermost sample dated by the MC-ICPMS method is out of range using the mean correction factor of 8. This is due to the fact that in this case the assumed ^{230}Th concentration of the detrital phase is larger than the total ^{230}Th concentration. Thus, the corrected concentration of ^{230}Th becomes negative, and the $^{230}Th/U$ age equation cannot be solved. Instead, the maximum value to maintain positive results and the minimum value of the confidence range of the correction factor (6 and 4, respectively) is used to estimate the age range for this sample.

The TIMS ages corrected with an ($^{238}U/^{232}Th$) of 8 are still not in stratigraphic order and in general exhibit older ages than the results from MC-ICPMS. This suggests that the scatter in the TIMS data is not solely due to contamination with initial ^{230}Th. Differences in spike calibration can be excluded as the reason for the apparently too

old TIMS ages since an inter-laboratory comparison did not show significant differences [*Hoffmann et al.* 2007]. In contrast, it is speculated that a relatively large contribution of the background intensity to the ^{230}Th signal is the reason for this scatter, which also limits the general precision that can be achieved by TIMS. However, taking into account the relatively large uncertainties of the TIMS ages, the TIMS age model is in agreement with the age model based on MC-ICPMS results.

Final age model for CG

The age model determined by the uncorrected ages is shown in Fig. 4.4 in gray with a slope of $0.00190(\pm 2 \cdot 10^{-5})$ ka/mm or $\approx 526\,\mu$m/a. The final age model for stalagmite CG is shown in red together with the corrected (correction factor of 8) MC-ICPMS ages (black circles). The final age model is based on a linear fit through the origin. All MC-ICPMS measurements were considered for this fit, but not the TIMS ages. The errors in the ages were also considered for this fit, resulting in the upper and lower confidence limits, which are also shown (Fig. 4.4, green lines). The resulting age model has a slope of $0.00184(\pm 2 \cdot 10^{-5})$ ka/mm or $\approx 543\,\mu$m/a.

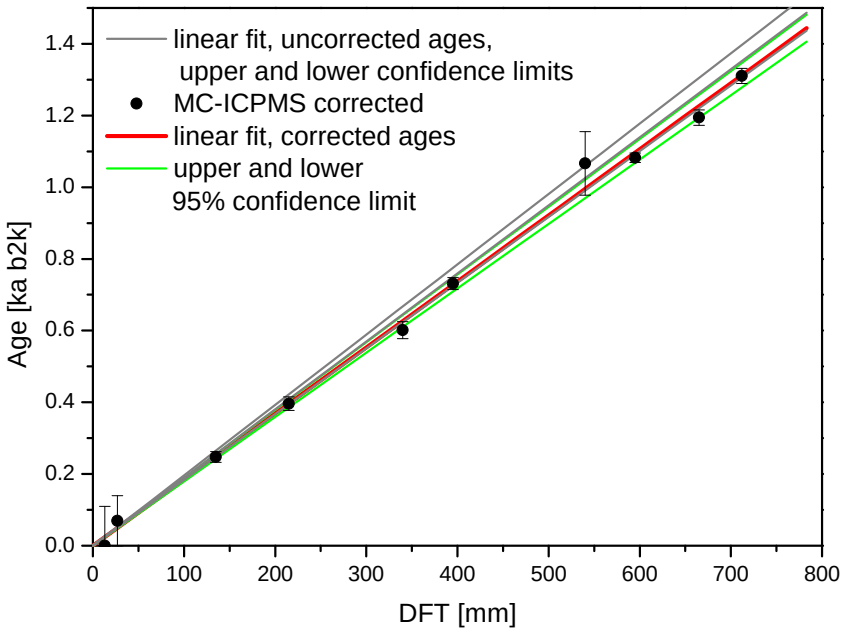

Figure 4.4: *MC-ICPMS dating results, corrected with a ($^{238}U/^{232}Th$) of 8 (filled black circles). The final age model determined by the a linear fit is shown as a red line; green lines indicate upper and lower confidence limits.*

4.1.2 Chronology of Cuba Pequeño

Stalagmite Cuba Pequeño was also dated by both the MC-ICPMS and TIMS method. The results are shown in Fig. 4.5. 18 ages were determined by the MC-ICPMS method and 20 ages by the TIMS method along the growth axis of the 420 mm long stalagmite. Fig. 4.5 shows uncorrected ages in blue (MC-ICPMS) and green (TIMS). In a first step, the ages were corrected with a (^{238}U/^{232}Th) of 0.8. Results are shown as open black (MC-ICPMS) and open red (TIMS) symbols. In addition, the results for the correction of ages with 8 is shown in filled black (MC-ICPMS) and filled red (TIMS) symbols. The ages show in general a step around a DFT of 240 mm. Below 240 mm DFT, the ages are not in stratigraphic order and show large scatter. A possible explanation for ages which are too old and largely scattering, is that recrystallization from aragonite to calcite took place in this part of the stalagmite. This could lead to loss of U and ages get too old. This possibility is studied in more detail below.

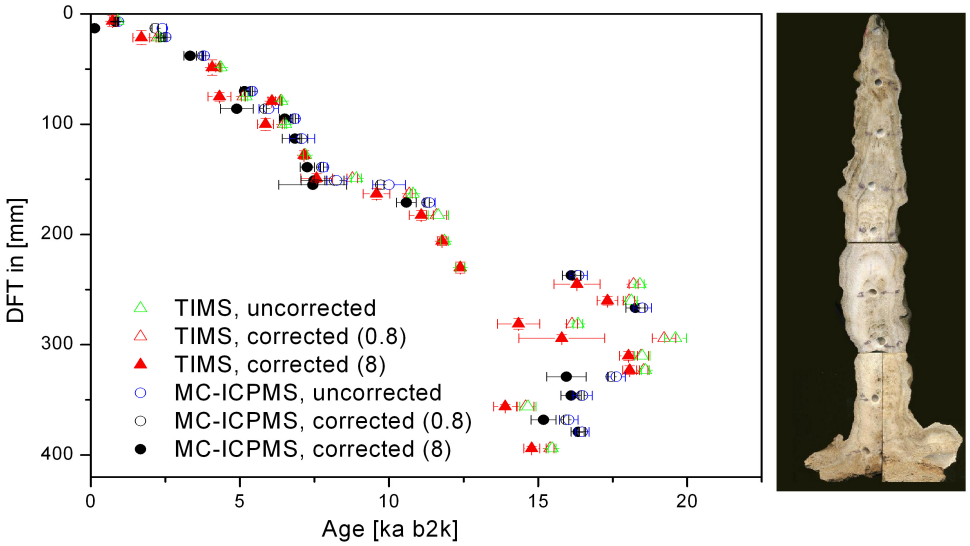

Figure 4.5: *MC-ICPMS and TIMS measurement results. Values are shown uncorrected, corrected with an (^{238}U/^{232}Th) of 0.8 and 8. Below 240 mm DFT the ages are not in stratigraphic order and show large scatter.*

As shown for stalagmite CG, the correction of all ages with a site specific correction factor is important for samples with a low (^{230}Th/^{232}Th) ratio. The determined ratios for CP are shown in Fig. 4.6 together with all ages. As found for CG, the lower limit for samples with high initial contamination is ≈80. 14 ages are below this activity ratio, indicating a high initial detrital contamination. In order to correctly account for this effect, the correction with the correction factor of 8 was applied to all samples. However, some samples are still not in stratigraphic order as shown in Fig. 4.5. Three samples around 150 mm DFT show the same age after correcting with the new correction. Therefore, these ages are considered reliable and were chosen also for the final age

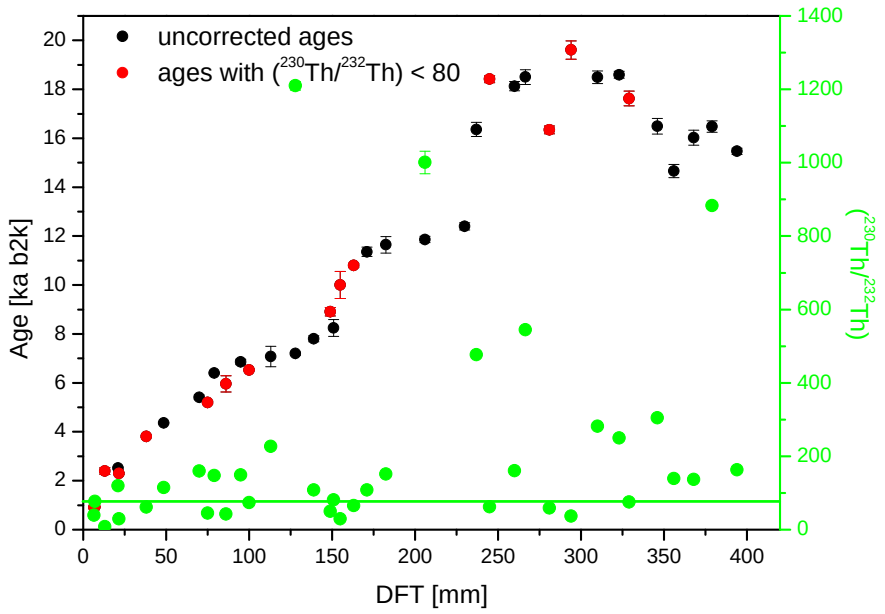

Figure 4.6: *Uncorrected ages of CP in comparison to the (^{230}Th/^{232}Th) ratio. The activity ratio of 80 is marked as a green line. Ages shown in red show an activity ratio below this threshold.*

model. In general, a discrepancy exists for one age at the top of the stalagmite around 13 mm DFT. This sample is not in stratigraphic order with the two ages above and has been disregarded for the final age model. Between 75 and 100 mm DFT, 6 ages are not in stratigraphic order, even after the correction. However, all ages are considered reliable and were considered for the final age model.

Two age models were established for stalagmite CP. Results are shown in Fig. 4.7 together with the estimated 95 % confidence limits. The age models were calculated with the algorithm provided by *Heegaard et al.* [2005]. For the age model in the older part, only the two ages at 350 mm and 400 mm DFT were considered. However, this part of the stalagmite is less datable as will be discussed below. Within the estimated errors of the age models, both corrected age models are in agreement with each other. In this study, therefore, all data concerning CP are shown with the age model corrected with the (^{238}U/^{232}Th) of 8.

The growth rate can be estimated by the derivative of the age model. Results for the corrected age model (factor of 8) are shown in Fig. 4.8. In general the stalagmite shows relatively low growth rates of 15 μm/a during the last 4 ka. The phase between 4 and 8 ka shows higher growth rates up to 40 μm/a. Between 8 ka and 12 ka, the growth rate is slower with a value of 15 μm/a. The growth rate in the part older than 12.5 ka is

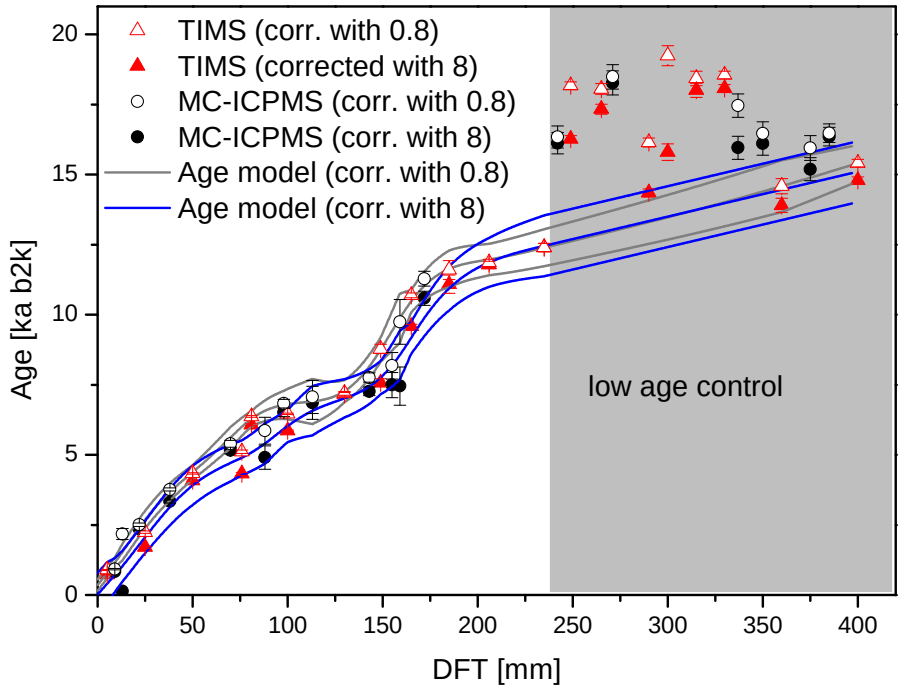

Figure 4.7: *Estimated age models for stalagmite CP, corrected with a ($^{238}U/^{232}Th$) of 0.8 (open symbols) and 8 (filled symbols).*

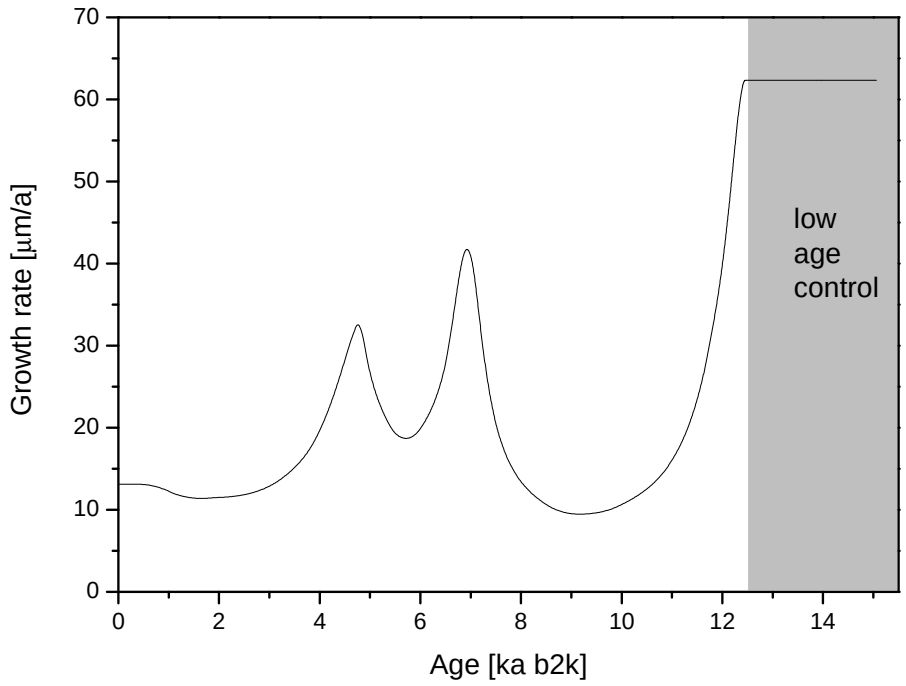

Figure 4.8: *Growth rates of stalagmite CP.*

generally less reliable due to the large scatter in the ages as shown above. The growth rate is higher in the older part, with values around 60 μm/a.

As can be seen in Fig. 4.9, the U content of CP varies largely along the growth axis. The U content in the lower part of the stalagmite is up to an order smaller than in the upper part in the stalagmite. U values above 250 mm DFT range from ≈1 to 13 ppm and values below 250 mm DFT from ≈ 0.3 to 3 ppm. The ages in the lower part with low U content show a larger scatter and are not in stratigraphic order. The stalagmite has an aragonitic structure in the upper part. Aragonite incorporates more U into the crystal lattice. The smaller U content in the bottom section and the large scatter in estimated ages can be explained by recrystallization from aragonite to calcite. This leads to open-system conditions and remobilization of U where ages get too high [*Holzkämper et al.* 2009]. This recrystallization has also been studied in biogenetic aragonitic coral samples by *Scholz et al.* [2004]. The aragonitic structure of stalagmite CP has been studied in more detail in the following sections with X-ray diffraction methods (XRD) and trace element concentrations determined by inductively coupled plasma optical emission spectroscopy (ICP-OES).

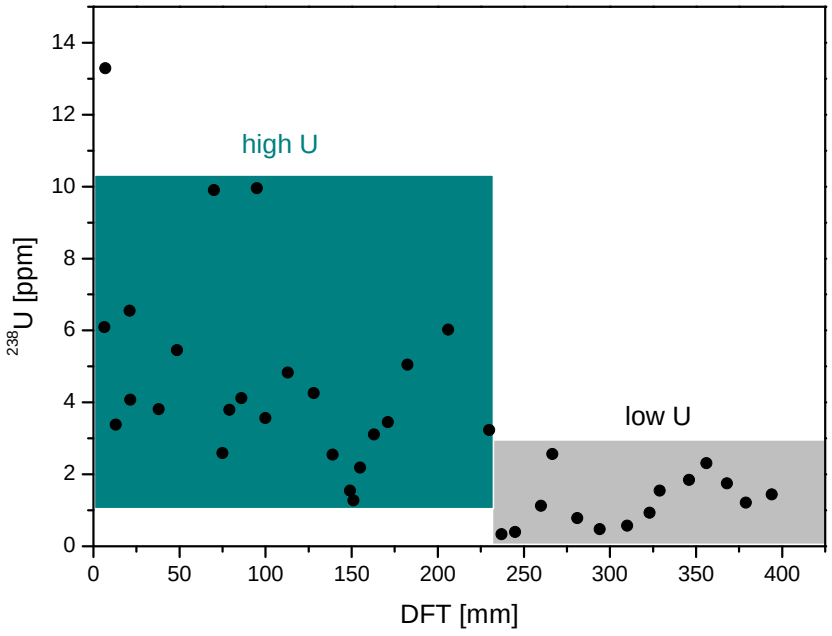

Figure 4.9: ^{238}*U content along the growth axis of the stalagmite. High Uranium content is found above 240 mm DFT, low Uranium content below 240 mm DFT.*

Aragonite/Calcite content (XRD)

The aragonite, calcite and quartz content along the growth axis of CP was studied with X-ray diffraction (XRD) analysis. The analyis was performed on 24 samples. Measurements were carried out at the Insitute for Geosciences (University of Heidelberg) on a Philips XPert PW 3020. Scans were made on an angle between 20° and 60°. All samples were evaluated with the EVA program for a semi-quantitative analysis. In addition, one sample at 220 mm DFT was evaluated with the Rietveld method to get a more quantitative result [*Rietveld* [1967], *Rietveld* [1969]]. The results are shown in Fig. 4.10. The aragonite content in the part below 250 mm DFT is negligible, all data show 100 % calcite. The calcite and aragonite content show a clear step at 250 mm DFT leading to lower calcite and higher aragonite content in the upper part of the stalagmite. The analysis with the Rietveld method at 220 mm DFT indicate more quantitative values, 70 % of calcite and 30 % aragonite. At the same DFT, the EVA method gives values of 83 % and 17 %, respectively. Hence, results of the EVA method are interpreted in a qualitative way.

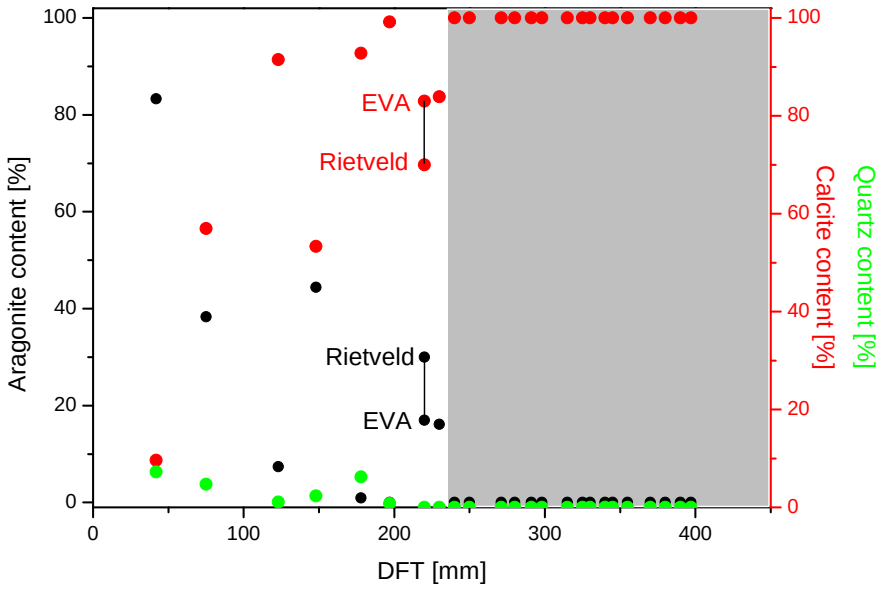

Figure 4.10: *Measurements of aragonite, calcite and quartz content along the growth axis of CP.*

Trace elements in stalagmite (ICP-OES)

Trace elements were measured along the growth axis of CP with 27 samples in order to confirm the transition from aragonite to calcite. The concentration of cations were determined at Heidelberg University using an ICP-OES VISTA MXP (VARIAN). The internal 1 σ-standard deviation is <1 % for Ca^{2+}, Mg^{2+} and Sr^{2+}. NIST 1643e is used as a standard, and its long-term 1 σ-reproducibility is 1 mg/l for Ca^{2+}, 0.4 mg/l for Mg^{2+}, and 6 μg/l for Sr^{2+}. Fig. 4.11 shows the results of the determined Mg/Ca and Sr/Ca ratios. The Mg/Ca ratio shows relatively low values around 2 in the upper part of the stalagmite above 250 mm DFT. Only the interval between 80 and 90 mm DFT shows a peak reaching a ratio of 10. Below 250 mm DFT, the stalagmite reveals relatively high Mg/Ca ratios around 12, with a dip reaching a ratio of around 8 between 350 and 370 mm DFT. The signal of the Sr/Ca ratio is anti-correlated. This indicates, that in the aragonitic interval above 250 mm DFT, as seen in the XRD analysis, Mg/Ca ratios are much lower than in the calcite part below 250 mm DFT and vice versa for Sr/Ca. This antibehaviour has also been found in aragonitic layers within a calcitic stalagmite by *McMillan et al.* [2005] in a stalagmite from the western Mediterranean. The authors attribute this effect to different partitioning behaviour of aragonite compared with calcite due to the different crystal structure [*Morse and MacKenzie* 1990].

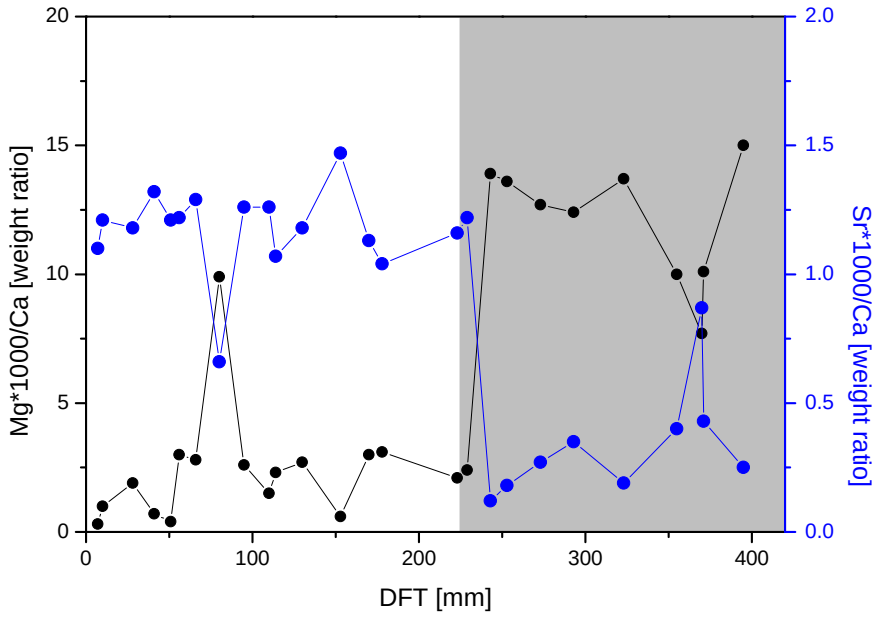

Figure 4.11: *Measurements of Sr/Ca and Mg/Ca along the growth axis of stalagmite CP as an indicator for aragonite below 250 mm DFT.*

4.1.3 Chronology of Cuba Medio

The third stalagmite, Cuba Medio, was dated solely with the TIMS method. The 13 ages are shown in Fig. 4.12 along the growth axis of the 520 mm long stalagmite. This stalagmite reveals an U content of ≈0.1 ppm, similar to CG. Since CM grew in a different cave system than the other two stalagmites (see section 2), the correction for determined ages was chosen to be the usual correction of 0.8. The results reveal a relatively short growth phase during the Holocene from ≈7 to 10 ka in the upper 22 mm of the stalagmite followed by several growth phases and hiati until 80 ka. Since the stalagmite grew relatively slowly, no more age determinations were possible in the 22 mm long the Holocene time slice. The stalagmite shows several hiati or phases of slower growth (at 23 mm, 62-71 mm, 142 mm, 153 mm, 234-241 mm, 353 mm, 406 mm and 460 mm DFT), which are indicated in red in Fig. 4.12. Hiati were visually determined. Based on the TIMS ages and the position of the hiati, the age model for the Holocene part of this stalagmite was determined by linear interpolation as shown in Fig. 4.13. Between 7 and 10 ka the slope of the linear fit is 0.143 (±0.033) ka/mm, which corresponds to growth rate of ≈7 μm/a. The second growth phase between 16 and 18 ka shows a slope of 0.041 ka/mm, equal to a growth rate of ≈24 μm/a. Analogously, the phase between 18 and 27 ka is 0.801 ka/mm (≈1 μm/a). In the next growth phase older than 27 ka, the slope is 0.124 ka/mm (≈8 μm/a).

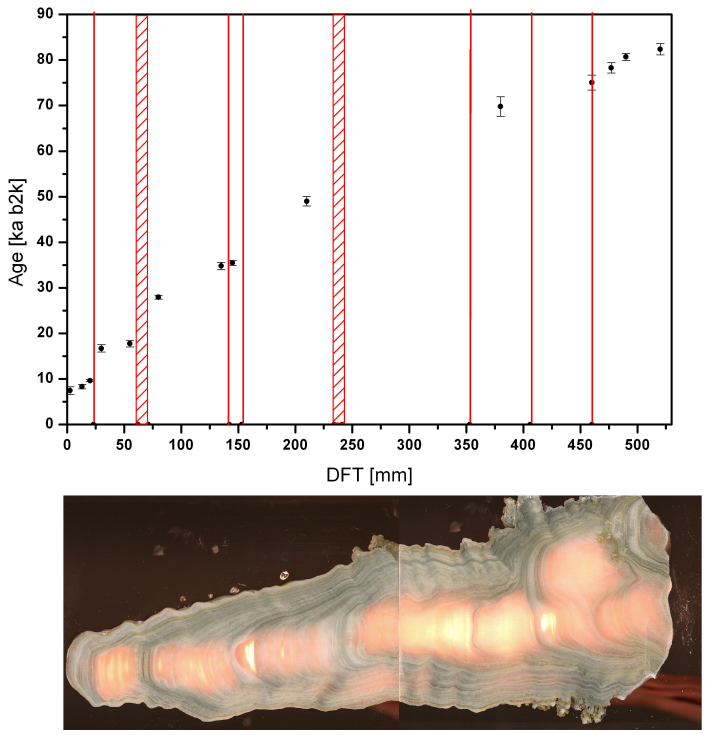

Figure 4.12: *TIMS ages of stalagmite CM. Hiati and intervals with slower growth rates are marked in red.*

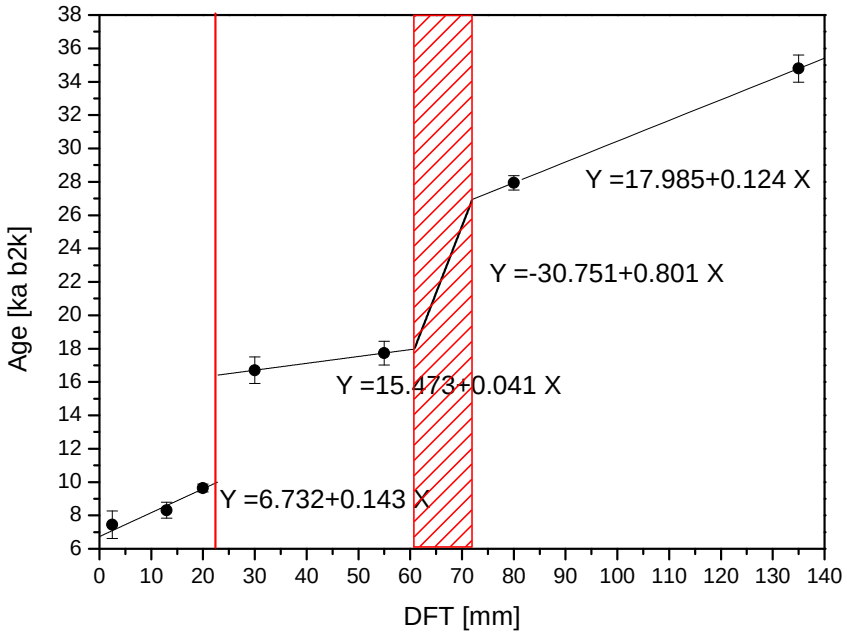

Figure 4.13: *Age model of CM based on linear interpolation, divided in 4 growth intervals.*

4.2 Stable isotopes

4.2.1 Cuba Grande

Stable oxygen and carbon isotopes were sampled at Innsbruck University with a micromill at a resolution of 1 mm for stalagmite CG (for details see *Spötl and Mattey* [2006]). Due to the high growth rate a resolution of ≈2 a is reached in this sample. All values are reported relative to the VPDB standard. Long term precision of the δ^{13}C and δ^{18}O values, estimated as the 1σ-standard deviation of replicate analysis, is 0.06 and 0.08 ‰, respectively [*Spötl and Vennemann* 2003]. Raw results for the stable isotope measurements can be found in the supplement. Using the age model as presented in Fig. 4.4, the stable isotope records are shown in Fig. 4.14. The temporal resolution of this record is 1.9 a per sample. The δ^{18}O signal has a mean value around -5.2 ‰ and shows a variability of 2.5 ‰ during the last 1.3 ka. In general, a trend towards lower δ^{18}O values is visible with a slope of 0.38 ‰/ka. For the δ^{13}C signal, the mean value is around -9.5 ‰, showing a variability of 2.5 ‰.

The criteria ('Hendy criteria') for recognizing conditions of deposition in isotopic equilibrium are (i) that δ^{18}O remains constant along a single growth layer while δ^{13}C

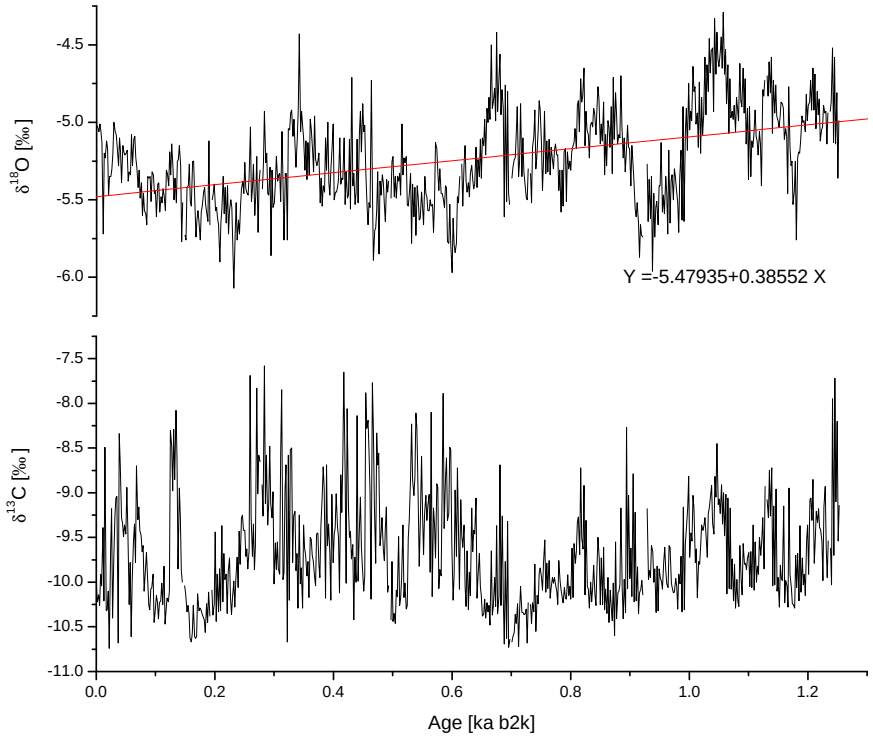

Figure 4.14: *δ^{18}O and δ^{13}C over the last 1.3 ka.*

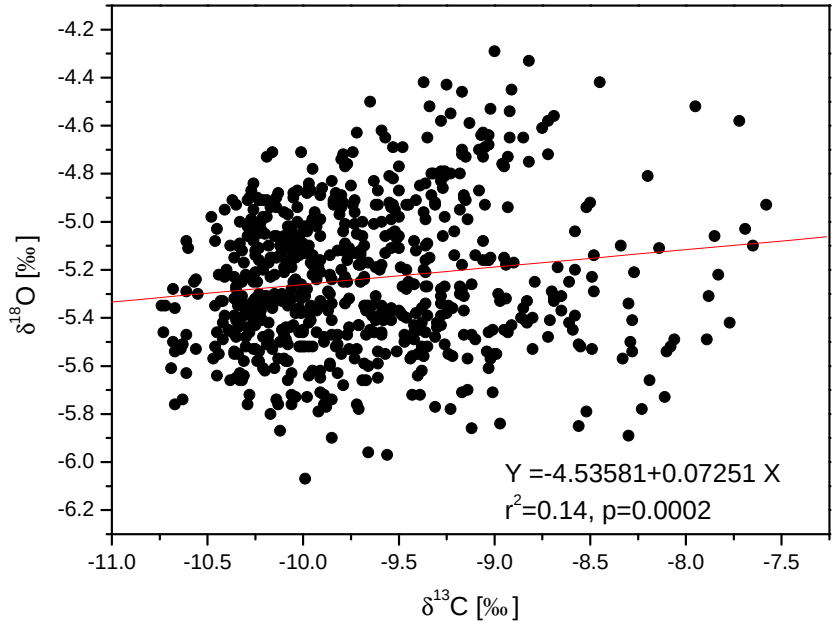

Figure 4.15: *$\delta^{18}O$ versus $\delta^{13}C$ signal along the growth axis of CG.*

varies irregularly, and (ii) that there is no correlation between δ^{18}O and δ^{13}C along a growth layer [*Hendy* 1971, *Schwarcz* 1986, *McDermott* 2004]. Growth layers in this stalagmite are not directly visible and, thus, measurements of stable isotopes along single growth layers were not applicable. The δ^{18}O signal is plotted against the δ^{13}C values along the growth axis in Fig. 4.15. However, the correlation of δ^{18}O with δ^{13}C along the growth axis may also be related to climate variability and is a less strict criterion to test for kinetic isotope fractionation [*Mickler et al.* 2006]. A linear fit through the data gives the equation of $\delta^{18}O = -4.54 + 0.7 \cdot \delta^{13}C$ with a correlation coefficient of $r^2 = 0.14$ and $p = 2 \cdot 10^{-4}$ indicating only a weak correlation between δ^{18}O and δ^{13}C along the growth axis.

4.2.2 Cuba Pequeño

Stable isotopes in stalagmite CP were measured at a spatial resolution of 0.2 mm. The temporal resolution is between 4 and 20 a. The stable isotopes using the corrected age model are shown in Fig. 4.16. In general, the δ^{18}O signal shows three different phases. During the oldest part from 12.5 to 9 ka, the δ^{18}O signal shows relatively high values around -1.5 ‰This phase is followed by a transition phase between 9 ka and 6 ka leading to lower δ^{18}O values around -3 ‰ during the last 6 ka. In general, the variability in the older part is more on centennial timescales whereas in the younger part millennial cycles are visible. The δ^{13}C signal shows values around 2 ‰ with a variability of 6 ‰ from peak to peak.

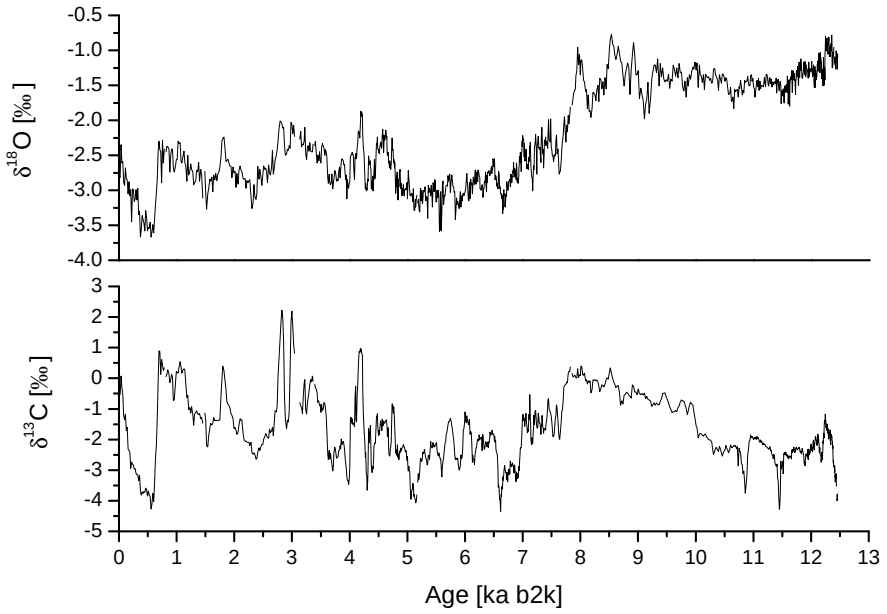

Figure 4.16: *Results of the stable isotopes measurements for $\delta^{18}O$ (upper panel) and $\delta^{13}C$ (bottom panel) versus age.*

Using the algorithm 'Rampfit' of *Mudelsee* [2000], a ramp function can be fitted to the δ^{18}O data. Results are shown in Fig. 4.17. This tool allows to detect climatic transitions in natural proxy data on statistical basis. The analysis detects the beginning of the transition at 8.5 ka (±0.35) ka and the end at 6.85 ka (±0.25) ka. The duration of the transition is around 1.65 ka (±0.55) ka and the midpoint is detected at 7.68 ka (±0.14) ka. The slope of the ramp function between 8.5 and 6.85 ka is 0.94 ‰/ka. The ramp was subtracted from the original δ^{18}O data for further investigation of the variability of the δ^{18}O signal. The detrended result is also shown in Fig. 4.17. For further spectral analysis, only the detrended record was used.

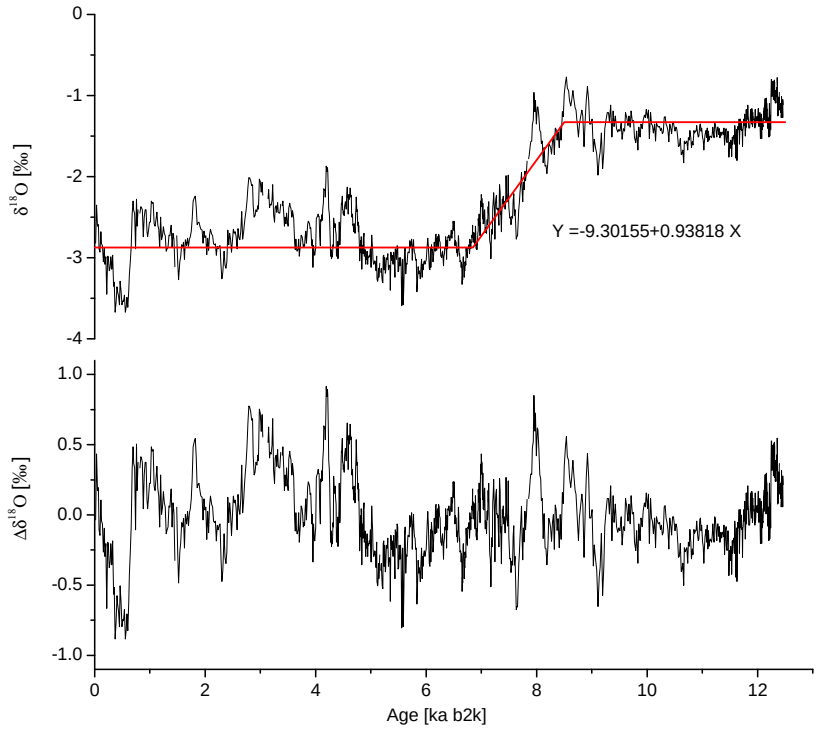

Figure 4.17: *Detected ramp function for the transition phase using the algorithm of Mudelsee [2000] (upper panel). The resulting $\delta^{18}O$ values after subtracting the ramp is shown in the lower panel.*

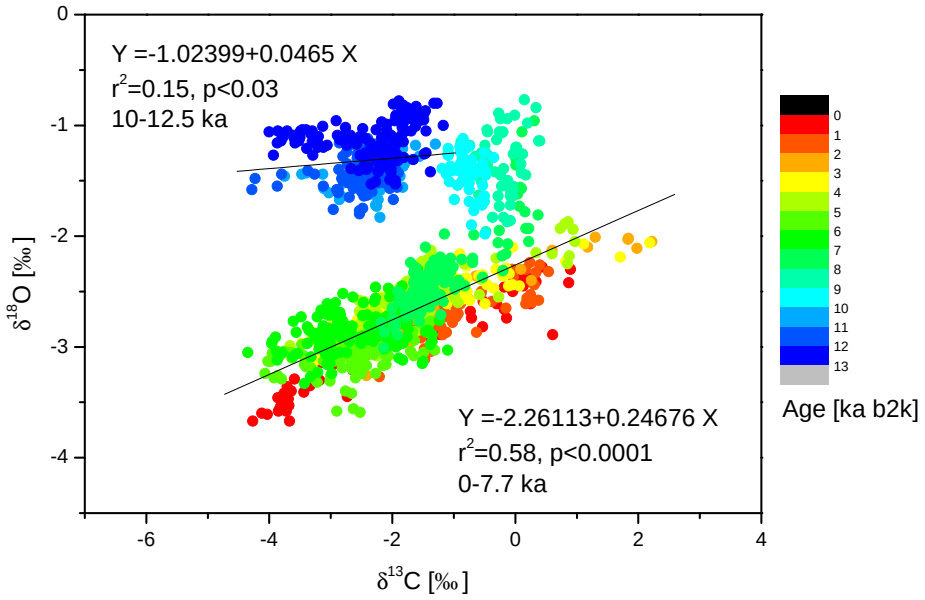

Figure 4.18: *$\delta^{18}O$ versus $\delta^{13}C$ signal along the growth axis of CP.*

The correlation between the raw δ^{18}O signal and the δ^{13}C signal is shown in Fig. 4.18. Two different slopes can be detected. During the last 8 ka, the correlation coefficient is r^2=0.58 and, therefore, higher than during the older time interval (r^2=0.18).

The stalagmite shows distinct growth layers so that several Hendy tests were possible. The results of the measurements of δ^{18}O and δ^{13}C along single growth layers are shown in Fig. 4.19. Four Hendy tests were conducted. Hendy test A ('HA') at 130 mm DFT (≈7 ka), where the growth rate is ≈40μm/a, HB at 184 mm DFT (≈10.9 ka, 15 μm/a), HC at 250 mm DFT (≈12.7 ka, 62μm/a) and HD at 270 mm DFT (≈13 ka, 62μm/a). The corresponding correlation coefficients of the isotopes are also shown in Fig. 4.19 on the right panel. All Hendy tests show a relatively stable δ^{18}O signal within a range of 0.5 ‰. In general, HA, HC and HD show a positive correlation of the stable isotopes, HB shows a negative correlation. However, the correlation is weak for all Hendy tests except for HD. This indicates a higher degree of kinetic fractionation in the lower part of the stalagmite according to the criteria given in *McDermott* [2004].

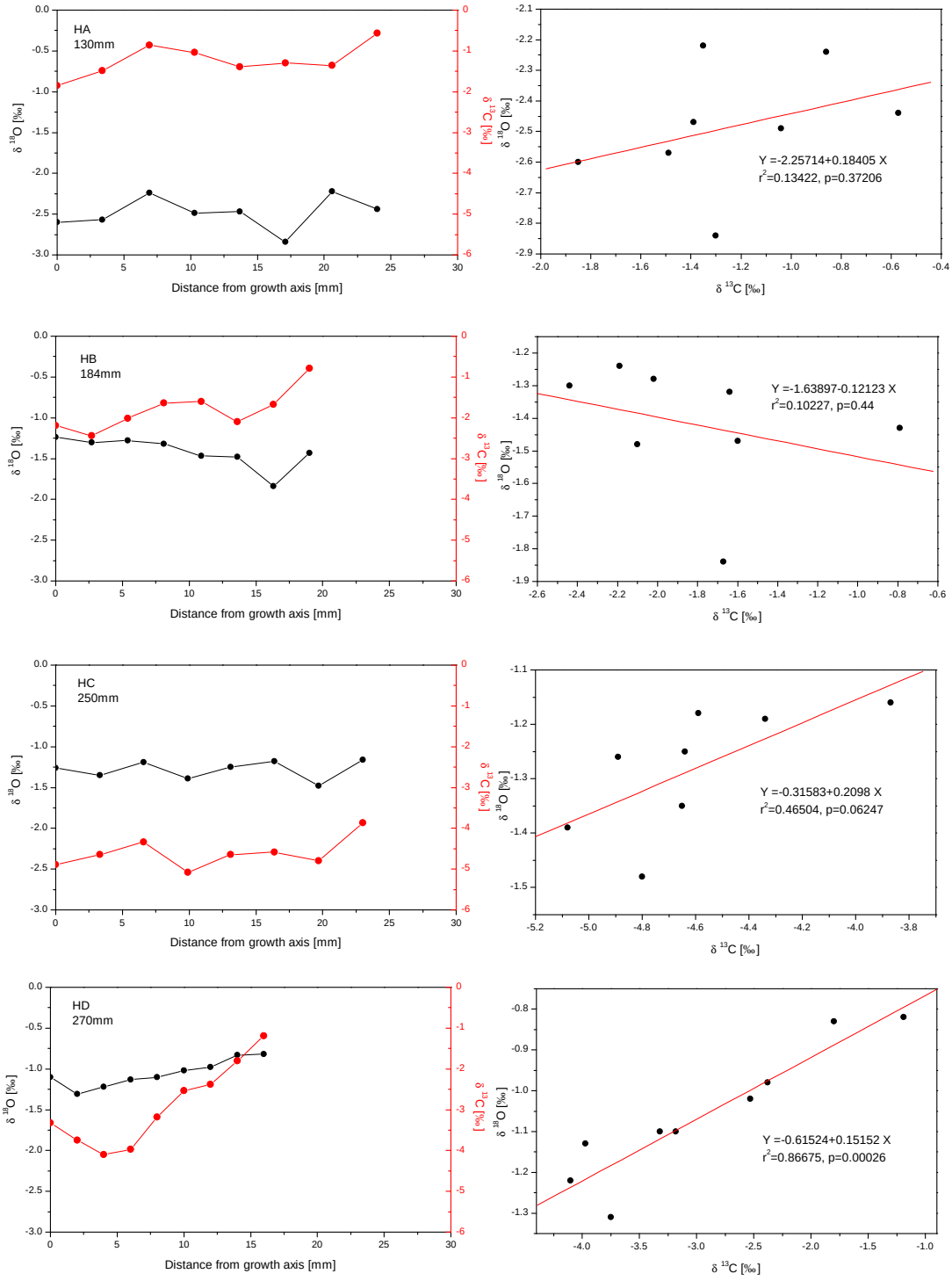

Figure 4.19: *Hendy tests along several growth layers of CP.*

4.2.3 Cuba Medio

Stable isotopes were measured in the upper 80 mm of stalagmite Cuba Medio at a resolution of 0.1 mm. Using the age model shown in Fig. 4.13, the δ^{18}O and δ^{13}C values are plotted against age in Fig. 4.20. Between 10 ka and 7 ka the temporal resolution is ≈15 a, between 16 and 18 ka it is ≈4 a, 80 a between 18 and 27 ka and 10 a in the time range older than 27 ka. The δ^{18}O record of CM shows a decline from 10 ka (≈-1 ‰) to 7 ka (≈-3.5 ‰) with a slope of 0.67 ‰/ka, the growth stop starts around 16 ka. Below the hiatus, the δ^{18}O values show a variability around 0 ‰and generally a higher level then between 7 and 10 ka. A slight minimum is visible around 22 ka. The δ^{13}C signal between 7-10 ka shows values between -8 and -4 ‰. In the time range between 16 and 27 ka the stalagmite reveals higher δ^{13}C values around a mean level of -2 ‰.

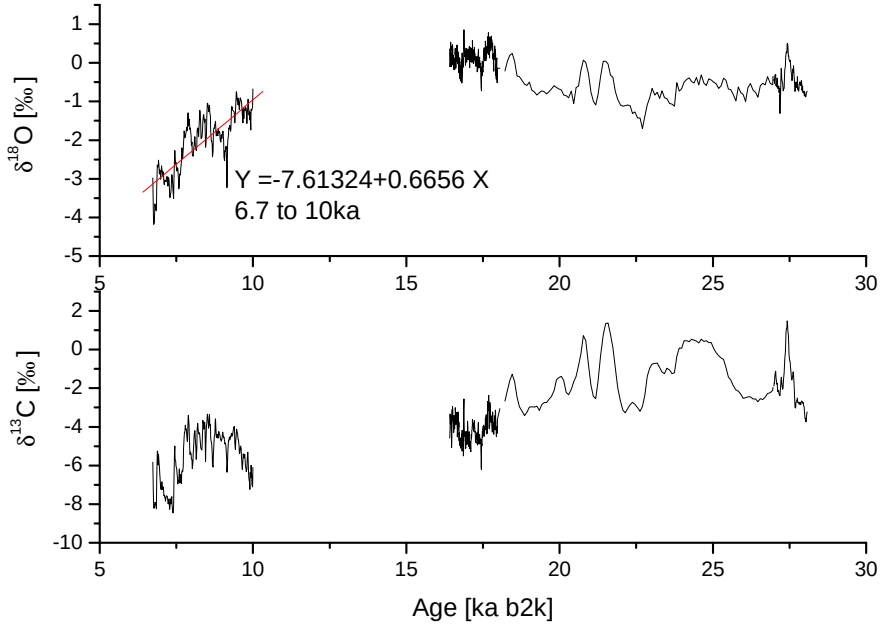

Figure 4.20: *Measured stable isotopes of stalagmite Cuba Medio plotted over time.*

Fig. 4.21 shows the δ^{18}O values in dependence of δ^{13}C. The plot shows 3 different clusters. In the younger growth phase between 7 and 10 ka (7 μm/a), the correlation between δ^{18}O an δ^{13}C reveals a r^2 of 0.84 ($p<0.0001$). In the growth phase between 16 and 18 ka, the correlation is lower with $r^2=0.34$ ($p<0.0001$) (24 μm/a). Between 18 and 28 ka, the correlation is $r^2=0.3$ ($p<0.0001$) (1 μm/a, 8 μm/a). In general, it is not straight forward to establish a relationship between growth rate and kinetic fractionation along the growth axis.

Since the stalagmite shows distinct growth layers, in total seven Hendy tests were

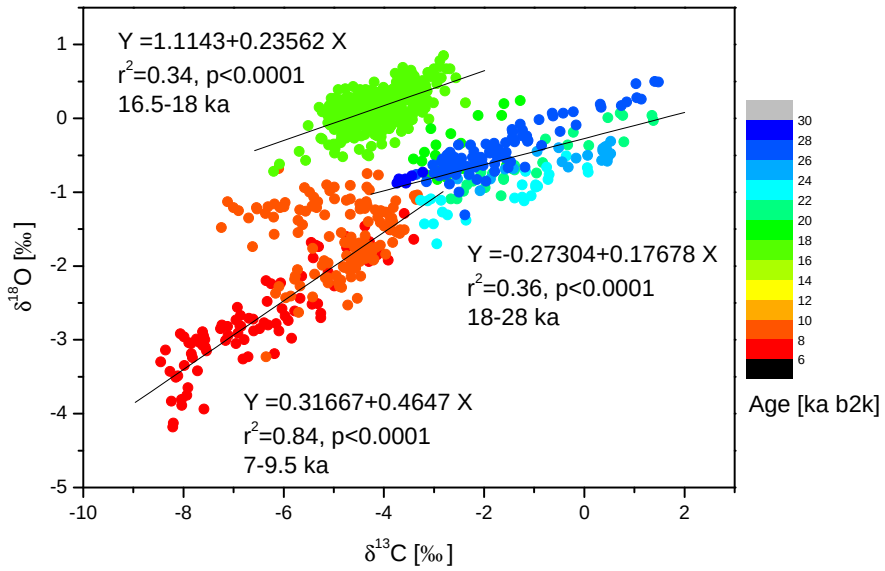

Figure 4.21: *$\delta^{18}O$ signal of CM in dependence of the $\delta^{13}C$ signal. Colours indicate the time range.*

conducted in order to study kinetic fractionation along single growth layers. Three Hendy tests were conducted in the Holocene slice of the stalagmite at a DFT of 4.9 mm (≈7.5 ka), 14.3 mm (≈8.5 ka), 18 mm (≈9.5 ka) (Fig. 4.22). The additional four Hendy tests at 34.5 mm, 57 mm, 72 mm and 77.2 mm can be found in the supplement. The corresponding correlation between $\delta^{18}O$ and $\delta^{13}C$ is also given in each plot. In Hendy test A (HA), both the $\delta^{18}O$ and the $\delta^{13}C$ signal are relatively stable over distance from the growth axis. HB shows less clear stable $\delta^{18}O$ values, both the $\delta^{18}O$ and $\delta^{13}C$ are increasing with distance from the growth axis. HC shows relatively stable $\delta^{18}O$ and $\delta^{13}C$ values. In all cases, the correlation between $\delta^{18}O$ and $\delta^{13}C$ is positive. HB and HC show a stronger positive correlation. This indicates a higher degree of kinetic fractionation than in HA according to the criteria given in *McDermott* [2004].

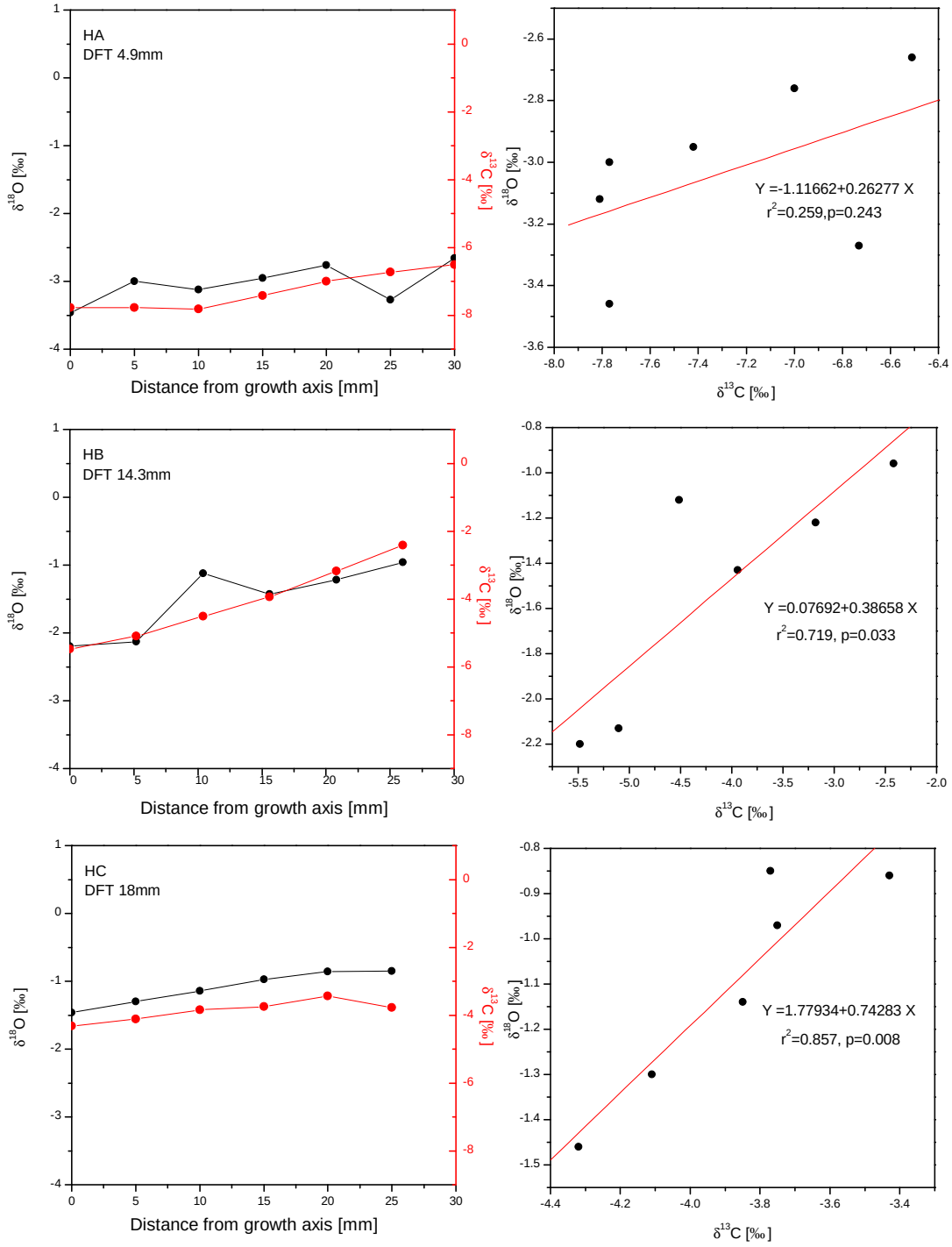

Figure 4.22: *Hendy tests along several growth layers of CM.*

4.3 Spectral analysis

4.3.1 Redfit, Cuba Grande

A frequency analysis of the stable isotope record was performed with the software 'Redfit 3.8' [*Schulz and Mudelsee* 2002]. This software is very useful for palaeoclimatic studies since it allows frequency analysis of records which are unevenly spaced in time. Hence, interpolation in the time domain is not necessary [*Schulz and Mudelsee* 2002]. Redfit splits a time series into n segments, which overlap by 50 %, the final spectral estimate is derived from averaging the n periodograms. For the analysis, the standard Welch I window was used. For the δ^{18}O values of stalagmite CG, the results can be found in Fig. 4.23. The number of segments were chosen to be n=3, n=4 and n=5. For n=3 (s. Fig. 4.23, upper panel), significant peaks above the 99 % confidence limit are centered at 482 (+759-183) a and 216(+82-47) a. The peak centered at 78 (+9-7) a reaches the 90 % confidence limit. The errors were calculated with the estimated 6 dB bandwidth error of 2.538. The same analysis was done for the n=4 segments (Fig. 4.23, middle panel). Results of the spectral analysis reveal frequencies centered around 386 (+607-146) a and 218 (+115-56) a, both reaching the 99 % limit and 79 (+11-9) a (over 80 % limit) with a bandwidth error of 3.172. For n=5, the frequencies are centered around 232 (+183-71) a (99 % limit) and 80 (+14-11) a (80 % limit); the bandwidth error is 3.812.

Results for the frequency analysis of the δ^{13}C signal are shown in Fig. 4.24. The upper panel shows the analysis with n=3, the estimated bandwidth error is 2.534. Significant peaks above the 99 % limit are centered around 465 (+666-172) a, 182 (+55-34) a and 69 (+7-5) a. Two peaks in the subdecadal range are reaching the 80 % level and are centered at 8 (+0.1-0.1) a and 7 (+0.1-0.1) a. Fig. 4.24, middle panel, shows the results for n=4. The bandwidth error is 3.177. Three peaks above the 99 % level are centered at 667 (∞,-343) a, 176 (+68-38) a and 70 (+9-7)a. Another peak around 8 (+0.1-0.1) a reaches the 80 % limit. The results for the analysis with n=5 are shown in Fig. 4.24, lower panel. One significant peak above the 99 % limit is centered at 232 (+182-71) a, and another peak above the 80 % limit is at 80 (+14-11) a.

Results for the frequency analysis are summarized in table 4.1. The frequency analysis in both the δ^{18}O and δ^{13}C records show variability on centennial and multidecadal time scales. In both records, the variability around 220 a and around 80 a seems to be a stable feature within the estimated error range. However, the 80 a variability is less significant than the 220 a variability.

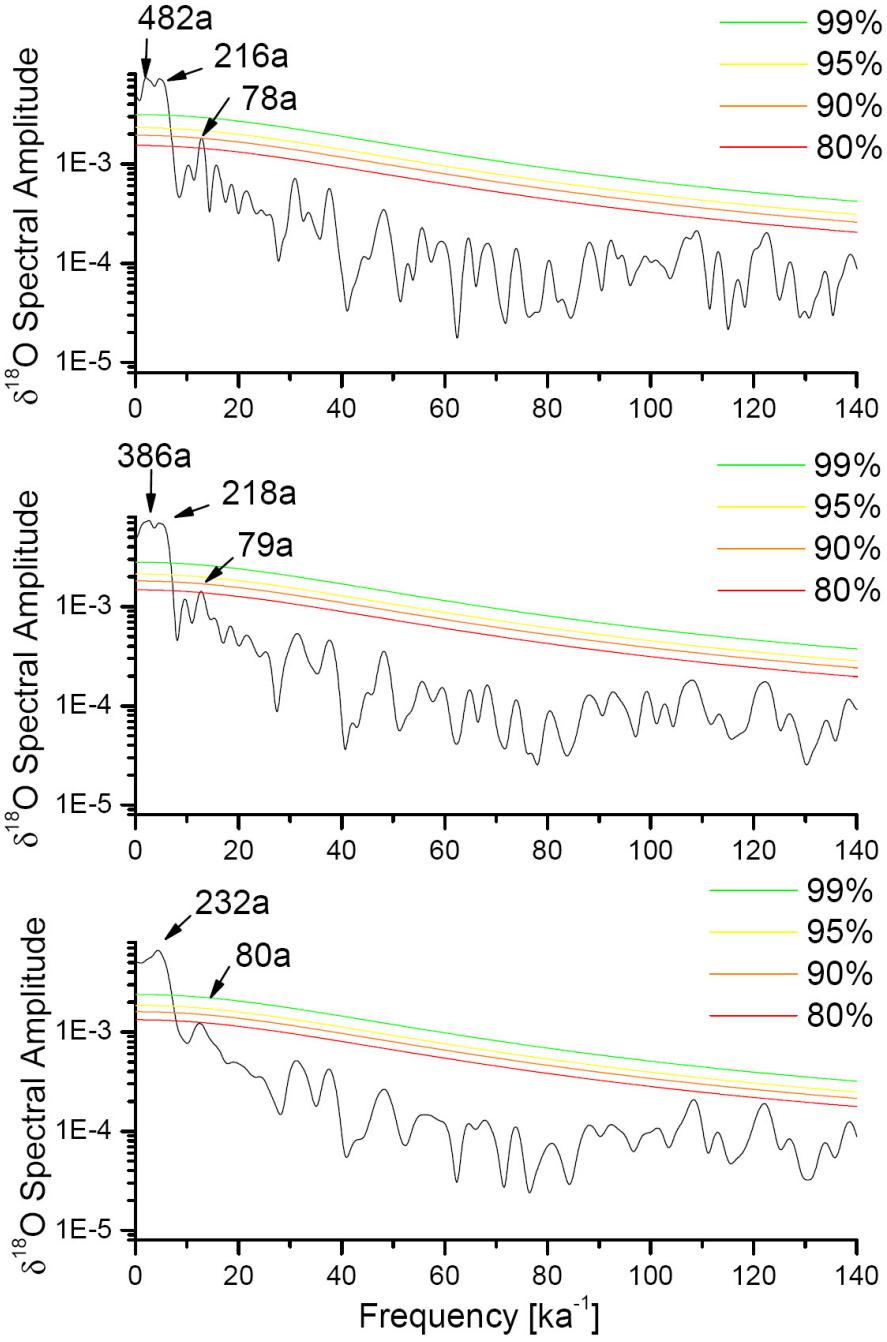

Figure 4.23: *Results of frequency analysis of $\delta^{18}O$ of CG. Upper panel: number of segments n=3; middle panel: n=4; lower panel: n=5. Centennial and multidecadal variability is indicated.*

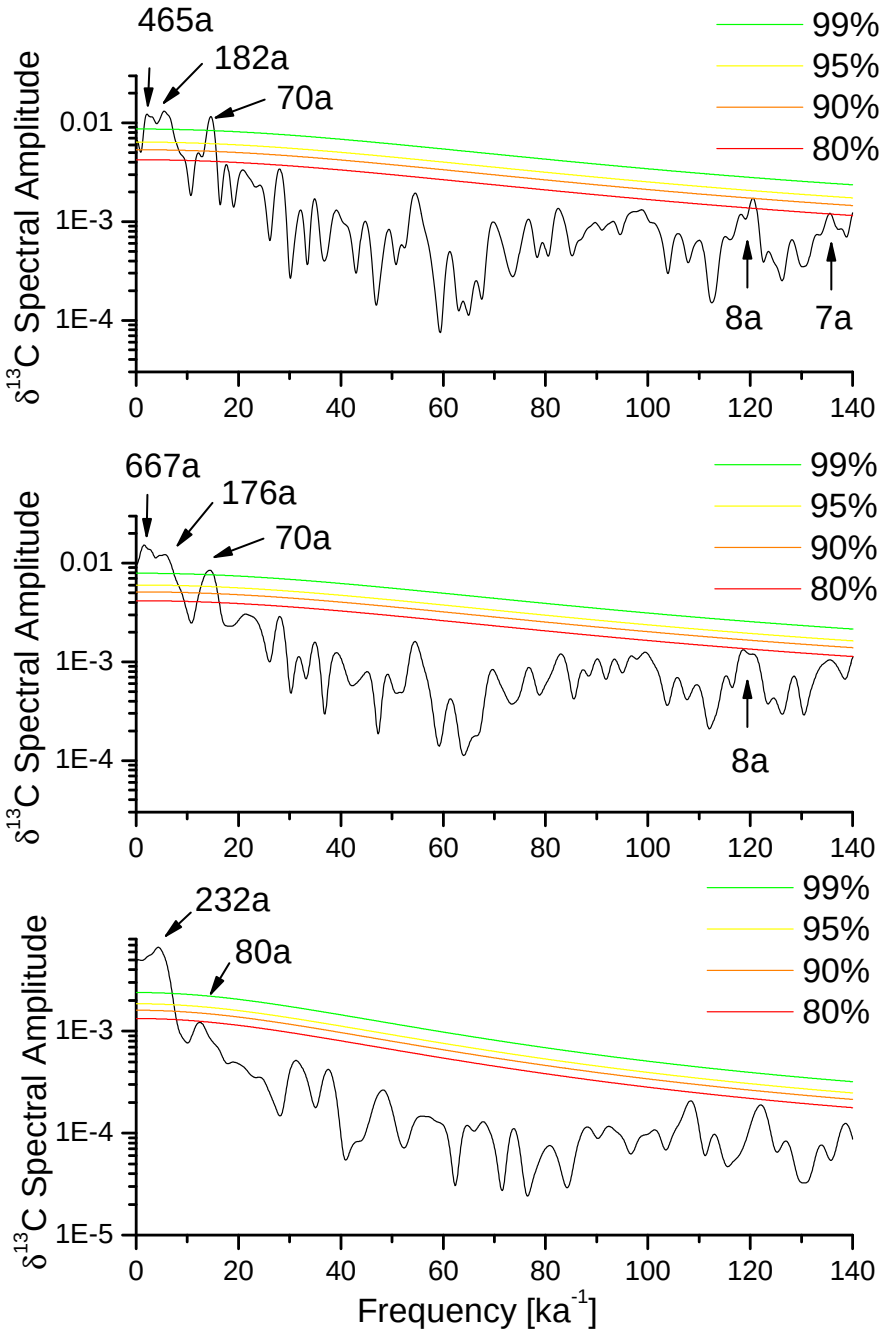

Figure 4.24: *Results of frequency analysis of $\delta^{13}C$ of CG. Upper panel: number of segments n=3; middle panel: n=4; lower panel: n=5. Centennial and multidecadal variability is indicated.*

	≥80 %	≥90 %	≥95 %	≥99 %
$\delta^{18}\mathbf{O}$				
n=3		78 (+9-7) a		482 (+759-183) a
				216 (+82-47) a
n=4	79 (+11-9) a			386 (+607-146) a
				218 (115-56) a
n=5	80 (+14-11) a			232 (+183-71) a
$\delta^{13}\mathbf{C}$				
n=3	8 (+0.1-0.1) a			465 (+666-172) a
	7 (+0.1-0.1) a			182 (+55-34) a
				69 (+7-5) a
n=4	8 (+0.1-0.1) a			667 (∞-343) a
				176 (+68-38) a
				70 (+9-7) a
n=5	80 (+14-11) a			232 (+182-71) a

Table 4.1: *Results of frequency analyses for stalagmite CG. Both records exhibit a variability around 80 and 220 a.*

4.3.2 Redfit, Cuba Pequeño

Fig. 4.25 shows the frequency analysis of the detrended δ^{18}O record (upper panel) and the δ^{13}C record of CP. Both records were cut at 12.5 ka in order to avoid uncertainties in the bottom part of the stalagmite with low age control. The number of segments was chosen to be 12 leading to a bandwidth error of 0.830. Two frequencies centered around 121 (+6-6) a and 137 (+8-7) a are above the 90 % limit in the δ^{18}O signal. The 150 (+10-9) a variability is pronounced over the 80 % level. Interestingly, a millennial scale variability around 2394 a (+380-1.2) ka nearly reaches the 80 % level. Similar centennial frequencies are also found in the δ^{13}C record centered around 111 (+5-5) a, 149 (+10-9) a and 176 (+14-12) a. In addition, two multicentennial frequencies of 259 (+31-25) a and 361 (+64-47) a are found.

Fig. 4.26 shows the results of the frequency analysis of the δ^{18}O record for two different time ranges. The upper analysis was done for the last 6.85 ka (taking into account the results of Rampfit, which detected a step at 6.85 ka) with a segment number of 5. The bandwidth error is 0.698. The lower analysis shows the results for the part older than 8.5 ka, which is the part avoiding the transition phase in CP. The number of segments was also chosen to be 5 and the bandwidth error is 1.205. The analysis of the last 6.85 ka shows a significant frequency reaching the 99 % level around 148 (+8-7) a. A centennial variability of 350 (+49-4) a is above the 90 % level. In addition, a millennial variability of 2678 a (+39-1.3) ka is above the 80 % level. In contrast, the millennial and multicentennial variability is not seen in the analysis of the older part. Only one frequency around 46 (+1-1) a reaches the 80 % level. A summary of detected frequencies is given in table 4.2. Both the records of δ^{18}O and δ^{13}C exhibit a variability around 150 a.

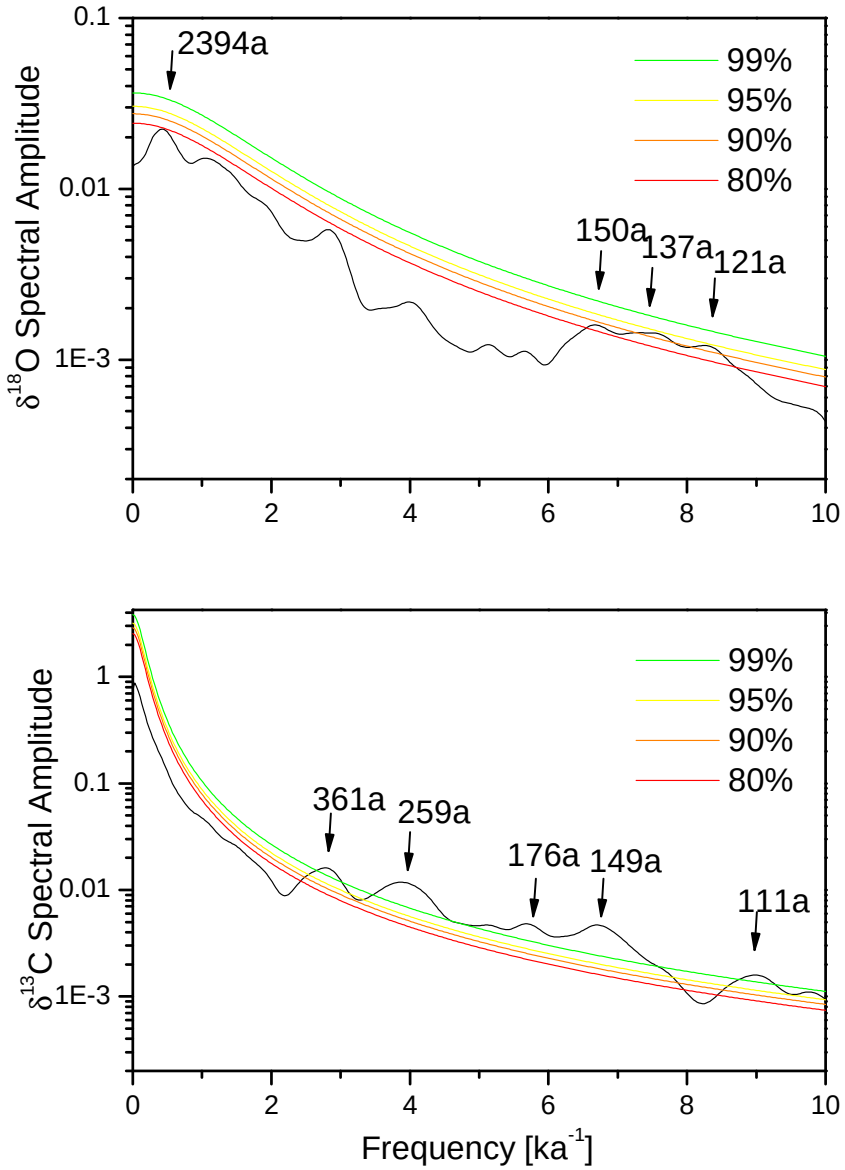

Figure 4.25: *Results of frequency analysis of the overall stable isotope signals of CP. Upper panel: $\delta^{18}O$ (detrended), lower panel: $\delta^{13}C$.*

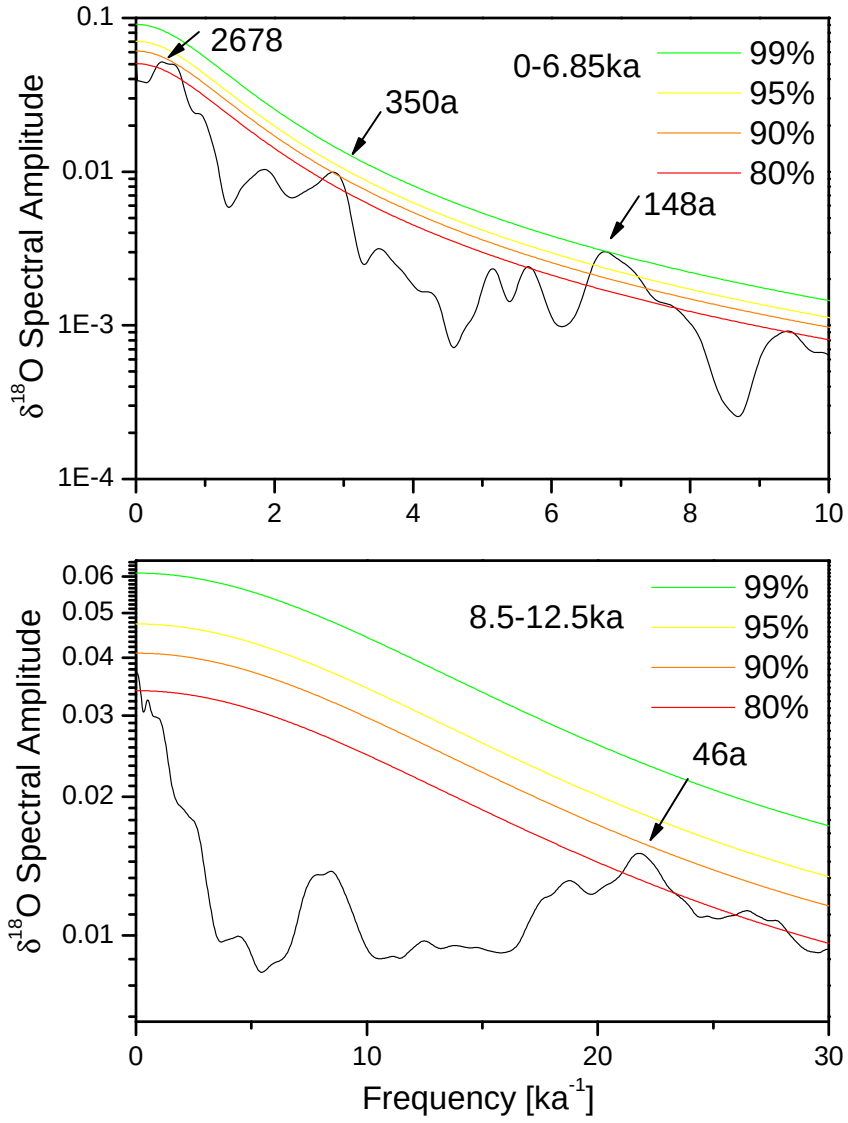

Figure 4.26: *Results of frequency analysis for CP. The upper panel shows the results for the last 6.85 ka, the lower panel results for the part older than 8.5 ka. Note the change of variabilities: the millennial scale variability is more significant in the younger part.*

	≥80 %	≥90 %	≥95 %	≥99 %
Detrended δ^{18}O				
12.5 ka	150 (+10-9) a	137 (+8-7) a		
n=12		121 (+6-6) a		
δ^{13}**C**				
12.5 ka				361 (+64-47) a
n=12				259 (+31-25) a
				176 (+14-12) a
				149 (+10-9) a
				111 (+5-5) a
δ^{18}**O**				
last 6.85 ka	2678 a (+39-1.3) ka	350 (+49-4) a		148 (+8-7) a
n=5				
12.5-8.5 ka	46 (+1-1) a			
n=5				

Table 4.2: *Results of frequency analyses for stalagmite CP.*

4.3.3 Redfit, Cuba Medio

The frequency analysis of the δ^{18}O record of CM between 7 and 10 ka is shown in Fig. 4.27. For the analysis, the same parameters as in CG were used. With a segment number of 3 (Fig. 4.27, upper panel), one peak centered around 105 (+6-5) a is above the 95 % confidence limit. The 90 % limit is reached by a variability of 121 (+8-7) a and 83 (+3-3) a. A centennial peak at 151 (+12-10) a is above 80 %. Similar results are found for n=4 (Fig. 4.27, middle panel). In agreement with the previous analysis, peaks are centered around 121 (+10-8) a, 104 (+7-6) a and 82 (+4-4) a. In addition, millennial variability is found around 1303 (+5054-577) a, but only slighlty above the 80 % limit. The analysis with n=5 (Fig. 4.27, lower panel) confirms the 106 (+9-8) a variability as well as the 82 (+5-5) a variability.

The δ^{13}C frequency analysis of CM is shown in Fig. 4.28. For n=3 (Fig. 4.28, upper panel), the 99 % limit is reached by a frequency of 148 (+12-10) a, 95 % by 163 (+14-12) a, 107 (+6-5) a and 78 (+3-3) a. A variability of 343 (+69-49) a and 59 (+2-2) a reach the 90 % confidence limit, whereas frequencies of 120 (+8-7) a and 93 (+4-4) a are less significant (80 % limit). For the number of n=4 (Fig. 4.28, middle panel), the frequencies of 149 (+15-12) a and 77 (+4-3) a reach the 99 % level, 95 % is reached by a variability of 102 (+7-6) a. Frequencies centered around 118 (+9-8) a and 59 (+2-2) a are less significant (over 80 % confidence limit). For the analysis for n=5 (Fig. 4.28, lower panel), the frequencies of 150 (+19-15) a and 78 (+5-4) a reach the 95 % limit. Above the 90 % level, a frequency of 106 (+9-8) a is found, and a variability of 59 (+3-2) a is higher than 80 % limit.

The estimated frequencies are summarized in table 4.3. A stable feature is the variability around 105 a as well as the 80 a variability in both the δ^{18}O and the δ^{13}C signal. Less significant, but in both records visible is a variability around 120 a. Only δ^{13}C shows more significant frequencies of around 150 a and 60 a.

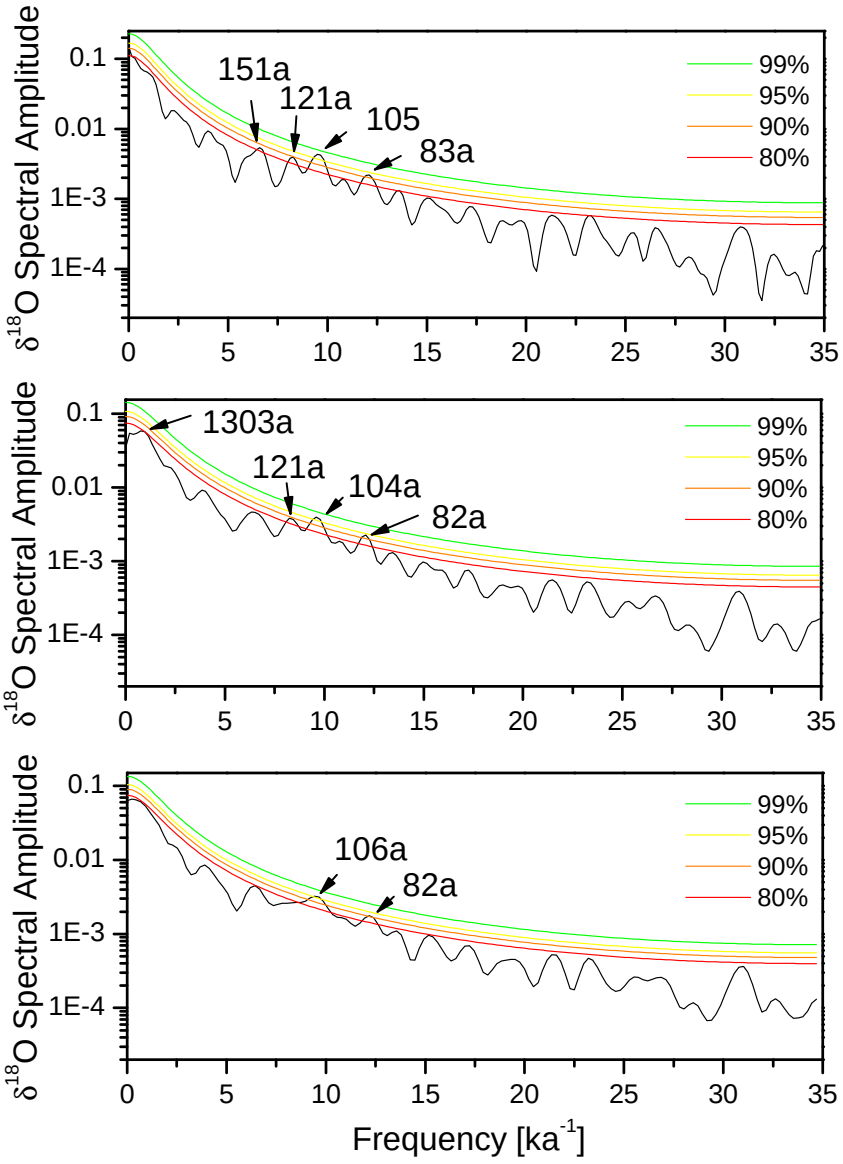

Figure 4.27: *Redfit analysis of $\delta^{18}O$ values of stalagmite CM for n=3 (upper panel), n=4 (middle panel) and n=5 (lower panel).*

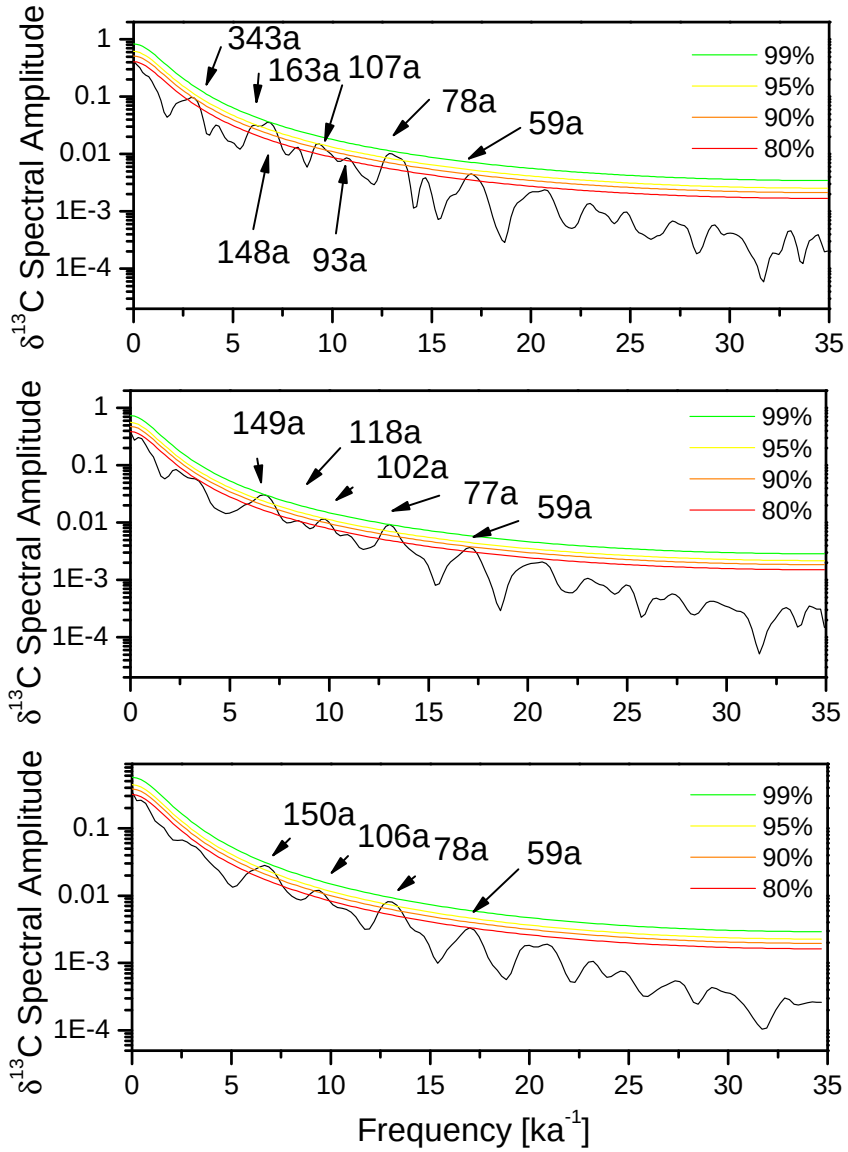

Figure 4.28: *Redfit analysis of $\delta^{13}C$ values of stalagmite CM for n=3 (upper panel), n=4 (middle panel) and n=5 (lower panel).*

	≥80 %	≥90 %	≥95 %	≥99 %
$\delta^{18}\mathbf{O}$				
n=3	151 (+12-10) a	121 (+8-7) a	105 (+6-5) a	
		83 (+3-3) a		
n=4	1303 (+5054-577) a	82 (+4-4) a	104 (+7-6) a	
	121 (+10-8) a			
n=5		82 (+5-5) a	106 (+9-8) a	
$\delta^{13}\mathbf{C}$				
n=3	120 (+8-7) a	343 (+69-49) a	163 (+14-12) a	148 (+12-10) a
	93 (+4-4) a	59 (+2-2) a	107 (+6-5) a	
			78 (+3-3) a	
n=4	118 (+9-8) a		102 (+7-6) a	149 (+4-3) a
	59 (+2-2) a			77 (+4-3) a
n=5	59 (+3-2) a	106 (+9-8) a	150 (+19-15) a	
			78 (+5-4) a	

Table 4.3: *Results of frequency analyses for stalagmite CM.*

4.3.4 Wavelet, Cuba Grande

Wavelet analysis is an interesting tool to investigate geophysical time series in more detail. It allows to detect dominant periodic signals, which can vary both in amplitude and frequency over a long period of time. A wavelet analysis of the 1.3 ka year old stalagmite CG is shown in Fig. 4.29. The analysis has been done using the algorithm of *Torrence and Compo* [1998]. The contour levels are chosen that 75 %, 50 %, 25 % and 5 % of the wavelet power is above each level, respectively. The cross hatched region is the cone of influence, where zero padding has reduced the variance. The black contour is the 5 % significance level using a red noise background spectrum. In contrast to frequency analysis, it is necessary to interpolate the examined data on a regular grid on the time axis for wavelet analysis. Since the time resolution of the isotopic record of stalagmite CG is approximately 2 years, the time resolution was linearly interpolated to a regular grid of 2 years. Fig. 4.29a shows the result of the wavelet analysis for the interpolated δ^{18}O record (left) and the global wavelet (right). The dashed line is the significance for the global wavelet. A pronounced centennial variability (≈220 a) can be seen in the range of 0.8-1.2 ka. A multicentennial variability (≈380 a) is indicated in the whole record. Interdecadal variability of periods lower than 10 years is also pronounced in the whole record until 0.15 ka (1850 A. D.). Fig. 4.29b shows the analysis for the detrended and interpolated δ^{18}O data. In general, the results are the same as in the undetrended case. Wavelet analysis of the δ^{13}C record is shown in Fig. 4.29c. In general, the record does not exhibit significant variability on multidecadal or centennial timescales. A weak multidecadal variability is detected around 0.1 and 0.5 ka, a subdecadal and centennial variability around 0.2 to 0.5 ka.

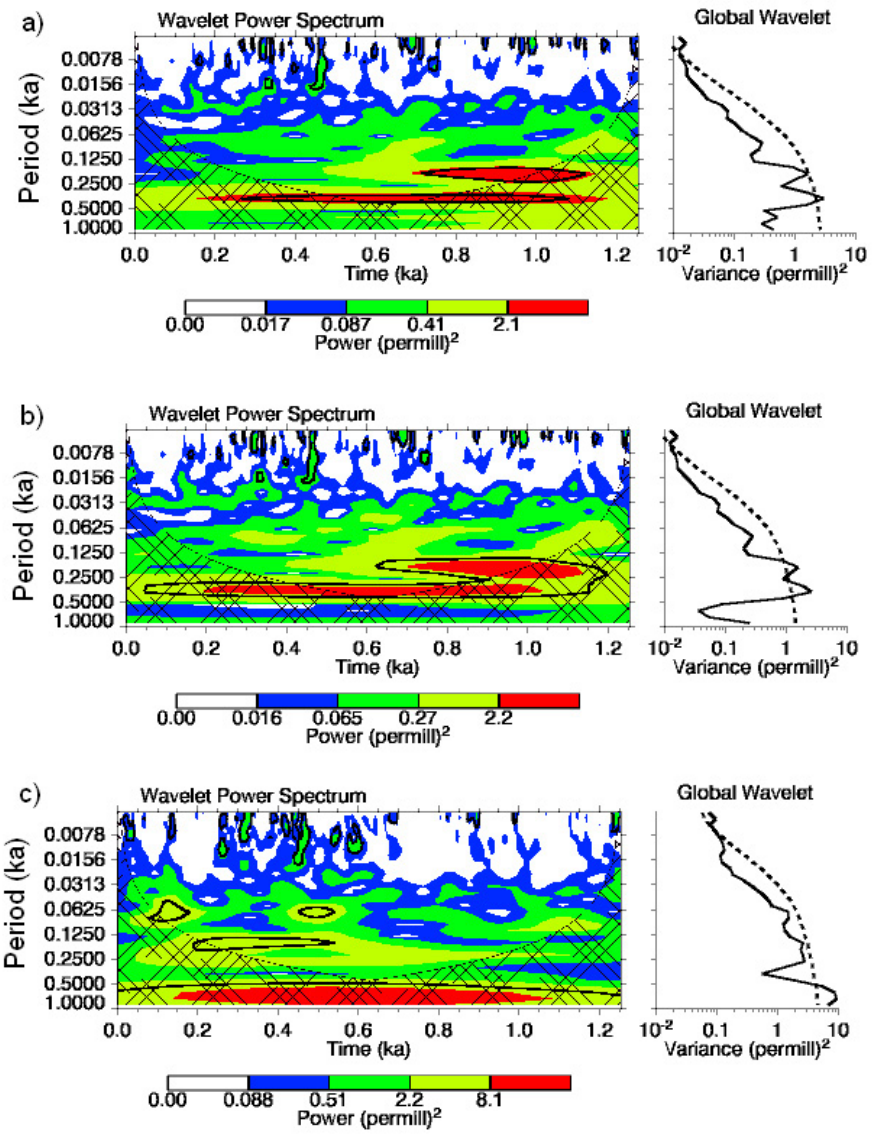

Figure 4.29: *Wavelet analysis of stalagmite CG (left) and global wavelet (right). (a) The wavelet analysis of the interpolated $\delta^{18}O$ record shows pronounced centennial variability (≈220 a in the range of 0.8-1.2 ka). A variability of 380 a is indicated in the overall record. Interdecadal variability is pronounced in the whole record until 0.15 ka (1850 A. D.). (b) Wavelet spectrum for the detrended $\delta^{18}O$ record. (c) Wavelet analysis of the $\delta^{13}C$ record.*

4.3.5 Wavelet, Cuba Pequeño

Wavelet analysis was also done for stalagmite CP in order to gather further insights of the temporal variability of frequency dependencies. The analysis was done as described for stalagmite CG. The interpolation for this stalagmite was chosen to be 7 years. Results are shown in Fig. 4.30. For all analyses, the records were cut at 12.5 ka in order to avoid the part with low age control. Fig. 4.30a shows the results for the analysis of the δ^{18}O signal for the overall detrended record. In general, millennial scale variability is found to occur during the last 2 ka. Multicentennial variability is more pronounced around 8 and 4 ka, respectively. Multidecadal variability is pronounced during the last 2, 4-8 ka and at the end of the record around 12 ka. The results for the last 6.85 ka analysis are shown in Fig. 4.30b. The features are the same as for the overall record. In addition, a millennial scale variability is shown to start at 6 ka, but not significant. The analysis of the part older than 8.5 ka is shown in Fig. 4.30c. Multicentennial variability is shown to last from 8.5 ka to 9.5 ka on a significant level. Fig. 4.30d shows the wavelet analysis for the overall δ^{13}C record. A clear change in variability occurs around 7 ka. This record was not detrended. Centennial variability is pronounced between 3 and 7 ka. Millennial variability also starts at 5 ka. Multidecadal variability is pronounced between 4 and 7 ka.

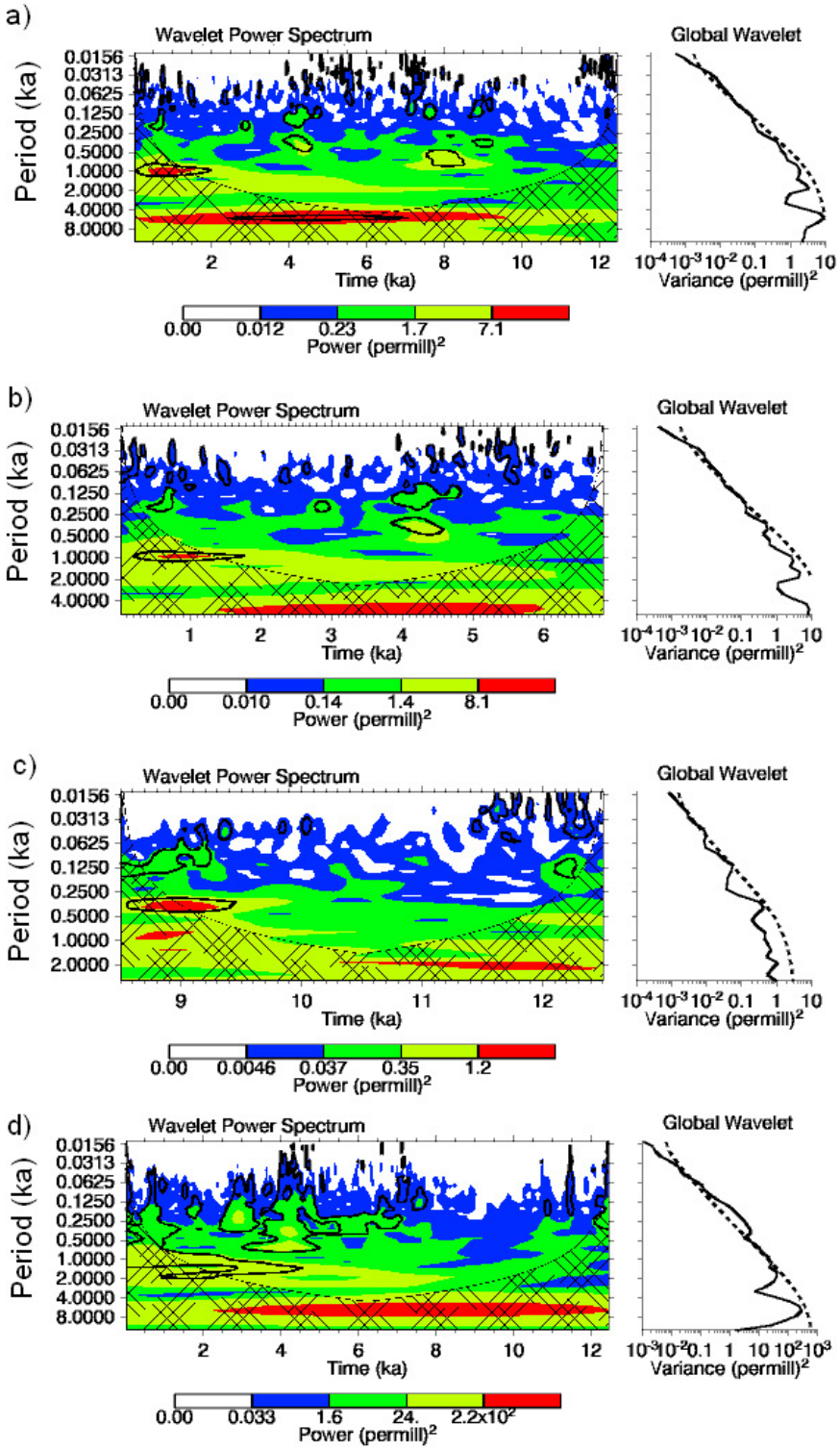

Figure 4.30: *Wavelet analysis of the stable isotope records of CP (left) and global wavelets (right). (a) Analysis of the detrended $\delta^{18}O$ record. (b) Analysis of the $\delta^{18}O$ record for the last 6.85 ka. (c) Analysis of the $\delta^{18}O$ record older than 8.5 ka. (d) Analysis for the whole $\delta^{13}C$ record.*

4.3.6 Wavelet, Cuba Medio

The wavelet analysis of the youngest growth phase between 7 and 10 ka of Cuba Medio is shown in Fig. 4.31 for the original δ^{18}O record, the detrended δ^{18}O record as well as the δ^{13}C record. Since in this time interval the time resolution is ≈15 years, the record were interpolated on a regular grid of 15 years. The wavelet analysis was done as explained for stalagmite CG. The wavelet analysis does not reveal any significant multicentennial variability. Only a weak multidecadal to centennial variability is found, centered around 7.5 ka and 8.5 ka.

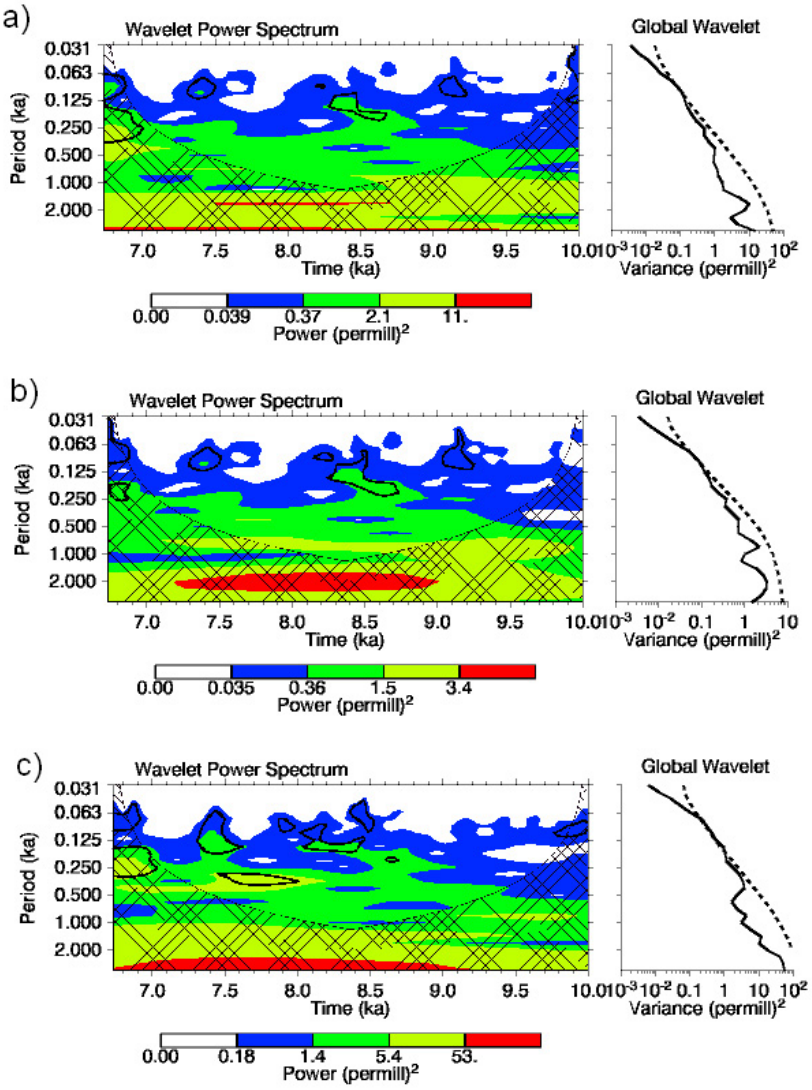

Figure 4.31: *Wavelet analysis for stalagmite CM in the time interval between 7 and 10 ka (left) and global wavelet (right) for (a) δ^{18}O record, (b) detrended δ^{18}O record and (c) δ^{13}C record.*

4.4 Cave Monitoring

In 2008, a cave monitoring program was conducted in order to study the hydrological behaviour of the two cave systems where the three investigated stalagmites grow. Dr. Jesús Pajón measured several cave parameters on a regular basis of two months, in total six field trips were conducted. Relevant data can be found in the supplement. In general, two drip sites in close proximity of the original stalagmite position were monitored. The locations of observed drip sites are indicated in Fig. 4.32 for Dos Anas cave system (CG and CP). CG is denoted as DAC01 and CP as DAC02. The original drip site is denoted with the letter 'O' (e. g., 'DAC01O'), the alternative drip site with the letter 'A' (e. g., 'DAC01A'). CM is indicated as STC. Samples for $\delta^{18}O$ analysis were sent to the stable isotope laboratory at Innsbruck University. The air temperature in Dos Anas Cave ranges from 21.3 to 21.5 °C over the year. Relative humidity in this cave system was measured to be between 96 % and 100 % all year round. Air temperatures of Santo Tomas Cave system range from 21.6 to 21.9 °C, and relative humidity ranges from 97 to 99 %.

Estimated drip rates analyses for the Dos Anas cave system (DAC) are shown in Fig. 4.33. The figure shows the drip rates of two drip sites in close distance to each other close to the original position of Cuba Grande (DAC01). Both drip sites show a positive response to the amount of precipitation. Highest drip rates are found in the

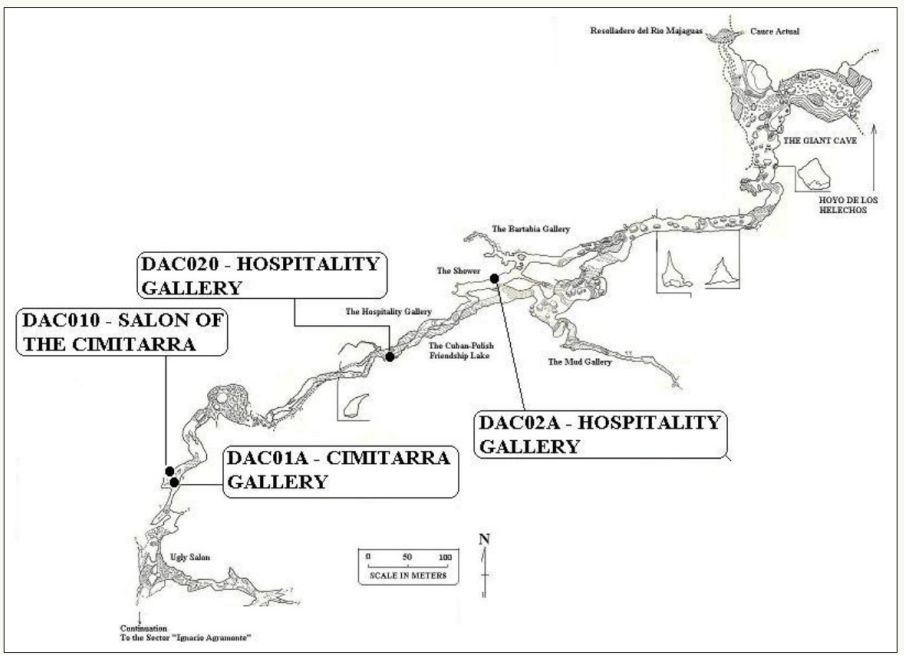

Figure 4.32: *Location of monitored drip sites in Dos Anas cave system with indicated positions around CG (DAC01) and CP (DAC02). The original drip site is denoted with the letter 'O', the alternative drip site with the letter 'A'.*

second rainfall season with a delay of 1-2 months. The drip rate of the alternative drip site shows more than 1 l/min. This equals a drip interval of 0.006 s with a mean drip volume of 0.1 ml/drip. Both drip sites seem to follow the amount of infiltration. For stalagmite CP (DAC02) in Dos Anas Cave and stalagmite CM in Santo Tomas Cave (STC), no continuous values of drip rates were established.

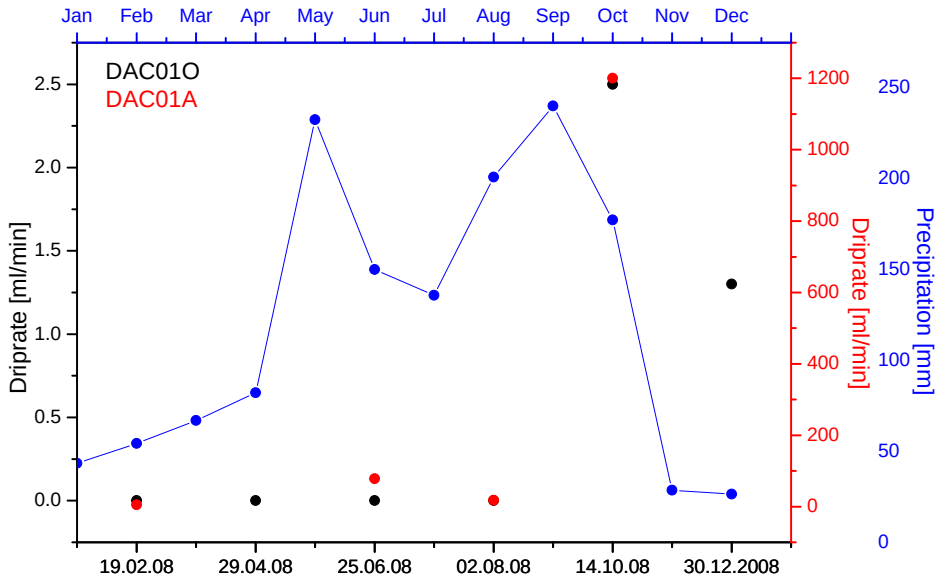

Figure 4.33: *Drip rates of selected drip sites close to the original position of CG in comparison with annual amount of rainfall.*

The measured δ^{18}O values of each water sample are shown in Fig. 4.34. Values vary from -1 ‰ to -5 ‰ in both cave systems. Lowest values are found in October, when the highest drip rates are observed. The δ^{18}O values of annual rainfall are also shown in Fig. 4.34 for comparison. The graph indicates that δ^{18}O values of rainfall are lowest during October, which is closely connected to the low δ^{18}O values in the drip water, highest drip rates and high rainfall amounts.

The δ^{18}O values and drip rate of the drip site around stalagmite CG (DAC01A) is shown in more detail in Fig. 4.35 together with the δ^{18}O values of precipitation. The mean value of the δ^{18}O values of the fast drip site around CG (DAC01A) is -4.1 ‰. This matches the summer precipitation δ^{18}O value. Calculated with the fractionation factors of *Kim and O'Neil* [1997], the expected δ^{18}O value in speleothem calcite is -5.71 ‰ in equilibrium at a temperature of 21.4 °C. With the fractionation factor of *Friedman et al.* [1977], the expected value in speleothem calcite is -5.35 ‰. The mean value of the last 50 a of the δ^{18}O signal of CG is -5.19 ‰. This closely matches the calculated values and it can be inferred that the summer rain signal has the strongest influence on the stalagmite δ^{18}O. Furthermore, the speleothem calcite is likely precipitated in equilibrium.

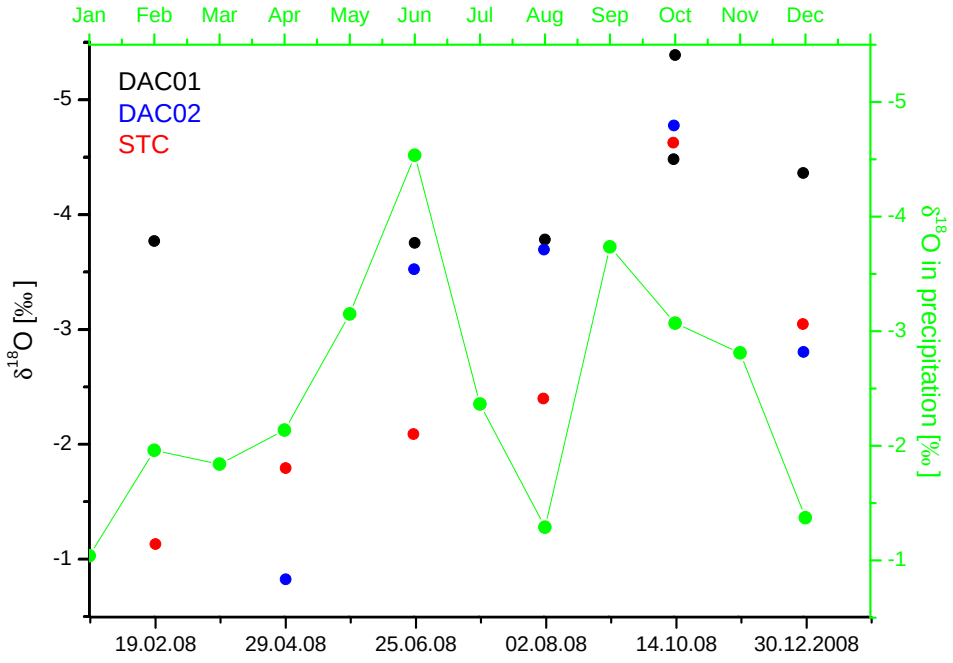

Figure 4.34: *Observed $\delta^{18}O$ values in all locations in comparison to rainfall $\delta^{18}O$ values.*

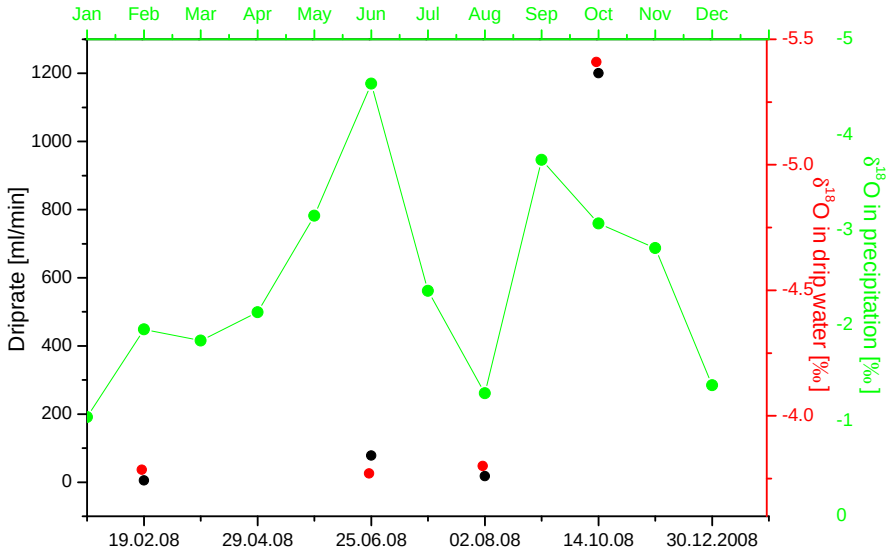

Figure 4.35: *Drip rates of drip site DAC01A close to CG, measured $\delta^{18}O$ values and $\delta^{18}O$ values in rainfall.*

4.5 Summary

Three Holocene stalagmites from north-western Cuba were studied. Two stalagmites (CG and CP) are from the Dos Anas cave system and differ in their general crystal structure. CG grew with a relatively high growth rate of ≈543 μm/a during the last 1.3 ka, CP with relatively low growth rates between 10 and 60 μm/a during the last 16 ka. CP consists of aragonite at the top, the bottom part is pure calcite. Since measured ages are apparently too old in this section, this leads to the conclusion that recrystallization from aragonite to calcite took place so that U was remobilized. This was further supported by aragonite/calcite measurements (XRD) and trace elements (ICP-OES). Both stalagmites were dated with two measurement techniques, TIMS and MC-ICPMS. Some samples of CG show very low (^{230}Th/^{232}Th) ratios, which is an indication for high detrital contamination. This has important implications for dating results. This study provides an alternative approach for detrital correction which was also applied for CP. The third stalagmite was dated solely with TIMS, and reveals several growth phases during the last 85 ka. The stalagmite grew during 7 and 10 ka with a growth rate of about ≈7 μm/a.

Stable isotopes (δ^{18}O and δ^{13}C) were measured along the growth axis of each stalagmite and along single growth layers of CP and CM. The resolution is about 2 a in CG, between 4 and 20 a in CP and around 15 a in CM. The δ^{18}O signal of CG shows a mean value of -5.2 ‰ with a variability of 2.5 ‰. A trend is visible with a slope of 0.38 ‰/ka. The δ^{13}C signal of CG is around -9.5 ‰ with a variability of 2.5 ‰. The dependency of both isotopic records along the growth axis do not reveal any correlation, indicating that calcite was precipitated in equilibrium. δ^{18}O values of the second stalagmite CP show a clear transition phase between 9 and 5 ka with a slope of 0.94 ‰/ka. Values between 12.5 and 9 ka are on a higher level of -1.5 ‰ than during the last 5 ka with values around -3 ‰. The δ^{13}C signal shows values around 2 ‰ with a variability of 6 ‰ peak to peak. In the Holocene time slice of CM ranging from 7-10 ka, this stalagmite reveals the same transition phase as CP. Values decline from -3.5 ‰ (10 ka) to -1 ‰(7 ka) with a slope of 0.67 ‰/ka, comparable to the slope of CP. This is highly important, since this transition phase is obviously detected in both records, indicating reproducibility. The δ^{13}C values in this time interval range between -8 ‰ and -4 ‰.

Stable isotopes were also measured along several growth layers of CP and CM. For CP, only the lower calcite part indicates kinetic fractionation. This is also indicated by the dependency of stable isotopes along the growth axis, no clear correlation is found, indicating a low degree of kinetic fractionation. For CM, in the Holocene time slice the stalagmite exhibits more kinetic fractionation at 8.5 ka and 9.5 ka than at 7.5 ka. The dependency of stable isotopes along the growth axis of CM reveal higher kinetic fractionation in the time slice between 7 and 10 ka then in the older part.

The frequency analysis of CG shows a variability of ≈80 a, 220 a and 480 a in both

isotope records. Within the error ranges, the isotope records of CP show frequencies around 110 a, 150 a and several multicentennial frequencies in the δ^{13}C record. The 350 a variability is most pronounced if we focus on the last 6.85 ka in the δ^{18}O record. In addition, millennial scale variability becomes visible. CM shows frequencies around 80 a, 110 a, 120 a and 150 a in both isotopic records.

The wavelet analysis shows that the 220 a variability is most pronounced between 0.8 and 1.2 ka in CG. The 80 a variability shows peaks around 0.1 ka and 0.5 ka before today, whereas centennial variability around 180 a is visible between 0.2 and 0.4 ka. CP reveals frequencies of around 150 a and 120 a in both isotope records. Those are pronounced around 1 ka, from 4-6 ka and at the end of the record. Millennial scale variability occurs during the last 5 ka. In general, the δ^{13}C record shows a change of variability on various timescales around 5 ka. The 80 a periodicity is most visible in CM around 7.5, 8.5 and 9.2 ka. Around 8.5 ka, also a centennial variability of 110 a to 120 a is pronounced.

A cave monitoring program was conducted in 2008. Two drip sites were studied around each stalagmite's original position. Main monitored parameters were drip rate and δ^{18}O values of drip waters. Drip rates were found to be highest in October, in agreement with the high precipitation amount in October. The δ^{18}O values of observed drip waters also show lowest values in October. Expected δ^{18}O values in speleothem calcite for equilibrium conditions, calculated for δ^{18}O values of drip waters, match observed δ^{18}O values in CG.

5 Reconstructed climate variability in the Northern Caribbean

Three stalagmite records from North Western Cuba were established using stable isotope analysis and Th/U-dating methods. The records cover the whole Holocene (CP and CG) and one stable isotope record (CM) dates back to 25 ka. In this section, the records from Cuba will be presented within the context of past climate reconstructions from the circum-Caribbean as well as in a broader context regarding past variability of the Atlantic as well as the Pacific region. Possible forcing mechanisms for the observed variability will be discussed on several timescales.

5.1 Intercomparison between samples

Along the growth axis of all three stalagmites, stable isotopes (δ^{18}O and δ^{13}C) were measured. A comparison of the three δ^{18}O records is shown in Fig. 5.1a and of the δ^{13}C signals in Fig. 5.1b. The stalagmites records overlap in two time ranges, between 7 ka to 11 ka (CP and CM) and during the last 1.3 ka (CP and CG) which will be discussed in separate, for δ^{18}O and δ^{13}C values.

The δ^{18}O signal of CP and CM show the same trend between 7 and 11 ka, and similar δ^{18}O values. The slopes in both isotopic records are similar (≈0.8 ‰/ka) and therefore it can be inferred that the transition between higher (around 10 ka) and lower (around 5 ka) δ^{18}O values is a reproducible pattern in Cuban stalagmites. For CM, the δ^{18}O values are slightly lower (up to ≈0.5 ‰) than for CP in the time range between 7 and 11 ka. CM shows low U contents and it can be inferred that this stalagmite consists mostly of calcite. The lower δ^{18}O values are therefore in agreement with the different fractionation between calcite and aragonite [*Kim et al.* 2007]. Different fractionation factors for both crystal types may explain a shift in δ^{18}O values of around 0.7 to 0.8 ‰ based on theoretical and experimental studies [*Kim et al.* 2007]. In caves, higher δ^{18}O values of up to 1.4 ‰ have been found in aragonite samples relative to calcite in Carlsbad Caves and Grotte De Clamouse [*Frisia et al.* 2002, *McMillan et al.* 2005].

The δ^{18}O values of CG are lower by ≈1.5 ‰ than CP during the last 1.3 ka. From the monitoring program, which was conducted during 2008, it can be inferred that recent drip water samples show a δ^{18}O value in agreement with the mean δ^{18}O value of the last 50 a of stalagmite CG. Hence, it can be assumed that CG depicts no evaporation or

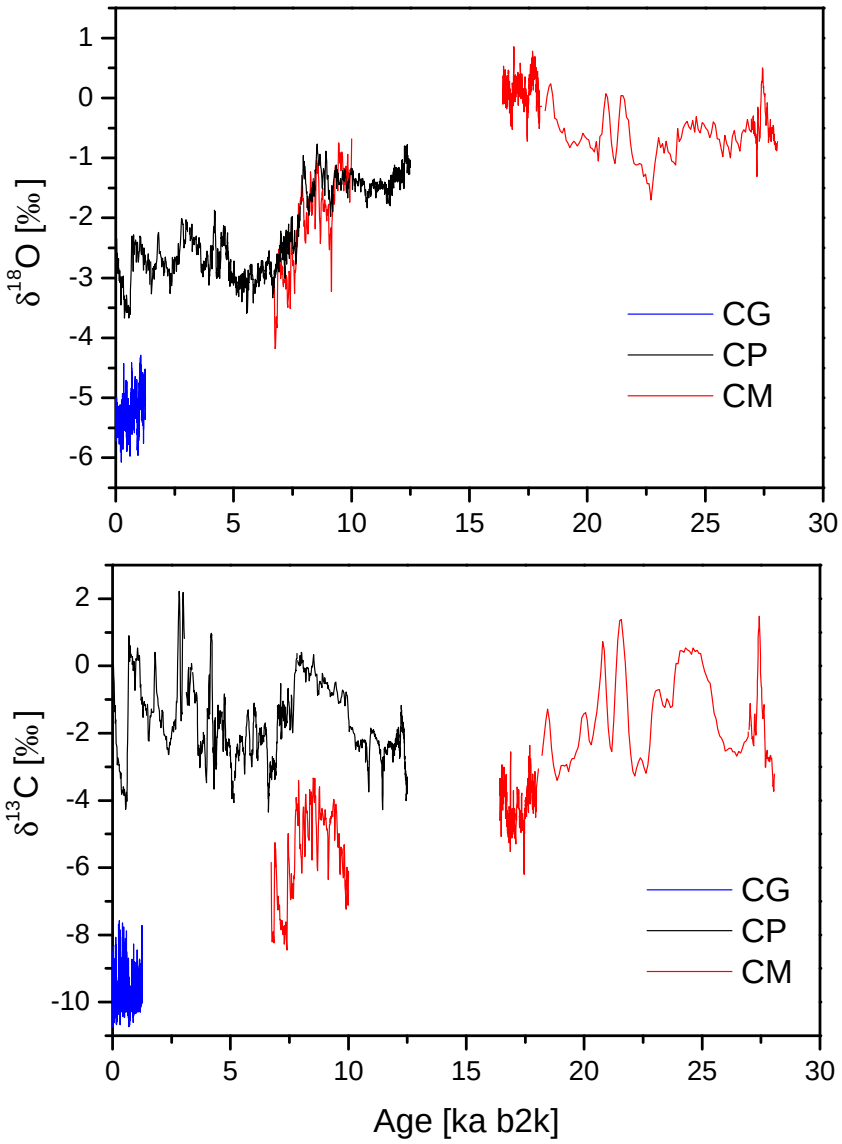

Figure 5.1: *Comparison of the three isotopic records of stalagmites CG, CP and CM. Upper panel: $\delta^{18}O$ values, lower panel: $\delta^{13}C$.*

kinetic effects during growth, the calcite was precipitated in equilibrium. The drip rate of this stalagmite is relatively high, which can explain the high growth rate and the precipitation under equilibrium conditions. This was in part further confirmed by the low correlation between δ^{18}O and δ^{13}C along the growth axis [*Hendy* 1971, *Mickler et al.* 2006]. Opposed to CG, which is pure calcite, stalagmite CP is partly aragonite. The different fractionation factors can lead to up to 1.4 ‰ higher δ^{18}O values in aragonite.

However, the level of CP is still 1 ‰ higher than expected. This could in part be related to the different drip behaviour of the drip site, which shows much lower drip rates than CG. Drip sites around CM and CP in general show lower driprates than for CG, which could explain the general shift between the records. Evaporation can take place, leading to more kinetic fractionation. This was in part confirmed by the Hendy tests along single growth layers of CP and CM. Also the correlation between isotopes along the growth axis of both isotopes confirms a general tendency to more kinetic fractionation.

In general, the comparison of the last 1 ka between CG and CP does not reveal any correlation, which might be due to low age control in CP in the upper part of the stalagmite. The only robust feature in both records seems to be the transition from high δ^{18}O values to low δ^{18}O values around 1 ka. Due to the low age control of CP at the top part, records were treated separately.

According to *Holzkämper et al.* [2009], C3 plants can lead to a relatively low δ^{13}C value in carbonates. The authors offer a range of -8 to -15 ‰ in calcite. If the vegetation above the cave is more a mixture between C3 and C4 plants, the recorded δ^{13}C values in stalagmites are more enriched [*McDermott* 2004]. E. g., [*Holzkämper et al.* 2009] refer to values between 1 and -7 ‰ in calcite. The δ^{13}C values in aragonite on the other hand, can be higher by up to 2 ‰ compared to calcite due to different fractionation factors. This is important for the observed δ^{13}C values in Cuban stalagmites. The δ^{13}C values in the time range between 7 and 11 ka show an offset of around 5 ‰ between CP and CM. The δ^{13}C level of CG is on a much lower level in comparison to CP. CG and CP are from the same cave system and of the same cave level of Dos Anas cave, so that changes in vegetation can be ruled out to explain those shifts in the δ^{13}C values. The different fractionation of δ^{13}C in calcite and aragonite can explain, why stalagmite CG (calcite) and CM (calcite) reveal lower δ^{13}C values and CP (aragonite) higher δ^{13}C values. In addition, kinetic fractionation (e. g., as shown in the Hendy tests, the kinetic plots and is presumably due to lower drip rates) takes place in stalagmite CP, leading to more enriched δ^{13}C values. Moreover, the kinetic fractionation can be different for all three stalagmites and can be attributed to lower drip rates, which are generally observed for CP and CM. In addition, processes such as fractionation/ kinetic enrichment in the soil zone can further lead to higher δ^{13}C values. Generally, it can be inferred that the observed δ^{13}C values of the stalagmites indicate more a mixture of C3/C4 vegetation than pure C3 vegetation. However, the influence on stalagmite δ^{13}C is rather complicated, processes in the soil zone, vegetation and open/closed system behaviour can lead to changes in δ^{13}C values. E. g., switches in the proportions of C3 and C4 vegetation need to be independently verified (i. e. by pollen studies) to constrain observed δ^{13}C values [*McDermott* 2004]. The main focus therefore lies on the study of the δ^{18}O signal and δ^{13}C is used in complement.

Comparing the frequency and wavelet analysis of all records is difficult since all

isotopic records have a different temporal resolution due to different growth rates and the records do not continuously overlap. However, a general feature between CP and CM seems to be the evaluated frequencies around 110 a and 150 a. The 110 a variability is most pronounced around 8.5 ka in CM, whereas around 4-6 ka in CP. In this time range, also a 150 a variability is pronounced. The 80 a variability on the other hand is seen in CG and CM. This is most pronounced around 7.5 a in CM. The variability in CG of 220 a and 480 a are not found to be significant in CM or CP. However, stalagmite CP shows a varying growth rate during the Holocene. In addition, age errors are relatively large. The only most robust feature of this record seems to be the change in variabilities around 5 ka, where also a millennial variability becomes visible. However, multicentennial variability is found in CG as well as in CP, but lack comparison. In comparison with other proxy archives, the observed variabilities around 80, 110, 220 a and multicentennial variability indicate a connection to solar variability (Section 3.4), which will be discussed in the following.

The focus of this work is climate variability in the Holocene, therefore mainly the stable isotope data of the last 12.5 ka will be discussed.

5.2 Interpretation of isotopic records

It has been shown that the stable isotope signal, which is recorded in stalagmites, is influenced by several processes (Section 2) which includes changes in the amount of precipitation, water source δ^{18}O, wind directions and temperature effects. In addition to those changes which happen above the cave, also processes in the soil zone as well as inside the cave play a crucial role.

For the circum-Caribbean area, several authors stated the amount effect being the most important driver of δ^{18}O values in rainfall on seasonal to interannual timescales. E. g., *Vuille et al.* [2003] discuss the amount effect from model-results in the Caribbean area as important influence on rainfall δ^{18}O. *Lachniet and Patterson* [2009c] found a relationship of -1.24 ‰/100mm in Belize and Panama rainfall. In addition, another relationship between Panama rainfall δ^{18}O and the amount of precipitation was established by *Lachniet and Patterson* [2006] and *Lachniet et al.* [2004b] between -1.6 and -2.85 ‰/100mm. Similar values were found by *Jones et al.* [2000] for Barbados with -2.2 to -2.75 ‰/100mm. However, δ^{18}O values of rainfall for Havana, Cuba, are covering only three years (GNIP database, *IAEA/WMO* [2006]) and cannot be used to establish a proper rainfall amount-δ^{18}O relationship for Cuban rainfall.

To study the relationship how changes in precipitation amount transfer into changes in stalagmite δ^{18}O, it is crucial to have long observational records of precipitation amount. Most meteorological stations in Cuba offer precipitation data for the time range between 1950 and 1980, which is too short to establish a proper rainfall amount-stalagmite δ^{18}O relationship, e. g. for the recent stalagmite CG. However, an attempt

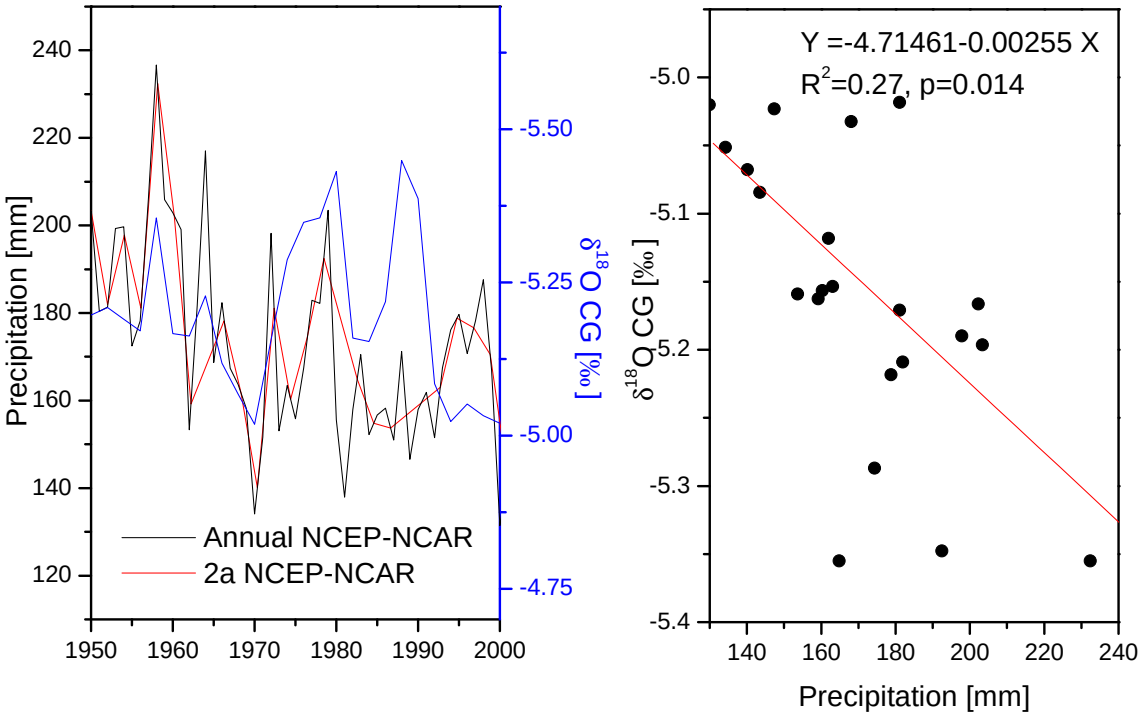

Figure 5.2: *$\delta^{18}O$ of CG vs precipitation amount. Left: values shown over time, right: transfer function.*

can be made with the NCEP-NCAR Reanalysis data which was already described in Section 3.3.1. This data covers the range between 1950 to 2010 and is shown as yearly averages in Fig. 5.2 (left) in black, the two years average is shown in red. For comparison, the interpolated (on a 2 a grid) stalagmite δ^{18}O values of CG are shown in blue. The transfer function from stalagmite CG δ^{18}O to amount of precipitation is calculated with a linear fit as shown in Fig. 5.2 (right). The slope of the transfer function is -0.0026 ‰/mm or -0.26 ‰/100mm. A study about stalagmites from Guatemala [*Medina-Elizalde et al.* 2010] suggest a value of -176 mm/‰ of stalagmite δ^{18}O. This leads to a slope of -0.57 ‰ in stalagmite δ^{18}O per 100 mm of rainfall increase. Compared to this slope, the stalagmite CG slope differs by a factor of 2. However, the δ^{18}O of CG reveals over the last 1.3 ka a variability of 1.5 ‰. The variability of the Guatemalan stalagmite of *Medina-Elizalde et al.* [2010] on the other hand, reveals a variability of 3 ‰ over the last 1.5 ka. This indicates, that both isotopic records also show a factor of 2 in terms of variability on longer timescales. The explanation for this behaviour might be differences on influences on δ^{18}O values in the soil zone. However, results from the monitoring program can not be used to study the transfer from δ^{18}O values of rainfall to δ^{18}O values in drip waters or stalagmite, because this program only covers values for one year and in addition, rainfall δ^{18}O values are not provided by the GNIP database for 2008. If no precise monitoring program is provided, changes in δ^{18}O

in rainfall due to rainfall amount can not be compared to changes in stalagmite δ^{18}O in dependency of rainfall amount, since processes in the soil zone remain unclear.

It is important to note that in general, the amount effect, e. g. more rainfall leading to lower δ^{18}O values in rainfall, can also be detected in Cuban stalagmites. The correlation between rainfall and stalagmite δ^{18}O allows an estimate of around -0.26 ‰/100mm as a transfer function. However, for this analysis, interpolation was necessary which reduces confidence in calculation the transfer function. Moreover, the NCEP-NCAR Reanalysis data for rainfall cover the time range between 1950 and 2010, but the age model of the stalagmite CG in this time interval shows large errors up to 200 a. Therefore the correlation, which is in general weak, might also be coincidence. This study therefore clearly refrains from calculating quantitative palaeo precipitation amounts and only uses changes in stalagmite δ^{18}O as qualitative indicator for past climate changes. Other effects, such as kinetic fractionation or changes in cave temperature also play a role. However, both effects are connected. If drier conditions occur, lower driprates are expected, leading to more kinetic fractionation and higher δ^{18}O values, which is the same direction as expected for the amount effect [*Lachniet* 2009a]. In the tropics, higher temperatures are indirectly connected to more rainfall and lower δ^{18}O values in precipitation [*Vuille et al.* 2003]. Higher temperatures in the cave system would have the same effect on the observed δ^{18}O values in speleothems. All these effects are therefore leading in the same direction. On the other hand, changes in water sources and contribution of each water source to rainfall δ^{18}O can also change the preserved δ^{18}O in stalagmites. The main water source of Caribbean rainfall, however, has been shown to be the Atlantic and Caribbean Sea [*Vuille et al.* 2003]. For further analyis, model results and continuous δ^{18}O measurements in precipitation are needed to infer proper estimates, which at this time are not available.

5.3 From recent to past

It has been shown that the recent climate variability in the Caribbean is influenced by both Atlantic and Pacific climate variability (Section 3). However, due to the fact that no growth layers are visible in stalagmite CG, exact dating of the upper part (e. g., the last 200 a) remains difficult, so that the comparison between observed climate indices, such as precipitation amount, or even teleconnection indices such as AMO and NAO (Atlantic) or ENSO (Pacific), will lead to large uncertainties in the interpretation. Therefore, it is necessary to look at a time interval longer than the time interval with low age control, which means that the comparison with proxy archives and reconstructions becomes necessary; especially, if the multidecadal variability or variability on longer timescales and possible forcing mechanisms shall be studied. For a proper comparison during the last 200 a, it is therefore necessary to compare the observed data in Cuban stalagmites with other high resolution archives which cover the whole period.

High resolution archives of the Caribbean area are still sparse. However, two climate records cover the last 200 a in high resolution and are shown in Fig. 5.3, which shows the stalagmite CG δ^{18}O values (blue) in comparison with stalagmite δ^{18}O values from the Yucatan peninsula (green) [*Medina-Elizalde et al.* 2010] and Caribbean Mg/Ca-SSTs from the Cariaco basin (black) reconstructed from *Black et al.* [2007] based on planktonic foraminifers (Globigerina bulloides). The grey bar indicates the interval in CG with low age control. In the following, higher temperatures and more precipitation are indicated on the top of the y-axis for easier comparison. The direction of each reconstruction in terms of climate parameters in also indicated. Stalagmite CG shows wetter conditions at 0.5 ka and a drying trend towards 0.35 ka. The same trend is observed in the stalagmite data from the Yucatan pensinsula [*Medina-Elizalde et al.*

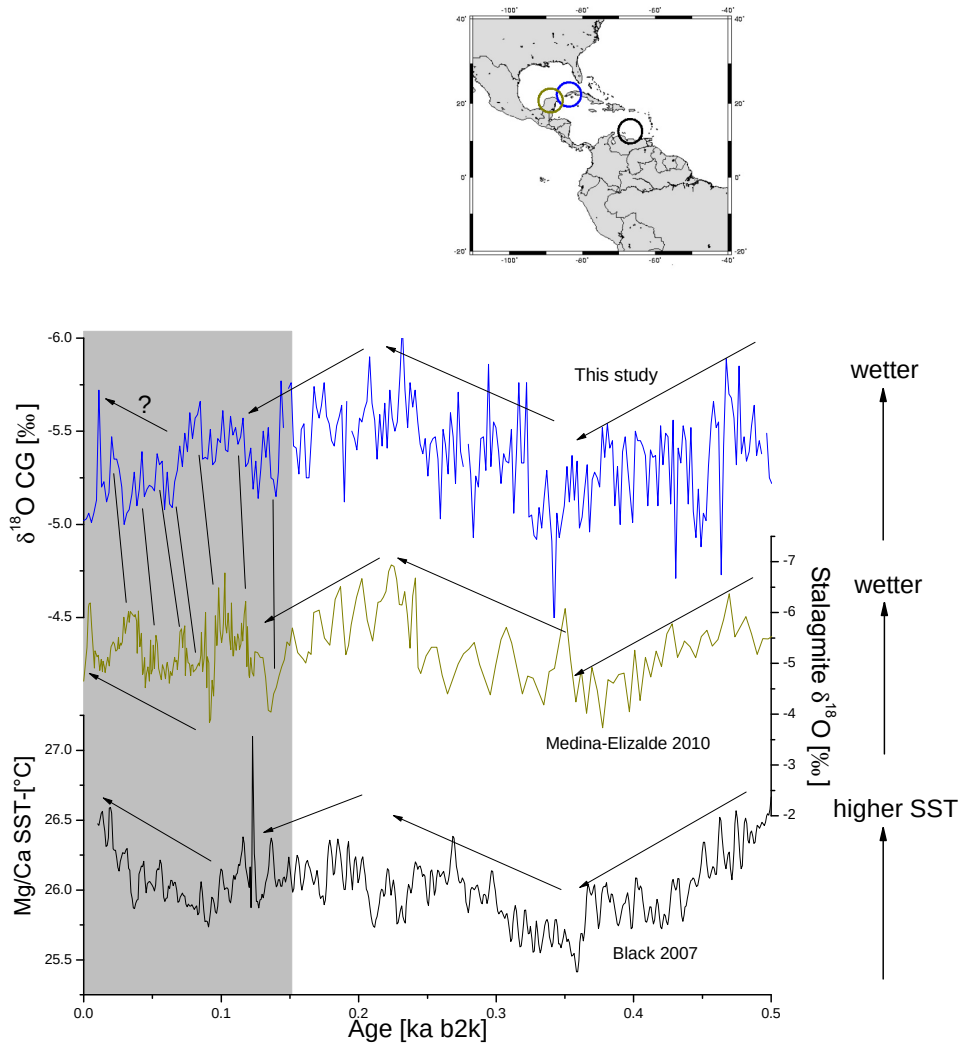

Figure 5.3: *δ^{18}O of CG in comparison with Caribbean proxy records during the last 500 a. The grey bar indicates the time range with low age control in CG.*

2010] as well as from warmer (0.5 ka) to colder SST (0.35 ka). In all three records, the conditions from 0.35 ka to 0.2 ka show a trend to wetter and warmer conditions, and back to colder/drier conditions until 0.125 ka. Driest conditions are then found again at 0.09 ka in the stalagmite record and SST record. Stalagmite CG on the other hand shows driest conditions around 0.06 ka. The general observed correlation between the records suggests, that the age model in the last ≈150 a of CG is not correct and show too young values by ≈30 a. The corresponding peaks in the other records during the last 150 a are indicated.

The authors of *Medina-Elizalde et al.* [2010] suggest as a possible forcing mechanism for observed stalagmite $\delta^{18}O$ values the movement of the ITCZ, in general a more northward ITCZ leading to higher precipitation. This is observed on an annual basis both in Yucatan as well as in Cuba (Section 3). However, this record discusses a variability of 200, 40, 24, 17, 12 and 8 years. The authors suggest solar forcing as one of the main forcing mechanisms, similar to findings by *Hodell et al.* [2001], which will be discussed in detail below. However, precipitation amount in Cuba seems to be highly correlated to Caribbean SST over the last 500 a in the way that higher SSTs lead to more rainfall over Cuba. This can be explained by higher evaporation rates, more condensation in the Caribbean basin, leading to more rainfall over Cuba [*George and Saunders* 2001, *Poveda et al.* 2006]. The question remains, what forces Caribbean SSTs. *Black et al.* [2007] detect a variability of 3 to 6 years and greater than 63 a. However, even if the 3 to 6 a variability lies well within the ENSO band, the authors do not detect a clear correlation to ENSO indices. Another forcing mechanism of Caribbean SSTs is the NAO, more NAO^+ conditions leading to lower SSTs [*Black et al.* 2007], also shown in Section 3. The variability on multidecadal timescales could not be connected to a multidecadal forcing mechanism since the peak in the spectral analysis is not well defined. The authors note that multidecadal scale variability can result from processes internal to the Earth's system, such as the thermohaline circulation. A possible candidate for this variability has been shown to be the AMO (Section 3), varying on timescales between 60 and 110 a. In general, model studies show that a more positive AMO is possibly connected to a stronger thermohaline circulation (Section 3.2.3, e. g. *Delworth and Mann* [2000]). In the Atlantic sector, a northward shift of the ITCZ can be observed during positive AMO phases (e. g. *Knight et al.* [2006]), as well as an increase of hurricane activity (e. g. *Goldenberg et al.* [2001]) and more precipitation in the Caribbean (e. g. *Sutton and Hodson* [2005]). The question therefore is, if the observed variability in CG can be related to changes in the thermohaline circulation.

Two reconstructions exist showing the AMO signal, e. g. *Gray et al.* [2004]. This records covers only the last 430 a. Since the age uncertainties in CG over the last 200 a are relatively large, the comparison with another archive is necessary. *Mann et al.* [2009] offers a reconstruction of the AMO signal over the last 1.4 ka. The authors use a

multiproxy approach, using more than thousand tree ring, ice-core, coral, sediment and other data spanning ocean and land regions of both hemispheres to reconstruct SST anomalies in both hemispheres. The reconstruction of Northern hemospheric Atlantic (AMO region) SST anomalies is shown in Fig. 5.4 (green) in comparison with CG (blue). However, for a correlation, both datasets were detrended and smoothed with an adjacent average (5 point for CG and 10 point for the AMO, since CG has a resolution of around 2 years and the AMO of 1 year). The age model of CG can be adapted as shown in Fig. 5.5, still in agreement with the original record. The correlation reaches a correlation coefficient r of -0.5 ($p=2 \cdot 10^{-16}$). This indicates, that Cuban precipitation amounts during the last 1.3 ka were connected to changes in North Atlantic SSTs, a higher SST in the North Atlantic leading to more precipitation in the Caribbean, which is in agreement with the idea about a more northward Atlantic ITCZ and eventually a stronger THC. However, it is important to note that the reconstruction of *Mann et al.* [2009] use a proxynetwork to establish the SST records. [*Mann et al.* 2009] uses this proxys and force climate models (GISS-ER and NCAR-CSM) to further study the climatic pattern during the Little Ice Age (LIA) as well as the Medieval Climate Anomaly (MCA), which are both covered by stalagmite CG and are discussed in the following.

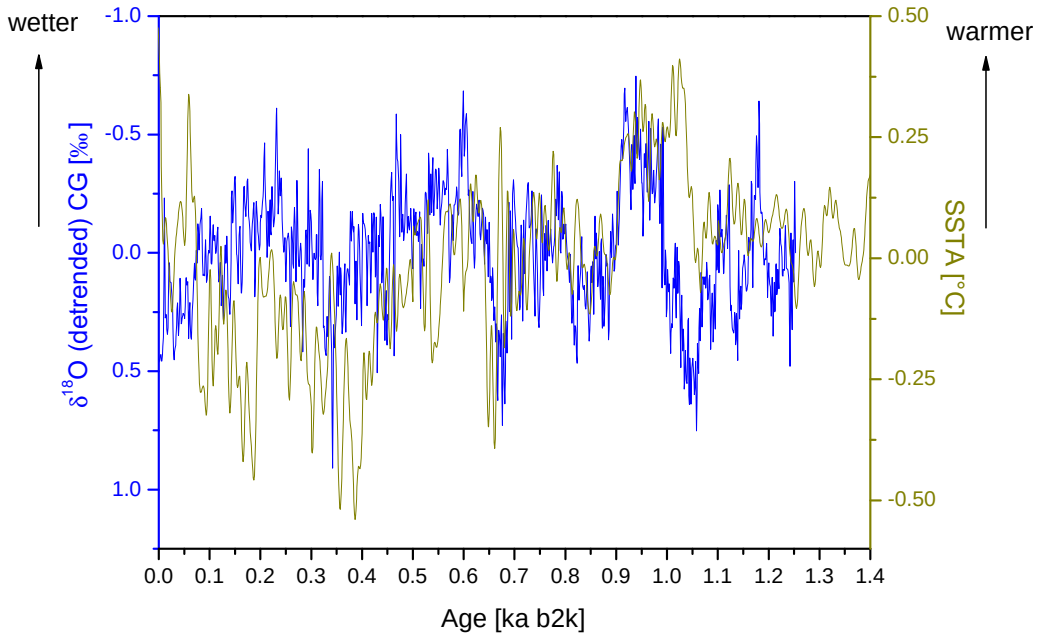

Figure 5.4: *Detrended $\delta^{18}O$ in comparison of AMO index reconstructed by Mann et al. [2009]. Higher SSTs in the North Atlantic are accompanied by higher precipiation amount and lower $\delta^{18}O$ values in Cuba.*

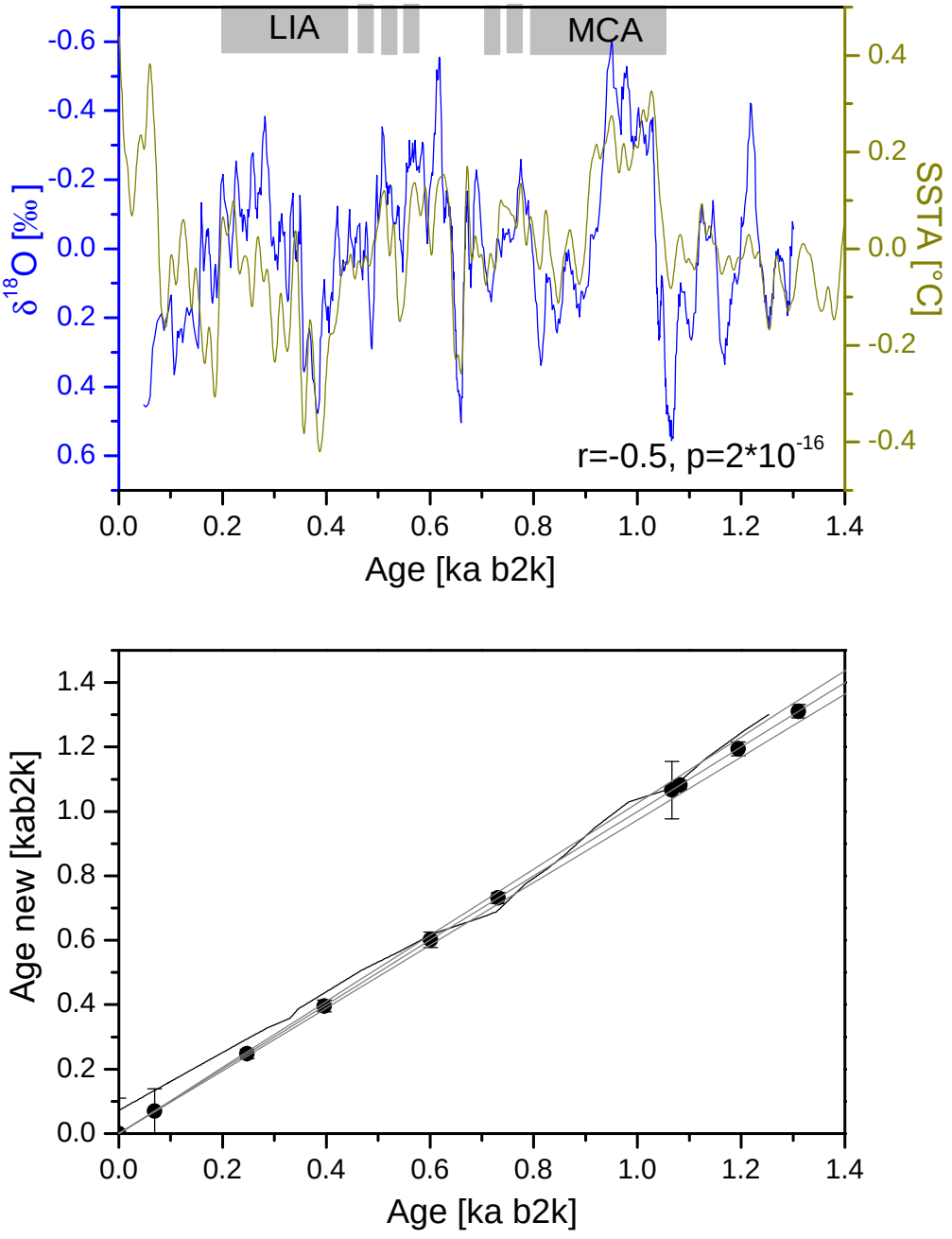

Figure 5.5: *Upper panel: CG and the AMO record of Mann et al. [2009] detrended and smoothed (10 a). Lower panel: old versus new age model of CG.*

5.4 Little Ice Age and Medieval Climate Anomaly

The Little Ice Age (LIA) as well as the Medieval Climate Anomaly (MCA) are also covered by another record of the Cariaco basin, the Titanium record of *Haug et al.* [2001]. A comparison of the CG isotope record and the Ti record is shown in Fig. 5.6. In this region, higher Ti concentrations in sediments are interpreted to reflect greater terrigenous input from riverine runoff and indicates greater precipitation and a more northerly mean latitude of the ITCZ [*Haug et al.* 2001]. Fig. 5.6 shows the comparison of the detrended CG data (blue) and the Cariaco data (black). In the time interval of the MCA (≈1.05 to 0.8 ka ago) and LIA (≈0.5 to 0.2 ka ago), both records show the same changes in precipitation. Less precipitation in Cuba coincides with less precipitation and a more southerly ITCZ in Cariaco during the LIA, and vice versa for the MCA. The position of the ITCZ over northern South America is also influenced by Atlantic sea surface conditions, making changes in the temperature gradient of the Atlantic an alternative driver for some component of the ITCZ variation [*Hughen et al.* 1996, *Black et al.* 1999, *Haug et al.* 2001]. *Haug et al.* [2001] note, that this may explain the coincidence between cold periods in the high-latitude North Atlantic [*Briffa et al.* 1992] and drier conditions over northern South America, particularly during the Little Ice Age.

The MCA seen in the Cariaco record was put into broader context by a study of *Trouet et al.* [2009]. The authors note, that in general the MCA was characterized by relative warmth over the North Atlantic/European region and much of the extra-tropical Northern Hemisphere. The MCA-LIA winter temperature difference is noted to be around 0.3 to 0.5°C. The widespread signature of the climatic shift from the MCA to the LIA implies, that changes in tropical SSTs were also involved [*Trouet et al.* 2009]. During the MCA, presumably governed by strong NAO^+ conditions, stronger westerlies may have led to enhanced Atlantic meridional overturning circulation (=THC), which in turn generated cross-equatorial salinity and SST anomalies in the tropical Atlantic and a related northward migration of the ITCZ. In addition, the enhanced THC may have accomodated a constructive feedback mechanism, for which evidence is provided by the Cariaco-record, that in turn could have reinforced La Niña-like conditions in the tropical Pacific [*Trouet et al.* 2009]. The authors note, that the modelled La-Niña state in the Pacific during the MCA is supported by marine proxy records that show warm SST anomalies in the western tropical Pacific [*Stott et al.* 2004] and cold anomalies in the central and eastern tropical Pacific [*Cobb et al.* 2003]. The La Niña-like conditions in the Pacific may also have been initiated by enhanced solar irradiance and/or reduced volcanic activity [*Mann et al.* 2005], and amplified and prolongued by an enhanced AMOC. The drying trend during the LIA was also found by *Hodell et al.* [2005b] on the Yucatan peninsula. This indicates, that in general, forcing mechanisms on Caribbean climate variability might be connected to changes in the THC. Compared to the study

of *Mann et al.* [2009], both studies suggest positive NAO conditions during the MCA as well as a positive AMO phase. It has been shown that the influence on the present Caribbean climate also includes the ENSO variability in the northern Caribbean. This possibility will be further discussed below.

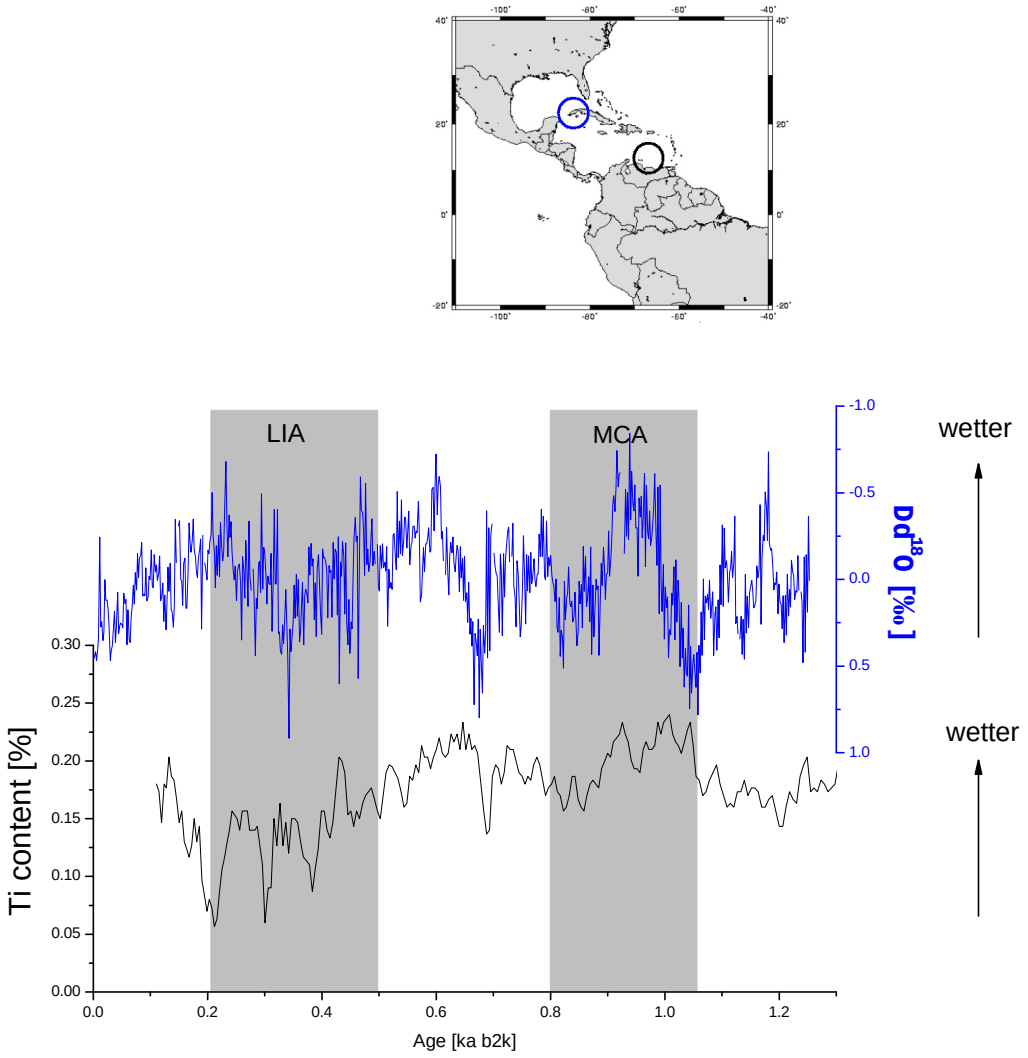

Figure 5.6: *Comparison of CG with Cariaco Ti record of Haug et al. [2001]. The MCA and LIA are shaded grey. Both records exhibit wetter conditions during the MCA and drier conditions during the LIA.*

5.5 Solar forcing

The frequency analysis of CG and the wavelet analysis strongly suggest a link to solar forcing. In both isotopic records, the variability of around 220 a is recorded. The good correlation with the AMO reconstrucion of *Mann et al.* [2009] could point to a connection of Cuban precipitation to Atlantic SSTs. Whether the observed changes in the AMO are due to the reconstruction method, e. g. based on several proxy records which all could be influenced by solar forcing, is not clear. This indicates the importance of the study of solar influence on the isotopic record of Cuba.

Several authors noted solar forcing as a potential driver of past Caribbean climatic changes. E. g., *Hodell et al.* [2001] note a variability around 208 a and compares the record with the solar ^{14}C record which reflects solar variability or a combination of solar forcing and oceanic response. Periods of higher solar activity correspond to times of lower cosmonuclide (^{14}C) production. Comparison of the Punta Laguna (Mexico) δ^{18}O of *Hodell et al.* [2001] and the ^{14}C production (Δ^{14}C) records shows an antiphase relation for the past 2000 years. Higher evaporation/precipitation (E/P) rates (higher δ^{18}O) coincides with lower ^{14}C production, implying that droughts occurred during times of increased solar activity. A similar relation between drought and high solar radiation has been demonstrated in lake sediment records from equatorial east Africa that span the past 1100 years [*Verschuren et al.* 2000], but opposite in Barbados between 6.7 ka and 3 ka by *Mangini et al.* [2007].

Fig. 5.7 (upper panel) shows the original δ^{18}O signal of CG and estimated Band Pass Filters, centered around 220 a (from 170 to 298 a) and around 80 a (from 71 to 81 a). The frequencies were chosen due to the results of the frequency analysis and the estimated band width error. The same Band Pass Filters were applied to the estimated δ^{18}O signal of CG as shown in Fig. 5.5, the results are shown in Fig. 5.7 (middle panel). The detrended radiogenic isotope ^{14}C is shown in Fig. 5.7 (lower panel) [*Stuiver et al.* 1998], as an estimate for solar activity, higher ^{14}C production rate indicates a weaker solar activity. The 220 a variability was shown to be strongest in the time interval from 0.8 to 1 ka in stalagmite CG. For easier comparison, the sum of both Band Pass Filters is shown for each δ^{18}O proxy in Fig. 5.8 in comparison to the original ^{14}C production rates. In the time interval between 0.8 ka and 1 ka, the isotopic records of Cuba show enhanced wet and dry periods, which can not be connected to extremes of ^{14}C production rates. On the other hand, solar minima in the younger time interval can also not be connected to extreme dry or wet conditions, especially during the Maunder (M), Spörer (S) and Wolf (W) minima.

With stalagmite CG, the study of *Hodell et al.* [2001] can not be confirmed. Stalagmite CG is connected to a cycle of 220 a but at this point it is not clear whether this is purely solar driven or not, the connection to solar influence varies with time. Especially the time intervals with strong solar minima, e. g. the Maunder (M), Spörer

(S) and Wolf (W) minima can not be correlated to extremely dry or wet phases in Cuba. The same seems to count for the studies of *Medina-Elizalde et al.* [2010] and *Black et al.* [2007]. A possible reason for the disagreement with *Hodell et al.* [2001] might be the low resolution of the sediment record and higher dating uncertainties. However, the correlation to the AMO reconstructed by *Mann et al.* [2009] states that, Cuban precipitation seems to be highly connected to North Atlantic SSTs.

However, the mechanism if and how changes in solar activity could cause precipitation shifts in the northern Caribbean is not certain. An amplifying mechanism is required to obtain a significant climate response from rather small variations in solar output.

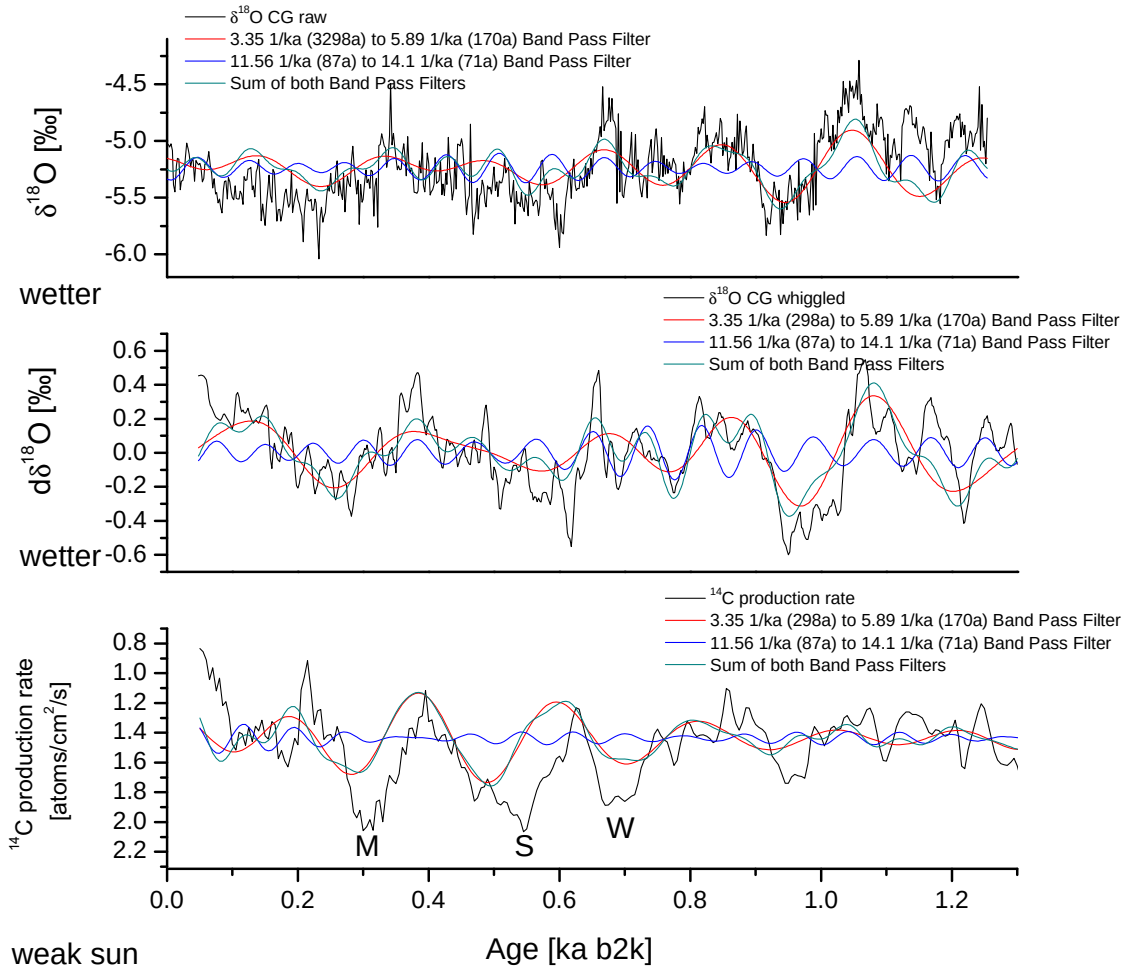

Figure 5.7: *Connection of raw Cuban $\delta^{18}O$ signal (top panel), whiggled $\delta^{18}O$ signal (middle panel) and solar variability (lower panel). The 220 a variability in CG is most pronounced between 0.8 and 1 ka, where no clear connection to solar variability is indicated.*

Hypothesized mechanisms include changes in the ultraviolet part of the solar spectrum, which affects ozone production and stratospheric temperature structure [*Haigh* 1996], and the effect of cosmic ray intensity on cloud formation and precipitation [*Van Geel et al.* 1999]. Sensitivity experiments conducted with atmospheric general circulation models imply that changes in solar output may affect global mean temperature, humidity, convection, and intensity of Hadley circulation in the tropics [*Rind and Overpeck* 1993, *Rind and Overpeck* 1995]. Any solar-forced change in the strength or position of Hadley circulation or tropical convective activity could therefore affect rainfall in the

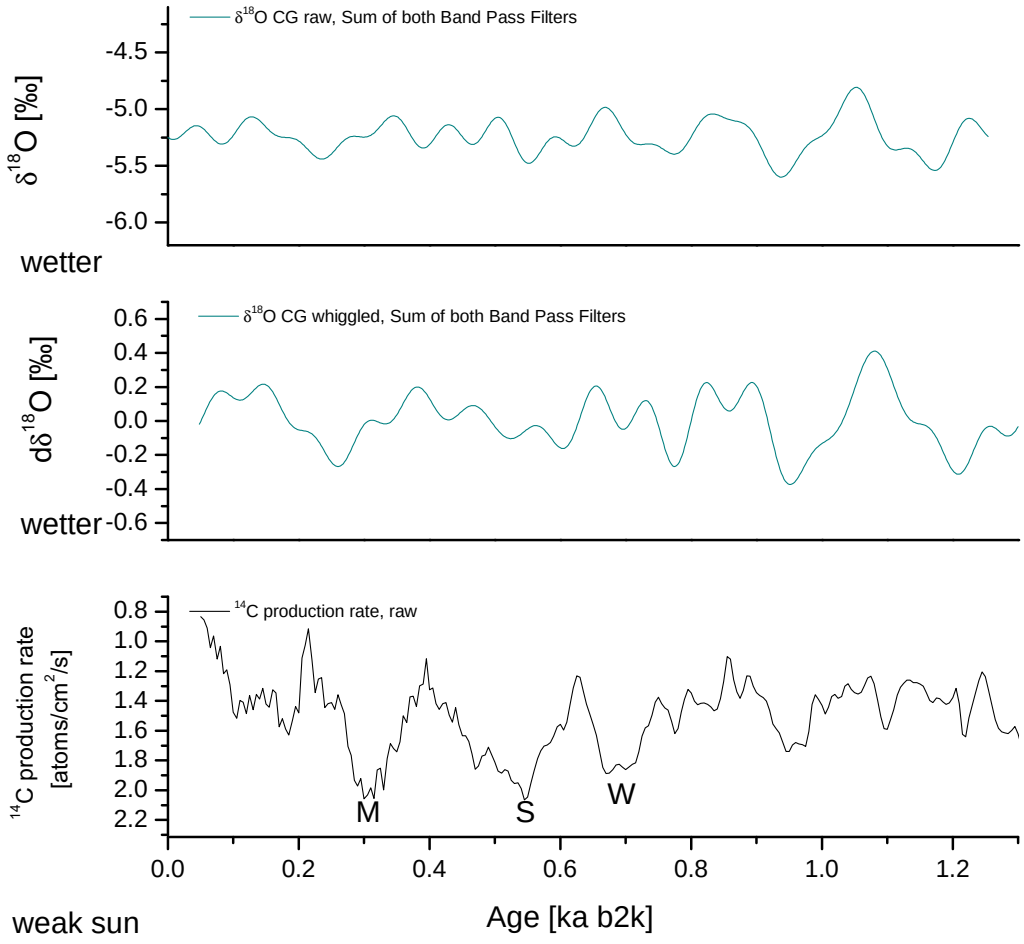

Figure 5.8: *Comparison of the sum of both Band Pass Filters for raw (upper panel), whiggled (middle panel) CG $\delta^{18}O$ data and solar variability (lower panel). In the time interval between 0.8 and 1 ka, the solar variability does not show extreme values, whereas the stalagmite data indicate enhanced periods of dry and wet conditions.*

Northern Caribbean [*Hodell et al.* 2001].

Another record from the Caribbean area showing solar variability is *Black et al.* [2004]. The authors note that observed δ^{18}O values of G. bulloides in the Cariaco basin show similarity with the 11 a sunspot cycle which suggests, that solar variability plays a role in influencing the hydrological balance of the circum-Caribbean. The δ^{18}O values are more negative (wetter or warmer conditions) when sunspot numbers are high. Similarly, a stalagmite from Barbados revealed wetter conditions during phases of stronger solar activity between 6.7 and 3 ka [*Mangini et al.* 2007]. [*Black et al.* 1999] show that during the last 800 a, stronger trade winds (cooler SSTs) as reconstructed from abundance of G. bulloides in sediments, largely correlate with a weaker sun.

On the other side, during the time range between 1730 and 1990 A. D., *Nyberg et al.* [2005] estimate the relationship between hurricane activity in the eastern Caribbean area, solar forcing and the AMO. The main controls on hurricane formation are SSTs and vertical wind shear [*Nyberg et al.* 2005]. The authors note, that during positive AMO phases, major hurricane activity was enhanced. Peaks and trends of higher major hurricane activity concur with lower total solar irradiance, and vice versa. For establishing a possible forcing mechanism, global circulation models (GCMs) have shown, that circulation changes in the upper stratosphere, induced by interactions between solar irradiance and ozone levels, may penetrate down to the troposphere, where surface winds and SLP are affected [*Shindell et al.* 2001]. The GCMs also indicate a forced shift towards decreased sea level pressure in the subtropical Atlantic during reduced total solar irradiance, which would result in weaker easterly trade winds, weaker wind shear and higher major hurricane activity.

However, the influence of the solar activity on Caribbean records is not clear. Other records providing evidence of solar forcing is a record of Oman [*Neff et al.* 2001]. The authors note reduced rainfall during strong solar minima during the Holocene. Millennial scale variability over the Holocene in connection with solar forcing was also evaluated by *Bond et al.* [2001] and will be discussed below with the record CP.

5.6 Mid- to Late-Holocene variability

It has been shown that climate variability in the northern Caribbean reconstructed from the Cuban stalagmite CG is highly connected to SSTs in the Northern Atlantic. So far only one study of *Hillesheim et al.* [2005] connected climate variability between 9 and 11.5 ka in the Caribbean area with the so called 'Bond events', which are cold events occurring in the Northern Atlantic. *Bond et al.* [2001] and *Bond et al.* [1997] showed, that during the Holocene, the subpolar North Atlantic area experienced several cold events with a quasi periodic cycle of 1500 a. The authors connect their observations with changes in solar output, e. g. production rates of cosmogenic nuclides ^{14}C and ^{10}Be (Fig. 5.9, orange, *Stuiver et al.* [1998]) on centennial to millennial timescales. The record of haematite stained grains developed by *Bond et al.* [2001] is shown in Fig. 5.9 (black). The events are numbered at the top according to *Bond et al.* [2001]. A higher amount of HSG is thought to be connected to colder temperatures so that ice-bearing surface waters are advected eastward from the Labrador sea and southward from the Nordic seas. These events during the Holocene were also detected in a sediment core off West Africa [*deMenocal et al.* 2000] (Fig. 5.9, red and blue). This study reconstructs warm and cold season SST anomalies relative to today based on counts of planktonic foraminiferal assemblages. In agreement with *Bond et al.* [1997], the authors find cold periods centered at 10.2 ka, 8.0 ka, 6.0 ka, 4.6 ka, 3.0 ka, 1.9 ka, 0.8 ka and 0.35 ka. Bond event 6 can not be resolved in the record off West Africa. The authors note that these millennial scale Holocene SST variations appear to have involved the entire North Atlantic basin [*Bond et al.* 1997, *O'Brien et al.* 1995, *Bianchi and McCave* 1999, *Keigwin* 1996] and involved large-scale ocean and atmosphere reorganizations that were completed within decades or centuries.

In comparison to the records of *Bond et al.* [2001] and *deMenocal et al.* [2000], the Cuban δ^{18}O record of CP is also shown in Fig. 5.9 (green). The grey bars indicate colder conditions in the North Atlantic except for Bond event 1 where drier conditions in Cuba are marked as well as in West Africa. Drier conditions can be found in Cuba centered at 10.2 ka, 9.5 ka, 8.6 ka, 8.0 ka, 3.1 ka, 1.8 ka, 0.9 ka and at the top of the stalagmite. Bond event 3 is divided in two peaks centered at 4.2 ka and 4.6 ka. Between 8 ka and 5 ka Bond event 4 is masked by the transition phase similar to which is observed in West Africa. The frequency analysis of CP does not show any millennial scale variability in the time range between 7 and 12.5 ka, the variability in this time range is more on the centennial timescale. The drier conditions during the Bond events in this time range are therefore less extreme than in the time range between 7 ka and today. A possible explanation for those observations is given in *Debret et al.* [2009]. The authors study millennial scale variability in the Atlantic region as well as in South American records. A strong transition took place in the mid-Holocene. The authors note that during the first part of the Holocene, the records reveal a stronger characterization

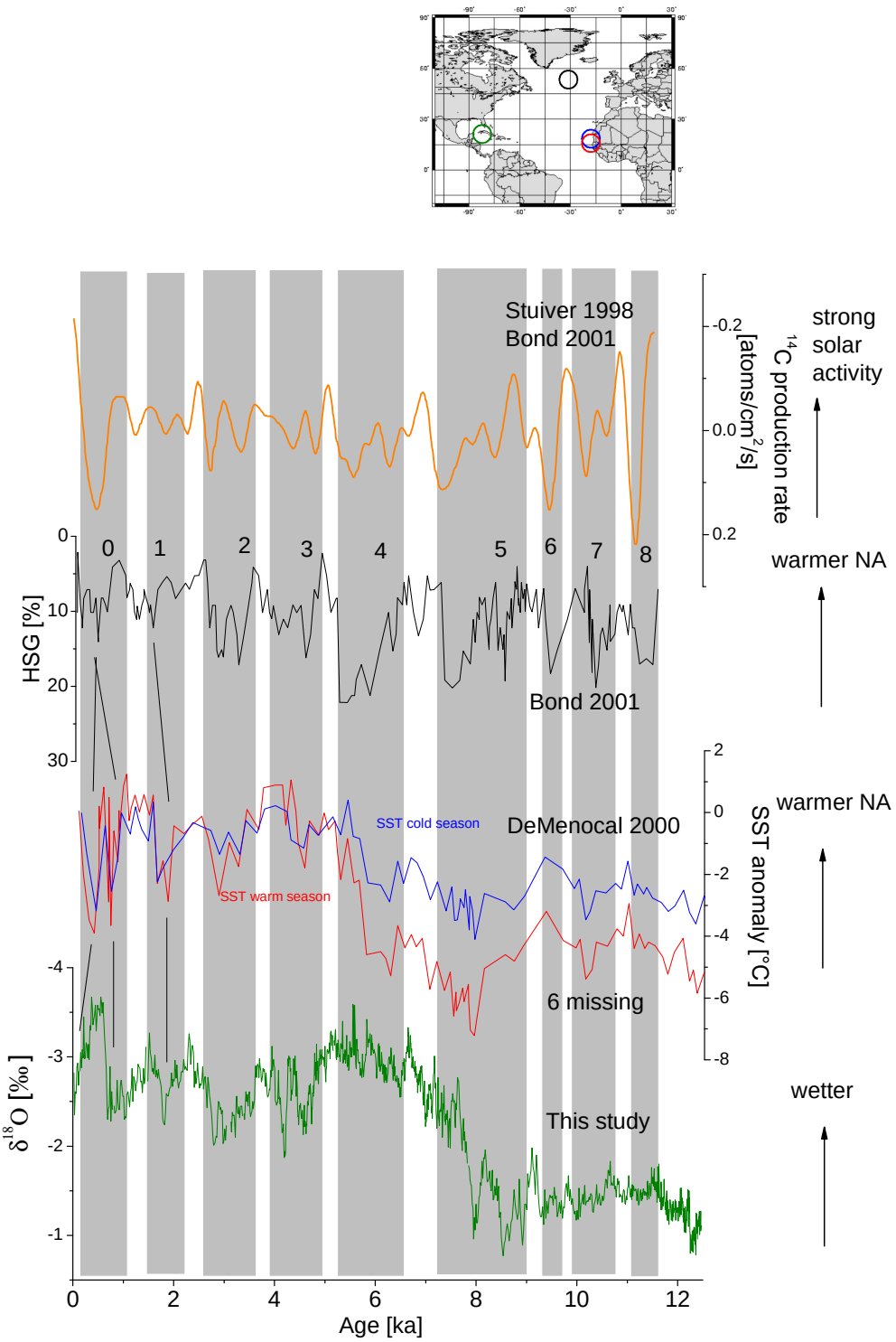

Figure 5.9: *Stalagmite $\delta^{18}O$ values (green) in comparison with North Atlantic records during the Holocene. The cold Bond events are marked with numbers and grey bars and correspond to cold SSTs in West Africa and drier conditions in Cuba.*

by solar activity (1000 years and 2500 years), the 2500 a cycle seems to be continuous over the Holocene. Internal forcings such as atmospheric or oceanic mechanisms could not be delineated. According to the authors, a global-influence climatic event, such as the 8.2 ka event, could alter the variability of palaeoclimatic records over short time periods without any direct linkage to solar forcing. In the early phase of the Holocene, the meltwater pulses together with a continuous sea level rise could prevent the THC from getting stabilized. In the mid-Holocene, the 1000 year cycle disappeared in favour of a cyclical internal (ocean) forcing. The Cuban stalagmite reveals quasi-periodicity of ≈1500 a, in agreement with the record provided by *deMenocal et al.* [2000], indicating that observed variability in the Cuban record might be connected to North Atlantic Bond events.

Another interesting feature is the trend which is observed in both the Altantic record from West Africa of *deMenocal et al.* [2000] and the Cuban record. Here, a trend to higher SSTs is also connected with lower δ^{18}O values in the Cuban stalagmite. *deMenocal et al.* [2000] explain the occurrence of this trend due to changes in regional upwelling conditions. The same effect will be discussed below. However, interestingly the trend starts in both records at the same time, indicating that a connection between the two records exist, also on orbital timescales.

Similarly, several dry events were found in a stalagmite record from Oman [*Neff et al.* 2001] centered at 6.3 ka, 7.4 ka, 8.3 ka, 9 ka and 9.5 ka ago, at times of strong solar minima and Bond events. However, the question how solar variability can induce a significant climate change, is still debatable. *Bond et al.* [2001] explains that GCM models have studied the atmosphere's dynamical response to solar forcing [*Shindell et al.* 1999, *Haigh* 1996]. The models imply that at times of reduced solar irradiance, the downward propagating effects triggered by changes in stratospheric ozone lead to cooling of the high northern latitude atmosphere, a slight southward shift of the northern subtropical jet and a decrease in the Northern Hadley circulation. Potentially, those responses on reduced irradiance could lead to the coincident increase in North Atlantic drift ice, cooling of both the ocean surface and the atmosphere above Greenland and reduced precipitation in low latitudes [*Bond et al.* 2001]. However, it is also important to study the deep ocean's response to reduced solar irradiance. Deep circulation proxies suggest reduced NADW production during at least some of the drift ice peaks [*Bond et al.* 2001]. The authors also compare their records with records from Greenland, Europe and the already discussed study by *deMenocal et al.* [2000]. All proxy records are in phase with each other, and taken together, discordant with the dominant modes of atmospheric, namely NAO, variability. Instead, the temperature patterns resemble those which accompany reduced NADW formation, such as which occurred during the Younger Dryas and 8.2 ka cold event, which will be discussed in separate below. Also, corresponding to the drift ice peaks, sea surface salinities are observed to decrease, indicating fresher conditions within the convecting regions, which clearly have the po-

tential to reduce the formation of NADW [*Bond et al.* 2001, *Dickson et al.* 1996]. The important implication here is, that a potential solar triggered reduction in North Atlantic thermohaline overturning might be an additional amplifying mechanism. It has been shown (Section 3.3.3) that a reduction in the THC would lead to drier conditions over the Northern Caribbean and a more southward ITCZ, which is in agreement with the Bond cycles.

5.7 ENSO

Since the present Caribbean climate variability shows connections to the Pacific ENSO phenomenon, it is therefore interesting to study potential ENSO connections during the Holocene. Two studies in the Caribbean region show the influence of ENSO during the Holocene. *Donnelly and Woodruff* [2007] reconstruct the hurricane activity during the middle-to late Holocene with storm-induced deposits stored in sediments in a coastal lagoon in Puerto Rico (Fig. 5.10, red). The authors note that during the last 5 ka, the hurricane activity recorded in Puerto Rico seems to be connected to ENSO. The ENSO activity was reconstructed from *Moy et al.* [2002] (Fig. 5.10, black), who study lake sediments from southern Ecuador. The light-coloured laminae exhibit variance in the ENSO band (2-8 years). The ENSO events become more frequently during the Holocene until 1200 years ago and decline towards present. Periods of high and low ENSO activity seem to alternate on a timescale of around 2000 years. The authors note that during the Holocene, their findings are consistent with a run of the Zebiak and Cane model [*Clement et al.* 2000] forced with orbitally induced changes in insolation, which results show an increase in both the amplitude and frequency towards the late Holocene. The connection to hurricane activity was then established by *Donnelly and Woodruff* [2007]. The authors note, that during intervals of high ENSO activity, the number of hurricanes recorded in Puerto Rican sediments is highly reduced. A possible explanation of those observations could be the connection to the amount of precipitation in Africa. This was reconstructed by [*Nguetsop et al.* 2004] by lake sediments with alkaliphilous diatoms from Lake Ossa in West Cameroon. Possibly, the amount of precipitation recorded in tropical Africa is related to the strength of the West African monsoon. Increased monsoonal strength in Africa results from a well-developed African easterly jet, producing increased cyclonic vorticity in the MDR. During intervals of increased monsoonal strength and cool ENSO phase, the African disturbances pass through a region of enhanced cyclonic vorticity, warm SSTs and low vertical shear, enhancing the development of hurricanes in the central and western portions of the MDR [*Donnelly and Woodruff* 2007]. However, it is important to note that controls on eastern equatorial Atlantic SST fluctuations independent of ENSO may also have played an important part in modulating the intensity of the West African monsoon over the Holocene [*Donnelly and Woodruff* 2007].

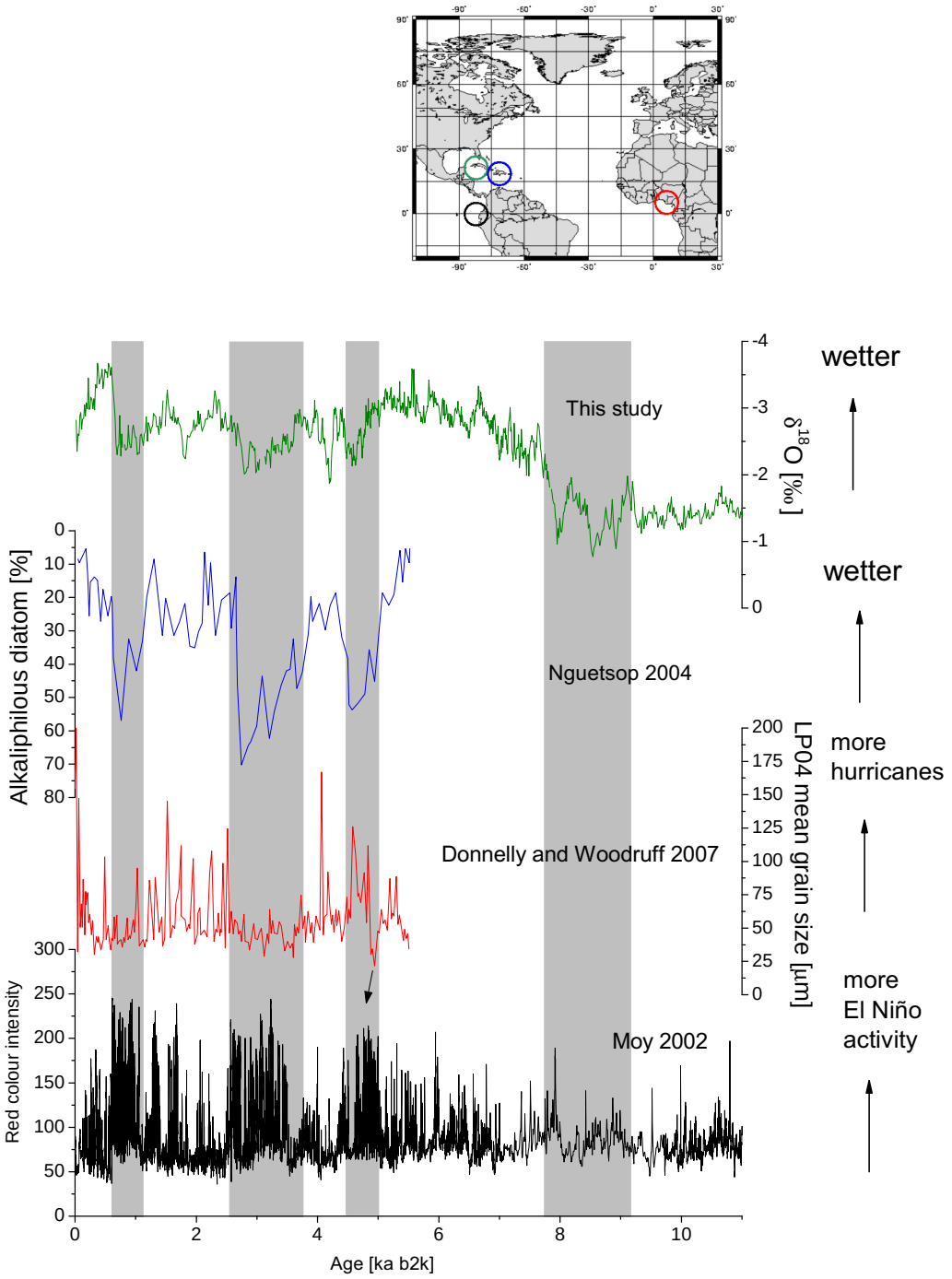

Figure 5.10: *Stalagmite $\delta^{18}O$ values in comparison with North Atlantic and ENSO records during the Holocene. A higher ENSO activity (grey bars) coincides with drier conditions in Cuba, less African monsoon and less hurricanes in Puerto Rico.*

In comparison to those records, the δ^{18}O data of CP is shown in Fig. 5.10 (green). It is important to note, that in observational data, several authors have shown a reduction in precipitation during the late rainfall season, which is also described as the hurricanes season. This is consistent with the CP data, as shown in Fig. 5.10. Several dry phases in the Cuban record coincide with enhanced ENSO activity recorded in Ecuador, e. g. around 1 ka, around 2.5 to 3.5 ka and around 4.5 to 5 ka. The question therefore is, if Cuban precipitation is steered solely by SSTs in the Northern Atlantic (THC) or by SSTs in the Pacific region (ENSO). This question is hard to answer, since only a few Holocene ENSO records exist, which makes comparisons difficult. *Moy et al.* [2002] discusses a possible connection to Bond events, which pacing is similar to the one observed in the ENSO record. Bond events tend to occur during periods of low ENSO activity, immediately followed by a period of high ENSO activity, which suggests that there might be a link between the both systems. On the other hand, the pacing of the solar ^{14}C record shares spectral coherency at a period of around 2000 years, the time series do not seem to be consistently associated with each other [*Moy et al.* 2002]. However, if the main mechanism of Cuban records remain Altantic SSTs which by themselves are connected to the strength of the THC, this might also lead to an influence of the THC on the ENSO system in the Pacific. A weaker THC has been shown to increase ENSO variability on millennial timescales [*Zhang and Delworth* 2005]. The frequency analysis of CP as well as the wavelet analysis do reveal a change of variability on several timescales around 5 ka, which indicates that the system must have changed around 5 ka. This is also stated by *Debret et al.* [2009], who state that a 1000 a solar driven variability was replaced by a 1500 a variability in the Northern Atlantic at around 5 ka, which might be connected to a stabilization of the THC after sea level was close to its maximum. However, the connection between changes in the THC and ENSO during the Holocene remains debatable and needs further study. The resolution of the stalagmite δ^{18}O data is not high enough to resolve the ENSO band, which in addition could further prove the ENSO connection.

Another study of the Caribbean region dealing with the ENSO phenomenon is [*Lachniet et al.* 2004b]. The authors reconstruct past changes in precipitation with a stalagmite from Panama, the δ^{18}O values are shown in Fig. 5.11 (black). The authors note drying conditions in Panama during high ENSO activity from *Moy et al.* [2002]. The data of stalagmite CG is shown in Fig. 5.11 (blue). The general features found in the stalagmite of Panama seem to be found also in Cuba. The authors do not detect any variability which could be connected to solar variability, and attribute subdecadal variability to connections to ENSO. If it remains true, that ENSO variability remains the only control to Panamian rainfall, the comparison with the *Moy et al.* [2002] record during the last 1 ka is difficult to approach, since the errors in the age model seems to be rather high in the sediment record. However, the comparison indicates that drier conditions during higher ENSO activity are found in Panama as well as in Cuba on

longer timescales, which was further confirmed by stalagmite CP.

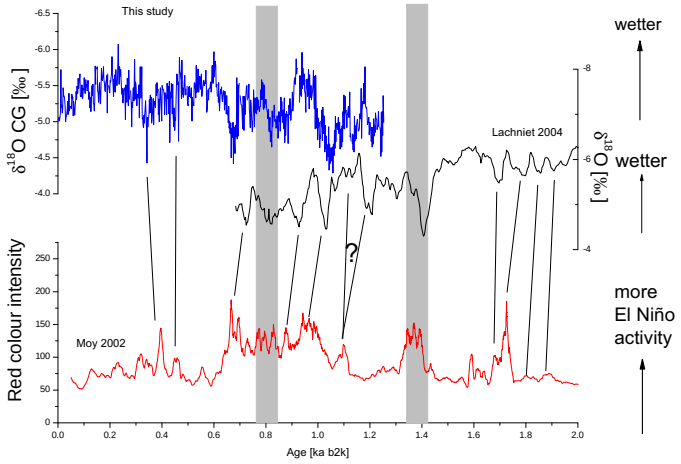

Figure 5.11: *Comparison of CG (blue) and Panama (black) $\delta^{18}O$ values recorded in stalagmites. The comparison with the ENSO record suggests drier conditions during more El Niño activity (red). Grey bars indicate strong periods of ENSO.*

5.8 Holocene Transition

The $\delta^{18}O$ signal of CP as well as of CM shows a clear transition from higher $\delta^{18}O$ values (drier conditions) to lower $\delta^{18}O$ values (wetter conditions) in the time interval from 10 to 5 ka (s. Fig. 5.12, green (CP) and black (CM)). This transition is clearly visible in both records. Superimposed on this transition are other dry/wet events which will be discussed separately. The transition to wetter conditions during the Holocene is recorded in several climate proxies in the Caribbean region. E. g., in the Cariaco basin, the trend to wetter conditions started after the Younger Dryas, reaching the peak between 10.5 ka and 5.5 ka during the Holocene thermal maximum [*Haug et al.* 2001]. However, as indicated in Fig. 5.12, several other proxies from the more northern part indicate a later transition. The record of *Hodell et al.* [1991], e. g. (Fig. 5.12, blue) is located in Haiti and shows nearly the same trend to wetter conditions in the lake sediment as in Cuba. The general trend has been attributed to the change from low to high water levels and increasing precipitation. During the late Holocene, the record shows a return to drier conditions. The authors compare their results with the Insolation at 10 °N (August minus February) to get an estimate for the intensity of the annual cycle. An increased annual cycle is thought to cause higher precipitation [*Hastenrath* 1984]. Since the long term-changes are similar, the authors conclude that long-term changes in evaporation/ precipitation ratio are controlled in general by orbitally forced variations. However, direct orbital forcing alone can not

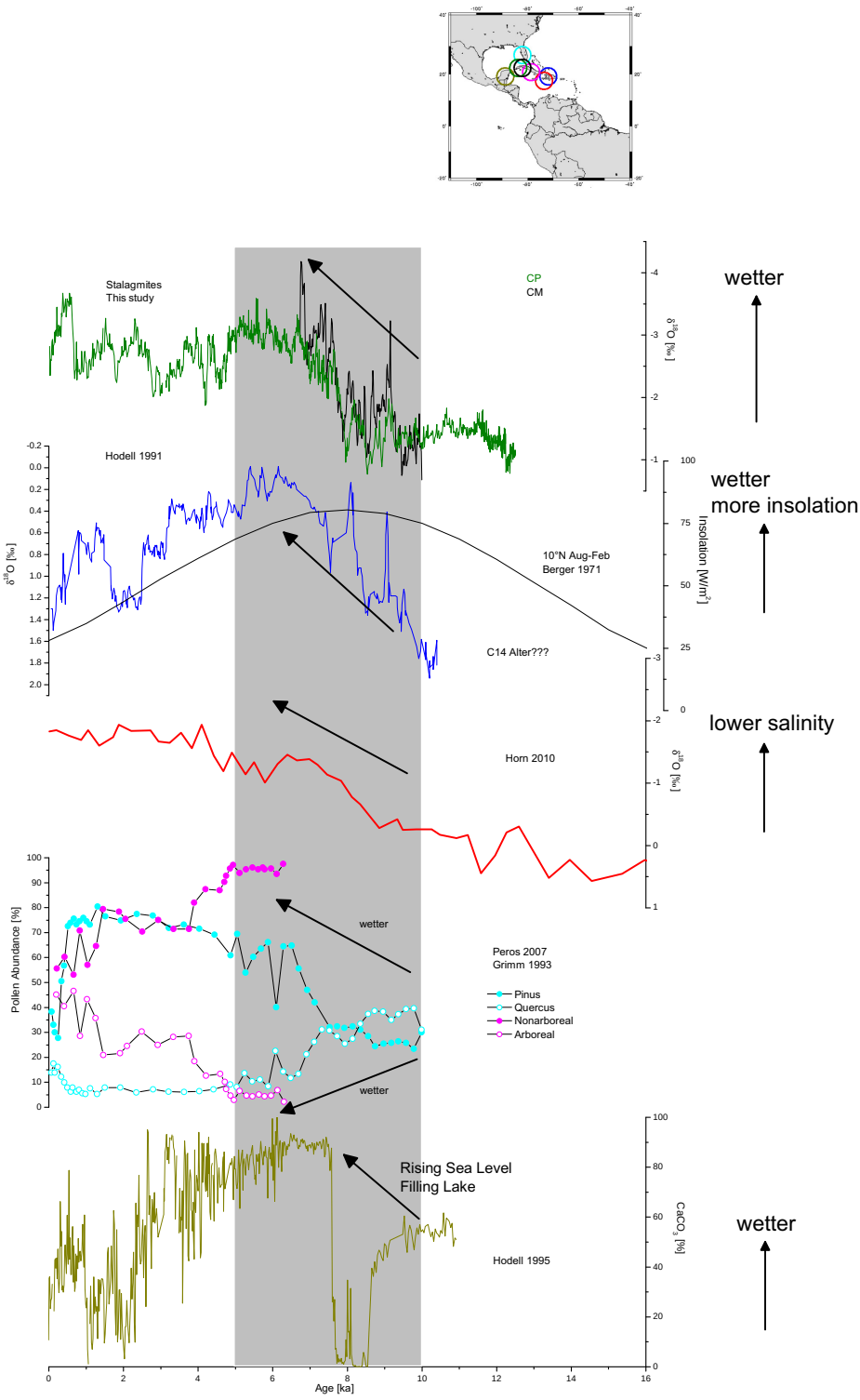

Figure 5.12: *Stalagmite $\delta^{18}O$ values in comparison with circum Caribbean records during the mid-Holocene (grey bar).*

explain the magnitude of rate of water-level change [*Hodell et al.* 1991]. The records of Cuba do not show a return to drier conditions at the late Holocene. Instead, they tend to stay at the same δ^{18}O level during the last 5 ka, on which several millennial scale patterns are superimposed. A possible explanation for this behavior is offered by a sediment record close to Haiti (*Horn* [2010], Fig. 5.12, red). Here, the δ^{18}O values of planktonic (surface) foraminifers are shown. Interestingly, the range in δ^{18}O values of 2.5 ‰ between early and late Holocene is the same as observed in the Cuban stalagmite. This could point to a possible connection to Caribbean sea surface δ^{18}O on orbital timescales. Cuba is relatively close to the source of precipitation, e. g. the North Atlantic and the Caribbean Sea. Therefore, if major transitions are observed in stalagmites, which are close to the source, it might indicate the importance of a investigation for those changes [*Lachniet* 2009a]. Interestingly, the change in surface δ^{18}O might be due to changes in upwelling, similar to the one observed in *deMenocal et al.* [2000], which might indicate a connection to West African SSTs. The transition was described already in Ch. 4.2 and characterized with an algorithm by *Mudelsee* [2000]. On the other hand, the sea surface δ^{18}O values do not show high variability during the last 5 ka, which indicates that the variability observed in CP is due to changes in precipitation amount during the last 5 ka and before the transition phase.

A further indicator for mid-Holocene climate change in the Caribbean area comes from pollen records from a sediment core from Lake Tulane, Florida [*Grimm et al.* 1993] (Fig. 5.12, cyan). Together with the sediment record Laguna de la Leche in central Cuba [*Peros et al.* 2007], both records indicate a near-synchronous initiation of wetter Pinus-dominated system in both locations at around 6.5 ka. *Peros et al.* [2007] argues that increasing wetness was caused by a decrease in insolation and an elevated sea level from the earlier to the later Holocene. However, based on the synchroneity of the events, the authors conclude that relative sea level rise could be a dominant cause of middle Holocene vegetation changes on sites around the south eastern United states. *Hodell et al.* [1995] provided a sediment record from Lake Chichancanab in Mexico. The estimated $CaCO_3$ record is also shown in Fig. 5.12 in dark-green. The authors note a generally wet phase between 3 and 6 ka. The conditions earlier then 6 ka were connected to sea level rise and lake filling.

5.9 8.2 ka event

In Greenland ice cores, the 8.2 ka event is the most pronounced Holocene climate anomaly. Air temperatures dropped by 6±2 ° and snow accumulation was reduced by 20 % [*Alley et al.* 1997]. This event is thought to have resulted from rapid drainage of a large volume of freshwater at a rate as high as 5.2 Sv (1 Sv = 10^6 m^3/s) from glacial lakes Agassiz and Ojibway to the North Atlantic Ocean via Hudson strait [*Clark et al.* 2002, *Barber et al.* 1999, *Teller et al.* 2002]. The freshwater influx is thought to have

inhibited the THC, cooled sea surface temperature by 1.5-3 ° and provoked regional climate changes. In Europe, temperatures decreased within 200 years and hydrological change was noted from northern Europe to North Africa [*von Grafenstein et al.* 1998, *Baldini et al.* 2002, *Magny and Bégeot* 2004]. In addition, atmospheric reorganizations are noted in palaeoclimatic records from North America [*Dean et al.* 2002]. In the tropics, *Gasse* [2000] noted low African lake levels.

Fig. 5.13 (green) shows the δ^{18}O signal of the Cuban stalagmite CP. The δ^{18}O values were deramped with the method explained in Ch. 4.2. The δ^{18}O values of CM are also shown in Fig. 5.13 (black) with a linear trend substracted to account for the mid-Holocene transition. The δ^{18}O values of both stalagmites show the lowest values in the time range around 8 ka, indicating drier conditions. In the Caribbean area, *Hughen et al.* [1996] denoted enhanced trade winds (s. Fig. 5.13, red) and *Lachniet et al.* [2004a] found drier conditions in Costa Rica captured by stalagmites δ^{18}O values (s. Fig. 5.13, orange). *Hillesheim et al.* [2005] also connected drier conditions in Guatemala with the 8.2 ka event (s. Fig. 5.13, blue). *Hodell et al.* [1995] also found drier conditions in a lake in Mexico measuring the δ^{18}O values of gastropods (s. Fig. 5.13, brown). For comparison, the Greenland ice core record is also shown in Fig. 5.13 (purple), indicated the colder conditions during this event.

Cheng et al. [2009] studied the 8.2 ka event in detail using stalagmite isotope records of China and Oman, which reveal a weak summer monsoon event, with a double-plunging structure that started at 8.21 $\pm$0.02 ka B.P. An identical, but antiphased pattern is also observed in two stalagmite records from eastern Brazil, indicating an intensified South American Summer Monsoon. The authors conclude that the 8.2 ka event can be tied in changes of the Atlantic Meridional Overturning circulation triggered by a lake draining event which can affect North Atlantic climate and latidudinal position of the ITCZ.

Lachniet et al. [2004a] interpret drier conditions in Costa Rica as a signal for a weaker Central American monsoon, which is possibly related to global atmospheric and /or oceanic reorganization during the 8.2 ka event. Strengthening of the trade winds and /or a southward displacement of the North Atlantic anticyclone would have resulted in decreased strength and /or southward displacement of the ITCZ [*Giannini et al.* 2000] (Section 3). This could explain the weakened trade winds in the western tropcial Atlantic [*Hughen et al.* 1996] and dry conditions [*Hastenrath* 1984]. If SSTs were reduced basin-wide at the 8.2 ka event, this also could lead to drier conditions in the Caribbean area [*Lachniet et al.* 2004a]. Colder SSTs were also noted in subtropical West Africa by *deMenocal et al.* [2000]. Cooler SSTs can also result in delayed onset and early end dates of the Caribbean rainy season [*Enfield and Alfaro* 1999] and may indirectly result in higher δ^{18}O values in the stalagmite data of *Lachniet et al.* [2004a] by temperature forcing of decreased rainout.

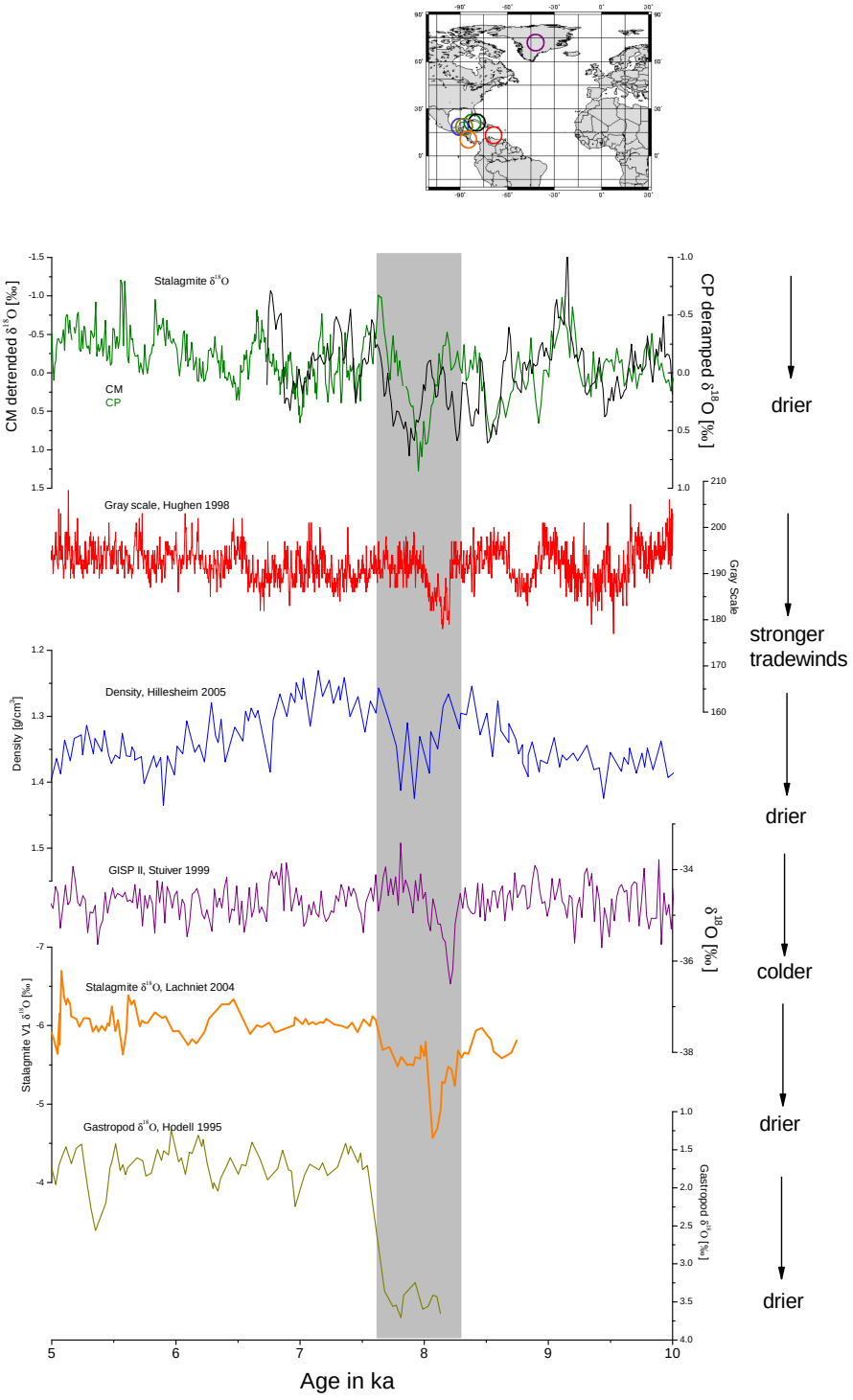

Figure 5.13: *Stalagmite $\delta^{18}O$ values in comparison with circum Caribbean records during the 8.2 ka event (grey bar). Drier conditions in Cuba coincide with stronger trade winds in Cariaco, drier conditions in Guatemala, colder conditions in the Northern Atlantic and drier conditions in Panama.*

5.10 Younger Dryas and Preboreal

During the last deglaciation, the Younger Dryas as a cold period have been recognized from records throughout the North Atlantic. The distribution of these records suggests, that changes were caused by a reorganization of the North Atlantic thermohaline circulation [*Hughen et al.* 1996]. Previous studies of the last glacial-to-interglacial cycle have reported similarities between climate change in the Caribbean and the high-latitude North Atlantic on a variety of timescales [*Hughen et al.* 1996, *Hillesheim et al.* 2005]. The most detailed records of the last deglaciation and Holocene in the Caribbean come from studies of laminated sediments in the Cariaco Basin off the coast of Venezuela [*Hughen et al.* 1996, *Haug et al.* 2001]. Fig. 5.14 shows a comparison between records from the Cariaco Basin and the developed δ^{18}O record of Cuba (CP) during the Younger Dryas. As shown in Section 4.1, the age control is given only back to 12.5 ka which justifies the cut off at 12.5 ka. The Younger Dryas ranges from ≈11.5 ka to 12.75 ka and depicts a cold period following the last deglaciation and Bølling Allerød warm period. The Cariaco record (Fig. 5.14, black, *Haug et al.* [2001]) shows the Titanium concentration of a sediment core. During the Younger Dryas cold period, low Titanium concentrations in the Cariaco Basin reflect a time of reduced precipitation which was also indicated over much of the tropical Atlantic [*Haug et al.* 2001]. The Cariaco record which is shown in purple *Hughen et al.* [1996] shows the grey scale of a sediment record. The colours have been interpreted to be a signal for the position of the ITCZ in connection with trade winds. When the ITCZ is farthest south (winter), rainfall is at a minimum and strong trade winds induce upwelling. When the ITCZ is more north (summer), the trade winds and upwelling diminishs. This results in annual deposition of a lighter-coloured plankton-rich layer followed by a darker-coloured terrigenous grain-rich layer [*Hughen et al.* 1996]. Lighter colours (lower numbers in colour scale) resemble stronger trade winds. The GISP2 δ^{18}O record from Greenland [*Stuiver et al.* 1995] is also plotted in Fig. 5.14 (black). The isotopic record shows temperature changes, lower δ^{18}O values correspond to lower temperatures. The δ^{18}O signal of CP is also shown in Fig. 5.14 (green). During the Younger Dryas cold period (s. GISP 2 record), Cuba shows up to 1 ‰ higher values than during the Preboreal. The drier conditions during the Younger Dryas were also found in the Cariaco record [*Haug et al.* 2001]. This corresponds also to stronger trade winds [*Hughen et al.* 1996].

The similarity of the four records indicate a common forcing mechanism between high-latitude North Atlantic and the Caribbean. *Hughen et al.* [1996] notes that a reduction of North Atlantic SST would result in increased annually averaged trade winds over the tropical North Atlantic. The authors conclude that shifts in the North Atlantic thermohaline circulation, in addition to causing observed changes in high-latitude records, could have influenced trade-wind strength in the tropical Atlantic and caused the productivity record in the Cariaco basin. In addition, the Titanium

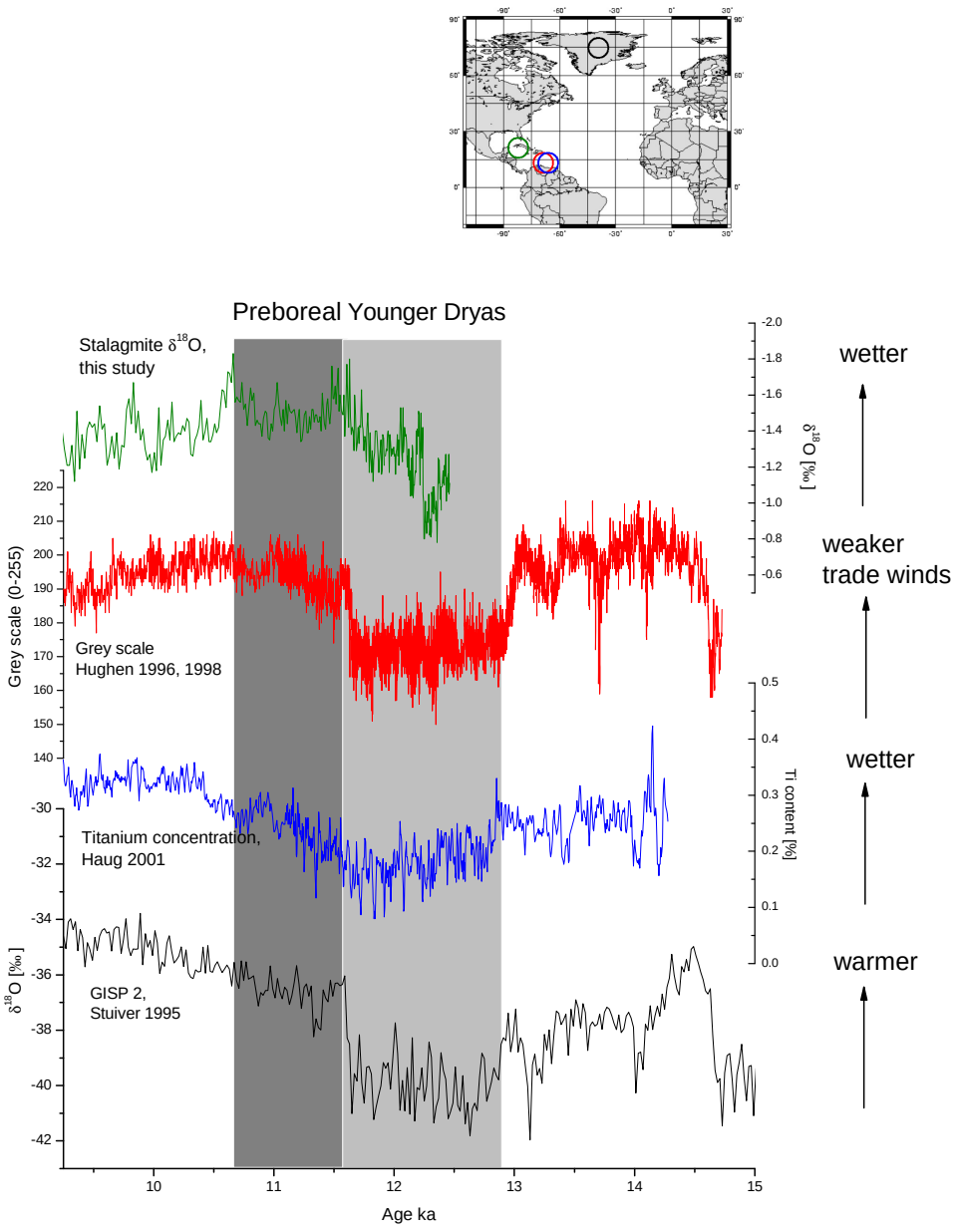

Figure 5.14: *Stalagmite $\delta^{18}O$ values in comparison with circum Caribbean and North Atlantic proxy records during the Younger Dryas (light grey)-Preboreal (dark grey) transition.*

record of the Cariaco basin [*Haug et al.* 2001] shows low metal concentrations which indicates a time of reduced precipitation. The authors note that the record reflects the mean latitudinal position of the ITCZ causing both more precipitation and less trade wind driven upwelling in the Cariaco region. During the Younger Dryas, the ITCZ is therefore thought to be in a more southern position than during Preboreal. The change from drier to wetter conditions after the Younger Dryas is also found in Cuba which can be explained by the more southward ITCZ.

5.11 Summary

Three stalagmite records from Cuba were studied to reconstruct past climate variability in the Northern Caribbean. The stalagmites were dated by U-series dating methods (MC-ICPMS and TIMS). Stalagmite CG grew during the last 1.3 ka, CP during the last 12.5 ka and the Holocene slice of CM grew during 7 and 10 ka. As climate proxy, stable isotopes such as δ^{18}O and δ^{13}C are studied.

- **Precipitation reconstruction**
  Observations and climate models show that the amount effect is the dominant influence on δ^{18}O values in rainfall. More rainfall in the Caribbean leads to lower δ^{18}O values in precipitation. This signal was shown to be transferred through the soil into the cave, lower δ^{18}O values were observed in cave drip waters during the second rainfall season. In addition, it has been shown that a correlation exists between recorded stalagmite δ^{18}O values and observational rainfall amounts, also indicating lower δ^{18}O values in times of more rainfall. Therefore, the recorded δ^{18}O values in stalagmites can be interpreted as past changes in precipitation amount.

- **North Atlantic influence**
  The influence of North Atlantic SSTs on Caribbean precipitation was shown to be found in observations as well as in climate models. Higher North Atlantic SSTs lead to more precipitation in Cuba. This could be due to a stronger thermohaline circulation and a more northward ITCZ in this region. Stalagmite CG as well as CP show a connection to North Atlantic SSTs. The connection of CG to a AMO reconstruction shows that higher SSTs in the North Atlantic are connected to lower δ^{18}O values on centennial and multidecadal timescales. Frequency analysis of CG suggests a variability of 220 a and 80 a. The 80 a variability is in agreement with observed variability in the AMO signal. During the MCA, CG reveals lower δ^{18}O values (wetter conditions) and vice versa for the LIA. The same connection to North Atlantic SSTs was found in stalagmite CP indicating millennial scale variability connected to the Bond cycles. However, the frequency analysis in this stalagmite is not sufficient to find the exact 1500 a cycle. Strong cold events in the Northern Atlantic such as the 8.2 ka event and the Younger Dryas are also connected to a less strong THC and drier conditions in Cuba. The orbital variability of CP is shown to be connected to the source δ^{18}O.

- **Solar influence**
  The solar influence in the Caribbean area was studied by the comparison of the δ^{18}O signal of CG with cosmogenic (^{14}C) production rates. The comparison does not reveal a clear connection during extreme solar minima (Maunder, Spörer and Wolf minima) on centennial timescales. However, a possible connection to solar

variability is discussed on North Atlantic SSTs on millennial timescales (Bond cycles), with higher solar activity leading to higher SSTs and wetter conditions in Cuba.

- **Pacific influence**
  During a Pacific El Niño event, the Caribbean was shown to experience both a drier than average followed by a wetter than average rainy season on a seasonal timescale. Results from climate models indicate higher δ^{18}O values in precipitation due to drier conditions in the Caribbean. Hence, also the two Cuban records are possibly connected to Pacific variability.

This study in general emphasizes that climate variability in the Caribbean area is highly complex. Several processes in both oceanic basins, Atlantic and Pacific, influence precipitation patterns in the Caribbean area.

6 Conclusions and Outlook

In this study, three stalagmite records from North Western Cuba were studied to reconstruct past climate variability in the Northern Caribbean. All stalagmites were dated by U-series dating methods, MC-ICPMS and TIMS, and a new correction method was established to account for detrital contamination in stalagmite CG and CP. Stalagmite CG grew during the last 1.3 ka, CP during the last 12.5 ka and the Holocene slice of CM between 7 and 10 ka. As a climate indicator, stable isotopes such as δ^{18}O and δ^{13}C were studied. It has been shown that higher precipitation in Cuba leads to lower δ^{18}O values in precipitation due to the amount effect. This signal is also transmitted through the soil zone, lower δ^{18}O values in stalagmites reflecting wetter conditions. δ^{18}O values recorded in stalagmites can therefore be interpreted as past changes in precipitation.

It has been shown that the reconstructed climate of the Northern Caribbean has a variability of 220 a and 80 a, especially between 0.8 and 1 ka ago. Initially, this suggests a *solar forcing* of Caribbean precipitation, the solar Suess/de Vries and Gleissberg cycle. However, the connection to solar variability was shown to be non-steady, especially weak solar activity such as the Maunder-, Spörer- and Wolf-Minima can not be connected to especially dry or wet phases in Cuba. However, the Cuban record exhibits a good correlation with an *Atlantic Multidecadal Oscillation (AMO)* record, which indicates a connection to Atlantic SSTs during the last 1.3 ka. This can be explained in the context of variability in the *thermohaline circulation (THC)*. In a positive AMO phase, model results as well as observations show similar changes: the *inner-tropical convergence zone (ITCZ)* is in a more northern position and this leads to higher precipitation in the Caribbean, with higher SSTs leading to a higher degree of evaporation on the sea surface, more convection and more precipitation over Cuba, which is well reflected in stalagmite CG during the last 1.3 ka.

Similar results were found by comparing the second stalagmite CP, which grew during the whole Holocene, to records from the Northern Atlantic. North Atlantic cold events (*Bond-events*), which exhibit a variability of 1500 a, could be connected to drier conditions as recorded in the Cuban stalagmite. Again, this can be explained with a less strong thermohaline circulation during North Atlantic cold events. This was also shown for Atlantic cold events, such as the *8.2 ka event*, and the cold *Younger Dryas* phase. On orbital timescales, the δ^{18}O trend of CP shows a connection to another marine surface δ^{18}O record, indicating an influence of the *source* $\delta^{18}O$ on the CP record.

In addition, observations also show a variability in Cuban precipitation which is

connected with the *El Niño-Southern Oscillation (ENSO)*. A comparison of an ENSO record reveals strong connection to drier conditions in CG and CP during El Niño phases in the past. ENSO is thought to lead to a more southward ITCZ in the Pacific region and to less rainfall in the Northern Caribbean. However, the connection between Atlantic SST anomalies and Pacific SST anomalies is not clear at this point. Possible explanation for the observed dry conditions in Cuba during the Holocene could be a less strong thermohaline circulation from the Atlantic side. This could infer changes in the Pacific region, allowing the ITCZ in a more northward position which enhances ENSO variability. The thermohaline circulation therefore could be a possible driver of ENSO variability during the Holocene on millennial timescales. However, if ENSO variability is seen as an independent oscillator, the connection to the Atlantic sector can also lead to changes in the THC. Further records are needed to investigate this possible link between THC and ENSO, especially from the ENSO region.

From this study further prospects can be drawn out: MC-ICPMS offers high resolution datings and should be used for future dating of Cuban stalagmites, especially very young and low Uranium samples. High resolution trace elements profiles might give further climatic information. Thinsections and high resolution XRD analysis are needed to better quantify the transition from aragonite to calcite. Longer monitoring programs are desirable for a proper estimate of the transfer function between stable isotopes in rainfall and stable isotopes in stalagmites.

The results observed in this study contribute to the understanding of Caribbean climate variability. The past Caribbean climate variability during the Holocene was shown to vary on several timescales ranging from multidecadal to millennial. The Holocene climate is shown to be highly variable. For a further understanding of the role of anthropogenic influence on climate, the Holocene results will be compared to the last Interglacial in the following project CaribClim II. Furthermore, the comparison with model results promises a deeper understanding of the variability on several timescales, revealing more precise information about possible source effects.

7 Supplementary data

Supplementary Table 1: ^{230}Th/U results for stalagmite CG measured with MC-ICPMS

Distance from top	^{238}U	^{232}Th	(^{230}Th/^{232}Th)	(^{230}Th/^{238}U)	(^{234}U/^{238}U)	Age uncorrected	Age corrected with (^{238}U/^{232}Th)=0.8±0.2	Age corrected with (^{238}U/^{232}Th)=8±4
[mm]	[ng/g]	[ng/g]	measured activity ratios			[ka b2k]	[ka b2k]	[ka b2k]
13	135.2 ±0.5	0.7393 ±0.0021	6.50 ±0.05	0.01160 ±0.00010	2.345 ±0.004	0.534 ±0.005	0.467 ±0.034	[0; 0.110]
27	135.5 ±0.5	0.1815 ±0.0014	11.56 ±0.10	0.00507 ±0.00004	2.342 ±0.004	0.227 ±0.002	0.211 ±0.008	0.067 +0.070 -0.067
135	136.2 ±0.5	0.0318 ±0.0004	79.81 ±1.24	0.00610 ±0.00010	2.361 ±0.004	0.273 ±0.004	0.270 ±0.004	0.246 ±0.015
215	124.1 ±0.4	0.0385 ±0.0003	93.57 ±1.08	0.00950 ±0.00010	2.360 ±0.004	0.431 ±0.005	0.427 ±0.005	0.394 ±0.019
340	104.8 ±0.4	0.0352 ±0.0006	127.18 ±3.41	0.01399 ±0.00031	2.363 ±0.004	0.639 ±0.015	0.635 ±0.015	0.599 ±0.024
395	134.4 ±0.5	0.0343 ±0.0003	198.40 ±1.86	0.01656 ±0.00014	2.360 ±0.004	0.759 ±0.007	0.756 ±0.007	0.729 ±0.017
540	91.4 ±0.3	0.1367 ±0.0016	54.71 ±0.67	0.02676 ±0.00023	2.347 ±0.004	1.242 ±0.011	1.224 ±0.014	1.064 ±0.089
595	90.6 ±0.3	0.0147 ±0.0001	438.97 ±3.46	0.02328 ±0.00016	2.302 ±0.004	1.100 ±0.008	1.098 ±0.008	1.080 ±0.013
665	99.1 ±0.4	0.0285 ±0.0003	271.78 ±2.63	0.02554 ±0.00023	2.266 ±0.004	1.227 ±0.011	1.224 ±0.011	1.192 ±0.022
712	101.4 ±0.3	0.0194 ±0.0002	438.07 ±5.93	0.02750 ±0.00030	2.247 ±0.004	1.332 ±0.015	1.330 ±0.015	1.309 ±0.021

Supplementary Table 2: $^{230}Th/U$ results for stalagmite CG measured with TIMS

Distance from top	^{238}U	^{232}Th	$(^{230}Th/^{232}Th)$	$(^{230}Th/^{238}U)$	$(^{234}U/^{238}U)$	Age uncorrected	Age corrected with $(^{238}U/^{232}Th)=0.8\pm0.2$	Age corrected with $(^{238}U/^{232}Th)=8\pm4$
[mm]	[ng/g]	[ng/g]	measured activity ratios			[ka b2k]	[ka b2k]	[ka b2k]
40	199.3 ±0.4	0.31652 ±0.00570	9.6 ±0.9	0.0050 ±0.0005	2.349 ±0.007	0.227 ±0.022	0.208 ±0.022	0.038 +0.07 -0.38
80	184.7 ±0.4	0.05784 ±0.00174	44.0 ±6.7	0.0045 ±0.0007	2.340 ±0.008	0.204 ±0.031	0.201 ±0.031	0.167 ±0.032
118	154.3 ±0.3	0.00588 ±0.00006	301.2 ±24.9	0.0038 ±0.0003	2.342 ±0.007	0.169 ±0.015	0.169 ±0.015	0.165 ±0.015
179	126.7 ±0.3	0.05356 ±0.00080	74.1 ±5.9	0.0103 ±0.0008	2.335 ±0.007	0.475 ±0.038	0.470 ±0.038	0.424 ±0.042
260	136.2 ±0.3	0.01059 ±0.00008	574.4 ±21.1	0.0146 ±0.0005	2.378 ±0.007	0.666 ±0.025	0.665 ±0.025	0.657 ±0.025
305	142.3 ±0.3	0.04312 ±0.00074	132.9 ±5.5	0.0132 ±0.0005	2.402 ±0.007	0.595 ±0.022	0.591 ±0.023	0.559 ±0.029
376.5	147.5 ±0.2	0.02325 ±0.00034	297.8 ±24.5	0.0154 ±0.0012	2.341 ±0.008	0.713 ±0.059	0.711 ±0.058	0.694 ±0.058
470	131.8 ±0.1	0.00824 ±0.00009	1147.5 ±59.9	0.0235 ±0.0012	2.339 ±0.004	1.194 ±0.057	1.194 ±0.056	1.087 ±0.057
520	130.9 ±0.3	0.06297 ±0.00063	150.0 ±9.3	0.0236 ±0.0014	2.348 ±0.007	1.096 ±0.067	1.091 ±0.068	1.039 ±0.069
616	121.6 ±0.2	0.13238 ±0.00225	85.5 ±4.3	0.0305 ±0.0014	2.285 ±0.008	1.458 ±0.070	1.444 ±0.070	1.325 ±0.091

650	121.2 ±0.2	0.01477 ±0.00014	655.3 ±45.6	0.0261 ±0.0018	2.259 ±0.008	1.262 ±0.090	1.260 ±0.088	1.247 ±0.087
720	116.2 ±0.2	0.06888 ±0.00103	164.8 ±10.0	0.0320 ±0.0019	2.253 ±0.008	1.552 ±0.091	1.545 ±0.095	1.479 ±0.096

Analytical errors are at 95% confidence levels.

All ratios are activity ratios as indicated by parantheses.

All ages are given relative to the year 2000 (ka b2k).

The degree of detrital ^{230}Th contamination is indicated by the measured (^{230}Th/^{232}Th).

$$\left(\frac{^{230}Th}{^{238}U}\right)_A(T)=(1-e^{-\lambda_{230}T})+\left(\left(\frac{^{234}U}{^{238}U}\right)(T)-1\right)\frac{\lambda_{230}}{\lambda_{230}-\lambda_{234}}(1-e^{-(\lambda_{230}-\lambda_{234})T})$$ where T is the age of the sample.

Supplementary Table 3: ^{230}Th/U results for stalagmite CM measured with TIMS

Distance from top [mm]	δU [‰]	^{238}U [µg/g]	^{232}Th [ng/g]	^{230}Th [pg/g]	Age uncorrected [ka]	Age corrected with (^{238}U/^{232}Th) =0.8 [ka]
2.5	508.146 ±13.267	0.09109 ±0.00012	0.0140 ±0.0003	0.149 ±0.016	7.442 ±0.816	7.439 ±0.836
13	443.858 ±7.788	0.10281 ±0.00010	0.0672 ±0.0010	0.179 ±0.010	8.324 ±0.461	8.311 ±0.473
20	473.123 ±5.145	0.08575 ±0.00007	0.1718 ±0.0009	0.176 ±0.004	9.679 ±0.240	9.640 ±0.238
30	426.618 ±17.997	0.09770 ±0.00017	0.0630 ±0.0007	0.326 ±0.014	16.720 ±0.821	16.707 ±0.805
55	402.304 ±8.968	0.15801 ±0.00017	0.2714 ±0.0024	0.548 ±0.020	17.770 ±0.726	17.735 ±0.723
80	434.458 ±5.782	0.21494 ±0.00043	0.5121 ±0.0025	1.154 ±0.015	27.992 ±0.435	27.945 ±0.434
135	452.935 ±8.367	0.18152 ±0.00036	0.2676 ±0.0022	1.196 ±0.023	34.821 ±0.810	34.792 ±0.791
145	531.468 ±6.043	0.24079 ±0.00014	0.4489 ±0.0035	1.704 ±0.022	35.511 ±0.557	35.477 ±0.553
210	385.876 ±12.642	0.09831 ±0.00020	0.5032 ±0.0027	0.822 ±0.012	49.093 ±1.036	48.991 ±1.046
380	404.568 ±9.017	0.10091 ±0.00020	0.0953 ±0.0005	1.125 ±0.024	69.813 ±2.116	69.794 ±2.096
460	481.794 ±8.382	0.09048 ±0.00007	0.3551 ±0.0024	1.127 ±0.016	75.119 ±1.654	75.048 ±1.650
477	489.240 ±3.684	0.26524 ±0.00016	0.3637 ±0.0022	3.422 ±0.035	78.296 ±1.154	78.272 ±1.156
490	485.678 ±2.419	2.21624 ±0.00066	0.5119 ±0.0029	29.140 ±0.189	80.695 ±0.758	80.691 ±0.753
520	513.654 ±3.236	0.27223 ±0.00011	1.0854 ±0.0035	3.706 ±0.038	82.436 ±1.219	82.367 ±1.199

Supplementary Table 4: ^{230}Th/U results for stalagmite CP measured with TIMS

Distance from top [mm]	δU [‰]	^{238}U [µg/g]	^{232}Th [ng/g]	^{230}Th [pg/g]	Age uncorrected [ka b2k]	Age corrected with (^{238}U/^{232}Th) =0.8±0.2 [ka b2k]	Age corrected with (^{238}U/^{232}Th) =8±4 [ka b2k]
5	3979.08 ±6.24	6.0869 ±0.0037	19.645 ±0.140	4.13 ±0.08	0.904 ±0.02	0.886 ±0.02	0.723 ±0.09
25	3692.12 ±10.64	4.0689 ±0.0069	41.023 ±0.303	6.54 ±0.12	2.295 ±0.04	2.233 ±0.05	1.694 ±0.28
50	3687.91 ±8.39	5.4508 ±0.0044	26.784 ±0.096	16.48 ±0.09	4.360 ±0.03	4.330 ±0.03	4.069 ±0.12
76	3744.28 ±17.77	2.5900 ±0.0026	39.246 ±0.391	9.42 ±0.11	5.202 ±0.06	5.111 ±0.07	4.314 ±0.38
81	3820.08 ±8,69	3.7957 ±0.0038	21.709 ±0.070	17.19 ±0.07	6.398 ±0.03	6.364 ±0.03	6.070 ±0.13
100	3739.56 ±6.16	3.5679 ±0.0018	40.808 ±0.127	16.19 ±0.06	6.526 ±0.03	6.458 ±0.04	5.857 ±0.27
130	3776.02 ±4.51	4.2583 ±0.0021	3.307 ±0.015	21.42 ±0.19	7.196 ±0.07	7.191 ±0.07	7.151 ±0.07
149	3503.85 ±21.64	1.5452 ±0.0015	33.688 ±1.077	9.02 ±0.16	8.906 ±0.17	8.770 ±0.18	7.567 ±0.53
165	3366.61 ±8.24	3.1096 ±0.0031	60.340 ±0.308	21.2 ±0.16	10.802 ±0.09	10.677 ±0.10	9.579 ±0.45
185	3359.41 ±8.00	5.04488 ±0.0045	45.359 ±0.862	36.90 ±1.04	11.646 ±0.34	11.589 ±0.34	11.082 ±0.4
206	3341.55 ±13.32	6.0216 ±0.0060	8.325 ±0.242	44.63 ±0.45	11.860 ±0.13	11.851 ±0.13	11.773 ±0.14
235	3501.85 ±10.84	3.2308 ±0.0052	0.426 ±0.004	25.91 ±0.29	12.395 ±0.15	12.395 ±0.15	12.387 ±0.15
249	3589.69 ±9.85	0.3989 ±0.0004	14.216 ±0.037	4.75 ±0.03	18.416 ±0.14	18.201 ±0.15	16.304 ±0.77
265	3528.18 ±11.85	1.1241 ±0.0021	15.111 ±0.073	13.00 ±0.12	18.129 ±0.19	18.047 ±0.19	17.327 ±0.35
290	3481.49 ±12.69	0.7795 ±0.0016	25.535 ±0.110	8.09 ±0.07	16.338 ±0.16	16.135 ±0.18	14.342 ±0.71
300	3438.17 ±12.36	0.4696 ±0.0005	29.005 ±0.119	5.73 ±0.10	19.606 ±0.37	19.222 ±0.39	15.793 ±1.44
315	3411.33 ±9.08	0.5705 ±0.0006	4.334 ±0.026	6.55 ±0.09	18.494 ±0.26	18.446 ±0.26	18.029 ±0.3
330	3475.90 ±6.65	0.9261 ±0.0005	8.091 ±0.020	10.84 ±0.07	18.596 ±0.14	18.542 ±0.14	18.070 ±0.23
360	3491.92 ±8.52	2.3121 ±0.0014	29.050 ±0.320	21.70 ±0.38	14.655 ±0.27	14.577 ±0.28	13.893 ±0.38
400	3402.62 ±12.15	1.4428 ±0.0027	15.986 ±0.053	13.97 ±0.10	15.469 ±0.13	15.399 ±0.13	14.785 ±0.27

Supplementary Table 5: ^{230}Th/U results for stalagmite CP measured with MC-ICPMS

Distance from top [mm]	δU [‰]	^{238}U [µg/g]	^{232}Th [ng/g]	^{230}Th [pg/g]	Age uncorrected [ka b2k]	Age corrected with (^{238}U/^{232}Th) =0.8±0.2 [ka b2k]	Age corrected with (^{238}U/^{232}Th) =8±4 [ka b2k]
9	3951.33 ±8.95	13.289 ±0.155	22.21 ±0.29	9.14 ±0.10	0.921 ±0.02	0.911 ±0.01	0.827 ±0.05
13	3714.49 ±4.18	3.379 ±0.141	128.01 ±5.32	5.69 ±0.24	2.396 ±0.14	2.158 ±0.11	0.128 + 1.26 - 0.12
22	3451.69 ±7.28	6.549 ±0.074	17.07 ±0.23	10.93 ±0.12	2.514 ±0.04	2.497 ±0.02	2.351 ±0.08
38	3767.31 ±7.79	3.807 ±0.030	30.95 ±0.23	10.24 ±0.08	3.806 ±0.05	3.757 ±0.03	3.331 ±0.21
70	3720.46 ±7.92	9.902 ±0.113	43.57 ±0.49	37.27 ±0.41	5.411 ±0.09	5.385 ±0.03	5.153 ±0.14
88	3813.29 ±4.21	4.118 ±0.162	76.20 ±2.98	17.38 ±0.68	5.963 ±0.33	5.837 ±0.05	4.894 ±0.55
98	3604.00 ±7.62	9.951 ±0.109	57.49 ±0.66	46.01 ±0.51	6.853 ±0.11	6.817 ±0.04	6.506 ±0.18
113	3767.19 ±3.93	4.823 ±0.197	19.64 ±0.80	23.85 ±0.98	7.082 ±0.42	7.038 ±0.03	6.846 ±0.43
143	3687.86 ±8.19	2.541 ±0.026	23.51 ±0.24	13.57 ±0.14	7.803 ±0.12	7.747 ±0.05	7.257 ±0.24
155	3318.06 ±116.11	1.273 ±0.036	15.17 ±0.17	6.61 ±0.07	8.247 ±0.34	8.169 ±0.32	7.484 ±0.43
159	3430.14 ±3.69	2.182 ±0.086	88.93 ±3.20	14.01 ±0.51	10.000 ±0.55	9.721 ±0.11	7.443 ±1.14
172	3302.92 ±7.48	3.452 ±0.037	42.05 ±0.44	24.32 ±0.29	11.355 ±0.19	11.276 ±0.07	10.579 ±0.33
242	3559.24 ±10.52	0.329 ±0.004	1.37 ±0.02	3.48 ±0.04	16.359 ±0.29	16.334 ±0.10	16.113 ±0.3
271	3485.30 ±8.41	2.563 ±0.028	10.26 ±0.14	29.93 ±0.32	18.504 ±0.30	18.479 ±0.10	18.264 ±0.32
337	3400.88 ±7.10	1.543 ±0.017	41.79 ±0.42	16.88 ±0.19	17.625 ±0.30	17.454 ±0.11	15.950 ±0.66
350	3437.36 ±8.40	1.844 ±0.022	11.71 ±0.16	19.12 ±0.25	16.493 ±0.32	16.453 ±0.09	16.106 ±0.34
375	3501.64 ±8.39	1.744 ±0.021	24.37 ±0.35	17.85 ±0.24	16.026 ±0.31	15.940 ±0.09	15.183 ±0.42
385	3484.15 ±8.84	1.212 ±0.011	2.68 ±0.03	12.69 ±0.12	16.480 ±0.23	16.466 ±0.08	16.347 ±0.24

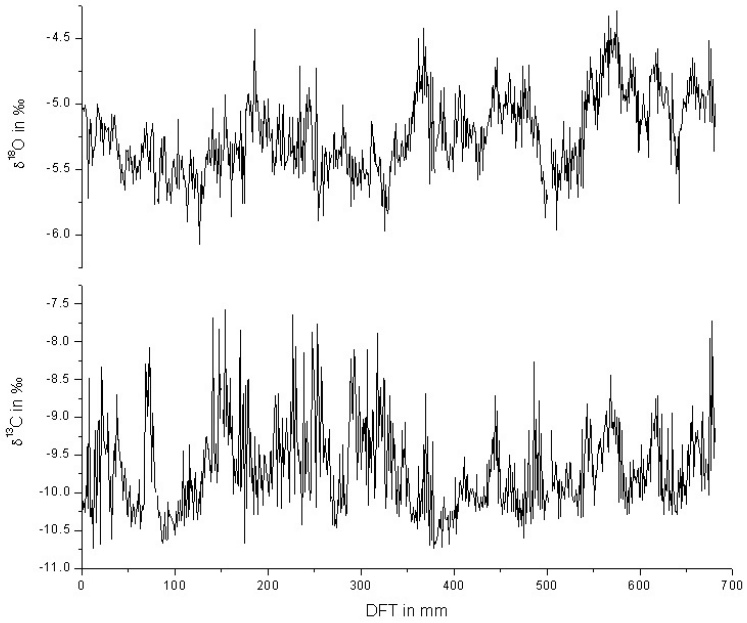

Figure 7.1: *Measured isotopes versus distance from top for stalagmite Cuba Grande.*

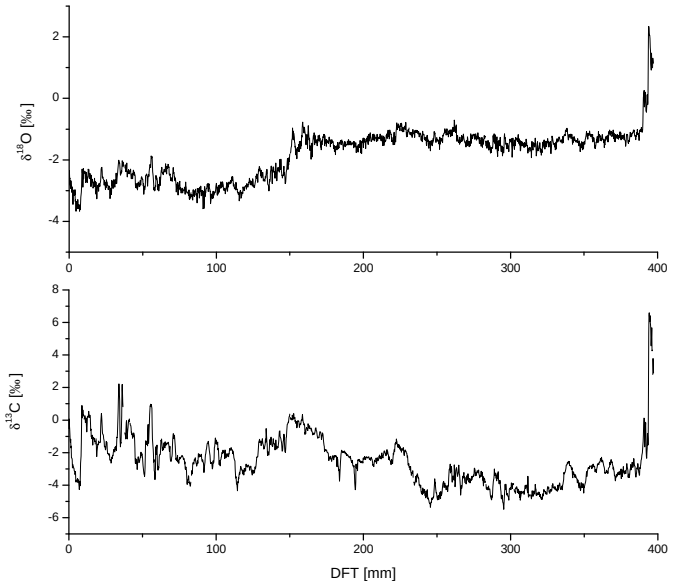

Figure 7.2: *Measured isotopes versus distance from top for stalagmite Cuba Pequeño.*

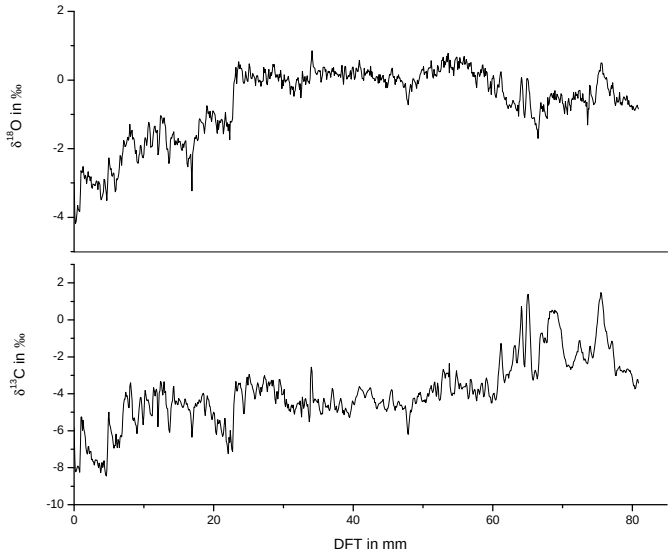

Figure 7.3: *Measured isotopes versus distance from top for stalagmite Cuba Medio.*

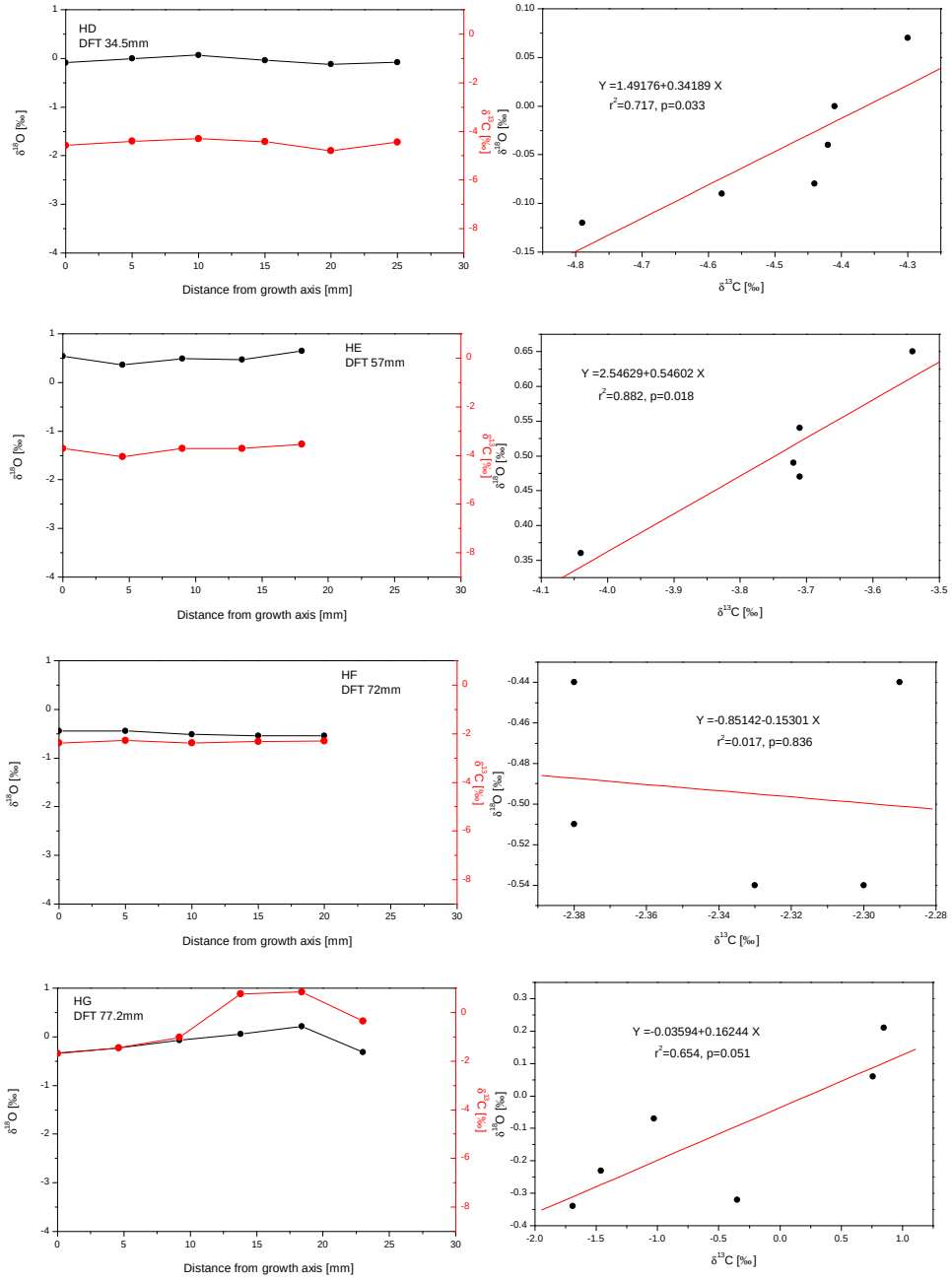

Figure 7.4: *Additional Hendy tests of CM.*

Supplementary Table 6: XRD results for stalagmite CP.

Distance from top	Calcite content	Aragonite content	Quartz content
[mm]	[%]	[%]	[%]
42	9.6	83.3	7.2
75	57	38.3	4.7
123	91.5	7.4	1.1
148	53.3	44.4	2.3
178	92.8	0.9	6.2
197	99.2	0	0.8
220	83 (EVA) 70 (Rietveld)	17 (EVA) 30 (Rietveld)	0
230	83.9	16.1	0
240	100	0	0
250	100	0	0
271	100	0	0
280	100	0	0
291	100	0	0
298	100	0	0
315	100	0	0
325	100	0	0
330	100	0	0
340	100	0	0
345	100	0	0
355	100	0	0
370	100	0	0
380	100	0	0
390	100	0	0
397	100	0	0

Supplementary Table 7: OES results for stalagmite CP.

Distance from top [mm]	Mg*1000/Ca [weight ratio]	Sr*1000/Ca [weight ratio]
7	0.3	1.1
10	1	1.21
28	1.9	1.18
41	0.7	1.32
51	0.4	1.21
56	3	1.22
66	2.8	1.29
80	9.9	0.66
95	2.6	1.26
110	1.5	1.26
114	2.3	1.07
130	2.7	1.18
153	0.6	1.47
170	3	1.13
178	3.1	1.04
223	2.1	1.16
229	2.4	1.22
243	13.9	0.12
253	13.6	0.18
273	12.7	0.27
293	12.4	0.35
323	13.7	0.19
355	10	0.4
370	7.7	0.87
371	10.1	0.43
395	15	0.25

Supplementary table 8: Monitoring program.

Dripsite	Datum	Drip rate [ml/min]	$\delta^{18}O$ [$^{o}/_{oo}$]	Air temperature [°C]	Relative Humidity [%]
DAC01O	19.02.08	0	-	21.3	98
	29.04.08	0	-	21.4	98
	25.06.08	0	-	21.3	98
	02.08.08	0	-	21.4	99
	14.10.08	2.5	-4.48	21.4	99
	30.12.08	1.3	-4.36	21.4	97
DAC01A	19.02.08	5	-3.88	21.4	100
			-3.69		
	29.04.08	-	-	-	-
	25.06.08	78	-3.77	21.5	99
	02.08.08	18	-3.8	21.4	100
	14.10.08	1200	-5.41	21.4	100
	30.12.08	-	-	-	-
DAC02O	19.02.08	0	-	21.4	99
	29.04.08	0	-	21.4	99
	25.06.08	-	-3.52	21.5	99
	02.08.08	-	-3.69	21.4	100
	14.10.08	-	-4.77	21.4	100
	30.12.08	-	-2.8	21.4	99
DAC02A	19.02.08	-	-	-	-
	29.04.08	0.3	-0.82	21.3	96
	25.06.08	-	-	-	-
	02.08.08	-	-	-	-
	14.10.08	-	-	-	-
	30.12.08	-	-	-	-
STCO	19.02.08	0	-	21.9	99
	29.04.08	0	-	21.8	98
	25.06.08	-	-2.09	21.8	98
	02.08.08	-	-2.4	21.9	99
	14.10.08	0.1	-4.63	21.8	98
	30.12.08	-	-3.05	21.6	97
STCA	19.02.08	-	-1.14	21.9	99
			-1.13		
	29.04.08	-	-2.36	21.8	98
			-1.23		
	25.06.08	-	-	21.8	98
	02.08.08	-	-	21.9	99
	14.10.08	-	-	21.8	98
	30.12.08	-	-	21.6	97

References

Alley, R. B., P. A. Mayewski, T. Sowers, M. Stuiver, K. C. Taylor, and P. U. Clark (1997). Holocene climate instability: A prominent, widespread event 8200 years ago. *Geology,* Vol. 25, 483–486.

Amador, J. A. (1998). A climatic feature of the tropical Americas: the trade wind easterly jet. *Tópicos Meteorológicos y Oceanográficos,* Vol. 5, 91–102.

Amador, J. A. and V. Magaña (1999). Dynamics of the low-level jet over the Caribbean Sea. In *23rd Conference on Hurricanes and Tropical Meteorology*, Volume 5, pp. 868–869. Dallas, TX: American Meteorological Society.

Baldini, J. U. L., F. McDermott, and I. J. Fairchild (2002). Structure of the 8200 year cold event revealed by a speleothem trace element record. *Science,* Vol. 296, 2203–2206.

Barber, D. C., A. Dyke, C. Hillaire-Marcel, A. E. Jennings, J. T. Andrews, M. W. Kerwin, G. Bilodeau, R. McNeely, J. Southon, M. D. Morehead, and J. Gagnon (1999). Forcing of the cold event of 8,200 years ago by catastrophic drainage of Laurentide lakes. *Nature,* Vol. 400, 344–348.

Bard, E., G. Raisbeck, F. Yiou, and J. Jouzel (2000). Solar irradiance during the last 1200 years based on cosmogenic nuclides. *Tellus Series B-Chemistry Physics Meteorology,* Vol. 52, 985–992.

Battisti, D. S. and A. C. Hirst (1989). Interannual variability in a tropical atmosphere ocean model-influence of the basic state, ocean geometry and nonlinearity. *Journal of Atmospheric Sciences,* Vol. 46, 1687–1712.

Beck, J. W., D. A. Richards, R. L. Edwards, B. W. Silverman, P. L. Smart, D. J. Donahue, S. Hererra-Osterheld, G. S. Burr, L. Calsoyas, A. J. T. Jull, and D. Biddulph (2001). Extremely large variations of atmospheric C-14 concentration during the last glacial period. *Science,* Vol. 292, 2453–2458.

Berger, A. (1978). Long-term variations of daily insolation and Quaternary climate changes. *Journal of Atmospheric Sciences,* Vol. 35, 2362–2367.

Bianchi, G. G. and I. N. McCave (1999). Holocene periodicity in North Atlantic climate and deep-ocean flow south of Iceland. *Nature,* Vol. 397, 515.

Bjerknes, J. (1964). Atlantic air-sea interaction. In *Advances in geophysics*, pp. 1–82. New York: Academic Press.

Bjerknes, J. (1969). Atmospheric teleconnections from the equatorial Pacific. *Monthly Weather Review,* Vol. 97, 163–172.

Black, D. E., M. A. Abahazi, R. C. Thunell, A. Kaplan, E. J. Tappa, and L. C. Peterson (2007). An 8-century tropical Atlantic SST record from the Cariaco Basin: Baseline variability, twentieth-century warming, and Atlantic hurricane frequency. *Paleoceanography,* Vol. 22, PA4204.

Black, D. E., L. C. Peterson, J. T. Overpeck, A. Kaplan, M. N. Evans, and M. Kashgarian (1999). Eight Centuries of North Atlantic Ocean Atmosphere Variability. *Science,* Vol. 286, 1709.

Black, D. E., R. C. Thunell, A. Kaplan, L. C. Peterson, and E. J. Tappa (2004). A 2000-year record of Caribbean and tropical North Atlantic hydrographic variability. *Paleoceanography,* Vol. 19, PA2022.

Bond, G., B. Kromer, J. Beer, R. Muscheler, M. N. Evans, W. Showers, S. Hoffmann, R. Lotti-Bond, I. Hajdas, and G. Bonani (2001). Persistent solar influence on North Atlantic climate during the Holocene. *Science,* Vol. 294, 2130–2136.

Bond, G., W. Showers, M. Cheseby, R. Lotti, P. Almasi, P. deMenocal, P. Priore, H. Cullen, I. Hajdas, and G. Bonani (1997). A Pervasive Millennial-Scale Cycle in North Atlantic Holocene and Glacial Climates. *Science,* Vol. 278, 1257.

Bourdon, B., S. P. Turner, G. M. Henderson, and C. C. Lundstrom (2003). Introduction to U-series geochemistry. In B. Bourdon, G. M. Henderson, C. C. Lundstrom, and S. P. Turner (Eds.), *Uranium-series Geochemistry.* Washington, DC: Mineralogical Society of America.

Brand, U. and J. Veizer (1983). Origin of coated grains: trace element constraints. In T. M. Peryt (Ed.), *Coated Grains*, pp. 9–26. Berlin: Springer-Verlag.

Briffa, K. R., P. D. Jones, T. S. Bartholin, D. Eckstein, F. H. Schweingruber, W. Karlén, P. Zetterberg, and M. Eronen (1992). Fennoscandian summers from ad 500: temperature changes on short and long timescales. *Climate Dynamics,* Vol. 7, 111.

Cane, M. A. (2005). The evolution of El Niño, past and future. *Earth and Planetary Science Letters,* Vol. 230, 227–240.

Charles, C. D., J. Rind, J. Jouzel, R. D. Koster, and R. G. Fairbanks (1994). Glacial-interglacial changes in moisture sources for Greenland: Influences on the ice core record of climate. *Science,* Vol. 263, 508–511.

Chen, A. A. and M. Taylor (2002). Investigating the link between early season Caribbean rainfall and the El Niño + 1 year. *International Journal of Climatology,* Vol. 22, 87–106.

Cheng, H., D. Fleitmann, R. Lawrence Edwards, X. Wang, F. W. Cruz, A. S. Auler, A. Mangini, Y. Wang, X. Kong, S. J. Burns, and A. Matter (2009). Timing and structure of the 8.2 kyr B.P. event inferred from δ^{18}O records of stalagmites from China, Oman, and Brazil. *Geology,* Vol. 37, No. 11, 1007–1010.

Cheng, W., C. M. Bitz, and J. C. H. Chiang (2007). Adjustment of the global climate to an abrupt slowdown of the Atlantic meridional overturning circulation. In A. Schmittner, J. C. H. Chiang, and S. Hemming (Eds.), *Past and Future Changes of the Ocean's Meridional Overturning Circulation: Mechanisms and Impacts.* Washington, DC: Academic Press.

Chiang, J. C. H. (2009). The Tropics in Palaeoclimate. *Annual Reviews Earth and Planetary Sciences,* Vol. 37, 263–297.

Chiang, J. C. H., W. Cheng, and C. M. Bitz (2008). Fast teleconnections to the tropical Atlantic sector from Atlantic thermohaline adjustment. *Geophysical Research Letters,* Vol. 35, L07704.

Clark, I. and P. Fritz (1997). *Environmental Isotopes in Hydrology.* New York: Lewis Publishers.

Clark, P. U., N. G. Pisias, T. F. Stocker, and A. J. Weaver (2002). The role of the thermohaline circulation in abrupt climate change. *Nature,* Vol. 415, 863–869.

Clement, A. C., R. Seager, and M. A. Cane (2000). Suppression of El Niño during the mid-Holocene by changes in the Earth's orbit. *Paleoceanography,* Vol. 15, 731–737.

Cobb, K. M., C. D. Charles, H. Cheng, and R. L. Edwards (2003). El Niño/Southern Oscillation and tropical Pacific climate during the last millennium. *Nature,* Vol. 424, 271.

Cole, J. E., D. Rind, R. S. Webb, J. Jouzel, and R. Healy (1999). Climatic controls on interannual variability of precipitation δ^{18}O: Simulated influence of temperature, precipitation amount, and vapor source region. *Journal of Geophysical Research,* Vol. 104, 14223–14235.

Cubasch, U., R. Voss, G. C. Hegerl, J. Wazskewitz, and T. J. Crowley (1997). Simulation of the influence of solar radiation variations on the global climate with an ocean-atmosphere general circulation model. *Climate Dynamics,* Vol. 13, 757–767.

Curtis, J., D. A. Hodell, and M. Brenner (1996). Climate variability on the Yucatan Peninsula (Mexico) during the past 3500 yr, and implications for Maya cultural evolution. *Quaternary Research,* Vol. 46, 37–47.

Dansgaard, W. (1964). Stable isotopes in precipitation. *Tellus,* Vol. 16, 438–468.

Dean, W. E., R. M. Forester, and J. P. Bradbury (2002). Early Holocene change in atmospheric circulation in the Northern Great Plains: An upstream view of the

8.2 ka cold event. *Quaternary Science Reviews,* Vol. 21, 1763–1775.

Debret, M., D. Sebag, X. Crosta, N. Massei, J.-R. Petit, E. Chapron, and V. Bout-Roumazeilles (2009). Evidence from wavelet analysis for a mid-Holocene transition in global climate forcing. *Quaternary Science Reviews,* Vol. 28, 2675–2688.

Delworth, T. L., S. Manabe, and R. J. Stouffer (1993). Interdecadal variations of the thermohaline circulation in a coupled ocean-atmopshere model. *Journal of Climate,* Vol. 6, 1993–2011.

Delworth, T. L., S. Manabe, and R. J. Stouffer (1997). Multidecadal climate variability in the Greenland Sea and surrounding regions: a coupled model simulation. *Geophysical Research Letters,* Vol. 24, 257–260.

Delworth, T. L. and M. E. Mann (2000). Observed and simulated multideadal variability in the Northern Hemisphere. *Climate Dynamics,* Vol. 16, 661–676.

deMenocal, P., J. Ortiz, T. Guilderson, and M. Sarnthein (2000). Coherent High- and Low-Latitude Climate Variability During the Holocene Warm Period. *Science,* Vol. 288, 2198–2202.

Dickson, R., J. Lazier, J. Meincke, P. Rhines, and J. Swift (1996). Long-term coordinated changes in the convective activity of the North Atlantic. *Progress in Oceanography,* Vol. 38, 241–295.

Dong, B. W. and R. T. Sutton (2002). Adjustment of the coupled ocean-atmosphere system to a sudden change in the Thermohaline Circulation. *Geophysical Research Letters,* Vol. 29, 1728.

Dong, B. W., R. T. Sutton, and A. A. Scaife (2006). Multidecadal modulation of El Niño-Southern Oscillation (ENSO) variance by Atlantic Ocean sea surface temperatures. *Geophysical Research Letters,* Vol. 33, L08705.

Donnelly, J. P. and J. D. Woodruff (2007). Intense hurricane activity over the past 5,000 years controlled by El Niño and the West African monsoon. *Nature,* Vol. 447, 465–468.

Dorale, J. A., R. L. Edwards, E. Ito, and L. A. Gonzales (1998). Climate and vegetation history of the midcontinent from 75 to 25 ka: a speleothem record from Crevice Cave, Missouri, USA. *Science,* Vol. 282, 1871–1874.

Dreybrodt, W. (1988). *Processes in Karst Systems.* Berlin: Springer.

Dreybrodt, W. (1999). Chemical kinetics, speleothem growth and climate. *Boreas,* Vol. 28, 347–356.

Enfield, D. B. (1996). Relationship of inter-American rainfall to tropical Atlantic and Pacific SST variability. *Gephysical Research Letters,* Vol. 23, 3305–3308.

Enfield, D. B. and E. J. Alfaro (1999). The dependence of Caribbean rainfall on the interaction of the tropical Atlantic and Pacific Oceans. *Journal of Climate,* Vol. 12, 2093–2103.

Enfield, D. B., A. M. Mestas-Nuñez, and P. J. Trimble (2001). The Atlantic multidecadal oscillation and its relation to rainfall and river flows in the continental US. *Geophysical Research Letters,* Vol. 28, 2077–2080.

Fairchild, I. J., C. L. Smith, A. Baker, L. Fuller, C. Spötl, D. Mattey, F. McDermott, and E. I. M. F. (2006). Modification and preservation of environmental signals in speleothems. *Earth-Science Reviews,* Vol. 75, 105–153.

Fairchild, I. J. and P. C. Treble (2009). Trace elements in speleothems as recorders of environmental change. *Quaternary Science Reviews,* Vol. 28, 449–4680.

Fensterer, C., D. Scholz, D. Hoffmann, A. Mangini, and J. M. Pajón (2010). ^{230}Th/U-dating of a late Holocene low uranium speleothem from Cuba. *IOP Conf. Series: Earth and Environmental Science,* Vol. 9, 012015.

Finnigan (2004). Finnigan Neptune Hardware Manual. Technical report, Thermo Electron GmbH.

Fleitmann, D., S. J. Burns, U. Neff, M. Mudelsee, A. Mangini, and A. Matter (2004). Palaeoclimatic interpretation of high-resolution oxygen isotope profiles derived from annually laminated speleothems from southern Oman. *Quaternary Science Reviews,* Vol. 23, 935–945.

Folland, C. K., A. W. Colman, D. P. Rowell, and M. K. Davey (2001). Predictability of northeast Brazil rainfall and real-time forecast skill, 1987-98. *Journal of Climate,* Vol. 14, 1937–1958.

Folland, C. K., D. E. Parker, and T. N. Palmer (1986). Sahel rainfall and worldwide sea temperatures, 1901-85. *Nature,* Vol. 320, 602–607.

Friedman, I., J. R. O'Neil, and M. Fleischer (1977). Compilation of stable isotope fractionation factors of geochemical interest. *U. S. Geological Survey Professional Paper,* Vol. P0440-KK, 12.

Frisia, S., A. Borsato, I. J. Fairchild, F. McDermott, and E. M. Selmo (2002). Aragonite-calcite relationships in speleothems (Grotte De Clamouse, France): environment, fabrics, and carbonate geochemistry. *Journal of Sedimentary Research,* Vol. 72, 687–699.

Gamble, D. W., D. B. Parnell, and S. Curtis (2008). Spatial variability of the Caribbean mid-summer drought and relation to north Atlantic high circulation. *International Journal of Climatology,* Vol. 28, 343–350.

Gasse, F. (2000). Hydrological changes in the African tropics since the last glacial maximum. *Quaternary Science Reviews,* Vol. 19, 189–211.

George, S. E. and M. A. Saunders (2001). North Atlantic Oscillation impact on tropical north Atlantic winter atmospheric variability. *Geophysical Research Letters,* Vol. 28, 1015–1018.

Giannini, A., Y. Kushnir, and M. A. Cane (2000). Interannual Variability of Caribbean Rainfall, ENSO, and the Atlantic Ocean. *Journal of Climate,* Vol. 13, 297–311.

Giannini, A., Y. Kushnir, and M. A. Cane (2001a). Interdecadal Changes in the ENSO Teleconnection to the Caribbean Region and the North Atlantic Oscillation. *Journal of Climate,* Vol. 14, 2867–2879.

Giannini, A., Y. Kushnir, and M. A. Cane (2001b). Seasonality in the impact of ENSO and the North Atlantic High on Caribbean Rainfall. *Physics and Chemistry of the Earth (B),* Vol. 28, No. 2, 143–147.

Goldenberg, S. B., C. W. Landsea, A. M. Mestas-Nuñez, and W. M. Gray (2001). The recent increase in Atlantic hurricane activity: Causes and implications. *Science,* Vol. 293, 474–479.

Goldenberg, S. B. and L. J. Shapiro (1996). Physical mechanism for the association of El Niño and West African rainfall with major hurricane activity. *Journal of Climate,* Vol. 9, 1169–1187.

Gonfiantini, R., M.-A. Roche, J.-C. Olivry, J.-C. Fontes, and G. M. Zuppi (2001). The altitude effect on the isotopic composition of tropical rains. *Chemical Geology,* Vol. 181, 147–167.

Gonzalez, L. A. and K. C. Lohmannn (1988). Controls on mineralogy and composition of spelean carbonates: Carlsbad Caverns, New Mexico. In N. P. James and P. W. Choquette (Eds.), *Paleokarst*, pp. 81–101.

Grabczak, J., J. Niewodniczanski, and K. Rozanski (1983). Isotope stratification in high mountain glaciers: Examples from the Peruvian Andes and Himalaya. *Journal of Glaciology,* Vol. 29, 417–424.

Granger, O. E. (1985). Caribbean climates. *Progress in Physical Geography,* Vol. 9, No. 1, 16–43.

Gray, S. T., L. J. Graumlich, J. L. Betancourt, and G. T. Pederson (2004). A tree-ring based reconstruction of the Atlantic Multidecadal Oscillation since 1567 A.D. *Geophysical Research Letters,* Vol. 31, L12205.

Gray, W. M. (1968). Global view of the origin of tropical disturbances and storms. *Monthly Weather Review,* Vol. 96, 669–700.

Grimm, E., G. L. Jacobson Jr., W. A. Watts, B. C. S. Hansen, and K. A. Maasch (1993). A 50,000-year record of climate oscillations from Florida and its temporal correlation with the Heinrich events. *Science,* Vol. 216, 198–200.

Haigh, J. (1996). The Impact of Solar Variability on Climate. *Science,* Vol. 272, 981–984.

Hastenrath, S. (1976). Variations in low-latitude circulation and extreme climatic events in the tropical Americas. *Journal of Atmospheric Science,* Vol. 33, 20–215.

Hastenrath, S. (1978). On the modes of tropical circulation and anomalies. *Journal of Atmospheric Science,* Vol. 35, 22220–22231.

Hastenrath, S. (1984). Interannual variability and annual cycle: Mechanisms of circulation and climate in the tropical Atlantic sector. *Monthly Weather Review,* Vol. 112, 1097–1107.

Haug, G. H., D. Günther, L. C. Peterson, D. M. Sigman, K. A. Hughen, and B. Aeschlimann (2001). Southward Migration of the Intertropical Convergence Zone Through the Holocene. *Science,* Vol. 293, 1304.

Haug, G. H., D. Günther, L. C. Peterson, D. M. Sigman, K. A. Hughen, and B. Aeschlimann (2003). Climate and the Collapse of Maya Civilization. *Science,* Vol. 299, 1731.

Heegaard, E., H. J. B. Birks, and R. J. Telford (2005). Relationships between calibrated ages and depth in stratigraphical sequences: an estimation procedure by mixed-effect regression. *The Holocene,* Vol. 15, No. 4, 612–618.

Hellstrom, J. C. (2006). U-Th dating of speleothems with high initial ^{230}Th using stratigraphical constraint. *Quaternary Geochronology,* Vol. 1, 289–295.

Henderson-Sellers, A. and P. J. Robinson (1986). *Contemporary Climatology.* Essex (UK): Longman.

Hendy, C. H. (1971). The isotopic geochemistry of speleothems - I. The calculation of the effects of different modes of formation on the isotopic composition of speleothems and their applicability as paleoclimatic indicators. *Geochimica et Cosmochimica Acta,* Vol. 35, 801–824.

Hillesheim, M. B., D. A. Hodell, B. W. Leyden, M. Brenner, J. H. Curtis, F. S. Anselmetti, D. Ariztegui, D. G. Buck, T. P. Guilderson, M. F. Rosenmeier, and D. W. Schnurrenberger (2005). Climate change in lowland Central America during the late deglacial and early Holocene. *Journal of Quaternary Science,* Vol. 20, 363–376.

Hodell, D., M. Brenner, J. H. Curtis, and T. Guilderson (2001). Solar forcing of drought frequency in the Maya Lowlands. *Science,* Vol. 292, 1367–1369.

Hodell, D., J. H. Curtis, and M. Brenner (1995). Possible role of climate in the collapse of Classic Maya civilization. *Nature,* Vol. 375, 391–394.

Hodell, D., J. H. Curtis, G. A. Jones, A. Higuera-Gundy, M. Brenner, M. W. Binford, and K. T. Dorsey (1991). Reconstruction of Caribbean climate change over the

past 10,500 years. *Nature,* Vol. 352, 790–793.

Hodell, D. A., F. S. Anselmetti, D. Ariztegui, M. Brenner, J. H. Curtis, A. Gilli, D. A. Grzesik, T. J. Guilderson, A. D. Müller, M. B. Bush, A. Correa-Metrio, J. Escobar, and S. Kutterolf (2008). An 85-ka record of climate change in lowland Central America. *Quaternary Science Reviews,* Vol. 27, 1152–1165.

Hodell, D. A., M. Brenner, and J. H. Curtis (2005a). Terminal Classic drought in the northern Maya lowlands inferred from multiple sediment cores in Lake Chichancanab (Mexico). *Quaternary Science Reviews,* Vol. 24, 1413–1427.

Hodell, D. A., M. Brenner, J. H. Curtis, R. Medina-González, E. I.-C. Can, A. Albornaz-Pat, and T. P. Guilderson (2005b). Climate change on the Yucatan Peninsula during the Little Ice Age. *Quaternary Research,* Vol. 63, 109–121.

Hoffmann, D. L. (2008). ^{230}Th isotope measurements of femtogram quantities for U-series dating using multi ion counting (MIC) MC-ICPMS. *International Journal of Mass Spectrometry,* Vol. 275, 75–79.

Hoffmann, D. L., J. Prytulak, D. A. Richards, T. Elliot, C. D. Coath, P. L. Smart, and D. Scholz (2007). Procedures for accurate U and Th isotope measurements by high precision MC-ICPMS. *International Journal of Mass Spectrometry,* Vol. 264, 97–109.

Holzkämper, S. (2004). *Dating and Interpretation of Secondary Carbonate Deposits from the Last Interglacial.* Ph. D. thesis, Heidelberg Academy of Sciences, Heidelberg.

Holzkämper, S., K. Holmgren, J. Lee-Thorp, S. Talma, A. Mangini, and T. Partridge (2009). Late Pleistocene stalagmite growth in Wolkberg Cave, South Africa. *Earth and Planetary Science Letters,* Vol. 282, 212–221.

Horn, C. (2010). *Spatial variations of the phaseshift between ocean surface warming, evaporation and changes of continental ice volume at terminations I and II.* Ph. D. thesis, IFM-GEOMAR, Leibniz Institute for Marine Sciences, Kiel. In prep.

Huang, Y. and I. J. Fairchild (2001). Partitioning of Sr^{2+} and Mg^{2+} into calcite under karst-analogue experimental conditions. *Geochimica et Cosmochimica Acta,* Vol. 65, 47–62.

Hughen, K., J. T. Overpeck, L. C. Peterson, and S. E. Trumbore (1996). Rapid climate changes n the tropical Atlantic during the last deglaciation. *Nature,* Vol. 380, 51–54.

Hurrell, J. W., Y. Kushnir, G. Ottersen, and M. Visbeck (2003). An overview of the North Atlantic Oscillation. The North Atlantic Oscillation: Climatic Significance and Environmental Impact. *Geophysical Monograph,* Vol. 134, 1–35. American Geophysical Union.

Hurrell, J. W., M. Visbeck, A. Buslacchi, R. A. Clarke, T. L. Delworth, R. R. Dickson, W. E. Johns, K. P. Koltermann, Y. Kushnir, D. Marshall, C. Mauritzen, M. S. McCartney, A. Piola, C. Reason, G. Reverdin, F. Schott, R. Sutton, I. Wainer, and D. Wright (2006). Atlantic Climate Variability and Predictability: A CLIVAR Perspective. *Journal of Climate,* Vol. 19, 5100–5121.

IAEA/WMO (2006). Global Network of Isotopes in Precipitation. The GNIP Database. Accessible at: http://www.iaea.org/water.

IPCC (2007). *Climate Change 2007: The Physical Science Basis. Contribution of Working Group I to the Fourth Assessment Report of the Intergovernmental Panel on Climate Change*. Cambridge, United Kingdom and New York, NY, USA: Cambridge University Press. Solomon, S., D. Qin, M. Manning, Z. Chen, M. Marquis, K. B. Averyt, M. Tignor and H. L. Miller (Eds.).

Ivanovich, M. and R. S. Harmon (1993). *Uranium Series Disequilibrium: Applications to Environmental Problems*. Oxford: Clarendon Press.

Jevrejeva, S., J. C. Moore, and A. Grinsted (2003). Influence of the Arctic Oscillation and El Niño-Southern Oscillation (ENSO) on ice conditions in the Baltic Sea: The wavelet approach. *Journal of Geophysical Research,* Vol. 108, No. D21, 4677.

Jones, I. C., J. L. Banner, and J. D. Humphrey (2000). Estimating recharge in a tropical karst aquifer. *Water Resources Research,* Vol. 36, 1289–1299.

Jones, P. D., K. Briffa, T. Osborn, J. Lough, T. van Ommen, B. Vinther, J. Luterbacher, E. Wahl, F. Zwiers, M. Mann, G. Schmidt, C. Ammann, B. Buckley, K. Cobb, J. Esper, H. Goosse, N. Graham, E. Jansen, T. Kiefer, C. Kull, M. Küttel, E. Mosley-Thompson, J. Overpeck, N. Riedwyl, M. Schulz, A. Tudhope, R. Villalba, H. Wanner, E. Wolff, and E. Xoplaki (2009). High-resolution palaeoclimatology of the last millennium: a review of current status and future prospects. *The Holocene,* Vol. 19, No. 1, 3–49.

Jury, M., B. A. Malmgren, and A. Winter (1997). Implications of summertime seas level pressure anomalies in the tropical Atlantic region. *Journal of Climate,* Vol. 10, 789–804.

Jury, M., B. A. Malmgren, and A. Winter (2007). Subregional precipitation climate of the Caribbean and relationships with ENSO and NAO. *Journal of Geophysical Research,* Vol. 112, D16107.

Jury, M. R. (2009). An interdecadal American rainfall mode. *Journal of Geophysical Research,* Vol. 114, D08123.

Kalnay, E., M. Kanamitsu, R. Kistler, W. Collins, D. Deaven, L. Gandin, M. Iredell, S. Saha, G. White, J. Woollen, Y. Zhu, A. Leetmaa, R. Reynolds, M. Chelliah, W. Ebisuzaki, W. Higgins, J. Janowiak, K. C. Mo, C. Ropelewski, J. Wang,

R. Jenne, and D. Joseph (1996). The NCEP/NCAR 40-year reanalysis project. *Bulletin of American Meteorological Society,* Vol. 77, 437–470.

Kaufmann, G. (2003). Stalagmite growth and palaeo-climate: the numerical perspective. *Earth and Planetary Science Letters,* Vol. 214, 521–266.

Keigwin, L. D. (1996). The Little Ice Age and Medieval Warm Period in the Sargasso Sea. *Science,* Vol. 274, 1504.

Kerr, R. A. (2000). A North Atlantic climate pacemaker for the centuries. *Science,* Vol. 288, 1984–1985.

Kerr, R. A. (2005). Atlantic Climate Pacemaker for Millennia Past, Decades Hence? *Science,* Vol. 309, No. 5731, 41–43.

Kim, S.-T. and J. R. O'Neil (1997). Equilibrium and nonequilibrium oxygen isotope effects in synthetic carbonates. *Geochimica et Cosmochimica Acta,* Vol. 61, 3461–3475.

Kim, S.-T., J. R. O'Neil, C. Hillaire-Marcel, and A. Mucci (2007). Oxygen isotope fractionation between synthetic aragonite and water: influence of temperature and Mg^{2+} concentration. *Geochimica et Cosmochimica Acta,* Vol. 71, 4704–4715.

Knight, J. R., R. J. Allan, C. K. Folland, M. Vellinga, and M. E. Mann (2005). A signature of persistent natural thermohaline circulation cycles in observed climate. *Geophysical Research Letters,* Vol. 32, L20708.

Knight, J. R., C. K. Folland, and A. A. Scaife (2006). Climate impacts of the Atlantic Multidecadal Oscillation. *Geophysical Research Letters,* Vol. 33, L17706.

Knudsen, M. F., P. Riisager, B. H. Jacobsen, R. R. Muscheler, I. Snowball, and M.-S. Seidenkrantz (2009). Taking the pulse of the Sun during the Holocene by joint analysis of ^{14}C and ^{10}Be. *Geophysical Research Letters,* Vol. 36, L16701.

Kushnir, Y., Y. Tourre, and B. Rajagopalan (1997). Decadal and multidecadal variability in Atlantic SST and sea level pressure. *Proceedings of the Atlantic Climate Variability Meeting,*, 24–26 September. Lamont Doherty Earth Observatory, Columbia University.

Lachniet, M. S. (2009a). Climatic and environmental controls on speleothem oxygen-isotope values. *Quanernary Science Reviews,* Vol. 28, 412–432.

Lachniet, M. S. (2009b). Sea surface temperature control on the stable isotopic composition of rainfall in Panama. *Geophysical Research Letters,* Vol. 36, L03701.

Lachniet, M. S., Y. Asmerom, S. J. Burns, W. P. Patterson, V. J. Polyak, and G. O. Seltzer (2004a). Tropical response to the 8200 yr B.P. cold event? Speleothem isotopes indicate a weakened early Holocene monsoon in Costa Rica. *Geology,* Vol. 32, 957–960.

Lachniet, M. S., S. J. Burns, D. R. Piperno, Y. Asmerom, V. J. Polyak, C. M. Moy, and K. Christenson (2004b). A 1500-year El Niño/Southern Oscillation and rainfall history for the Isthmus of Panama from speleothem calcite. *Journal of Geophysical Research,* Vol. 109, D20117.

Lachniet, M. S. and W. P. Patterson (2006). Use of correlation and multiple stepwise regression to evaluate the climatic controls on the stable isotope values of Panamanian surface waters. *Journal of Hydrology,* Vol. 324, 115–140.

Lachniet, M. S. and W. P. Patterson (2009c). Oxygen isotope values of precipitation and surface waters in northern Central America (Belize and Guatemala) are dominated by temperature and amount effects. *Earth and Planetary Science Letters,* Vol. 284, 435–446.

Lea, D. W., P. A. Martin, D. K. Pak, and H. J. Spero (2002). Reconstructing a 350 ky history of sea level using planktonic Mg/Ca and oxygen isotope records from a Cocos Ridge core. *Quanernary Science Reviews,* Vol. 21, 283–293.

Lean, J. and D. Rind (1998). Climate forcing by changing solar radiation. *Journal of Climate,* Vol. 11, 3069–3094.

Li, W., J. Lundberg, A. P. Dickin, D. C. Ford, H. P. Schwarcz, R. McNutt, and D. Williams (1989). High precision mass-spectrometric uranium-series dating of cave deposits and implications for palaeoclimate studies. *Nature,* Vol. 339, 534–536.

Ludwig, K. R. and D. M. Titterington (1994). Calculation of ^{230}Th/U isochrons, ages, and errors. *Geochimica et Cosmochimica Acta,* Vol. 58, 5031–5042.

Magny, M. and C. Bégeot (2004). Hydrological changes in the European midlatitudes associated with freshwater outbursts from Lake Agassiz during the Younger Dryas event and the early Holocene. *Quaternary Research,* Vol. 61, 181–192.

Malmgren, B. A., A. Winter, and D. Chen (1998). El Niño-Southern Oscillation and North Atlantic Oscillation control of Caribbean climate. *Journal of Climate,* Vol. 11, 2713–2717.

Mangini, A., P. Blumbach, P. Verdes, C. Spötl, D. Scholz, H. Machel, and S. Mahon (2007). Combined records from a stalagmite from Barbados and from lake sediments in Haiti reveal variable seasonality in the Caribbean between 6.7 and 3 ka BP. *Quaternary Science Reviews,* Vol. 26, 1332–1342.

Mangini, A., C. Spötl, and P. Verdes (2005). Reconstruction of temperature in the Central Alps during the past 2000 yr from a δ^{18}O stalagmite record. *Earth and Planetary Science Letters,* Vol. 235, 741–751.

Mann, M. E., M. A. Cane, S. E. Zebiak, and A. Clement (2005). Volcanic and Solar Forcing of the Tropical Pacific over the Past 1000 Years. *Journal of Climate,* Vol. 18, 447.

Mann, M. E., Z. Zhang, S. Rutherford, R. S. Bradley, M. K. Hughes, D. Shindell, C. Ammann, G. Faluvegi, and F. Ni (2009). Global Signatures and Dynamical Origins of the Little Ice Age and Medieval Climate Anomaly. *Science,* Vol. 326, 1256.

Martis, A., G. J. van Oldenborgh, and G. Burgers (2002). Predicting rainfall in the Dutch Caribbean-More than El Niño? *International Journal of Climatology,* Vol. 22, 1219–1234.

Mayewski, P. A., E. E. Rohling, J. C. Stager, W. Karlén, K. A. Maasch, L. D. Meeker, E. A. Meyerson, F. Gasse, S. van Kreveld, K. Holmgren, J. Lee-Thorp, G. Rosqvist, F. Rack, M. Staubwasser, R. R. Schneider, and E. J. Steig (2004). Holocene climate variability. *Quaternary Research,* Vol. 62, 243–255.

McCabe, G. J., M. A. Palecki, and J. L. Betancourt (2004). Pacific and Atlantic Ocean influences on multidecadal drought frequency in the United States. *Proceedings of the National Academy of Sciences, U.S.A.,* Vol. 101, 4136–4141.

McDermott, F. (2004). Palaeo-climate reconstruction from stable isotope variations in speleothems: a review. *Quaternary Science Reviews,* Vol. 23, 901–918.

McMillan, E. A., I. J. Fairchild, S. Frisia, A. Borsato, and F. McDermott (2005). Annual trace element cycles in calcite-aragonite speleothems: evidence of drought in the western Mediterranean 1200-1100 yr BP. *Journal of Quarternary Science,* Vol. 20, No. 5, 423–433.

Medina-Elizalde, M., S. J. Burns, D. W. Lea, Y. Asmerom, L. von Gunten, V. Polyak, M. Vuille, and A. Karmalkar (2010). High resolution stalagmite climate record from the Yucatán Peninsula spanning the Maya terminal classic period. *Earth and Planetary Science Letters,* Vol. 298, 255–262.

Mestas-Nuñez, A., D. B. Enfield, and C. Zhang (2007). Water vapor fluxes over the Intra-Americas Sea: seasonal and interannual variability and associations with rainfall. *Journal of Climate,* Vol. 20, No. 9, 1910–1922.

Mestas-Nuñez, A., C. Zhang, and D. B. Enfield (2005). Uncertainties in estimating moisture fluxes over the Intra-Americas sea. *Journal of Hydrometeorology,* Vol. 6, 696–709.

Mühlinghaus, C., D. Scholz, and A. Mangini (2007). Modelling stalagmite growth and δ^{13}C as a function of drip interval and temperature. *Geochimica et Cosmochimica Acta,* Vol. 71, 2780–2790.

Mickler, P. J., L. A. Stern, and J. L. Banner (2006). Large kinetic isotope effects in modern speleothems. *Geological Society of America Bulletin,* Vol. 118, 65–81.

Morse, J. W. and F. T. MacKenzie (1990). *Geochemistry of Sedimentary Carbonates.* Amsterdam: Elsevier.

Moy, C. M., G. O. Seltzer, D. T. Rodbell, and D. M. Anderson (2002). Variability of El Niño/Southern oscillation activity at millennial timescales during the Holocene epoch. *Nature,* Vol. 420, 162–165.

Mudelsee, M. (2000). Ramp function regression: a tool for quantifying climate transitions. *Computers & Geosciences,* Vol. 26, 293–307.

Muscheler, R., F. Joos, S. A. Mueller, and . Snowball (2005). How unusual is today's solar activity? *Nature,* Vol. 436, E3–E4.

Musgrove, M., J. L. Banner, L. E. Mack, D. M. Combs, E. W. James, H. Cheng, and R. L. Edwards (2001). Geochronology of late Pleistocene to Holocene speleothems from central Texas: implications for regional paleoclimate. *Geological Society of America Bulletin,* Vol. 113, 1532–1543.

Mysak, L. and S. A. Venegas (1998). Decadal climate oscillations in the Arctic: A new feedback loop for atmosphere-ice-ocean interactions. *Geophysical Research Letters,* Vol. 25, 3607–3610.

Neff, S., J. Burns, A. Mangini, M. Mudelsee, D. Fleitmann, and A. Matter (2001). Strong coherence between solar variability and the monsoon in Oman between 9 and 6 kyr ago. *Nature,* Vol. 411, 290–293.

Neff, U. (2001). *Massenspektrometrische Th/U-Datierung von Höhlensintern aus dem Oman: Klimaarchive des asiatischen Monsuns*. Ph. D. thesis, Heidelberg Academy of Sciences, Heidelberg.

Nguetsop, V. F., S. Servant-Vildary, and M. Servant (2004). Late Holocene climatic changes in west Africa, a high resolution diatom record from equatorial Cameroon. *Quaternary Science Reviews,* Vol. 23, 591–609.

Núñez Jiménez, A., N. Viña, M. Acevedo, J. Mateo, M. Itturalde-Vinent, and A. Graña (1988). Cuevas y Carsos, Editorial Científico-Técnica. Technical report, Ministerio de Cultura, Ciudad de Habana, Cuba.

Nyberg, J., B. A. Malmgren, A. Winter, M. R. Jury, K. Halimeda Kilbourne, and T. M. Quinn (2005). Low Atlantic hurricane activity in the 1970s and 1980s compared to the past 270 years. *Nature,* Vol. 447, 698–701.

O'Brien, S. R., P. A. Mayewski, L. D. Meeker, D. A. Meese, M. S. Twickler, and S. I. Whitlow (1995). Complexity of Holocene Climate as Reconstructed from a Greenland Ice Core. *Science,* Vol. 270, 1962.

Pajón, J. M., I. Hernández, F. Ortega, and J. Macle (2001). Periods of wet climate in Cuba: evaluation of expression in karst of Sierra de San Carlos. In V. Markgraf (Ed.), *Interhemispheric Climate Linkages*, Chapter 13, pp. 217–226. San Diego: Academic Press.

Parise, M., M. V. Valdés, R. Potenza, U. del Vecchio, A. Marangella, F. Maurano, and L. D. Torres (2005). Geological and morphological observations in the Eastern part of the Gran Caverna de Santo Tomás, Cuba (results of the 'Santo Tomás 2003' speleological expedition). *Cave and Karst Science, Transactions of the British Cave Research Association,* Vol. 32, No. 1.

Patterson, W. P., G. R. Smith, and K. C. Lohmann (1993). Continental paleothermometry and seasonality using the isotopic composition of aragonitic otoliths of freshwater fishes. *Geophysical Monograph,* Vol. 78, 191–202.

Peros, M. C., E. G. Reinhardt, and A. M. Davis (2007). A 6000-year record of ecological and hydrological changes from Laguna de la Leche, north coastal Cuba. *Quaternary Research,* Vol. 67, 69–82.

Poage, M. A. and C. P. Chamberlain (2001). Empirical relationships between elevation and the stable isotope composition of precipitation and surface waters: considerations for studies of paleoelevation change. *American Journal of Science,* Vol. 301, 1–15.

Poveda, G., P. R. Waylen, and R. S. Pulwarty (2006). Annual and inter-annual variability of the present climate in northern South America and southern Mesoamerica. *Palaeogeography, Palaeoclimatology, Palaeoecology,* Vol. 234, 3–27.

Pozo-Vàzquez, D., M. J. Esteban-Parra, F. S. Rodrigo, and Y. Castro-Diez (2000). An analysis of the variability of the North Atlantic Oscillation in the time and the frequency domain. *International Journal of Climatology,* Vol. 20, 1675–1692.

Reed, R., W. J. Campell, L. A. Rasmussen, and D. G. Rogers (1961). Evidence of a down propagating, annual wind reversal in the equatorial stratosphere. *Journal of Geophysical Research,* Vol. 66, 813–818.

Rein, B., A. Lückge, L. Reinhardt, F. Sirocko, A. Wolf, and W.-C. Dullo (2005). El Niño variability off Peru during the last 20,000 years. *Paleoceanography,* Vol. 20, PA4003.

Richards, D. A. and J. A. Dorale (2003). Uranium-series chronology and environmental applications of speleothems. *Reviews in Mineralogy & Geochemistry,* Vol. 52, 407–460.

Rietveld, H. M. (1967). Line Profiles of Neutron Powder-diffraction Peaks for Structure Refinement. *Acta Crystallographica,* Vol. 22, 151–152.

Rietveld, H. M. (1969). A Profile Refinement Method for Nuclear and Magnetic Structures. *Journal of Applied Crystallography,* Vol. 2, 65–71.

Rind, D. and J. Overpeck (1993). Hypothesized causes of decade-to-century-scale climate variability: Climate model results. *Quaternary Science Reviews,* Vol. 12, 357.

Rind, D. and J. Overpeck (1995). Modeling the Possible Causes of Decadal-to-Millennial-Scale Variability. In N. R. C. Climate Research Committee (Ed.), *Natural Climate Variability on Decade-to-Century Time Scales*, pp. 187–198. Washington DC: National Academy Press.

Rogers, J. C. (1988). Precipitation variability over the Caribbean and tropical Americas associated with the Southern Oscillation. *Journal of Climate,* Vol. 1, 172–182.

Romanov, D., G. Kaufmann, and W. Dreybrodt (2008). Modeling stalagmite growth by first principles of chemistry and physics of calcite precipitation. *Geochimica et Cosmochimica Acta,* Vol. 72, 423–437.

Ropelewski, C. F. and M. S. Halpert (1986). North American precipitation and temperature patterns associated with the El Niño/Southern Oscillation. *Monthly Weather Review,* Vol. 114, 2352–2362.

Ropelewski, C. F. and M. S. Halpert (1987). Global and regional scale precipitation patterns associated with the El Niño/Southern Oscillation. *Monthly Weather Review,* Vol. 115, 1606–1626.

Ropelewski, C. F. and M. S. Halpert (1989). Precipitation patterns associated with the high index phase of the southern oscillation. *Journal of Climate,* Vol. 2, 268–284.

Ropelewski, C. F. and M. S. Halpert (1996). Quantifying southern oscillation-precipitation relationships. *Journal of Climate,* Vol. 9, 1043–1059.

Rowell, D. P. (2003). The impact of Mediterranean SSTs on the Sahelian rainfall season. *Journal of Climate,* Vol. 16, 849–862.

Rowell, D. P., C. K. Folland, K. Maskell, J. A. Owen, and M. N. Ward (1992). Modelling the influence of global sea-surface temperatures on the variability and predictability of seasonal Sahel rainfall. *Geophysical Research Letters,* Vol. 19, 905–908.

Rowell, D. P., C. K. Folland, K. Maskell, and M. N. Ward (1995). Variability of summer rainfall over tropical North-Africa (1906-92) observations and modelling. *Quarterly Journal of the Royal Meteorological Society,* Vol. 121, 669–704.

Rozanski, K., L. Araguás-Araguás, and R. Gonfiantini (1993). Isotopic patterns in modern global precipitation. In P. K. Swart, K. L. Lohmann, J. McKenzie, and S. Savin (Eds.), *Climate Change in Continental Isotopic Records*, pp. 1–37. Washington, DC: American Geophysical Union.

Rudloff, W. (1981). *World-Climates, with Tables of Climatic Data and Practical Suggestions*. Stuttgart: Wissenschaftliche Verlagsgesellschaft mbH.

Saunders, M. A. and A. R. Harris (1997). Statistical evidence links exceptional

1995 Atlantic Hurricane season to record sea warming. *Geophysical Research Letters,* Vol. 24, 1255–1258.

Schlesinger, M. and N. Ramankutty (1994). An oscillation in the global climate system of period 65-70 years. *Nature,* Vol. 367, 723–726.

Schmittner, A., C. Appenzeller, and T. F. Stocker (2000). Enhanced Atlantic freshwater export during El Niño. *Geophysical Research Letters,* Vol. 27, 1163–1167.

Scholz, D. and D. Hoffmann (2008). ^{230}Th/U-dating of fossil corals and speleothems. *Quaternary Science Journal,* Vol. 57/1-2, 52–76.

Scholz, D., A. Mangini, and T. Felis (2004). U-series dating of diagenetically altered fossil reef corals. *Earth and Planetary Science Letters,* Vol. 218, 163–178.

Schrag, D. P., J. F. Adkins, K. McIntyre, J. L. Alexander, D. A. Hodell, C. D. Charles, and J. F. McManus (2002). The oxygen isotopic composition of seawater during the last glacial maximum. *Quaternary Science Reviews,* Vol. 21, 331–342.

Schrag, D. P., G. Hampt, and D. W. Murray (1996). Pore fluid constraints on the temperature and oxygen isotopic composition of the glacial ocean. *Science,* Vol. 272, 1930–1932.

Schulz, M. and M. Mudelsee (2002). REDFIT: estimating red-noise spectra directly from unevenly spaced paleoclimatic time series. *Computers & Geosciences,* Vol. 28, 421–426.

Schwarcz, H. P. (1986). Geochronology and isotopic geochemistry of speleothems. In P. Fritz and J. C. Fontes (Eds.), *Handbook of Environmental Isotope Geochemistry*, pp. 271–303. Amsterdam: Elsevier.

Seager, R., M. Ting, M. Davis, M. Cane, N. Naik, J. Nakamura, C. Li, E. Cook, and D. W. Stahle (2009). Mexican drought: an observational modeling and tree ring study of variability and climate change. *Atmósfera,* Vol. 22, No. 1, 1–31.

Shapiro, L. J. (1982). Hurricane climatic fluctuations. Part II: Relation to large-scale circulation. *Monthly Weather Review,* Vol. 110, 1007–1013.

Shapiro, L. J. and S. B. Goldenberg (1998). Atlantic Sea Surface Temperatures and Tropical Cyclone Formation. *Journal of Climate,* Vol. 11, 578–590.

Sharp, Z. (2007). *Principles of Stable Isotope Geochemistry.* Upper Saddle Ricer, NJ: Pearson Prentice Hall.

Shindell, D., D. Rind, N. Balachandran, J. Lean, and P. Lonergan (1999). Solar Cycle Variability, Ozone, and Climate. *Science,* Vol. 284, 305–308.

Shindell, D. T., G. A. Schmidt, M. E. Mann, D. Rind, and A. Waple (2001). Solar Forcing of Regional Climate Change During the Maunder Minimum. *Science,* Vol. 294, 2149.

Solanski, S., I. G. Usoskin, B. Kromer, M. Schüssler, and J. Beer (2004). Unusual activity of the Sun during recent decades compared to the previous 11,000 years. *Nature,* Vol. 431, 1084–1087.

Spence, J. M., M. A. Taylor, and A. A. Chen (2004). The effect of concurrent sea-surface temperature anomalies in the tropical Pacific and Atlantic on Caribbean rainfall. *International Journal of Climatology,* Vol. 24, 1531–1541.

Spötl, C. and D. Mattey (2006). Stable isotope microsampling of speleothems for palaeoenvironmental studies: a comparison of microdrill, micromill and laser ablation techniques. *Chemical Geology,* Vol. 235, 48–58.

Spötl, C. and T. Vennemann (2003). Continuous-flow IRMS analysis of carbonate minerals. *Rapid Communications of Mass Spectrometry,* Vol. 17, 1004–1006.

Stephenson, D., V. Pavan, and R. Bojariu (2000). Is the North Atlantic Oscillation a random walk? *International Journal of Climatology,* Vol. 20, 1–18.

Stocker, T. F. and L. A. Mysak (1992). Climatic fluctuations on the century time scale: a review on high resolution proxy data and possible mechanisms. *Climate Change,* Vol. 20, 227–250.

Stott, L., K. Cannariato, R. Thunell, G. H. Haug, A. Koutavas, and S. Lund (2004). Decline of surface temperature and salinity in the western tropical Pacific Ocean in the Holocene epoch. *Nature,* Vol. 431, 56.

Stuiver, M., P. M. Grootes, and T. F. Braziunas (1995). The GISP2 δ^{18}O Climate Record of the Past 16,500 Years and the Role of the Sun, Ocean, and Volcanoes. *Quaternary Research,* Vol. 44, No. 3, 341–354.

Stuiver, M., P. J. Reimer, E. Bard, W. Beck, G. S. Burr, K. A. Hughen, B. Kromer, F. G. McCormac, J. van der Pflicht, and M. Spurk (1998). INTCAL98 radiocarbon age calibration, 24,000 cal BP. *Radiocarbon,* Vol. 40, 1041–1083.

Sutton, R. T. and D. L. R. Hodson (2005). Atlantic Ocean forcing of North American and European summer climate. *Science,* Vol. 309, 115–118.

Tarutani, T., R. N. Clayton, and T. K. Mayeda (1969). The effect of polymorphism and magnesium substitution on oxygen isotope fractionation between calcium carbonate and water. *Geochimica et Cosmochimica Acta,* Vol. 33, 987–996.

Taylor, M. A., D. B. Enfield, and A. A. Chen (2002). Influence of the tropical Atlantic versus the tropical Pacific on Caribbean rainfall. *Journal of Geophysical Research,* Vol. 107, No. C9, 3127.

Teller, J. T., D. W. Leverington, and J. D. Mann (2002). Freshwater outbursts to the oceans from glacial Lake Agassiz and their role in climate change during the last deglaciation. *Quaternary Science Reviews,* Vol. 21, 879–887.

Terakado, Y. and A. Masuda (1988). The co-precipitation of rare-earth elements with calcite and aragonite. *Chemical Geology,* Vol. 69, 103–110.

Timmermann, A., U. Krebs, F. Justino, H. Goosse, and T. Ivanochko (2005). Mechanisms for millennial-scale global synchronization during the last glacial period. *Paleoceanography,* Vol. 20, PA4008.

Timmermann, A., M. Latif, R. Voss, and A. Grotzner (1998). Northern Hemispheric interdecadal variability: a coupled air-sea mode. *Journal of Climate,* Vol. 11, 1906–1931.

Timmermann, A., Y. Okumura, S. I. An, A. Clement, B.Dong, E. Guilyardi, A. Hu, J. H. Jungclaus, M. Renold, T. F. Stocker, R. J. Stouffer, R. Sutton, S.-P. Xie, and J. Yin (2007). The Influence of a weakening of the Atlantic meridional overturning circulation on ENSO. *Journal of Climate,* Vol. 20, 4899–4919.

Torrence, C. and G. P. Compo (1998). A Practical Guide to Wavelet Analysis. *Bulletin of American Meteorological Society,* Vol. 79, 61–78. Accesible at http://paos.colorado.edu/research/wavelets/.

Trenberth, K. E. (1997). The Definition of El Niño. *Bulletin of American Meteorological Society,* Vol. 78, 2771–2777.

Trouet, V., J. Esper, N. E. Graham, A. Baker, J. D. Scourse, and D. C. Frank (2009). Persistent Positive North Atlantic Oscillation Mode Dominated the Medieval Climate Anomaly. *Science,* Vol. 324, 78.

Van Geel, B., O. M. Raspopov, H. Renssen, J. van der Plicht, V. A. Dergachev, and H. A. J. Meijer (1999). The role of solar forcing upon climate change. *Quaternary Science Reviews,* Vol. 18, 331.

Vellinga, M. and P. Wu (2004). Low-Latitude Freshwater Influence on Centennial Variability of the Atlantic Thermohaline Circulation. *Journal of Climate,* Vol. 17, 4498–4511.

Verschuren, D., K. R. Laird, and B. F. Cumming (2000). Rainfall and drought in equatorial east Africa during the past 1,100 years. *Nature,* Vol. 403, 410.

von Grafenstein, U., H. Erlenkeuser, J. Müller, J. Jouzel, and S. Johnsen (1998). The cold event 8200 years ago documented in oxygen isotope records of precipitation in Europe and Greenland. *Climate Dynamics,* Vol. 14, 73–81.

Vose, R. S., R. L. Schmoyer, P. M. Steurer, T. C. Peterson, R. Heim, T. R. Karl, and J. Eischeid (1992). The Global Historical Climatology Network: long-term monthly temperature, precipitation, sea level pressure, and station pressure data. *Carbon Dioxide Information Analysis Center Communications,* Vol. 17, ORNL/ CDIAC–53, NDP–041. Oak Ridge National Laboratory, Oak Ridge, TN.

Vuille, M., R. S. Bradley, M. Werner, R. Healy, and F. Keimig (2003). Modeling δ^{18}O in precipitation over the tropical Americas: 1. Interannual variability and climatic controls. *Journal of Geophysical Research,* Vol. 108, No. D6, 4174.

Waliser, D., Z. Shi, J. R. Lanzante, and A. H. Oort (1999). The Hadley Cell circulation: assessing NCEP/NCAR reanalysis and sparse in-situ estimates. *Climate Dynamics,* Vol. 15, 719–735.

Walter, K. and H.-F. Graf (2002). On the changing nature of the regional connection between the North Atlantic Oscillation and sea surface temperature. *Journal of Geophysical Research,* Vol. 107, No. D17, 4338.

Wang, C. (2002a). Atmospheric Circulation Cells Associated with the El Niño-Southern Oscillation. *Journal of Climate,* Vol. 15, 399–419.

Wang, C. (2002b). Atlantic Climate Variability and Its Associated Atmospheric Circulation Cells. *Journal of Climate,* Vol. 15, 1516–1536.

Wanner, H., J. Beer, J. Bütikofer, T. J. Crowley, U. Cubasch, J. Flückiger, H. Goosse, M. Grosjean, F. Joos, J. O. Kaplan, M. Küttel, S. A. Müller, I. C. Prentice, O. Solomina, T. F. Stocker, P. Tarasov, M. Wagner, and M. Widmannm (2008). Mid- to Late Holocene climate change: an overview. *Quaternary Science Reviews,* Vol. 27, 1791–1828.

Wanner, H., S. Brönnimann, C. Casty, D. Gyalistras, J. Luterbacher, C. Schmutz, D. B. Stevenson, and E. Yoplaki (2001). North Atlantic Osclillation, Concepts and Studies. *Surveys in Geophysics,* Vol. 22, 321–382.

Waple, A., M. E. Mann, and R. S. Bradley (2000). Long-term patterns of solar irradiance forcing in model experiments and proxy based surface temperature reconstructions. *Climate Dynamics,* Vol. 18, No. 7, 563–578.

Wedepohl, H. K. (1995). The composition of the continental crust. *Geochimica et Cosmochimica Acta,* Vol. 59, 1217–1232.

Zebiak, S. E. and M. A. Cane (1987). A model El Ninño-Southern Oscillation. *Monthly Weather Review,* Vol. 115, 2262–2278.

Zhang, R. and D. L. Delworth (2005). Simulated Tropical Response to a Substantial Weakening of the Atlantic Thermohaline Circulation. *Journal of Climate,* Vol. 18, 1853–1860.

Danksagung

An dieser Stelle möchte ich mich bei all jenen bedanken, die diese Arbeit ermöglicht, zu ihrem Gelingen beigetragen und mich auf dem Weg durch die Doktorarbeit begleitet haben.
Besonders bedanken möchte ich mich bei Prof. Dr. Augusto Mangini, für die spannende Fragestellung und die wertvolle Betreuung dieser Arbeit. Dafür, dass sein Büro immer offen steht, er sich immer Zeit zum Diskutieren nimmt und immer offen war für neue Ideen.
Ebenfalls ein großer Dank geht an Prof. Dr. Denis Scholz, der als Mitantragsteller des CariClim-Projektes diese Arbeit mit betreut hat. Die konstruktive Kritik und das offene Ohr haben mir fachlich und menschlich immer einen Weg gewiesen! Vielen Dank auch für das Korrekturlesen!
Ein großer Dank an Prof. Dr. Aeschbach-Hertig, der sich freundlicherweise bereit erklärt hat, das Zweitgutachten für diese Arbeit zu übernehmen.
Den Auslandsaufenthalt in England wurde erst durch Dirk und Denis möglich, bei denen ich mich herzlich bedanken möchte! Für die Einblicke ins MC-ICPMS und in britische Lebensweisen!
Andrea, danke für die Unterstützung beim Monitoring und beim Aragonit! Für das Korrekturlesen und dafür, dass sie mir das 'Ommm' beigebracht hat!
Danke an René, für das unermüdliche Beibringen von TIMS, auf dass ein Count kommt.
Many thanks also go to Cyril and Wei, for the wonderful cooperation and the fruitful and nice time in Bremen!
Vielen Dank an die tolle Arbeitsgruppe, das 'beste Büro der Welt', und an alle Freunde, die mich während meiner Doktorandenzeit begleitet haben und mir zeigten, was wirklich wichtig ist im Leben!
Ganz besonders möchte ich meinen Eltern danken, die mir mein Studium erst ermöglichten und mir während der gesamten Studien- und Doktorandenzeit immer mit unermüdlichem Rat und Tat zur Seite standen. Ebenfalls möchte ich mich bei meiner Schwester und bei meiner Großmutter bedanken, die mich immer wertvoll unterstützen und immer ein offenes Ohr für mich haben.